THE MINISTRY OF SCIENCE AND HIGHER EDUCATION OF THE RUSSIAN FEDERATION



ST. PETERSBURG STATE POLYTECHNICAL UNIVERSITY

JOURNAL

Physics and Mathematics

VOLUME 19, No.2, 2026

Peter the Great St. Petersburg
Polytechnic University
2026

ST. PETERSBURG STATE POLYTECHNICAL UNIVERSITY JOURNAL.
PHYSICS AND MATHEMATICS

JOURNAL EDITORIAL COUNCIL

A.I. Borovkov – vice-rector for perspective projects;
VA.I. Rudskoy – full member of RAS;
A.E. Zhukov – corresponding member of RAS.

JOURNAL EDITORIAL BOARD

V.K. Ivanov – Dr. Sci. (phys.-math.), prof., SPbPU, St. Petersburg, Russia, – editor-in-chief;
A.E. Fotiadi – Dr. Sci. (phys.-math.), prof., SPbPU, St. Petersburg, Russia, – deputy editor-in-chief;
V.M. Kapralova – Candidate of Phys.-Math. Sci., associate prof., SPbPU, St. Petersburg, Russia, – executive secretary;
V.I. Antonov – Dr. Sci. (phys.-math.), prof., SPbPU, St. Petersburg, Russia;
I.B. Bezprozvanny – Dr. Sci. (biology), prof., The University of Texas Southwestern Medical Center, Dallas, TX, USA;
A.V. Blinov – Dr. Sci. (phys.-math.), prof., SPbPU, St. Petersburg, Russia;
A.S. Cherepanov – Dr. Sci. (phys.-math.), prof., SPbPU, St. Petersburg, Russia;
D.V. Donetski – Dr. Sci. (phys.-math.), prof., State University of New York at Stony Brook, NY, USA;
V.V. Dubov – Dr. Sci. (phys.-math.), prof., SPbPU, St. Petersburg, Russia;
D.A. Firsov – Dr. Sci. (phys.-math.), prof., SPbPU, St. Petersburg, Russia;
P.A. Karaseov – Dr. Sci. (phys.-math.), prof., SPbPU, St. Petersburg, Russia;
A.S. Kheifets – Ph.D., prof., Australian National University, Canberra, Australia;
O.S. Loboda – Candidate of Phys.-Math. Sci., associate prof., SPbPU, St. Petersburg, Russia;
J.B. Malherbe – Dr. Sci. (physics), prof., University of Pretoria, Republic of South Africa;
V.M. Ostryakov – Dr. Sci. (phys.-math.), prof., SPbPU, St. Petersburg, Russia;
V.E. Privalov – Dr. Sci. (phys.-math.), prof., SPbPU, St. Petersburg, Russia;
E.M. Smirnov – Dr. Sci. (phys.-math.), prof., SPbPU, St. Petersburg, Russia;
A.V. Solov'yov – Dr. Sci. (phys.-math.), prof., MBN Research Center, Frankfurt am Main, Germany;
A.K. Tagantsev – Dr. Sci. (phys.-math.), prof., Swiss Federal Institute of Technology, Lausanne, Switzerland;
I.N. Toptygin – Dr. Sci. (phys.-math.), prof., SPbPU, St. Petersburg, Russia.

The journal is included in the List of leading peer-reviewed scientific journals and other editions to publish major findings of theses for the research degrees of Doctor of Sciences and Candidate of Sciences.

The publications are presented in the VINITI RAS Abstract Journal and Ulrich's Periodical Directory International Database.

The journal is published since 2008 as part of the periodical edition 'Nauchno-tekhnicheskie vedomosti SPb-GPU'.

The journal is registered with the Federal Service for Supervision in the Sphere of Telecom, Information Technologies and Mass Communications (ROSKOMNADZOR). Certificate ПИ № ФС77-52144 issued December 11, 2012.

The journal is in the **Web of Science** (Emerging Sources Citation Index), **Scopus,** the **Russian Science Citation Index** (RSCI) and the **Directory of Open Access Journals** (DOAJ) databases.

© Scientific Electronic Library (http://www.elibrary.ru).

No part of this publication may be reproduced without clear reference to the source.

The views of the authors may not represent the views of the Editorial Board.

Address:
195251 Politekhnicheskaya St. 29, St. Petersburg, Russia.
Phone: 8 (812) 552-62-16.
http://ntv.spbstu.ru/physics

© Peter the Great St. Petersburg
Polytechnic University, 2026

МИНИСТЕРСТВО НАУКИ И ВЫСШЕГО ОБРАЗОВАНИЯ РОССИЙСКОЙ ФЕДЕРАЦИИ



НАУЧНО-ТЕХНИЧЕСКИЕ ВЕДОМОСТИ

САНКТ-ПЕТЕРБУРГСКОГО ГОСУДАРСТВЕННОГО ПОЛИТЕХНИЧЕСКОГО УНИВЕРСИТЕТА

Физико-математические науки

ТОМ 19, №2, 2026

Санкт-Петербургский политехнический
университет Петра Великого
2026

НАУЧНО-ТЕХНИЧЕСКИЕ ВЕДОМОСТИ САНКТ-ПЕТЕРБУРГСКОГО ГОСУДАРСТВЕННОГО ПОЛИТЕХНИЧЕСКОГО УНИВЕРСИТЕТА. ФИЗИКО-МАТЕМАТИЧЕСКИЕ НАУКИ

РЕДАКЦИОННЫЙ СОВЕТ ЖУРНАЛА

Боровков А.И., проректор по перспективным проектам;
Жуков А.Е., чл.-кор. РАН;
Рудской А.И., академик РАН.

РЕДАКЦИОННАЯ КОЛЛЕГИЯ ЖУРНАЛА

Иванов В.К., д-р физ.-мат. наук, профессор, СПбПУ, СПб., Россия, – главный редактор;
Фотиади А.Э., д-р физ.-мат. наук, профессор, СПбПУ, СПб., Россия, – зам. главного редактора;
Капралова В.М., канд. физ.-мат. наук, доцент, СПбПУ, СПб., Россия – ответственный секретарь;
Антонов В.И., д-р физ.-мат. наук, профессор, СПбПУ, СПб., Россия;
Безпрозванный И.Б., д-р биол. наук, профессор, Юго-Западный медицинский центр Техасского университета, Даллас, США;
Блинов А.В., д-р физ.-мат. наук, профессор, СПбПУ, СПб., Россия;
Донецкий Д.В., д-р физ.-мат. наук, профессор, университет штата Нью-Йорк в Стоуни-Брук, США;
Дубов В.В., д-р физ.-мат. наук, профессор, СПбПУ, СПб., Россия;
Карасёв П.А., д-р физ.-мат. наук, профессор, СПбПУ, СПб., Россия;
Лобода О.С., канд. физ.-мат. наук, доцент, СПбПУ, СПб., Россия;
Малерб Й.Б., Dr.Sc. (Physics), профессор, университет Претории, ЮАР;
Остряков В.М., д-р физ.-мат. наук, профессор, СПбПУ, СПб., Россия;
Привалов В.Е., д-р физ.-мат. наук, профессор, СПбПУ, СПб., Россия;
Смирнов Е.М., д-р физ.-мат. наук, профессор, СПбПУ, СПб., Россия;
Соловьёв А.В., д-р физ.-мат. наук, профессор, Научно-исследовательский центр мезобионаносистем (MBN), Франкфурт-на-Майне, Германия;
Таганцев А.К., д-р физ.-мат. наук, профессор, Швейцарский федеральный институт технологий, Лозанна, Швейцария;
Топтыгин И.Н., д-р физ.-мат. наук, профессор, СПбПУ, СПб., Россия;
Фирсов Д.А., д-р физ.-мат. наук, профессор, СПбПУ, СПб., Россия;
Хейфец А.С., Ph.D. (Physics), профессор, Австралийский национальный университет, Канберра, Австралия;
Черепанов А.С., д-р физ.-мат. наук, профессор, СПбПУ, СПб., Россия.

Журнал с 2002 г. входит в Перечень ведущих рецензируемых научных журналов и изданий, в которых должны быть опубликованы основные результаты диссертаций на соискание ученых степеней доктора и кандидата наук.

Сведения о публикациях представлены в Реферативном журнале ВИНИТИ РАН, в международной справочной системе «Ulrich's Periodical Directory».

С 2008 года выпускается в составе сериального периодического издания «Научно-технические ведомости СПбГПУ».

Журнал зарегистрирован Федеральной службой по надзору в сфере информационных технологий и массовых коммуникаций (Роскомнадзор). Свидетельство о регистрации ПИ № ФС77-52144 от 11 декабря 2012 г.

Журнал индексируется в базах данных **Web of Science** (Emerging Sources Citation Index), **Scopus**, а также включен в базы данных **«Российский индекс научного цитирования»** (РИНЦ), размещенную на платформе Научной электронной библиотеки на сайте http://www.elibrary.ru, и **"Directory of Open Access Journals"** (DOAJ).

При перепечатке материалов ссылка на журнал обязательна.

Точка зрения редакции может не совпадать с мнением авторов статей.

Адрес редакции и издательства:

Россия, 195251, Санкт-Петербург, ул. Политехническая, д. 29.

Тел. редакции 8 (812) 552-62-16.

http://ntv.spbstu.ru/physics

© Санкт-Петербургский политехнический университет Петра Великого, 2026

Contents

Condensed matter physics

Kniazeva M. A., Zhukova N. S., Vakulenko A. F. *The effect of electric field switching modes on polarization properties of the lead zirconate-titanate-based epitaxial heterostructures* 9

Simulation of physical processes

Ermakova K. K., Zasimova M. A., Ivanov N. G. *Study of vortex flows generated by a pulsed turbulent buoyant jet* 16

Adiatullin V. R., Galaev S. A., Ris V. V., Zasimova M. A., Ivanov N. G. *On the instability of counterflowing wall jets in a ventilated cavity* 27

Baranov M. A., Tsybin O. Yu. *Supercomputer simulation of the dynamics of oligomers of a number of amino acids (Gly, Ala, Trp, Val) in the infrared electromagnetic field* 39

Dolzhenko D. I., Letkiman E. D. *The influence of a silica trench profile on the photosensitivity of a CMOS-compatible APD in the visible range* 57

Alifov A. A. *The mixed parametric and self-oscillations: The effect of nonlinear parametric excitation and delays on them causing self-oscillations* 68

Experimental technique and devices

Kozlovskiy S. S., Gunkov P. S., Berdnikov Ya. A., Donskikh-Tyrsa V. A. *The thickness determination of coatings by X-ray fluorescent analysis using a calibration curve obtained by calculations* 76

Physical electronics

Khujaniyozov J. B., Umirzakov B. E., Tashmukhamedova D. A., Loboda V. V., Abduvayitov A. A. *The influence of Ar^+ and Cd^+ ion implantation on the composition and electronic structure of monocrystalline zinc telluride* 84

Klevtsov A. I., Karaseov P. A., Titov A. I. *Radiation defect formation during sequential ion bombardment of alpha-gallium oxide* 98

Physical materials technology

Zhurikhina V. V., Babich E. S., Terpitskiy A. N., Nuritdinov I., Rakhmatov M. A., Eshbekov A. A. *Plasmonic nanomaterials formed by ion exchange in glass: properties and applications* 107

Nassif A., Yousef R., Yousef A., Kadhim Sh. A. *Structural properties of some nanocrystalline spinel chromites prepared by solid-state reaction method* 136

Biophysics and medical physics

Goncharov I. D., Sadova A. I., Nuzhin I. M., Tenitskaya P. A., Kurdyumova I. V., Gorkovskaia A. A., Khodorkovskiy M. A., Alekseev A. A. *Differences in the interaction of RAD51 and UvsX recombinases with DNA revealed by single-molecule experiments* 147

Nuclear physics

Bannikov E. V., Berdnikov Ya. A., Larionova D. M., Kotov D. O., Basirov K. N., Borisov I. I. *Azimuthal dependences of the nuclear modification factors of π^0 mesons in Cu+Au collisions at an energy of 200 GeV and U+U collisions at 193 GeV* 160

Kruashvili D. V., Berdnikov Ya. A. *Double longitudinal spin asymmetry of J/ψ mesons produced in proton-proton collisions with longitudinal polarization* 171

Mechanics

Smirnova N. A. *The damping of pendulum oscillations using a parametric controller* 178

Содерж ние

Физика конденсированного состояния

Князева М. А., Жукова Н. С., Вакуленко А. Ф. *Влияние режимов переключения электрического поля на поляризационные свойства эпитаксиальных гетероструктур на основе цирконата-титаната свинца* 9

Математическое моделирование физических процессов

Ермакова К. К., Засимова М. А., Иванов Н. Г. *Исследование вихревых течений, сформированных импульсной турбулентной плавучей струей* 16

Адиатуллин В. Р., Галаев С. А., Рис В. В., Засимова М. А., Иванов Н. Г. *О неустойчивости встречных пристенных струй в вентилируемой полости* 27

Баранов М. А., Цыбин О. Ю. *Суперкомпьютерное моделирование динамики олигомеров ряда аминокислот (Gly, Ala, Trp, Val) в электромагнитном поле инфракрасного диапазона* 39

Долженко Д. И., Леткиман Е. Д. *Влияние профиля траншеи из диоксида кремния на фоточувствительность КМОП-совместимого лавинного фотодиода видимого диапазона* 57

Алифов А. А. *Смешанные параметрические и автоколебания: действие на них нелинейного параметрического возбуждения и запаздывания, вызывающего автоколебания* 68

Приборы и техника физического эксперимента

Козловский С. С., Гуньков П. С., Бердников Я. А., Донских-Тырса В. А. *Определение толщины покрытий методом рентгенофлуоресцентного анализа с использованием градуировочной зависимости, полученной расчетным путем* 76

Физическая электроника

Хужаниёзов Ж. Б., Умирзаков Б. Е., Ташмухамедова Д. А., Лобода В. В., Абдувайитов А. А. *Влияние имплантации ионов Ar^+ и Cd^+ на состав и электронную структуру монокристаллического теллурида цинка* 84

Клевцов А. И., Карасев П. А., Титов А. И. *Образование устойчивых радиационных повреждений при последовательной ионной бомбардировке альфа-оксида галлия* 98

Физическое материаловедение

Журихина В. В., Бабич Е. С., Терпицкий А. Н., Нуритдинов И., Рахматов М. А., Эшбеков А. А. *Плазмонные наноматериалы, формируемые методом ионного обмена в стекле: свойства и применение* 107

Нассиф А., Юсеф Р., Юсеф А., Кадхим Ш. А. *Структурные свойства двух нанокристаллических хромшпинелей, полученных методом твердофазной реакции (статья на английском языке)* 136

Биофизика и медицинская физика

Гончаров И. Д., Садова А. И., Нужин И. М., Теницкая П. А., Курдюмова И. В., Горьковская А. А., Ходорковский М. А., Алексеев А. А. *Различия во взаимодействии рекомбиназ RAD51 и UvsX с ДНК, выявленные в экспериментах на уровне одиночных молекул* 147

Ядерная физика

Банников Е. В., Бердников Я. А., Ларионова Д. М., Котов Д. О., Басиров К. Н., Борисов И. И. *Азимутальные зависимости факторов ядерной модификации π^0-мезонов в столкновениях релятивистских ядер меди и золота при энергии 200 ГэВ и ядер урана при 193 ГэВ* 160

Круашвили Д. В., Бердников Я. А. *Двойная продольная спиновая асимметрия (J/ψ)-мезонов, рожденных в продольно-поляризованных протон-протонных столкновениях* 171

Механика

Смирнова Н. А. *Подавление колебаний маятника с помощью параметрического регулятора* 178

CONDENSED MATTER PHYSICS

Original article
DOI: https://doi.org/10.18721/JPM.19201

THE EFFECT OF ELECTRIC FIELD SWITCHING MODES ON POLARIZATION PROPERTIES OF THE LEAD ZIRCONATE-TITANATE-BASED EPITAXIAL HETEROSTRUCTURES

M. A. Kniazeva✉, *N. S. Zhukova*, *A. F. Vakulenko*

Peter the Great St. Petersburg Polytechnic University, St. Petersburg, Russia

✉ kniazeva.maria225@yandex.ru

Abstract. In order to extend the serviceability of ferroelectric devices, this paper proposes an experimental approach (for the first time) to clearing up the mechanism of polarization fatigue development in a lead zirconate titanate-based ferroelectric thin film. For this purpose, the influence of the recording pulse sequence configuration on the polarization of a selected object has been analyzed. The coercive field (CF) and remanent polarization of ferroelectric hysteresis loops were compared under two electric field application modes (they differed in the order of positive and negative pulses). The change in CF components was found to be insignificant during cyclic switching, whereas the difference between CF values reached 10% or more after pauses between the measurements. Experiments showed that the polarity of the final pulse of the switching signal set favorable conditions for stabilizing domains in the film whose dipole moment was aligned with the pulse polarity, and after resuming the measurements, a field of higher intensity was required to reverse the polarization.

Keywords: ferroelectric, epitaxial thin film, polarization fatigue, remanent polarization

Funding: The reported study was funded by Russian Science Foundation (Project No. 24-22-00453 "The effect of epitaxial strain on the structure switching in the antiferroelectric heterostructures based on lead hafnate").

C**itation:** Kniazeva M. A., Zhukova N. S., Vakulenko A. F., The effect of electric field switching modes on polarization properties of the lead zirconate titanate-based epitaxial heterostructures, St. Petersburg State Polytechnical University Journal. Physics and Mathematics. 19 (2) (2026) 9–15. DOI: https://doi.org/10.18721/JPM.19201

This is an open access article under the CC BY-NC 4.0 license (https://creativecommons.org/licenses/by-nc/4.0/)

Научная статья
УДК 538.956
DOI: https://doi.org/10.18721/JPM.19201

ВЛИЯНИЕ РЕЖИМОВ ПЕРЕКЛЮЧЕНИЯ ЭЛЕКТРИЧЕСКОГО ПОЛЯ НА ПОЛЯРИЗАЦИОННЫЕ СВОЙСТВА ЭПИТАКСИАЛЬНЫХ ГЕТЕРОСТРУКТУР НА ОСНОВЕ ЦИРКОНАТА-ТИТАНАТА СВИНЦА

М. А. Князева✉, *Н. С. Жукова*, *А. Ф. Вакуленко*

Санкт-Петербургский политехнический университет Петра Великого, Санкт-Петербург, Россия

✉ kniazeva.maria225@yandex.ru

Аннотация. С целью продления работоспособности устройств на основе сегнетоэлектриков, в работе впервые предложен экспериментальный подход к выяснению механизма развития поляризационной усталости в тонкой сегнетоэлектрической пленке на основе цирконата-титаната свинца. Для этого проанализировано влияние

© Kniazeva M. A., Zhukova N. S., Vakulenko A. F., 2026. Published by Peter the Great St. Petersburg Polytechnic University.

конфигурации последовательности записывающих импульсов на поляризацию выбранного объекта. При двух режимах приложения электрического поля (они различались порядком следования положительных и отрицательных импульсов) было проведено сравнение значений коэрцитивного поля (КП) и остаточной поляризации сегнетоэлектрических петель гистерезиса. Установлено, что в моменты циклических переключений изменение компонент КП незначительно, тогда как после пауз между измерениями разница между значениями КП достигала %10 и более. Эксперименты показали, что полярность завершающего импульса переключающего сигнала задает благоприятные условия для стабилизации в пленке доменов, дипольный момент которых сонаправлен с полярностью импульса, и после возобновления измерений требуется поле большей величины для изменения поляризации на противоположную.

Ключевые слова: сегнетоэлектрик, эпитаксиальная гетероструктура, поляризационная усталость, остаточная поляризация, цирконат-титанат свинца

Финансирование: Исследование выполнено при финансовой поддержке гранта Российского научного фонда (Проект № 24-22-00453 «Влияние эпитаксиальных натяжений на структурные переключения в антисегнетоэлектрических гетероструктурах на основе гафната свинца»).

Ссылка для цитирования: Князева М. А., Жукова Н. С., Вакуленко А. Ф. Влияние режимов переключения электрического поля на поляризационные свойства эпитаксиальных гетероструктур на основе цирконата-титаната свинца // Научно-технические ведомости СПбГПУ. Физико-математические науки. 2026. Т. 19. № 2. С. 9–15. DOI: https://doi.org/10.18721/JPM.19201

Статья открытого доступа, распространяемая по лицензии CC BY-NC 4.0 (https://creativecommons.org/licenses/by-nc/4.0/)

Introduction

Thin-film ferroelectric capacitors attract considerable interest due to their wide range of applications. One such application is ferroelectric random access non-volatile memory (FeRAM), combining the high speed of random-access memory with the ability to retain data when power is switched off [1, 2]. In such devices, information is written by applying pulses of a certain polarity: a negative pulse sets the memory cell to logic “0”, while a positive pulse sets it to logic “1”. The key advantage of these devices lies in their material: ferroelectrics provide fast polarization switching and non-volatile data storage without a constant power supply.

However, one of the main obstacles to commercialization of ferroelectric devices is polarization fatigue, i.e., a decrease in remanent polarization after a large number of write cycles. As a result of fatigue, the states corresponding to logic “0” and “1” become less distinguishable.

This phenomenon has been the focus of much research, and several possible causes of polarization fatigue have been proposed. According to [3], the main mechanisms involve inhibition of domain nucleation and freezing of domain walls in the ferroelectric crystal. Beyond identifying these mechanisms, many studies have analyzed such contributing factors as capacitor and electrode materials [4–6], operating temperature [7], size effects [8], applied field parameters [9], and others. Nevertheless, many fundamental and applied questions remain unresolved.

The goal of this work is to find an effective approach to extending the service life of ferroelectric devices that would additionally provide insight into the mechanism of polarization fatigue.

Exploratory approach to the problem

The proposed approach to identifying the mechanism of polarization fatigue in the object of study, a thin ferroelectric PZT film, is discussed here for the first time. Our objective was to experimentally assess how the configuration of the writing pulse sequence affects the polarization properties of this film. To this end, a voltage was applied to the film in each write cycle as a sequence consisting of two pairs of triangular pulses with positive and negative polarity. We needed to determine how the coercive field and remanent polarization evolve over time under two different pulse sequence configurations.

© Князева М. А., Жукова Н. С., Вакуленко А. Ф., 2026. Издатель: Санкт-Петербургский политехнический университет Петра Великого.

In the first case, a pair of positive pulses was applied to the film first, followed by a pair of negative pulses.

In the second case, the order of the pulse pairs was reversed.

Two parameters of the ferroelectric hysteresis loops recorded in each write cycle were monitored: the magnitudes of the remanent polarization $|\mathbf{P}_r|$ and the coercive field $|\mathbf{E}_c|$.

The remanent polarization $\mathbf{P}_r$ is a vector quantity that retains its value in a ferroelectric capacitor after the electric field is removed; its change under repeated field application characterizes the polarization fatigue of the material.

The coercive field $\mathbf{E}_c$ corresponds to the electric field that must be applied to the crystal to reverse the sign of the polarization.

Based on the measurement results, we plotted the positive and negative components of $\mathbf{E}_c$ and $\mathbf{P}_r$ as functions of the number of write cycles for the different sequence configurations.

Analysis of the obtained dependences makes it possible to assess the effect of the pulse sequence configuration on the processes occurring in the ferroelectric film.

Methods

Sample preparation. The object of study was an epitaxial $PbZr_{0.3}Ti_{0.7}O_3/LaSr_{0.7}Mn_{0.3}O_3$ (PZT/LSMO) heterostructure grown on a $SrTiO_3$ (STO) substrate by pulsed laser deposition. The PZT and LSMO layers (the latter serving as the bottom electrode) were 60 and 50 nm thick, respectively. The fabrication procedure is described in more detail in [10], where it is given for a similar sample. Gold electrodes 60 nm thick were deposited onto the film (Fig. 1,*a*). To improve adhesion of the contact, a 4.8-nm chromium interlayer was deposited between the film and the electrodes.

Measurement details. The triangular pulses of the control field had an amplitude of ±8 V and a duration of 0.02 s. The choice of the triangular shape was dictated by the results in [11], where such writing pulses were used for slow cycling at a very low frequency.

The measurements were performed in series of 50 write cycles with 2-minute pauses between the series. The objective in the first stage of the study was to examine the polarization properties of the ferroelectric film over a small number of switching cycles (on the order of 10^3 write cycles), so as to focus on the film behavior in the absence of fatigue signs [3].

A ferroelectric hysteresis loop was recorded in each write cycle using the Sawyer–Tower method [12]. This method consists in measuring the charge of a reference capacitor series-connected to the sample. The measurement circuit was modified within the framework of the double-wave method [13, 14] to eliminate the dielectric and conductive contributions, which would otherwise distort the results. Fig. 1,*b* shows an example of a hysteresis loop recorded in each cycle, along with the approach used to determine the parameters of the $\mathbf{P}_r$ and $\mathbf{E}_c$ vectors.

The positive (E_c^+) and negative (E_c^-) components of the coercive field $\mathbf{E}_c$ are defined as the electric field at which the remanent polarization reaches half the value of the corresponding $\mathbf{P}_r$ components (P_r^+ and P_r^-).

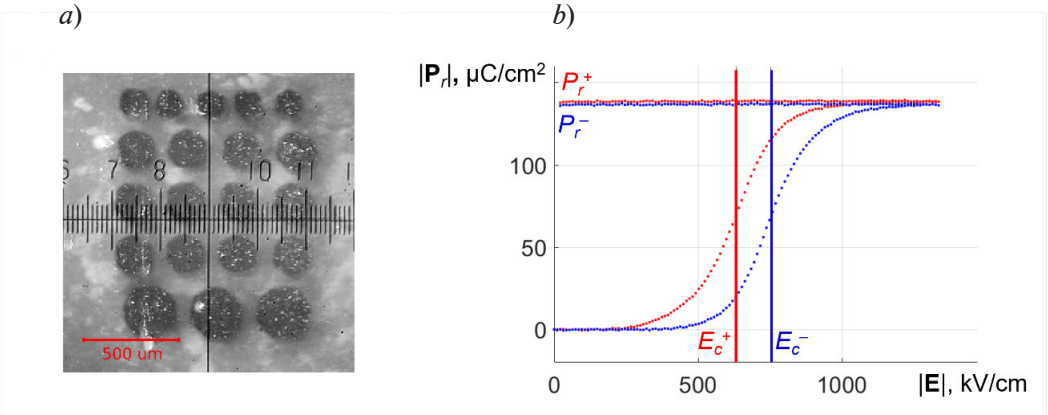


Fig. 1. Photograph of electrodes deposited on the film (*a*);
example of ferroelectric hysteresis loop measured in each write cycle (*b*);
P_r^+, P_r^- are the remanent polarization components; E_c^+, E_c^- are the coercive field components

Results and discussion

Fig. 2 shows the coercive field components as functions of the number of write cycles N for the two pulse sequence configurations. The vertical dashed line marks the point at which the pulse sequence configuration was changed. The differences between the measurement series, each consisting of 50 write cycles, are apparent from the plots. The coercive field components E_c^+ and E_c^- change only slightly for both pulse sequence configurations during cyclic switching, whereas jumps in $|\mathbf{E}|$ are observed after pauses between measurements. The amplitude of these jumps can reach 10% or more of the initial values.

Analyzing the dependence $|\mathbf{E}_c|(N)$, we can conclude that the effect of the pulse sequence configuration on E_c manifests itself as a correlation between the polarity of the last applied pulse and the amplitude of the jump in E_c after a pause between measurements.

If the preceding measurement series ended with pulses of negative polarity, then the amplitude of E_c^+ increased noticeably after the pause, while that of E_c^- decreased, and vice versa.

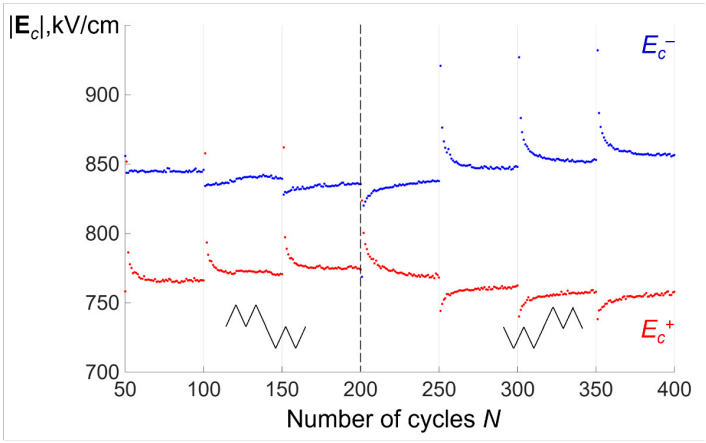


Fig. 2. Coercive field components $\mathbf{E}_c$ as functions of the number of write cycles for the two pulse sequence configurations
(the vertical dashed line marks the point at which the configuration was switched)

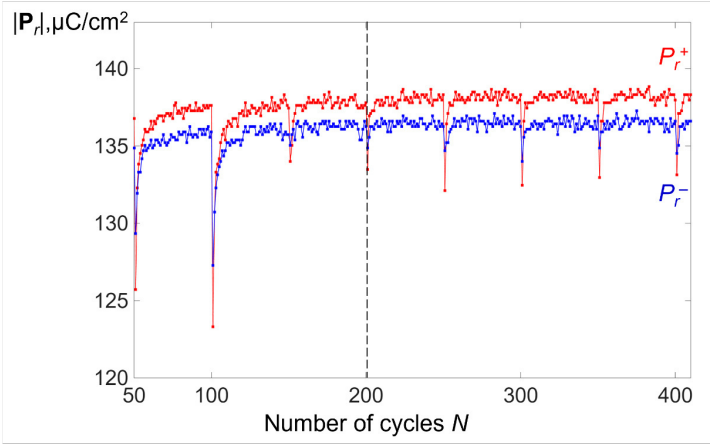


Fig. 3. Remanent polarization components $\mathbf{P}_r$ as functions of the number of write cycles for the two pulse sequence configurations

Taking into account the physical meaning of the coercive field E_c, this observation can be interpreted as follows: the polarity of the final writing pulse creates conditions under which domains whose dipole moments are oriented along the pulse direction become stabilized in the ferroelectric crystal.

Fig. 3 shows the remanent polarization components $\mathbf{P}_r$ as functions of the number of write cycles. As in Fig. 2, the experimental points belonging to individual measurement series are well distinguishable, and the pauses between the series are accompanied mainly by minor drops in $|\mathbf{P}_r|$. However, unlike the dependence $|\mathbf{E}_c|(N)$, changing the pulse sequence configuration from "two positive–two negative" to "two negative–two positive" has no qualitative effect on the behavior of $|\mathbf{P}_r|(N)$.

Conclusion

This study was conducted to evaluate how the configuration of switching pulses affects the remanent polarization and coercive field in a thin epitaxial lead zirconate titanate film. The analysis showed that the polarity of the final pulse applied to the film in a series of write cycles influences the jump in $|\mathbf{E}_c|$, creating favorable conditions for stabilizing domains whose dipole moments are aligned with the pulse polarity. No correlations were found between the polarity of this pulse and the sign of remanent polarization after the measurements were resumed.

We plan to further develop the approach proposed in this paper. One direction for future work is to gradually bring the writing parameters closer to those used in practical data storage devices, namely, by increasing the number of write cycles and reducing pulse duration.

REFERENCES

1. **Scott J. F., Kammerdiner L., Parris M., et al.,** Switching kinetics of lead zirconate titanate submicron thin-film memories, J. Appl. Phys. 64 (2) (1988) 787–792.

2. **Scott J. F.,** Applications of modern ferroelectrics, Science. 315 (5814) (2007) 954–959.

3. **Tagantsev A. K., Stolichnov I., Colla E. L., Setter N.,** Polarization fatigue in ferroelectric films: Basic experimental findings, phenomenological scenarios, and microscopic features, J. Appl. Phys. 90 (3) (2001) 1387–1402.

4. **Auciello O., Gifford K. D., Lichtenwalner D. J., et al.,** A review of composition-structure-property relationships for PZT-based heterostructure capacitors, Integr. Ferroelectr. 6 (1–4) (1995) 173–187.

5. **Nakamura T., Nakao Y., Kamisawa A., Takasu H.,** Preparation of $Pb(Zr,Ti)O_3$ thin films on Ir and IrO_2 electrodes, Jpn. J. Appl. Phys. 33 (9S) (1994) 5207–5210.

6. **Bornand V., Trolier-McKinstry S., Takemura K., Randall C. A.,** Orientation dependence of fatigue behavior in relaxor ferroelectric–$PbTiO_3$ thin films, J. Appl. Phys. 87 (8) (2000) 3965–3972.

7. **Taylor D. J., Larsen P. K., Dormans G. J. M., de Vierman A. E. M.,** Pulse switching characterization of organometallic chemical vapor deposited $PbZr_xTi_{1-x}O_3$ thin films for high-density memory applications, Integr. Ferroelectr. 7 (1–4) (1995) 123–138.

8. **Lee J. J., Thio C. L., Desu S. B.,** Electrode contacts on ferroelectric $Pb(Zr_xTi_{1-x})O_3$ and $SrBi_2Ta_2O_9$ thin films and their influence on fatigue properties, J. Appl. Phys. 78 (8) (1995) 5073–5078.

9. **Jin L., Li F., Zhang S.,** Decoding the fingerprint of ferroelectric loops: Comprehension of the material properties and structures, J. Am. Ceram. Soc. 97 (1) (2014) 1–27.

10. **Andreeva N. V., Vakulenko A. F., Petraru A., et al.,** Low-temperature dynamics of ferroelectric domains in $PbZr_{0.3}Ti_{0.7}O_3$ epitaxial thin films studied by piezoresponse force microscopy, Appl. Phys. Lett. 107 (15) (2015) 152904.

11. **Colla E. L., Taylor D. V., Tagantsev A. K., Setter N.,** Discrimination between bulk and interface scenarios for the suppression of the switchable polarization (fatigue) in $Pb(Zr,Ti)O_3$ thin films capacitors with Pt electrodes, Appl. Phys. Lett. 72 (19) (1998) 2478–2480.

12. **Sawyer C. B., Tower C. H.,** Rochelle salt as a dielectric, Phys. Rev. 35 (3) (1930) 269–273.

13. **Fukunaga M., Noda Y.,** New technique for measuring ferroelectric and antiferroelectric hysteresis loops, J. Phys. Soc. Jpn. 77 (6) (2008) 064706.

14. **Fukunaga M., Noda Y.,** Improvement of the double-wave method for ferroelectric hysteresis loops and its application to multiferroic $EuMn_2O_5$, J. Korean Phys. Soc. 55 (2(1)) (2009) 888–892.

СПИСОК ЛИТЕРАТУРЫ

1. **Scott J. F., Kammerdiner L., Parris M., Traynor S., Ottenbacher V., Shawabkeh A., Oliver W. F.** Switching kinetics of lead zirconate titanate submicron thin-film memories // Journal of Applied Physics. 1988. Vol. 64. No. 2. Pp. 787–792.

2. **Scott J. F.** Applications of modern ferroelectrics // Science. 2007. Vol. 315. No. 5814. Pp. 954–959.

3. **Tagantsev A. K., Stolichnov I., Colla E. L., Setter N.** Polarization fatigue in ferroelectric films: Basic experimental findings, phenomenological scenarios, and microscopic features // Journal of Applied Physics. 2001. Vol. 90. No. 3. Pp. 1387–1402.

4. **Auciello O., Gifford K. D., Lichtenwalner D. J., Dat R., Al-Shareef H. N., Bellur K. R., Kincon A. I.** A review of composition-structure-property relationships for PZT-based heterostructure capacitors // Integrated Ferroelectrics. 1995. Vol. 6. No. 1–4. Pp. 173–187.

5. **Nakamura T., Nakao Y., Kamisawa A., Takasu H.** Preparation of $Pb(Zr,Ti)O_3$ thin films on Ir and IrO_2 electrodes // Japanese Journal of Applied Physics. 1994. Vol. 33. No. 9S. Pp. 5207–5210.

6. **Bornand V., Trolier-McKinstry S., Takemura K., Randall C. A.** Orientation dependence of fatigue behavior in relaxor ferroelectric–$PbTiO_3$ thin films // Journal of Applied Physics. 2000. Vol. 87. No. 8. Pp. 3965–3972.

7. **Taylor D. J., Larsen P. K., Dormans G. J. M., de Vierman A. E. M.** Pulse switching characterization of organometallic chemical vapor deposited $PbZr_xTi_{1-x}O_3$ thin films for high-density memory applications // Integrated Ferroelectrics. 1995. Vol. 7. No. 1–4. Pp. 123–138.

8. **Lee J. J., Thio C. L., Desu S. B.** Electrode contacts on ferroelectric $Pb(Zr_xTi_{1-x})O_3$ and $SrBi_2Ta_2O_9$ thin films and their influence on fatigue properties // Journal of Applied Physics. 1995. Vol. 78. No. 8. Pp. 5073–5078.

9. **Jin L., Li F., Zhang S.** Decoding the fingerprint of ferroelectric loops: Comprehension of the material properties and structures // Journal of the American Ceramic Society. 2014. Vol. 97. No. 1. Pp. 1–27.

10. **Andreeva N. V., Vakulenko A. F., Petraru A., Soni R., Kohistedt H., Fiulimonov A. V., Rudskoy A. I., Vakhrushev S. B., Pertsev N. A.** Low-temperature dynamics of ferroelectric domains in $PbZr_{0.3}Ti_{0.7}O_3$ epitaxial thin films studied by piezoresponse force microscopy // Applied Physics Letters. 2015. Vol. 107. No. 15. P. 152904.

11. **Colla E. L., Taylor D. V., Tagantsev A. K., Setter N.** Discrimination between bulk and interface scenarios for the suppression of the switchable polarization (fatigue) in $Pb(Zr,Ti)O_3$ thin films capacitors with Pt electrodes // Applied Physics Letters. 1998. Vol. 72. No. 19. Pp. 2478–2480.

12. **Sawyer C. B., Tower C. H.** Rochelle salt as a dielectric // Physical Review. 1930. Vol. 35. No. 3. Pp. 269–273.

13. **Fukunaga M., Noda Y.** New technique for measuring ferroelectric and antiferroelectric hysteresis loops // Journal of the Physical Society of Japan. 2008. Vol. 77. No. 6. P. 064706.

14. **Fukunaga M., Noda Y.** Improvement of the double-wave method for ferroelectric hysteresis loops and its application to multiferroic $EuMn_2O_5$ // Journal of the Korean Physical Society. 2009. Vol. 55. No. 2 (Part 1). Pp. 888–892.

THE AUTHORS

KNIAZEVA Maria A.
Peter the Great St. Petersburg Polytechnic University
29 Politechnicheskaya St., St. Petersburg, 195251, Russia
kniazeva.maria225@yandex.ru
ORCID: 0000-0003-1120-2102

ZHUKOVA Natalia S.
Peter the Great St. Petersburg Polytechnic University
29 Politechnicheskaya St., St. Petersburg, 195251, Russia
zhukovaaa3781@gmail.com

VAKULENKO Aleksandr F.
Peter the Great St. Petersburg Polytechnic University
29 Politechnicheskaya St., St. Petersburg, 195251, Russia
sasha705@mail.ru
ORCID: 0000-0001-5541-3409

СВЕДЕНИЯ ОБ АВТОРАХ

КНЯЗЕВА Мария Александровна – *кандидат физико-математических наук, доцент Высшей инженерно-физической школы Санкт-Петербургского политехнического университета Петра Великого.*
195251, Россия, г. Санкт-Петербург, Политехническая ул., 29
kniazeva.maria225@yandex.ru
ORCID: 0000-0003-1120-2102

ЖУКОВА Наталья Сергеевна – *студентка Института электроники и телекоммуникаций Санкт-Петербургского политехнического университета Петра Великого.*
195251, Россия, г. Санкт-Петербург, Политехническая ул., 29
zhukovaaa3781@gmail.com

ВАКУЛЕНКО Александр Феликсович – *кандидат физико-математических наук, старший преподаватель Высшей инженерно-физической школы Санкт-Петербургского политехнического университета Петра Великого.*
195251, Россия, г. Санкт-Петербург, Политехническая ул., 29
sasha705@mail.ru
ORCID: 0000-0001-5541-3409

Received 04.12.2025. Approved after reviewing 08.12.2025. Accepted 08.12.2025.
Статья поступила в редакцию 04.12.2025. Одобрена после рецензирования 08.12.2025. Принята 08.12.2025.

© Peter the Great St. Petersburg Polytechnic University, 2026

SIMULATION OF PHYSICAL PROCESSES

Original article
DOI: https://doi.org/10.18721/JPM.19202

STUDY OF VORTEX FLOWS GENERATED BY A PULSED TURBULENT BUOYANT JET

K. K. Ermakova, M. A. Zasimova, N. G. Ivanov✉

Peter the Great St. Petersburg Polytechnic University, St. Petersburg, Russia

✉ ivanov_ng@spbstu.ru

Abstract. In the paper, the results of numerical modeling of the formation and propagation of vortex structures generated by a pulsed turbulent buoyant jet have been presented for the Reynolds number Re = $1.5 \cdot 10^4$, the parameter $P = 3.65$, and the Grashof number Gr = $3.9 \cdot 10^5$. A three-dimensional turbulent flow model based on the unsteady Reynolds equations was adopted. The angle α between the jet and gravity directions was varied from 0° to 180°. The turbulent puff movement was tracked up to the moment when the maximum velocity value in the puff became equal to 3.5% of the inlet velocity. For various α values, the power-law relationships describing the propagation of the turbulent puff and a decrease in the maximum velocity value and temperature within the puff were obtained.

Keywords: mixed convection, turbulent puff, pulsed jet, numerical simulation

Funding: The reported study was funded by Russian Science Foundation (Grant No. 24-19-00437).

Citation: Ermakova K. K., Zasimova M. A., Ivanov N. G., Study of vortex flows generated by a pulsed turbulent buoyant jet, St. Petersburg State Polytechnical University Journal. Physics and Mathematics. 19 (2) (2026) 16–26. DOI: https://doi.org/10.18721/JPM.19202

This is an open access article under the CC BY-NC 4.0 license (https://creativecommons.org/licenses/by-nc/4.0/)

Научная статья
УДК 532.517
DOI: https://doi.org/10.18721/JPM.19202

ИССЛЕДОВАНИЕ ВИХРЕВЫХ ТЕЧЕНИЙ, СФОРМИРОВАННЫХ ИМПУЛЬСНОЙ ТУРБУЛЕНТНОЙ ПЛАВУЧЕЙ СТРУЕЙ

К. К. Ермакова, М. А. Засимова, Н. Г. Иванов✉

Санкт-Петербургский политехнический университет Петра Великого,
Санкт-Петербург, Россия

✉ ivanov_ng@spbstu.ru

Аннотация. Представлены результаты численного моделирования распространения вихревых облаков, сформированных импульсной турбулентной плавучей струей, для числа Рейнольдса Re = $1{,}5 \cdot 10^4$, параметра $P = 3{,}65$ и числа Грасгофа Gr = $3{,}9 \cdot 10^5$. Была принята модель трехмерного турбулентного течения, описываемого нестационарными уравнениями Рейнольдса. Угол между направлениями подачи струи и гравитационной силы α варьировался в диапазоне от 0° до 180°. Движение вихревого облака прослеживалось вплоть до момента, когда максимальное значение скорости в облаке становилось равным 3,5% от входной скорости. Для различных значений α получены степенные зависимости, описывающие распространение вихревого облака

© Ermakova K. K., Zasimova M. A., Ivanov N. G., 2026. Published by Peter the Great St. Petersburg Polytechnic University.

вдоль направления подачи струи и падение максимальной скорости и температуры в облаке.

Ключевые слова: смешанная конвекция, вихревое облако, импульсная струя, численное моделирование

Финансирование: Исследование выполнено при финансовой поддержке Российского научного фонда (грант № 24-19-00437).

Ссылка для цитирования: Ермакова К. К., Засимова М. А., Иванов Н. Г. Исследование вихревых течений, сформированных импульсной турбулентной плавучей струей // Научно-технические ведомости СПбГПУ. Физико-математические науки. 2026. Т. 19. № 2. С. 16–26. DOI: https://doi.org/10.18721/JPM.19202

Статья открытого доступа, распространяемая по лицензии CC BY-NC 4.0 (https://creativecommons.org/licenses/by-nc/4.0/)

Introduction

Turbulent jet flows are common in nature and in engineering, arising when a liquid or gas is discharged through an opening due to an applied pressure difference. The dynamics of turbulent jets have been studied experimentally and theoretically for many years [1, 2]. The findings are essential for a wide range of applications, including the design of ventilation systems, where supply jets govern air distribution, heat distribution, humidity, and contaminant concentration [3]. Heat sources also affect air distribution in practical scenarios of indoor ventilation; in some cases, their effect is comparable to that of the supplied air, and free convection develops under their influence [4].

Air in indoor ventilation systems is typically supplied at a constant flow rate. Most studies of ventilation flows have focused on the behavior of turbulent jets under steady inlet conditions. As requirements for air quality and thermal comfort become more stringent, new technical solutions are proposed. One such solution is to supply air at a variable flow rate, either gradual or intermittent. It is assumed that unsteady air supply could improve ventilation efficiency under certain conditions [5]. The effects of unsteady mechanisms for air supply are discussed in detail in the review [6], summarizing the available studies and technical solutions and concluding that the fundamentals of unsteady ventilation require further investigation.

This paper addresses a model problem of a single pulsed discharge of fluid into a quiescent environment. The vortex ring [7–9] is one of the best-known flows produced by a pulsed discharge. In addition to vortex rings, pulsed discharges can generate puffs and unsteady jets, depending on the duration and velocity of the discharge. According to [8], the vortex structures formed by a pulsed jet are characterized by the dimensionless parameter

$$P = (L_0/d)^{1/3},$$

where d is the diameter of the orifice through which the jet is supplied, L_0 is the piston stroke length ($L_0 = V_0 t_0$), t_0, V_0 are the duration and the velocity of the jet discharge.

The parameter P can be interpreted as a characteristic length of the volume added by the pulsed jet to the ambient environment, divided by the orifice diameter. Turbulent puffs (or turbulent vortex clouds) form at $1.6 < P < 8$. Vortex rings appear at smaller P; unsteady jets develop at larger values.

Experimental modeling of turbulent puffs [10, 11] was based on a technique involving repeated pulsed discharges and ensemble averaging of the monitored puff parameters. This approach has made it possible to establish several important self-similar properties of turbulent puff propagation over time, predicted theoretically in [7].

A numerical study in [12] considered the formation and motion of turbulent puffs under isothermal conditions, using an axisymmetric formulation. The study showed that the flow during a pulsed jet discharge can be divided into two phases: an initial phase, including jet discharge and puff formation, and a subsequent self-similar phase, where the velocity profiles within the fully

© Ермакова К. К., Засимова М. А., Иванов Н. Г., 2026. Издатель: Санкт-Петербургский политехнический университет Петра Великого.

developed puff remain similar to each other at successive time points. The durations of these phases were determined. Later, numerical simulation of a pulsed gas–droplet jet in an axisymmetric formulation was carried out in [13], finding that the flow structure resembled that of single-phase flow for the range of governing parameters considered.

The experiments reported in [10] examined in detail the motion of vortex structures at a distance from the discharge source (the self-similar phase). The position of the turbulent puff was found to follow a power-law dependence for isothermal conditions: At^B, where $B = 0.25$. The puff velocity also varied over time following a power-law dependence, with an exponent $B = -0.75$. The parametric simulations in [12] were also approximated by these power-law dependences.

Unlike [12], our paper reports on numerical simulations of non-isothermal flow generated by a single pulsed buoyant jet discharged into a quiescent environment. We carried out a parametric investigation into the influence of the angle between the jet direction and the gravity vector on the structure of the resulting vortex flow.

Problem statement and computational procedure

Similar to the problem statement in our earlier paper [12], here we consider the flow of an incompressible fluid (air) in a half-space bounded by an impermeable solid wall (Fig. 1); however, the problem is now treated as three-dimensional.

Circular orifice *1* of diameter d (set to $d = 0.05$ m in the dimensional formulation) is located on the wall; a pulsed air jet is discharged through it normal to solid surface *2*. The coordinate origin is located at the orifice center, with the z-axis directed into the domain normal to the bounding wall. The flow is assumed symmetric with respect to the mid-plane of the inlet orifice, so a symmetry condition is applied at the boundary *3* ($x = 0$). The remaining boundaries of the computational domain (*4*) are open (permeable). The dimensions of the computational domain are $24d \times 101d \times 120d$.

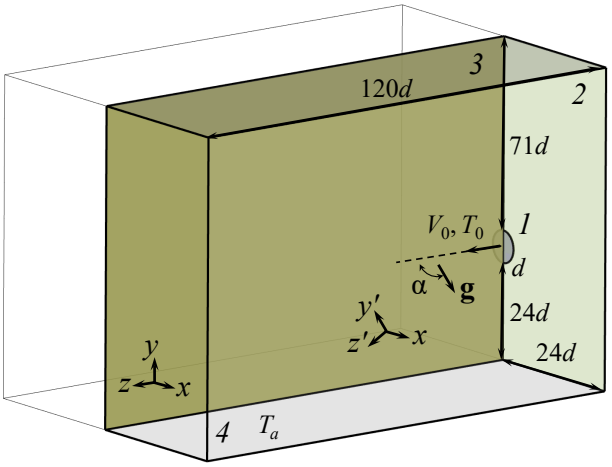


Fig. 1. Schematic diagram of computational domain: inlet orifice *1*, wall *2*, symmetry plane *3*, permeable boundary *4*;
d is the diameter of the inlet orifice; α is the angle between the jet direction and the gravity vector; the values of the parameters V_0, T_0, T_a and α are given in the text; **g** is the gravitational acceleration

The fluid is at rest at the initial time $t = 0$, and its temperature T_a is assumed uniform. During the period $0 \le t \le t_0$, fluid is discharged through the orifice at a constant velocity V_0 and temperature T_0. The following parameter values were adopted for simulations in the dimensional formulation:

$$V_0 = 4.28 \text{ m/s}, \; t_0 = 0.57 \text{ s},$$
$$\Delta T = T_0 - T_a = 20 \text{ K}, \; T_a = 293 \text{ K}.$$

Buoyancy effects were taken into account in the Boussinesq approximation: the value of $\beta \Delta T$ (β is the thermal expansion coefficient) is less than 0.07. The angle α between the jet direction and the gravity vector (see Fig. 1) was varied from 0° to 180° (at α = 0°, the jet was discharged in the direction of the gravity vector). Additional coordinate axes (x', y', z') were introduced for further data processing, with $x' = x$, and the y'-axis directed opposite to the gravity vector.

The problem is governed by three dimensionless parameters:

$$\text{Reynolds number Re} = V_0 d/\nu = 10 \cdot 1.5^4,$$
$$\text{parameter } P = (V_0 t_0/d)^{1/3} = 3.65,$$
$$\text{Grashof number Gr} = g\beta d^3 \Delta T/\nu^2 = 10 \cdot 3.9^5.$$

Note that these parameters were determined from the values of the quantities during the discharge phase. At this stage, the Richardson number $\mathrm{Ri} = Gr/Re^2$ was much less than unity, indicating predominantly forced convection. In later phases, as the characteristic velocity of the turbulent puff decreased, Ri values approached unity.

The simulations were run with a quasi-structured computational mesh containing 540,000 cells. An *O*-type grid topology was used for spatial discretization, with refinement near the orifice along both radial and axial directions; 44 cells were placed along the circumferential direction of the orifice and 22 along the radial direction. A mesh sensitivity study was carried out, showing that doubling the number of cells in each direction only slightly changed the characteristics of the vortex structures, so the solution obtained with the base mesh was assumed to be mesh-independent.

The problem was solved numerically in the ANSYS Fluent CFD package; the computational resources of the Polytechnic Supercomputer Center (scc.spbstu.ru) were used. Unsteady turbulent flow and heat transfer were simulated by solving the unsteady Reynolds-averaged Navier–Stokes (URANS) equations. The standard k–ε turbulence model was applied for closure. Constant values of turbulent viscosity ($\nu_{t0}/\nu = 10$) and turbulence intensity ($I_0 = 5\%$) were set at the inlet; these were converted into inlet values of k and ε in the code. These conditions correspond to a moderate turbulence level near the orifice. The turbulent Prandtl number was set to 0.9. Second-order spatial and temporal discretization schemes were used. The time step was $0.086V_0/d$. The total simulation time was about 3,000 convective time units $t' = tV_0/d$.

Motion and parameters of the turbulent puff

The motion of the vortex structure generated by the pulsed jet is illustrated for the case with an angle between the jet direction and the gravity vector $\alpha = 120°$. The flow structure resembled that described in [10] during the initial phase of puff formation and propagation (for $t' < 80$), due to the predominant role of forced convection. The contribution of natural convection becomes noticeable for $t' > 80$. Accordingly, analysis of the flow structure in this paper focuses on the main phase in the propagation of the turbulent puff, after the puff has fully developed.

Fig. 2 shows the fields of velocity magnitude, vorticity magnitude, and temperature at three points in time after the start of the pulsed jet discharge: $t' = 86$, 600, and 2910. The velocity values are normalized by the maximum velocity magnitude at each time point, $|\mathbf{V}_c|$. The center of the puff is taken as the point C $(0, y_c, z_c)$, where the velocity magnitude reaches its maximum at that time. The vorticity magnitudes are normalized by the maximum vorticity at that time, $\Omega_{\max}$. The temperature $\theta = (T - T_a)/(T_{\max} - T_a)$ is normalized by the difference between the maximum temperature within the puff at that time, $T_{\max}$, and the ambient temperature.

As seen from the vorticity field, the vortex structure at $t' = 86$ is elongated in the direction of jet discharge, but its shape gradually approaches a sphere (see Fig. 2,*a*). Elevated Ω values are localized in a region roughly $8d \times 8d \times 10d$ in size. The center of the puff only slightly deviates from the jet axis (it is at a distance less than d from the axis). By this point in time, the maximum velocity has dropped by about 75% relative to the discharge velocity V_0, and the temperature difference $(T_{\max} - T_a)$ has dropped by 78% relative to the initial difference $(T_0 - T_a)$.

At $t' = 600$, the characteristic dimensions of the puff grow to about $15d \times 15d \times 15d$, while the puff noticeably deviates from the initial direction: the velocity maximum is located at about $5d$ from the jet axis (see Fig. 2,*b*). The vorticity fields are asymmetric relative to the center of the vortex structure: the values in the lower part of the puff are larger than in the upper part. By this time, the strength of the puff is considerably weakened: the maximum of the velocity magnitude $|\mathbf{V}_c|$ is about 5% of the velocity V_0, and the temperature difference is less than 3% of the initial value.

By the time $t' = 2910$, the dimensions of the puff increase by roughly another factor of two in each direction, reaching about $30d \times 30d \times 30d$ (see Fig. 2,*c*). The flow activity continues to decay: the streamwise and cross-stream velocity components are comparable and do not exceed 2% of the inlet velocity. A thermal wake trailing behind the puff can be seen in the fields, moving even more slowly and essentially separated from the puff.

We should note that further evolution of the puff up until it stops completely cannot be reliably simulated by the URANS approach; eddy-resolving methods would be required to simulate the decay phase of turbulent flow, which is beyond the scope of this paper.

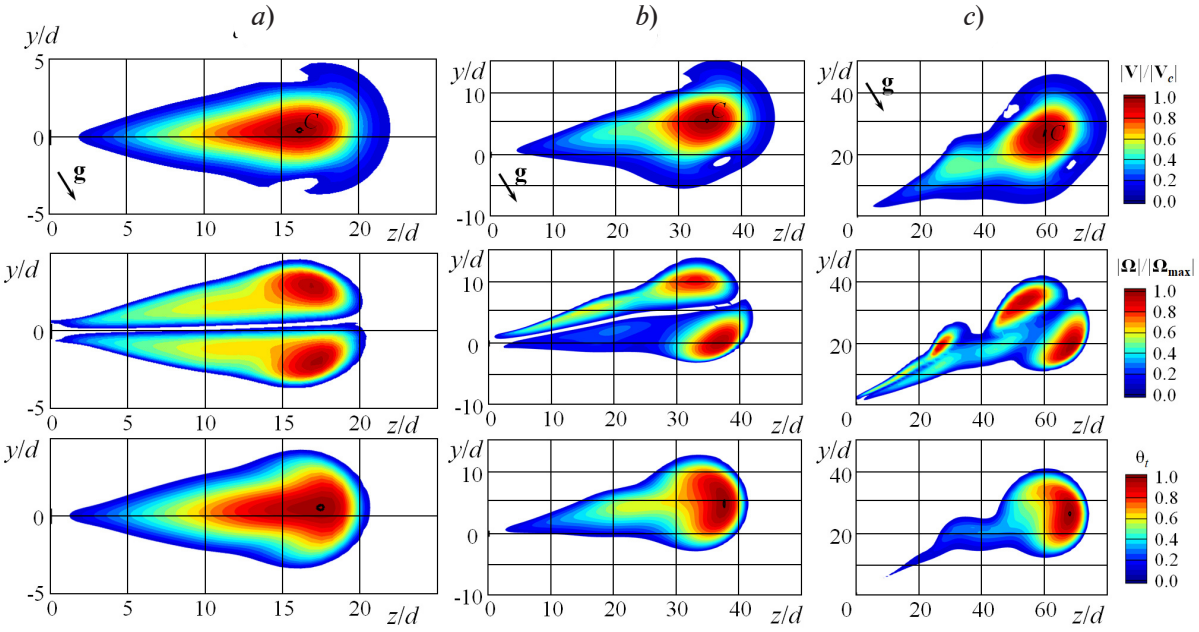


Fig. 2. Calculated fields of velocity magnitude (top row), vorticity magnitude (middle row), and temperature (bottom row) at three time points t': 86 (*a*), 600 (*b*), and 2910 (*c*). Case $\alpha = 120°$

Fig. 3 shows the evolution of the puff position over time and in space. Observation of the puff center position (solid line) starts when the center is located about three orifice diameters ($3d$) from the inlet orifice ($t' \approx 50$). After the puff is fully formed, when the point z_c has moved rapidly away from the source (at $t' > 100$), the trajectory curve of the puff center (see Fig. 3,*a*, the dependence $y_c(z_c)$) begins to deviate from the jet direction; the function $y_c(z_c)$ is close to cubic up to t' values on the order of 10^3.

The dependence $z_c(t)$ follows a power law with an exponent of 0.35 in the interval $100 < t' < 1000$; notably, the exponent in the self-similar phase should be equal to 0.25 for the propagation of an isothermal puff (according to [10]). Some deviation from these power-law dependences is observed for larger t' ($t' > 1000$), i.e., during the slow decay phase (low drift velocity). The puff center deviates substantially over the simulation period: the final position (the fields shown in Fig. 2,*c*) corresponds to the point (0, $27d$, $60d$).

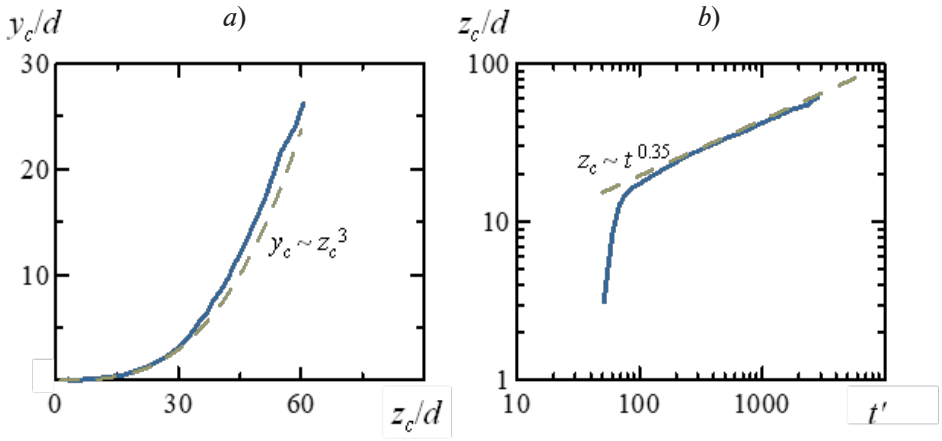


Fig. 3. Evolution of the position in maximum of vortex cloud velocity in space (*a*) and over time (*b*). Dashed lines mark the approximating functions

Fig. 4 shows the evolution of the maximum velocity magnitude $|\mathbf{V}_c|(t)$, as well as its streamwise ($V_{c,z}(t)$) and cross-stream ($V_{c,y}(t)$) components. The dashed lines in Fig. 4,*a* characterize the variation of $|\mathbf{V}_c|(t)$ following the power-law dependences with exponents of −0.75 and −0.40. Unlike the isothermal case [10], where the behavior of $V_c(t)$ in the self-similar phase follows a power-law dependence with a fixed exponent of −0.75, this behavior is only observed for the pulsed buoyant jet in the interval $100 < t' < 600$, when the streamwise velocity is much larger than the cross-stream component (see Fig. 4,*b*). The values of $V_{c,z}(t)$ and $V_{c,y}(t)$ approach each other at larger t', and the curve of the maximum velocity magnitude $|\mathbf{V}_c|(t)$ deviates from the earlier trend, following a new power-law dependence with an exponent of −0.4.

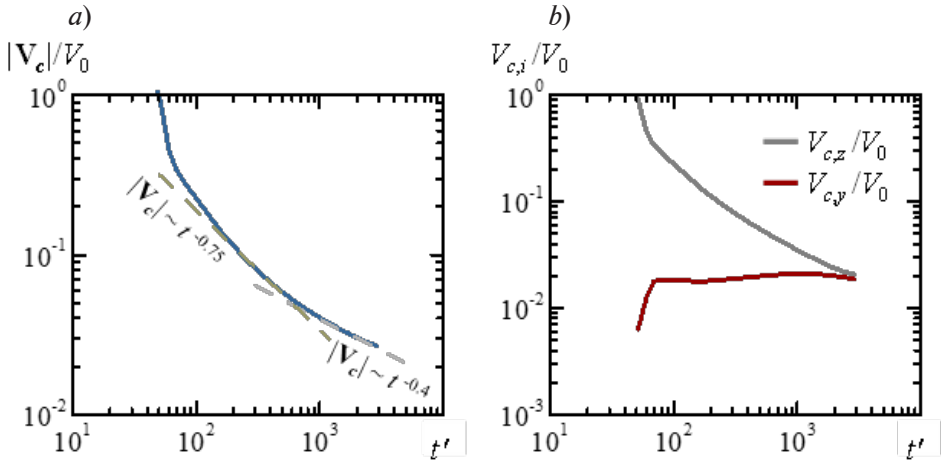


Fig. 4. Time evolution computed for maximum velocity magnitude of vortex cloud (*a*); its streamwise and cross-stream components (*b*)

Fig. 5 characterizes the time evolution of the characteristic temperature within the puff, showing the data for the normalized maximum temperature

$$\theta_{\max} = (T_{\max} - T_a)/(T_0 - T_a),$$

i.e., the temperature difference (normalized by the initial difference $T_0 - T_a$) between the instantaneous maximum temperature in the puff and the ambient temperature T_a.

Over the time interval considered, the dependence $\theta_{\max}(t)$ follows a power law with an exponent of −1.03. At $t' \approx 1400$, the maximum temperature difference $T_{\max} - T_a$ amounts to 1% of the initial value of $T_0 - T_a$.

The maximum velocity magnitude in the puff decreased less dramatically, to 3.5% of the jet velocity. It is worth repeating that analysis of further propagation of the puff, with predominant natural convection, lies beyond the scope of this paper.

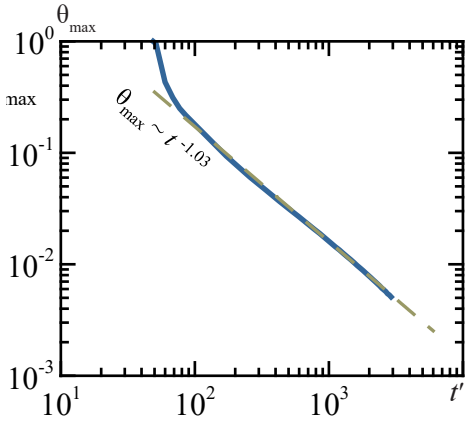


Fig. 5. Time evolution of maximum temperature in the vortex cloud
The dashed line marks the approximation of a segment of the dependence by a power-law function

Propagation of the puff as a function of pulsed jet direction

This section presents the results of parametric simulations for 7 cases that differ in the angle α between the jet direction and the gravity vector (the angle α was varied from 0° to 180° in steps of 30°). For each case, we considered time samples up to $t' < t'_{3.5\%}$, where $t'_{3.5\%}$ is the time when the maximum velocity magnitude $|\mathbf{V}_c|$ drops to 3.5% of the inlet velocity. Depending on the case, $t'_{3.5\%}$ ranged from 340 (α = 0°) to $2 \cdot 10^3$ (α = °180). Fig. 6,*a* shows the trajectories of the puff centers for all seven cases (curves characterizing the deviation in the position of the velocity maximum) in coordinates (x, y', z'); Fig. 6,*b* shows the distributions of velocity magnitude at the final time point in the sample, $t' = t'_{3.5\%}$. Evidently, the puff propagates along the jet axis for α = 0° and 180°; the puff deviates from this axis under the action of buoyancy forces for the other values of α. As the angle α increases, the length of the trajectory traveled by the puff up to a given decay level gradually increases, and so does the size of the puff (see Fig. 6,*b*).

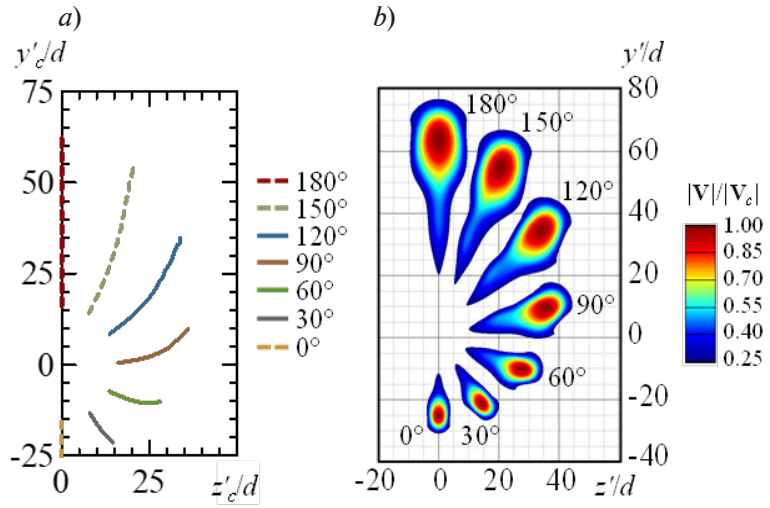


Fig. 6. Parametric simulations for different angles α: cloud center trajectories (*a*); distributions of velocity magnitude a $t' = t'_{3.5\%}$(*b*) (see text for details)

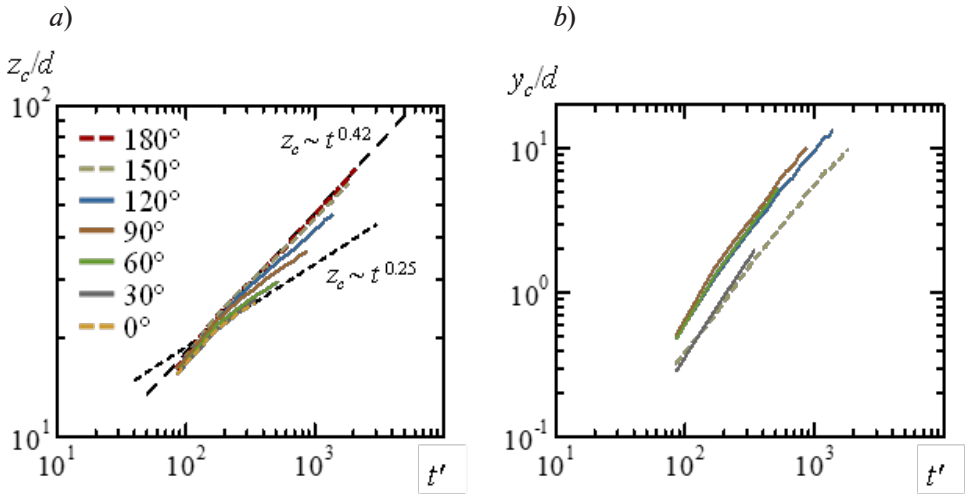


Fig. 7. Time evolution computed for the position of vortex cloud center for cases with different α (angle between the jet and gravity directions)

Fig. 7 shows the time evolution in the position of the puff center for the seven computational cases (the graphs are plotted in coordinates aligned with the jet direction). The family of curves $z_c(t)$, describing puff propagation along the jet direction, is supplemented by two dashed lines approximating the limiting power-law dependences (see Fig. 7,*a*). For $\alpha = 0°$, when the jet is discharged in the direction of gravity, the calculated data are approximated by a power-law dependence with an exponent of 0.25, which corresponds to the isothermal case [12]. In the opposite limiting case, when the pulsed jet is discharged upward and gravity accelerates it ($\alpha = 180°$), the computational data are approximated by a power-law dependence with an exponent of 0.42. Distinct stratification can be observed in the curves $y_c(t)$ in Fig. 7,*b*, characterizing the deviation of the puff from the jet direction: the largest deviation occurs when the jet is discharged perpendicular to the gravity vector ($\alpha = 90°$). The plots for $\alpha = 60°$ and 120°, describing the gradual deviation of the puff center, lie slightly below this curve. The difference between the curves plotted from the data for $\alpha = 30°$ and 150° is more pronounced: in these cases, the puff drifts away from the axis more slowly.

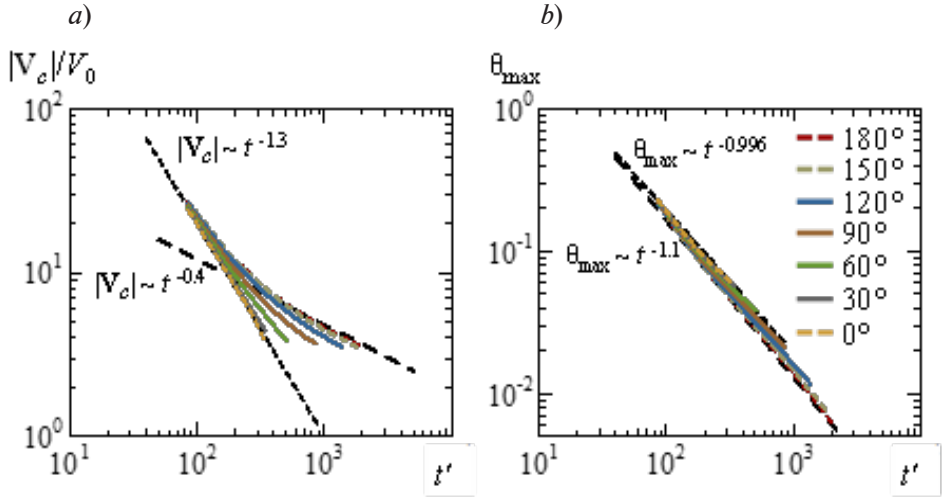


Fig. 8. Time evolution of normalized maximum velocity (*a*) and normalized maximum temperature (*b*) for cases with different angles α
The dashed lines mark power-law approximations for the limiting cases ($\alpha = 0°$ and $\alpha = 180°$)

Fig. 8 shows the curves characterizing the decay of the maximum velocity and normalized maximum temperature over time. As in Fig. 7,*a*, the families of curves are supplemented by dashed lines approximating the limiting power-law dependences (for $\alpha = 0°$ and $\alpha = 180°$). The puff decelerates most rapidly for $\alpha = 0°$, which is unsurprising: buoyancy exerts a significant braking effect. The evolution of $V_c(t)$ in this case follows a power-law dependence with an exponent of −1.3. In contrast, buoyancy weakens the deceleration of the puff for $\alpha = 180°$, and $V_c(t)$ decays over time with an exponent of −0.4. The differences in the decay of the characteristic puff temperature between the cases are less pronounced: all curves lie close to each other, and the exponents range from −0.996 for $\alpha = 0°$ to −1.100 for $\alpha = 180°$.

Conclusion

This study reports on the results from three-dimensional URANS simulations of non-isothermal flow generated by a single pulsed buoyant jet discharged into a quiescent environment. Forced convection dominated during the initial phase of turbulent puff formation and propagation, which lasted for less than 100 dimensionless time units. Natural convection made a substantial contribution at longer times.

Analysis of the flow structure focused on the main phase of puff propagation continuing up to the time when the maximum velocity magnitude $|\mathbf{V}_c|$ dropped to 3.5% of its inlet value.

Parametric simulations where the angle α between the jet and gravity directions was varied from 0° to 180° showed that the discharge direction of the pulsed buoyant jet strongly affects both the propagation trajectory of the puff and its decay rate. The dependence describing the

propagation of the puff along the jet direction follows a power law, with the exponent ranging from 0.25 (corresponding to the isothermal case) to 0.42, depending on the discharge direction.

The decrease in the maximum velocity within the puff over time is also approximated by a power law, with exponents between −1.3 and −0.4.

The decrease in the characteristic temperature within the puff is less sensitive to α (the angle between the jet and the gravity directions): the exponent is close to −1 for all cases considered.

Future research will focus on the behavior of vortex structures at different values of the parameter *P*, in particular, adopting scale-resolving simulation approaches.

REFERENCES

1. **Abramovich G. N., Girshovich T. A., Krasheninnikov S. Iu., et al.,** The theory of turbulent jets, Ed. by G. N. Abramovich, 2-nd ed., Nauka Publishing, Moscow, 1984 (in Russian).

2. **List E. J.,** Turbulent jets and plumes, Ann. Rev. Fluid Mech. 14 (Jan) (1982) 189–212.

3. **Grimitlin M. I.,** Raspredeleniye vozdukha v pomeshcheniyakh [Indoor air distribution], Published by AVOK Severo-Zapad [Ventilation, Heating, air Conditioning Association (VHCA) of engineers in the North-West], Saint-Petersburg, 2004 (in Russian).

4. **Davies Wykes M. S., Chahour E., Linden P.F.,** The effect of an indoor-outdoor temperature difference on transient cross-ventilation, Build. Environ. 168 (15 Jan) (2020) 10644.

5. **Fan M., Fu Z., Wang J., et al.,** A review of different ventilation modes on thermal comfort, air quality and virus spread control, Build. Environ. 212 (15 March) (2022) 108831.

6. **Mesenhöller E., Vennemann P., Hussong J.,** Unsteady room ventilation – A review, Build. Environ. 2020. Vol. 169 (Febr) (2020) 106595.

7. **Glezer A., Coles D.,** An experimental study of a turbulent vortex ring, J. Fluid Mech. 211 (Febr) (1990) 243–283.

8. **Shariff K., Leonard A.,** Vortex rings, Ann. Rev. Fluid Mech. 24 (Jan) (1992) 235–279.

9. **Akhmetov D. G.,** Vortex rings, Springer-Verlag, Berlin, Heidelberg, 2009.

10. **Sangras R., Kwon O. C., Faeth G. M.,** Self-preserving properties of unsteady round nonbuoyant turbulent starting jets and puffs in still fluids, ASME. J. Heat Transfer. 124 (3) (2002) 460–469.

11. **Ghaem-Maghami E., Johari H.**, Concentration field measurements within isolated turbulent puffs, ASME. J. Fluids Eng. 129 (2) (2007) 194–199.

12. **Zasimova M. A., Ris V. V., Ivanov N. G.,** Numerical simulation of the formation and motion of turbulent vortex clouds (puffs), Fluid Dyn. 58 (5) (2023) 882–893.

13. **Pakhomov M. A., Terekhov V. P.,** Distinctive features of propagation of a turbulent pulsed gas-droplet eddy cloud. Fluid Dyn. 59 (4) (2024) 687–699.

СПИСОК ЛИТЕРАТУРЫ

1. **Абрамович Г. Н., Гиршович Т. А., Крашенинников С. Ю. и др.** Теория турбулентных струй. Под ред. Г. Н. Абрамовича. -2е изд., перераб. и доп. М.: Наука, 1984. 716 с.

2. **List E. J.** Turbulent jets and plumes // Annual Review of Fluid Mechanics. 1982. Vol. 14. January. Pp. 189–212.

3. **Гримитлин М. И.** Распределение воздуха в помещениях. Изд. 3-е, доп. и испр. СПб.: АВОК Северо-Запад, 2004. 320 с.

4. **Davies Wykes M. S., Chahour E., Linden P.F.** The effect of an indoor-outdoor temperature difference on transient cross-ventilation // Building and Environment. 2020. Vol. 168. 15 January. P. 10644.

5. **Fan M., Fu Z., Wang J., Wang Z., Suo H., Kong X., Li H.** A review of different ventilation modes on thermal comfort, air quality and virus spread control // Building and Environment. 2022. Vol. 212. 15 March. P. 108831.

6. **Mesenhöller E., Vennemann P., Hussong J.** Unsteady room ventilation – A review // Building and Environment. 2020. Vol. 169. February. P. 106595.

7. **Glezer A., Coles D.** An experimental study of a turbulent vortex ring // Journal of Fluid Mechanics. 1990. Vol. 211. February. Pp. 243–283.

8. **Shariff K., Leonard A.** Vortex rings // Annual Review of Fluid Mechanics. 1992. Vol. 24. January. Pp. 235–279.

9. **Ахметов Д. Г.** Вихревые кольца. Новосибирск: ГЕО, 2007. 151 с.

10. **Sangras R., Kwon O. C., Faeth G. M.** Self-preserving properties of unsteady round nonbuoyant turbulent starting jets and puffs in still fluids // ASME. Journal of Heat Transfer. 2002. Vol. 124. No. 3. Pp. 460–469.

11. **Ghaem-Maghami E., Johari H.** Concentration field measurements within isolated turbulent puffs // ASME. Journal of Fluids Engineering. 2007. Vol. 129. No. 2. Pp. 194–199.

12. **Засимова М. А., Рис В. В., Иванов Н. Г.** Численное моделирование формирования и движения турбулентных вихревых облаков // Известия Российской академии наук. Механика жидкости и газа. 5 № .2023. С. 69–57.

13. **Пахомов М. А., Терехов В. И.** Особенности распространения газокапельного турбулентного импульсного вихревого облака // Известия Российской академии наук. Механика жидкости и газа. 2024. № 4. С. 55–68.

THE AUTHORS

ERMAKOVA Karina K.
Peter the Great St. Petersburg Polytechnic University
29 Politechnicheskaya St., St. Petersburg, 195251, Russia
karinak77777@mail.ru

ZASIMOVA Marina A.
Peter the Great St. Petersburg Polytechnic University
29 Politechnicheskaya St., St. Petersburg, 195251, Russia
zasimova_ma@spbstu.ru
ORCID: 0000-0002-4103-6574

IVANOV Nikolay G.
Peter the Great St. Petersburg Polytechnic University
29 Politechnicheskaya St., St. Petersburg, 195251, Russia
ivanov_ng@spbstu.ru
ORCID: 0000-0001-9897-5401

СВЕДЕНИЯ ОБ АВТОРАХ

ЕРМАКОВА Карина Константиновна – *студентка Физико-механического института Санкт-Петербургского политехнического университета Петра Великого.*
195251, Россия, г. Санкт-Петербург, Политехническая ул., 29
karinak77777@mail.ru

ЗАСИМОВА Марина Александровна – *кандидат физико-математических наук, доцент Высшей школы прикладной математики и вычислительной физики Санкт-Петербургского политехнического университета Петра Великого.*
195251, Россия, г. Санкт-Петербург, Политехническая ул., 29
zasimova_ma@spbstu.ru
ORCID: 0000-0002-4103-6574

ИВАНОВ Николай Георгиевич – *кандидат физико-математических наук, заведующий научно-исследовательской лабораторией гидродинамики, директор Физико-механического института Санкт-Петербургского политехнического университета Петра Великого.*
195251, Россия, г. Санкт-Петербург, Политехническая ул., 29
ivanov_ng@spbstu.ru
ORCID: 0000-0001-9897-5401

Received 27.11.2025. Approved after reviewing 08.12.2025. Accepted 08.12.2025.
Статья поступила в редакцию 27.11.2025. Одобрена после рецензирования 08.12.2025. Принята 08.12.2025.

© Peter the Great St. Petersburg Polytechnic University, 2026

Original article
DOI: https://doi.org/10.18721/JPM.19203

ON THE INSTABILITY OF COUNTERFLOWING WALL JETS IN A VENTILATED CAVITY

V. R. Adiatullin, S. A. Galaev, V. V. Ris, M. A. Zasimova, N. G. Ivanov✉

Peter the Great St. Petersburg Polytechnic University, St. Petersburg, Russia

✉ ivanov_ng@spbstu.ru

Abstract. The paper presents the results of numerical simulation of fluid flow in a rectangular room when fluid is supplied from two opposing slotted holes. The Reynolds number (Re) based on the height of the supply opening was varied from 20 to 140. For the given ratio of the lengths of the sides of the room, intensive self-oscillations developed due to instability arising when the supply jets interacted at Re ≥ 50. Already at a value of Re = 100 the flow became chaotic with a continuous frequency spectrum. The Strouhal number values corresponding to the main frequency of the oscillations depended weakly on Re and were approximately $3 \cdot 10^{-3}$.

Keywords: numerical simulation, plain jet, ventilated cavity, self-oscillations

Funding: The reported study was funded by Russian Science Foundation (Grant No. 24-19-00437).

Citation: Adiatullin V. R., Galaev S. A., Ris V. V., Zasimova M. A., Ivanov N. G., On the instability of counterflowing wall jets in a ventilated cavity, St. Petersburg State Polytechnical University Journal. Physics and Mathematics. 19 (2) (2026) 27–38. DOI: https://doi.org/10.18721/JPM.19203

This is an open access article under the CC BY-NC 4.0 license (https://creativecommons.org/licenses/by-nc/4.0/)

Научная статья
УДК 532.517
DOI: https://doi.org/10.18721/JPM.19203

О НЕУСТОЙЧИВОСТИ ВСТРЕЧНЫХ ПРИСТЕННЫХ СТРУЙ В ВЕНТИЛИРУЕМОЙ ПОЛОСТИ

В. Р. Адиатуллин, С. А. Галаев, В. В. Рис, М. А. Засимова, Н. Г. Иванов✉

[1] Санкт-Петербургский политехнический университет Петра Великого, Санкт-Петербург, Россия

✉ ivanov_ng@spbstu.ru

Аннотация. Представлены результаты численного моделирования течения жидкости в прямоугольном помещении при ее встречной подаче через два щелевых отверстия. Число Рейнольдса Re, построенное по высоте приточного отверстия, варьировалось в диапазоне от 20 до 140. Для рассмотренного соотношения длин сторон помещения, при Re ≥ 50 развиваются интенсивные автоколебания вследствие неустойчивости, которая проявляется при взаимодействии приточных струй. Уже при значении Re = 100 течение приобретает хаотический характер со сплошным спектром частот. Значения числа Струхаля, соответствующие основной частоте колебаний, слабо зависят от Re и составляют примерно $10 \cdot 3^{-3}$.

© Adiatullin V. R., Galaev S. A., Ris V. V. Zasimova M. A., Ivanov N. G., 2026. Published by Peter the Great St. Petersburg Polytechnic University.

Ключевые слова: численное моделирование, плоская струя, вентилируемая полость, автоколебания

Финансирование: Исследование выполнено при финансовой поддержке гранта Российского научного фонда № 24-19-00437.

Ссылка для цитирования: Адиатуллин В. Р., Галаев С. А., Рис В. В., Засимова М. А., Иванов Н. Г. О неустойчивости встречных пристенных струй в вентилируемой полости // Научно-технические ведомости СПбГПУ. Физико-математические науки. 2026. Т. 19. № 2. С. 27–38. DOI: https://doi.org/10.18721/JPM.19203

Статья открытого доступа, распространяемая по лицензии CC BY-NC 4.0 (https://creativecommons.org/licenses/by-nc/4.0/)

Introduction

When turbulent jet flows with a continuous frequency spectrum propagate in confined spaces, stable, statistically steady large-scale self-oscillations can develop [1]. The interaction of the jets with each other and with solid walls, including the conditions under which self-oscillating flow regimes can evolve, have been extensively studied in the context of jet control systems for pneumatic automation devices [2]. Low-frequency self-oscillations can also occur when air jets propagate in ventilated rooms. For instance, the behavior of self-oscillations in a ventilation system designed for a university lecture hall was considered in a combined computational and experimental study [3], analyzing air distribution in a real room whose geometry included a number of small-scale features, with ventilation provided by four standard fan coil units (a total of 16 supply sections). For such a complex configuration, it is challenging to analyze the causes of self-oscillations and to draw definitive conclusions.

The literature on this topic includes a number of studies that discuss the possible causes and conditions for sustaining stable self-oscillations in simplified configurations, with simplifications made in both geometry and jet supply method. For example, the interaction of free shear layers with simplified impingement configurations was analyzed in [4]. The experimental study in [5] reported on the propagation of a plane jet in a rectangular cavity, suggesting that secondary backflow plays a significant role in the development of self-oscillations by influencing the jet behavior in a confined space. Experimental studies of a round jet propagating in a model configuration typical of casting processes [6, 7], supplemented by subsequent numerical studies [8, 9], led to certain conclusions about the conditions required for self-oscillating flow regimes. Such a regime can be achieved with an extended open cavity on the surface of the confined space, providing some freedom for the fluid to flow in or out of the surrounding environment.

These conditions are, of course, not typical for ventilated rooms. Nevertheless, it was precisely these conditions in the test experiment described in [10, 11] that made it possible to observe the development of self-oscillating flow regimes. The model room where the plane jet propagated in the studies was a rectangular ventilated cavity with extended openings on the end wall. Low-frequency self-oscillations of a plane jet for this geometric configuration were reproduced and analyzed in detail using two-dimensional (2D) and three-dimensional (3D) unsteady Reynolds-averaged Navier–Stokes (URANS) simulations, as well as large eddy simulation (LES) [11–13].

Unsteadiness in jet flow observed for a propagating single jet is even more likely to occur when multiple jets interact (as demonstrated in our paper [3]). For example, an experimental study [14] found that the flow generated by two plane jets discharged toward each other in free space (away from the top and bottom walls of the cavity) was inherently unstable: the pressure field was periodically rearranged, alternately displacing the jets upward and downward. Stable self-oscillations also occur when two opposing near-wall plane jets are discharged toward each other: the oscillatory nature of jet interaction was established experimentally and numerically for rectangular cavities (model rooms) with various geometric parameters (see [15] and [16], respectively).

The interaction of opposing ceiling jets is characteristic for ventilation systems in passenger aircraft cabins. The flow structure under conditions typical of such ventilation systems was investigated

© Адиатуллин В. Р., Галаев С. А., Рис В. В., Засимова М. А., Иванов Н. Г., 2026. Издатель: Санкт-Петербургский политехнический университет Петра Великого.

numerically and experimentally in [17–19]; pronounced self-oscillations were detected in all cases. The computational domain in [17, 18] approximated an aircraft cabin model with obstacles, which complicated direct analysis of jet flow. The experimental study [19] adopted several simplifications (flat walls and no obstacles), but a radically simplified formulation, proposed in the numerical study [20], appears more suitable for parametric simulations. In that formulation, two slotted supply openings were placed symmetrically on opposite end walls near the ceiling, and two slotted exhaust openings were placed symmetrically near the floor in a rectangular room.

The geometry and flow rate through each supply opening used in [20] correspond to the Nielsen test case, which is well-recognized in ventilation research [21, 22]. According to this test case, an air jet is supplied from a slot located near the ceiling. The experimental data from the Nielsen test case are still widely used for validation of numerical results (see, for example, the 2025 study [23]; our 2020 paper [24] provides a fairly comprehensive review of the literature on this topic, as well as a reference to the open-access experimental database).

The main focus in [20] is on the patterns in the unsteadiness induced by air supply with a rapidly varying flow rate. However, we can assume based on the results from [15, 16] that the interaction of opposing jets should excite strong low-frequency self-oscillations due to hydrodynamic instability even under steady boundary conditions (at a constant flow rate). This important issue is not addressed in [20].

The goal of the present study is to analyze the conditions leading to the development of self-oscillations when opposing jets interact in a model room (cavity).

The relative dimensions of the room and the positions of the supply/exhaust openings correspond to the problem formulation adopted in [20].

Problem statement

We consider fluid flow in a rectangular room with the dimensions $3H \times H \times H$ (Fig. 1). Fluid is supplied through slotted openings with the height $h_{in} = 0.056H$, located on the two opposing end walls near the ceiling. Supply ducts of length H are attached to these openings. The fluid leaves the room through exhaust openings with the height $h_{out} = 0.16H$, placed on the same walls near the floor. The computational domain also includes exhaust ducts of length H attached to the exhaust openings. The widths of the supply and exhaust ducts equal the width of the room. The coordinate origin is at one of the lower corners of the room; the x-axis is directed longitudinally, and the y-axis is directed vertically.

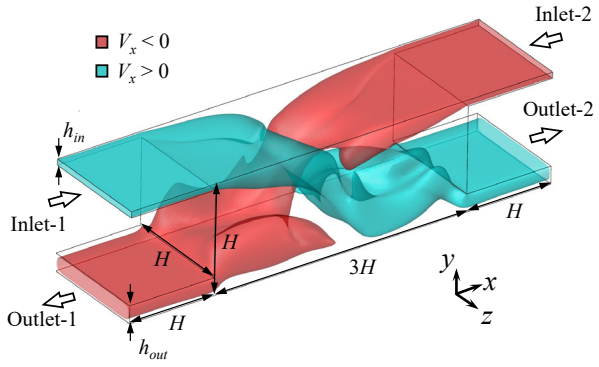


Fig. 1. Geometric model of computational domain: two isosurfaces of velocity $V_x > 0$ and $V_x < 0$ illustrate the flow structure at Re = 60; the heights of the supply openings (h_{in}) and exhaust openings (h_{out}) are shown, along with the supply and exhaust ducts (whose boundaries are labeled Inlet-1, Inlet-2 and Outlet-1, Outlet-2); the outlined arrows mark the directions of the jets

Uniform profiles of velocity V_0 are applied at the inlet faces of the supply ducts (labeled Inlet-1 and Inlet-2 in Fig. 1). A pressure outlet boundary condition (a fixed constant pressure) is applied at the outlet faces of the exhaust ducts (Outlet-1 and Outlet-2). All other boundaries are impermeable walls with no-slip conditions.

A system of unsteady Navier–Stokes equations is solved numerically for flow of an incompressible fluid with constant physical properties. The flow in the cavity is characterized by $\mathrm{Re} = h_{in}V_0/\nu$, constructed from the height of the supply slots and the average inlet velocity. We considered Re numbers from 20 to 140. This range allows performing simulations in the formulation excluding the uncertainty associated with turbulence models. The range was chosen to be roughly two orders of magnitude lower than the Re number used in [20–22] ($\mathrm{Re} = 5.5 \cdot 10^3$), which corresponds to full-scale ventilation conditions. Our reduced Re values can be interpreted as effective Re numbers constructed from the characteristic level of turbulent viscosity generated

by the turbulence model in the mixing layer at full-scale Re value. We should also note that the Re number constructed from the room height H takes values in the range of $(0.36–2.50)\cdot10^3$ for the cases considered (for example, H was used to determine Re values in [15]).

Parametric simulations in the considered Re range were performed on a single mesh of 860,000 cells, refined toward the supply and exhaust openings. A mesh sensitivity study was carried out for Re = 60 (unsteady flow) using meshes of 50,000, 370,000, and 860,000 cells. The time-averaged fields showed weak mesh dependence already for the 370,000-cell mesh: the distributions of average velocity obtained on meshes with 370,000 and 860,000 cells were nearly identical. Since the upper bound of the considered Re range is higher, we chose to use the mesh with the largest number of cells.

The simulations were performed in the ANSYS Fluent CFD package (version 2022R1) implementing the finite volume method. The following numerical options were selected. Convective fluxes through cell faces were computed using a second-order upwind scheme. An implicit second-order scheme was used for time advancement. The time step was set to $0.15h/V_0$. To obtain time-averaged flow parameters, samples were accumulated over durations exceeding 10,000 convective time units (h/V_0). The computations were performed using the resources of the Polytechnic Supercomputer Center (scc.spbstu.ru).

Computational results and discussion

The evolution of the flow structure with increasing Re is represented in Fig. 2, showing the distributions of velocity magnitude in the vertical midplane of the room ($z = H/2$) and the vertical velocity component in the horizontal midplane ($y = H/2$).

At low Re (Re = 20 for row I, Re = 40 for row II), the solution in the unsteady formulation converged to a steady state. The jet throw is small in this Re range: as the jets gradually descend

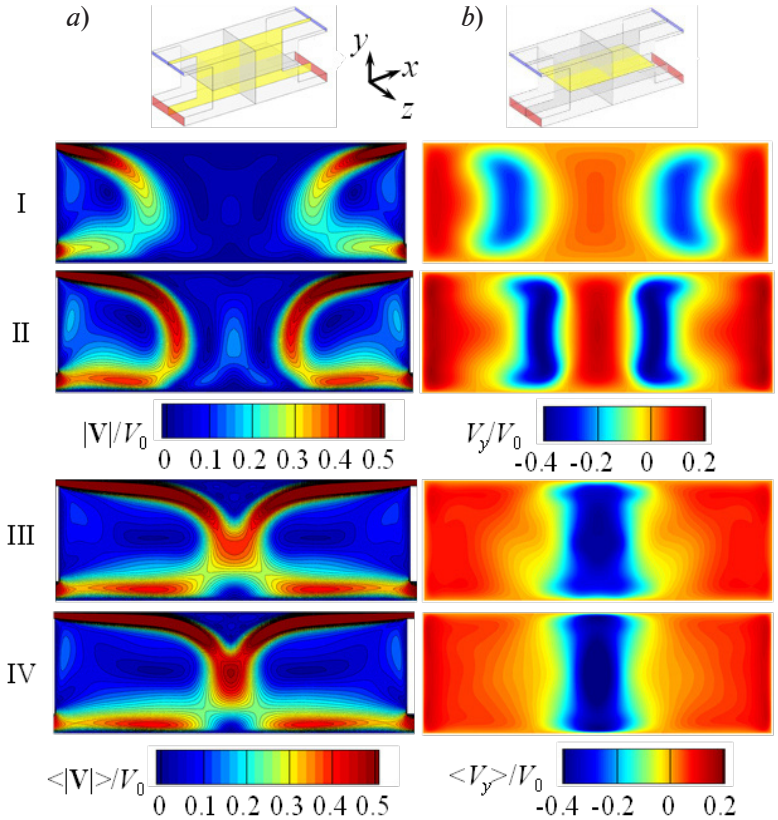


Fig. 2. Computational distributions of velocity magnitude in vertical midplane $z = H/2$ (a) and vertical velocity component in horizontal midplane $y = H/2$ (b) (the planes are shown in the schematics above) for different Re: 20 (I), 40 (II), 60 (III), and 100 (IV) The solution is steady for rows I and II and unsteady for rows III and IV, so the distributions are given for time-averaged quantities

toward the floor, they turn 180° at a short distance from the supply opening, and the fluid flows toward the corresponding exhaust openings. As Re increases, the jets penetrate deeper into the cavity, but the flow remains steady as long as they do not interact with each other.

Analyzing the data in Fig. 2, we can conclude that steady flow is essentially 3D in both cases, even though the jets considered are nominally plane. This is evident from the curvature of the vertical velocity fields in the horizontal midplane. This indicates an extended region of side wall influence in the spanwise direction due to significant viscous effects. The steady flow is symmetric in the longitudinal direction about the midplane $x = 1.5H$.

With a further increase in Re, the jet throw grows gradually; the jets reach the center of the room and begin to interact. The structure formed by the two opposing jets loses stability and the flow becomes unsteady. Accordingly, Fig. 2 shows time-averaged velocity fields for Re = 60 and 100 (rows III and IV). Already at Re = 60, a quasi-periodic flow is observed (the structure has several characteristic frequencies). This is evidenced by the instantaneous velocity fields shown in Fig. 3, as well as by the time evolution of velocity components at the monitoring points (Fig. 4,*a*). All the data presented correspond to the statistically steady regime (the portion of the sample where the average values are independent of time).

Instantaneous velocity fields for the unsteady regime at Re = 60 are shown in Fig. 3 for four time points covering one oscillation period T (see Fig. 4,*a*). The evolution of the velocity fields over time demonstrates intense interaction between the jets. The opposing plane jets retain a two-dimensional structure only in the initial stage of motion, deflecting toward one of the two side walls in the central part of the room. At time $t = T/4$ (midplane $x = 1.5H$), the flow in the right part moves in the positive direction of the x-axis, while in the left part it moves in the negative direction (row II in Fig. 3,*b*). The directions are reversed at time $t = 3T/4$ (see Fig. 4): the flow in the right part moves in the negative direction, and the flow in the left part in the positive direction (row IV in Fig. 3,*b*). The alternating reversal of regions with opposite flow directions is accompanied by periodic deformation of the downward flow, which rotates about a vertical axis, as clearly seen from comparing rows II and IV in Fig. 3,*a*. The upward flow at the periphery of the room also exhibits strong unsteadiness: the maxima of positive vertical velocity in the secondary flow periodically shift from one corner to the opposite one (see Fig. 3,*a*).

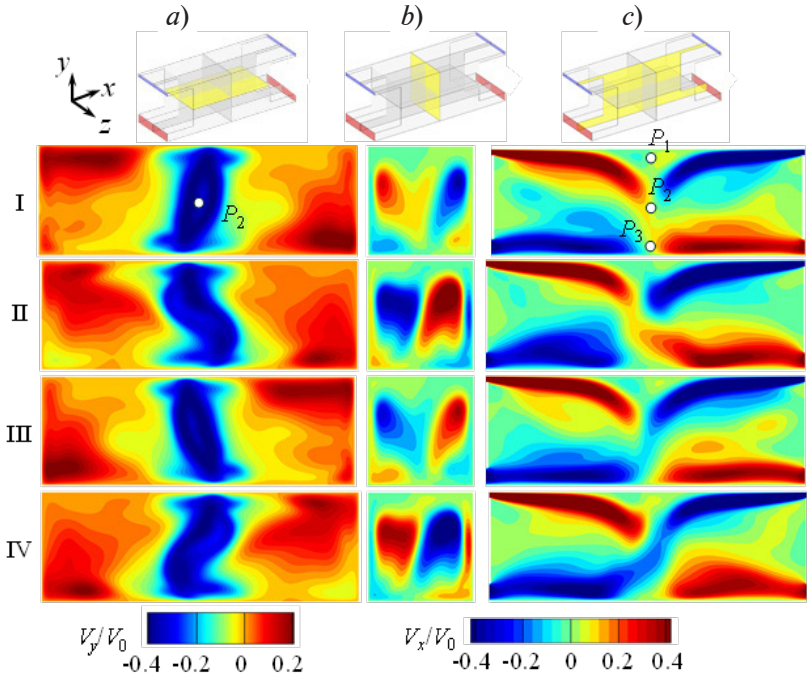


Fig. 3. Instantaneous distributions of vertical (*a*) and longitudinal (*b*) velocity components; velocity component in three room midplanes (*c*) at successive times t: 0 (I), $T/4$ (II), $T/2$ (III), $3T/4$ (IV);
T is the oscillation period; P_1–P_3 are monitoring points; Re = 60

Thus, the instantaneous velocity fields demonstrate an essentially three-dimensional nature of the unsteady flow; this is further illustrated by the instantaneous isosurfaces of longitudinal velocity (see Fig. 1). The time-averaged flow pattern is fairly uniform in the spanwise direction z; the degree of uniformity increases with increasing Re, as follows from comparing the averaged vertical velocity fields in the $y = H/2$ plane for Re = 60 and 100 (see Fig. 2). The jets in the time-averaged flow collide in the central part of the room, descending toward the floor together, where the flow is divided again and moves along the floor to the exhaust openings. The time-averaged patterns at Re = 60 and 100 are a logical continuation of the steady patterns at lower Re.

Fig. 4 shows the plots reflecting the time evolution of the longitudinal and vertical velocity components at three monitoring points P_1–P_3 for Re = 60 and 100. The points lie at the intersection of the vertical midplanes ($z = H/2$ и $x = 1.5H$), i.e., along the centerline of the room, at different heights:

point P_1 is located at half the distance of the supply opening from the ceiling ($y = H - h_{in}/2$),
point P_2 is located at the center of the room ($y = H/2$),
point P_3 is located at half the distance of the exhaust opening from the floor ($y = h_{out}/2$).

The fundamental oscillation period T is taken as the time scale in the plots. The value of T for each case was estimated from the power spectral density of velocity fluctuations.

It follows from the data in Fig. 4 that the flow regime at Re = 60 can be regarded as quasi-periodic, with nearly complete repeatability of the velocity fluctuations over successive oscillation periods, despite the presence of several frequencies. The power spectrum shows a pronounced fundamental frequency; the corresponding Strouhal number $\mathrm{Sh} = h_{in}/TV_0$ equals $2.5 \cdot 10^{-3}$. Intense fluctuations are detected at the central point, especially pronounced in the plot for the evolution of the V_x component; the alternating sign of the longitudinal velocity component reflects the periodic reversal of the flow direction along the x-axis. Even though point P_1 is relatively close to the ceiling, noticeable fluctuations of the vertical velocity component are detected there. Two maxima and two minima occur within one oscillation period T, indicating the alternating influence of the jets from opposite supply openings on the flow at that point. The fluctuation amplitude at point P_3, located in the low-velocity region, is about an order of magnitude lower than at points P_1 and P_2.

The velocity fluctuations at the monitoring points become random at Re = 100 (see Fig. 4,*b*). The self-oscillations become significantly more intense: the deviation of the longitudinal velocity component at the central point from its average (zero) value reaches $0.3V_0$. Notably, at this point the average vertical velocity component V_y also increases in magnitude, which corresponds to a narrowing of the central region with downward flow in the time-averaged flow pattern (see Fig. 2). The fluctuation intensity also increases in the low-velocity region (monitoring point P_3).

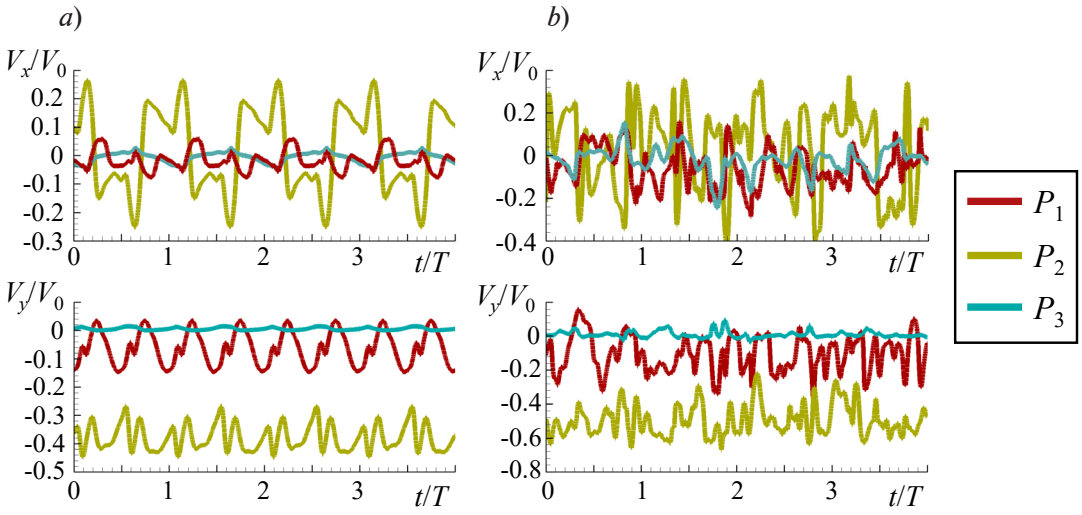


Fig. 4. Time evolution of longitudinal (V_x) and vertical (V_y) velocity components at three monitoring points P_1–P_3 for Re = 60 (*a*) and Re = 100 (*b*)

The spatial distribution of velocity fluctuation intensity for the same unsteady regimes (Re = 60 and 100) is shown in Fig. 5. The figure presents the root-mean-square (RMS) fields of the V_z velocity component in the vertical midplane $z = H/2$ and of the V_y component in the horizontal midplane $y = H/2$. Both distributions characterize the fluctuation intensity of the velocity component normal to the respective plane. It can be seen that fluctuations cover the entire flow domain even at Re = 60. The local maxima of V_y and V_z in the central part additionally indicate intense vertical and spanwise oscillations of the downward structure formed by the two jets. Comparable fluctuation intensities are also observed in the secondary flow region. Comparison of the spatial distributions confirms the significant increase in fluctuations with increasing Re, already inferred from the local data (see Fig. 4).

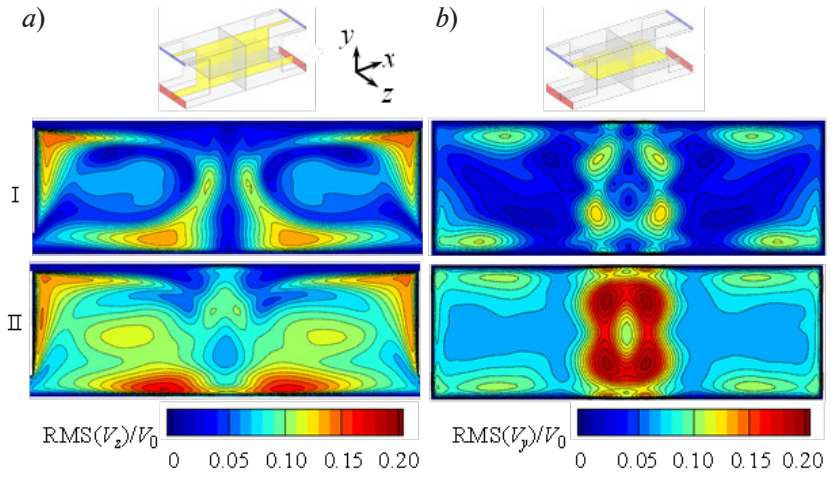


Fig. 5. Distributions of RMS values of velocity components V_z (*a*) and V_y (*b*) for Re = 60 (I) and Re = 100 (II)

The power spectral density (PSD) of the longitudinal velocity component V_x/V_0 at the central point P_2 for Re = 100 is shown in Fig. 6,*a*. The flow exhibits an almost continuous frequency spectrum (the spectrum is discrete for Re = 60) with a pronounced fundamental frequency. The Sh number corresponding to the fundamental frequency is Sh = $2.6 \cdot 10^{-3}$, which is only slightly different from the value obtained for Re = 60.

Fig. 6,*b* shows the dependence of the dimensionless fundamental frequency of velocity fluctuations on the Re number for all parametric cases. The vertical dashed line marks the boundary between steady (I) and unsteady (II) regimes: in all computational cases, the flow is steady for Re ≤ 40, while self-oscillations develop for Re ≥ 50. The dimensionless frequency remains nearly constant for the unsteady regimes over the considered Re range. The Sh numbers lie in the range of $(2.5-3.4) \cdot 10^{-3}$.

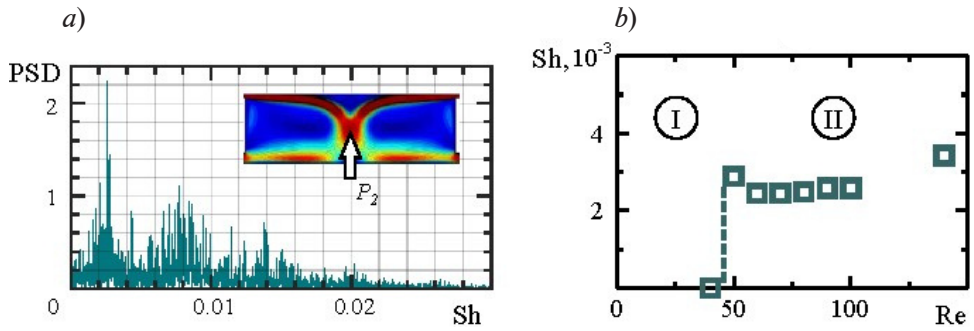


Fig. 6. Power spectral density of velocity component V_x at the central point of the room P_2 for Re = 100 (*a*); dependence of Sh number on Re number for all computed cases (*b*)
The vertical dashed line indicates the boundary between the steady (I) and unsteady (II) regimes

Conclusion

This paper reports on the results of three-dimensional simulations of fluid flow in a rectangular room with supply through two slotted openings located near the ceiling of opposing end walls, and exhaust through two slotted openings near the floor of the same end walls. The unsteady Navier–Stokes equations were solved numerically for Re numbers (defined using the height of the supply slot as the characteristic length) ranging from 20 to 140.

It was found that the flow generated by two opposing plane wall jets becomes unstable as soon as the jet throw becomes sufficient for them to interact directly. For the considered aspect ratio of the room, the flow is steady for $Re \leq 40$, while intense self-oscillations develop for $Re \geq 50$. The most intense velocity fluctuations occur in the central part of the room, where the downward flow combining the two jets rotates about a vertical axis and undergoes periodic deformation.

The fluctuations of the main structure with downward flow extend to the secondary upward flow. The unsteady flow rapidly becomes chaotic (already at $Re = 100$), with a continuous frequency spectrum.

A distinct fundamental oscillation frequency is observed over the range of Reynolds numbers considered, while the corresponding Strouhal number remains nearly constant at approximately $3 \cdot 10^{-3}$.

REFERENCES

1. **Moloy N. A., Taylor P. L.,** Oscillatory flow of a jet into a blind cavity, Nature. 224 (5225) (1969) 1192–1194.

2. **Alferov V. V., Vladimirov V. S., Novikov B. K., et al.,** Struynaya avtomatika v sistemakh upravleniya [Jet automation in control systems], Mashinostroyeniye Publishing, Moscow, 1975 (in Russian).

3. **Markov D., Ivanov N., Pichurov G., et al.,** On the procedure of draught rate assessment in indoor spaces, Appl. Sci. 10 (15) (2020) 5036.

4. **Rockwell D., Naudascher E.,** Self-sustained oscillations of impinging free shear layers, Ann. Rev. Fluid Mech. 11 (Jan) (1979) 67–94.

5. **Maurel A., Ern P., Zielinska B. J. A., Wesfreid J. E.,** Experimental study of self-sustained oscillations in a confined jet, Phys. Rev. E. 54 (4) (1996) 3643–3651.

6. **Lawson N. J., Davidson M. R.,** Crossflow characteristics of an oscillating jet in a thin slab casting mould, J. Fluids Eng. Trans. ASME. 121 (3) (1999) 588–595.

7. **Lawson N. J., Davidson M. R.,** Self-sustained oscillation of a submerged jet in a thin rectangular cavity, J. Fluids Struct. 15 (Jan) (2001) 59–81.

8. **Bensider N., Mataoui A., Aksouh M.,** Control of self-sustained jet oscillations in 3D thin rectangular cavity, Chem. Eng. Res. Des. 117 (Jan) (2017) 533–541.

9. **Zasimova M. A., Ivanov N. G., Krasikova A. D.,** Control of self-oscillations of a round turbulent jet propagating in a narrow rectangular cavity, Thermophys. Aeromech. 31 (4) (2024) 791–804.

10. **Mataoui A., Schiestel R., Salem A.,** Flow regimes of interaction of a turbulent plane jet into a rectangular cavity: experimental approach and numerical modelling, Flow Turbul. Combust. 67 (4) (2001) 267–304.

11. **Mataoui A., Schiestel R.,** Unsteady phenomena of an oscillating turbulent jet flow inside a cavity: Effect of aspect ratio, J. Fluids Struct. 25 (1) (2009) 60–79.

12. **Denisikhina D. M., Bassina I. A., Nikulin D. A., Strelets M. Kh.,** Numerical simulation of self-excited oscillation of a turbulent jet flowing into a rectangular cavity, High Temperature. 43 (4) (2005) 568–579.

13. **Zasimova M. A., Ivanov N. G., Ris V. V., Stepasheva E. D.,** Numerical modeling of the propagation of a turbulent jet flowing from a slot into a confined space, Thermophys. Aeromech. 32 (3) (2025) 623 – 635.

14. **Denshchikov V. A., Kondrat'ev V. N., Romashov A. N.,** Interaction between two opposed jets, Fluid Dyn. 13 (6) (1978) 924–926.

15. **Körner M., Shishkina O., Wagner C., Thess A.,** Properties of large-scale flow structures in an isothermal ventilated room, Build. Environ. 59 (Jan) (2013) 563–574.

16. **Wang C., Li Y., Ding P., et al.,** Analysis of airflow dynamics and instability in closed spaces ventilated by opposed jets using large eddy simulations, Build. 15 (10) (2025) 1707.

17. **Yang C., Zhang X., Yao Z., He F.,** The Large Eddy Simulation and stability analysis of flow field in a generic cabin, Procedia Eng. 121 (Dec) (2015) 1749–1756.

18. **Li J., Liu J., Wang C., et al.,** PIV experimental study of the large-scale dynamic airflow structures in an aircraft cabin: Swing and oscillation, Build. Environ. 125 (2) (2017) 180–191.

19. **Thysen J. H., van Hooff T., Blocken B., van Heijst G. J. F.,** Instantaneous characteristics of interacting opposing plane jets in a generic enclosure measured with PIV, Exp. Fluids. 64 (1) (2023) 19.

20. **van Hooff T., Blocken B.,** Mixing ventilation driven by two oppositely located supply jets with a time-periodic supply velocity: A numerical analysis using computational fluid dynamics, Indoor Built Environ. 29 (4) (2020) 603–620.

21. **Nielsen P. V., Restivo A., Whitelaw J. H.** The velocity characteristics of ventilated rooms, J. Fluids Eng. 100 (3) (1978) 291–298.

22. **Nielsen P. V.,** Specification of a two-dimensional test case, Aalborg University Publ., Aalborg, Denmark, November 1990.

23. **Buri S., Larkermani E., Georges L.,** Influence of the inlet boundary conditions on the LES performance for the cavity flow benchmark, E3S Web Conf. 672 (Dec) (2025) 02018.

24. **Zasimova M. A., Ivanov N. G., Markov D.,** Numerical modeling of air distribution in a test room with 2D sidewall jet. II. LES-computations for the room with finite width, St. Petersburg Polytechnical State University Journal. Physics and Mathematics. 13 (3) (2020) 65–79.

СПИСОК ЛИТЕРАТУРЫ

1. **Moloy N. A., Taylor P. L.** Oscillatory flow of a jet into a blind cavity // Nature. 1969. Vol. 224. No. 5225. Pp. 1192–1194.

2. **Алферов В. В., Владимиров В. С., Новиков Б. К., Строгалев В. П., Масленников С. Л.** Струйная автоматика в системах управления. М.: Машиностроение, 1975. 367 с.

3. **Markov D., Ivanov N., Pichurov G., Zasimova M., Stankov P., Smirnov E., Simova I., Ris V., Angelova R., Velichkova R.** On the procedure of draught rate assessment in indoor spaces // Applied Sciences. 2020. Vol. 10. No. 15. P. 5036.

4. **Rockwell D., Naudascher E.** Self-sustained oscillations of impinging free shear layers // Annual Review of Fluid Mechanics. 1979. Vol. 11. January. Pp. 67–94.

5. **Maurel A., Ern P., Zielinska B. J. A., Wesfreid J. E.** Experimental study of self-sustained oscillations in a confined jet // Physical Review E. 1996. Vol. 54. No. 4. Pp. 3643–3651.

6. **Lawson N. J., Davidson M. R.** Crossflow characteristics of an oscillating jet in a thin slab casting mould // Journal of Fluids Engineering Transactions of the ASME. 1999. Vol. 121. No. 3. Pp. 588–595.

7. **Lawson N. J., Davidson M. R.** Self-sustained oscillation of a submerged jet in a thin rectangular cavity // Journal of Fluids and Structures. 2001. Vol. 15. January. Pp. 59–81.

8. **Bensider N., Mataoui A., Aksouh M.** Control of self-sustained jet oscillations in 3D thin rectangular cavity // Chemical Engineering Research and Design. 2017. Vol. 117. January. Pp. 533–541.

9. **Засимова М. А., Иванов Н. Г., Красикова А. Д.** Управление автоколебаниями круглой турбулентной струи, распространяющейся в узкой прямоугольной полости // Теплофизика и аэромеханика. 2024. Т. 31. № 4. С. 771–785.

10. **Mataoui A., Schiestel R., Salem A.** Flow regimes of interaction of a turbulent plane jet into a rectangular cavity: experimental approach and numerical modelling // Flow, Turbulence and Combustion. 2001. Vol. 67. No. 4. Pp. 267–304.

11. **Mataoui A., Schiestel R.** Unsteady phenomena of an oscillating turbulent jet flow inside a cavity: effect of aspect ratio // Journal of Fluids and Structures. 2009. Vol. 25. No. 1. Pp. 60–79.

12. **Денисихина Д. М., Бассина И. А., Никулин Д. А., Стрелец М. Х.** Численное моделирование автоколебаний турбулентной струи, истекающей в прямоугольную полость // Теплофизика высоких температур. 2005. Т. 43. № 4. С. 568–579.

13. **Засимова М. А., Иванов Н. Г., Рис В. В., Степашева Е. Д.** Численное моделирование распространения турбулентной струи при истечении из щелевого отверстия в ограниченное пространство // Теплофизика и аэромеханика. 2025. Т. 32. № 3. С. 507–519.

14. **Денщиков В. А., Кондратьев В. Н., Ромашов А. Н.** О взаимодействии двух встречных струй // Известия Академии наук СССР. Механика жидкости и газа. 1978. № 6. С. 165–167.

15. **Körner M., Shishkina O., Wagner C., Thess A.** Properties of large-scale flow structures in an isothermal ventilated room // Building and Environment. 2013. Vol. 59. January. Pp. 563–574.

16. **Wang C., Li Y., Ding P., Chen H., Zhang Y., Xing Y.** Analysis of airflow dynamics and instability in closed spaces ventilated by opposed jets using large eddy simulations // Buildings. 2025. Vol. 15. No. 10. P. 1707.

17. **Yang C., Zhang X., Yao Z., He F.** The large eddy simulation and stability analysis of flow field in a generic cabin // Procedia Engineering. 2015. Vol. 121. December. Pp. 1749–1756.

18. **Li J., Liu J., Wang C., Wesseling M., Мьller D.** PIV experimental study of the large-scale dynamic airflow structures in an aircraft cabin: Swing and oscillation // Building and Environment. 2017. Vol. 125. No. 2. Pp. 180–191.

19. **Thysen J. H., van Hooff T., Blocken B., van Heijst G. J. F.** Instantaneous characteristics of interacting opposing plane jets in a generic enclosure measured with PIV // Experiments in Fluids. 2023. Vol. 64. No. 1. P. 19.

20. **van Hooff T., Blocken B.** Mixing ventilation driven by two oppositely located supply jets with a time-periodic supply velocity: a numerical analysis using computational fluid dynamics // Indoor and Built Environment. 2020. Vol. 29. No. 4. Pp. 603–620.

21. **Nielsen P. V., Restivo A., Whitelaw J. H.** The velocity characteristics of ventilated rooms // Journal of Fluids Engineering. 1978. Vol. 100. No. 3. Pp. 291–298.

22. **Nielsen P. V.** Specification of a two-dimensional test case. Aalborg, Denmark: Aalborg University, November 1990. 15 p.

23. **Buri S., Larkermani E., Georges L.** Influence of the inlet boundary conditions on the LES performance for the cavity flow benchmark // E3S Web of Conferences. 2025. Vol. 672. December. P. 02018.

24. **Засимова М.А., Иванов Н.Г., Марков Д.** Численное моделирование циркуляции воздуха в помещении при подаче из плоской щели. II. LES-расчеты для помещения конечной ширины // Научно-технические ведомости СПбГПУ. Физико-математические науки. 2020. Т. 3 № .13. С. 92–75.

THE AUTHORS

ADIATULLIN Vladislav R.
Peter the Great St. Petersburg Polytechnic University
29 Politechnicheskaya St., St. Petersburg, 195251, Russia
vlad-adia@mail.ru

GALAEV Sergey A.
Peter the Great St. Petersburg Polytechnic University
29 Politechnicheskaya St., St. Petersburg, 195251, Russia
galaev@spbstu.ru
ORCID: 0000-0001-7964-0200

RIS Vladimir V.
He dedicated 58 years to serving Peter the Great St. Petersburg Polytechnic University.

ZASIMOVA Marina A.
Peter the Great St. Petersburg Polytechnic University
29 Politechnicheskaya St., St. Petersburg, 195251, Russia
zasimova_ma@mail.ru
ORCID: 0000-0002-4103-6574

IVANOV Nikolay G.
Peter the Great St. Petersburg Polytechnic University
29 Politechnicheskaya St., St. Petersburg, 195251, Russia
ivanov_ng@spbstu.ru
ORCID: 0000-0001-9897-5401

СВЕДЕНИЯ ОБ АВТОРАХ

АДИАТУЛЛИН Владислав Рустамович – *аспирант, инженер научно-образовательного центра «Компьютерные технологии в аэродинамике и теплотехнике» Санкт-Петербургского политехнического университета Петра Великого.*
195251, Россия, г. Санкт-Петербург, Политехническая ул., 29
vlad-adia@mail.ru

ГАЛАЕВ Сергей Александрович – *кандидат технических наук, директор научно-образовательного центра «Компьютерные технологии в аэродинамике и теплотехнике» Санкт-Петербургского политехнического университета Петра Великого.*
195251, Россия, г. Санкт-Петербург, Политехническая ул., 29
galaev@spbstu.ru
ORCID: 0000-0001-7964-0200

РИС Владимир Вольдемарович – *кандидат технических наук; отдал служению Политехническому университету пятьдесят восемь лет.*

ЗАСИМОВА Марина Александровна – *кандидат физико-математических наук, доцент Высшей школы прикладной математики и вычислительной физики Санкт-Петербургского политехнического университета Петра Великого.*
195251, Россия, г. Санкт-Петербург, Политехническая ул., 29
zasimova_ma@mail.ru
ORCID: 0000-0002-4103-6574

ИВАНОВ Николай Георгиевич – *кандидат физико-математических наук, заведующий научно-исследовательской лабораторией гидродинамики, директор Физико-механического института Санкт-Петербургского политехнического университета Петра Великого.*
195251, Россия, г. Санкт-Петербург, Политехническая ул., 29
ivanov_ng@spbstu.ru
ORCID: 0000-0001-9897-5401

Received 07.12.2025. Approved after reviewing 12.12.2025. Accepted 12.12.2025.
Статья поступила в редакцию 07.12.2025. Одобрена после рецензирования 12.12.2025. Принята 12.12.2025.

© Peter the Great St. Petersburg Polytechnic University, 2026

Original article
DOI: https://doi.org/10.18721/JPM.19204

SUPERCOMPUTER SIMULATION OF THE DYNAMICS OF OLIGOMERS OF A NUMBER OF AMINO ACIDS (Gly, Ala, Trp, Val) IN AN INFRARED ELECTROMAGNETIC FIELD

M. A. Baranov✉, *O. Yu. Tsybin*

Peter the Great St. Petersburg Polytechnic University,
St. Petersburg, Russia

✉ baranovma1993@gmail.com

Abstract. Supercomputer simulation of several amino acid oligomers using the molecular dynamics method has made it possible for the first time to identify a complex of characteristics of both intrinsic intramolecular local vibrations, or normal modes, and forced vibrations when specifying an alternating electric field in the IR frequency range. Amplitude-time dependences of energy and electric dipole moment were obtained for oligomers of Gly, Ala, Trp, Val amino acids, the Fourier transform of which revealed their frequency spectra. The type of solvent model was shown to significantly affect the position of spectral peaks because of variations in local interactions and system dynamics. The interpretation of the obtained patterns made it possible to propose a non-contradictory model that satisfied the fundamental physical concepts of the intramolecular and intermolecular dynamics of groups of biomolecules. The model allows for intramolecular interactions of normal local vibrations, including those of the Fermi resonance type.

Keywords: molecular dynamics, simulation, amino acid, biomolecular electronics

Citation: Baranov M. A., Tsybin O. Yu., Supercomputer simulation of the dynamics of oligomers of a number of amino acids (Gly, Ala, Trp, Val) in the infrared electromagnetic field, St. Petersburg State Polytechnical University Journal. Physics and Mathematics. 19 (2) (2026) 39–56. DOI: https://doi.org/10.18721/JPM.19204

This is an open access article under the CC BY-NC 4.0 license (https://creativecommons.org/licenses/by-nc/4.0/)

Научная статья
УДК 53.093, 53.096, 57.031, 57.033, 57.038
DOI: https://doi.org/10.18721/JPM.19204

СУПЕРКОМПЬЮТЕРНОЕ МОДЕЛИРОВАНИЕ ДИНАМИКИ ОЛИГОМЕРОВ РЯДА АМИНОКИСЛОТ (Gly, Ala, Trp, Val) В ЭЛЕКТРОМАГНИТНОМ ПОЛЕ ИНФРАКРАСНОГО ДИАПАЗОНА

М. А. Баранов✉, *О. Ю. Цыбин*

Санкт-Петербургский политехнический университет Петра Великого,
Санкт-Петербург, Россия

✉ baranovma1993@gmail.com

Аннотация. Суперкомпьютерное моделирование методом молекулярной динамики ряда олигомеров аминокислот позволило впервые выявить для таких частиц особенности комплекса характеристик как собственных внутримолекулярных локальных колебаний (нормальных мод), так и вынужденных колебаний в растворе

© Baranov M. A., Tsybin O. Yu., 2026. Published by Peter the Great St. Petersburg Polytechnic University.

при задании электромагнитного поля в дальнем и среднем ИК-диапазонах, а также различных алгоритмов структуры растворителя. Для олигомеров аминокислот Gly, Ala, Trp, Val и их групп получены амплитудно-временные зависимости энергии и электрического дипольного момента, Фурье-преобразованием которых выявлены спектры частот. Впервые обнаружены и вычислены смещения спектральных пиков, вызванные различиями алгоритмов задания структуры растворителя. Интерпретация полученных закономерностей позволила предложить непротиворечивую модель, удовлетворяющую фундаментальным физическим представлениям о внутримолекулярной и межмолекулярной динамике групп биомолекул. Эта модель допускает внутримолекулярные взаимодействия нормальных локальных колебаний, в том числе по типу Ферми-резонанса.

Ключевые слова: молекулярная динамика, компьютерное моделирование, аминокислота, биомолекулярная электроника

Ссылка для цитирования: Баранов М. А., Цыбин О. Ю. Суперкомпьютерное моделирование динамики олигомеров ряда аминокислот (Gly, Ala, Trp, Val) в электромагнитном поле инфракрасного диапазона // Научно-технические ведомости СПбГПУ. Физико-математические науки. 2026. Т. 19. № 2. С. 39–56. DOI: https://doi.org/10.18721/JPM.19204

Статья открытого доступа, распространяемая по лицензии CC BY-NC 4.0 (https://creativecommons.org/licenses/by-nc/4.0/)

Introduction

Forced vibrational processes in biomolecules, driven by external electromagnetic fields, are of considerable importance for life sciences, medicine, microelectronics, nanotechnology, and experimental spectroscopy [1–13]. Computational analysis of the time-dependent total dipole moment (summed over all molecular charges) in the absence of an applied field revealed the sub-picosecond dynamics of intrinsic biomolecular vibrations [14, 15]. The intrinsic vibrational frequencies correspond to local normal modes and delocalized collective motions spanning the terahertz (THz) to infrared (IR) range. Molecular dynamics simulation computing the time-dependent total dipole moment under an applied electromagnetic field makes it possible to determine molecular conformations and IR absorption spectra of forced vibrations, yielding substantial scientific and applied results in modern bio- and nanophysics [10, 16–25]. For instance, molecular dynamics simulations were performed for monomers, dimers, and protofibrils of Aβ42 in the THz range, and the applicability of the method to the mid- and far-infrared ranges was also confirmed [20]. It was shown that Newtonian force-field mechanics is a valid approach in molecular dynamics for the mid- and far-infrared ranges, alongside quantum-mechanical calculations [17, 20, 21, 23, 24, 26–28]. Comparisons of molecular dynamics studies in these frequency ranges yield reasonably close agreement between the calculated spectral characteristics and experimental or theoretical data for both intrinsic and forced vibrations [6, 21–23].

For example, the assignments of the most intense intrinsic vibrations at the calculated frequencies (wavenumbers, cm^{-1}) are given for amino acid solutions:

1100, 1519, 1652, 3018, 3322, 3364, 3362 for alanine (Ala);
927, 1060, 1542, 1643, 3210, 3322, 3364, 3479 for glycine (Gly);
1048, 1533, 1640, 3030, 3325, 3361, 3479, 3663 for valine (Val);
784, 1403, 1495, 1536, 1646, 2917, 3325, 3562, 3766 for tryptophan (Trp).

These results are in agreement with theoretical and experimental data reported previously, although the extent of this agreement has not been quantified [26, 28].

© Баранов М. А., Цыбин О. Ю., 2026. Издатель: Санкт-Петербургский политехнический университет Петра Великого.

According to the established view, spectral components above roughly 200–800 cm^{-1} correspond to local intramolecular vibrations (normal modes), while those below this range are collective delocalized vibrations. The assignment of local oscillator bands to normal modes and their frequencies was discussed in numerous sources, for example, in [26].

The spectral window from 2600 to 900 cm^{-1} is reported in [29]. Nine characteristic vibrational bands (amides A, B, I, II, ..., VII) are prominent in the IR spectrum, with amides I and II falling between 1600–1700 cm^{-1} and 1500–1600 cm^{-1}, respectively. The unperturbed C=O stretching vibration (amide I) has a frequency of 1688 cm^{-1}; the corresponding spectral band shifts in the presence of water or other solvents and also depends on conformation. The N–H bending vibration (Amide II) occurs in the wavenumber range of 1530–1580 cm^{-1}. The Cα–N stretching vibration (Amide III) falls within the range of 1200–1340 cm^{-1}. The resonant field frequencies (fundamental frequencies of the square wave at 3335.66 and 1042.37 cm^{-1}) coincide with specific intrinsic local vibrations (asymmetric N–H stretching of Amide A and C–N stretching, respectively).

Recent advances in molecular dynamics yielded new supercomputer simulation results describing the dynamics of increasingly complex protein molecules under electric fields with various polarizations and modulations in the THz and IR ranges [30–33]. Oligomers are attracting growing attention as key functional units that enable proteins to initiate allostery and cooperativity [14, 15, 34–37].

The vibrational dynamics of oligomers driven by electromagnetic fields of different polarizations and time profiles was simulated for the first time over a range of wavenumbers, particularly in the far- and mid-infrared ranges [25].

The goal of this supercomputer study is to refine the analysis of forced vibrations of oligomers and their aggregates in solution, which is essential for advancing fundamental biological and biophysical understanding, as well as for a range of current and emerging applications.

Computational approach and validation

The computational approach we adopted relies on a methodology for supercomputer simulation of molecular dynamics that has already proven to be highly efficient and reliable [25, 29, 38–41].

The techniques previously developed for single molecules were also applied here to oligomers and their assemblies.

The dynamic simulations of molecular complexes were performed using the RSC Tornado cluster at the Polytechnic Supercomputer Center of Peter the Great St. Petersburg Polytechnic University, as described in detail in our previous work [33]. The cluster, with a peak performance of 10^{15} flops, comprises 668 dual-processor nodes (Intel Xeon E5-2697 *v*33), 56 of which are equipped with two NVIDIA K40 accelerators. This configuration allows generating, within a reasonable computation time, extensive databases of the time-dependent total dipole moment with trajectory durations up to 40 ns and a minimum sampling interval of 1 fs, thereby providing high resolution in the Fourier spectra over the far- and mid-infrared frequency ranges. The software suite included Avogadro, Visual Molecular Dynamics (VMD), and NAMD, along with additional custom Python scripts. The Packmol tool was used to place oligomers in groups of $p = 1, 2, ..., 20$ particles within a cubic water box with a side length of 70 E. Initial coordinate files for the Gly, Ala, Trp and Val oligomers in aqueous solution were generated using Avogadro. The results presented below are primarily from simulations of polyAlaN oligomers (initially modelled as α-helices) with different numbers of amino acid residues $N = 18$,... ,2 ,1. The VMD software was used to generate structural files based on the topology of molecular bonds, add water molecules and salt ions, visualize molecular systems, calculate the energy and dipole moments of conformationally flexible molecules. Newton's equations of motion were solved for each atom of the system, atomic coordinates, force field parameters, system temperature, pressure, etc. were determined at each time step. The time-dependent total dipole moment $\mu(t)$ was then computed from the instantaneous coordinates and velocities of the charged particles by summing the displacement vectors of each charge at each time step.

The change in the partial dipole moment $\Delta\mu_{n,j}$ at the jth time step of duration Δt corresponds to the spatial displacement of charge q_n by the vector $\Delta\mathbf{r}_{n,j}$:

$$\Delta\mu_{n,j} = q_n \Delta \mathbf{r}_{n,j} = q_n \left[r_{n,j} - r_{n,j-1} \right].$$

The time-dependent total dipole moment $\mu(t)$ was then obtained by summing the partial moments over all charges in the oligomer solution:

$$\mu(t) = \sum_j \sum_n^N q_n \Delta \mathbf{r}_{n,j}, \quad (1)$$

where N is the total number of charges.

The time series of the instantaneous total dipole moment, $\mu(t)$, represents a superposition of the local vibrational motions of all charged atoms within the molecule.

The wavenumber spectrum of these vibrational motions was obtained by Fourier transformation of the time-dependent total dipole moment, both for each individual oligomer and for the entire assembly of particles in the simulation cell. The algorithm for computing the time series relies on the independence of the fluctuations of the total dipole moment (1) from the origin of the displacement vectors $\Delta \mathbf{r}_{n,j}$. High resolution in the characteristic frequencies of the studied part of the Fourier spectrum was achieved due to its numerical equality to the ratio of the duration of the amplitude-time realization to the oscillation period.

The Fourier method employed here has the advantage of reproducing all spectral components within a specified wavenumber range, including higher harmonics and combination bands. The range is limited by half the sampling frequency but can be extended using the computational resources of the supercomputer.

An applied electric field induces charge displacements at characteristic IR frequencies and a polarization response altering the components and magnitude of the dipole moment. To ensure the most informative study, three types of electromagnetic fields were specified with plane spatial polarization along the coordinate axes (x,y,z), with components [E,0,0] and amplitudes from 0.01 to 0.50 V/nm:

a harmonic electric field,

a periodic sequence of unipolar rectangular pulses,

a symmetric square wave.

The square wave was chosen because it combines the properties of periodic pulse sequences and is of practical interest for microelectronics, particularly for controlled switching of molecular states and for probing anharmonic molecular dynamics. The feasibility and effectiveness of a square-wave electric field with a fundamental frequency in the IR range were tested and validated in several studies [14, 15, 23–25]. A similar square-wave electric field was used in molecular dynamics simulations of liquid water in the 20–500 GHz frequency range [40].

The strength of the local electric field acting on the charges within the molecule was varied over a wide range, from 0.004 to 0.400 V/nm. As in our previous works and in studies by other authors, the time dependence of the vibrational amplitudes was linear and did not lead to molecular fragmentation. Indeed, such fields exist only in the microscopic region near a charge and correspond to typical atomic intramolecular fields. This approach does not require comparison with macroscopic fields, which have different energy characteristics [42–44].

Based on the obtained data for the intrinsic vibrational spectra of oligomers, we applied the electric field $E(t)$ at a set of resonant frequencies corresponding to the following fundamental wavenumbers (in cm^{-1}):

5555, 4167, 3333, 1667, 1515, 1111, 1042, 980 and 200.

The energy characteristics corresponding to these wavenumbers are shown in Fig. 1.

The time evolution of the kinetic and potential energies of the particles and the system as a whole was computed simultaneously with the time-dependent dipole moment.

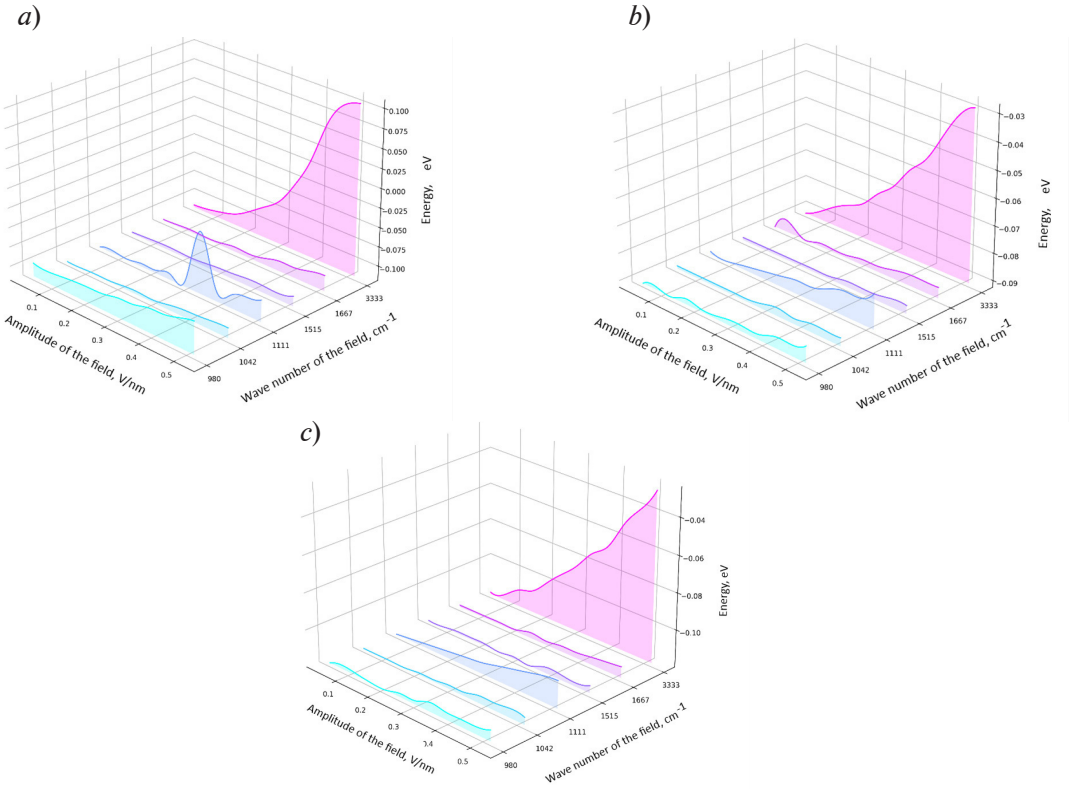


Fig. 1. Typical potential energy characteristics of Ala (*a*), Gly (*b*), Trp (*c*) molecules in aqueous solution obtained with an explicit solvent model. The figure shows 3D plots of energy as a function of square-wave amplitude of the electric field at selected wavenumbers (WN). Temperature: 298 K, time step: 5 fs

The most pronounced dependence on the strength of the alternating electric field was observed at the wavenumber 3333 cm^{-1}, corresponding to the asymmetric N−H stretching vibrations (Amide A) (see Fig. 1,*a*). This may also be related to preferential localization of vibrations in hydrogen-bond networks. The molecular energy at resonance depended to a greater extent on the applied field strength and to a lesser extent (or not at all) on the trajectory duration. The potential energy remained nearly constant in the field strength range from approximately 0.01 to 0.50 V/nm over the time interval from 0 to 510 ps for Gly and Trp, showing a more complex dependence for Ala, presumably due to the larger side chain (see Fig. 1,*b*).

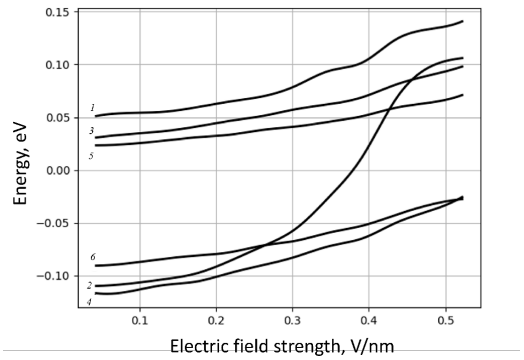


Fig. 2. Potential and kinetic energies of diphenyl-L-alanine (*1*, *2*), tryptophan (*3*, *4*), and glycine (*5*, *6*) in aqueous solution as function of field strength at t = 500 ps
Fundamental wavenumber of electric field: 3333 cm^{-1}

Fig. 2 shows the potential and kinetic energies of diphenyl-L-alanine, tryptophan, and glycine in aqueous solution as functions of the field strength at a fixed time t= 500 ps. Fundamental wavenumber of electric field: 3333 cm^{-1}. Notably, there is a linear increase in energy from very small field strengths at the fundamental frequency of 3333 cm^{-1} up to about 0.4 V/nm for glycine and tryptophan, and up to 0.2 V/nm for diphenyl-*L*-alanine. At other characteristic frequencies (e.g., 980 and 200 cm^{-1}), both types of energy were nearly independent of the field strength, which is consistent with the data in Fig. 1,*a*.

Shifts in the spectral peaks along the wavenumber scale were observed, depending on the algorithms chosen for local interactions and system dynamics. Specifically, the virtual molecular systems differed in the way water (solvent) was added: either as an implicit solvent or as an explicit solvent (with water molecules added), i.e., using the coarse-grained model [45].

In the latter case, the volume and complexity of computations increase significantly because it is necessary to set the parameters and states of the water molecules, the size of the water box, etc. The generalized Born implicit solvent (GBIS) method was used for the former case. It is a fast but approximate method for calculating molecular electrostatics in a solvent, described by the Poisson–Boltzmann equation, which models water as a dielectric continuum:

$$\nabla \times \left[\varepsilon(\mathbf{r})\nabla\varphi(\mathbf{r})\right] = -\rho^{f}(\mathbf{r}) - \sum_{i} c_{i}^{\infty} z_{i} e_{0} \exp\left[\frac{-z_{i} e_{0}\varphi(\mathbf{r})}{k_{\mathrm{B}} T}\right], \quad (2)$$

where $\varepsilon(\mathbf{r})$ is the dielectric permittivity of the medium, φ is the electric potential, $\rho^{f}(\mathbf{r})$ is the charge density in the medium, c^{∞}_{i} is the concentration of the ith ion at infinity, z_i is the valence of the ith ion, k_{B} is the Boltzmann constant, T is the temperature.

This method allows simulating atomic structures without including explicit water, i.e., without adding hydrogen and oxygen atoms and without computing their coordinates. Using an implicit solvent significantly accelerates the simulations and greatly reduces the size of the output files (roughly in a 1 : 50 GB ratio), which was a key factor in this study.

Amino acid molecules were placed in a periodic system with a cubic water cell (with a side length of 70 E, independent of the molecular sizes). The distance from the outermost molecule to the cell boundary was 15 E. Solvation of molecules was simulated by the TIP3W water model, corresponding to three atoms of the water molecule at three interaction points. Such models provide high computational efficiency and are used in many applications for molecular dynamics simulation. The chosen water model was also used with the CHARMM force field. The difference lies in the Lennard–Jones parameters: unlike TIP3, the CHARMM version of the model assigns these parameters to hydrogen atoms in addition to the oxygen parameters in the water molecule [46, 47]. Many similar studies used this water model, but the frequency shifts of intrinsic vibrations associated with different algorithms were not discussed previously [48, 49].

Simulation results

Fig. 3 shows the spectral characteristics of water in the periodic system of cubic cells, computed in this paper using the explicit solvent model; the ranges of intrinsic vibrations of water molecules known from the literature are also shown for comparison [50].

The Fourier spectrum of the electric dipole moment of water molecules was calculated using the VMD IR Spectral Density Calculator plugin; the duration of the amplitude-time realization was 20 ns.

Analyzing the spectra in Fig. 3, we can conclude that the vibrational bands of water molecules are close to the positions of the intrinsic vibrational peaks of biomolecules [20, 30, 31, 33]. The resonant spectral effects of forced vibrations under an applied electric field, observed in the total dipole moments of oligomer assemblies, are similar in energy characteristics to those found for single amino acid molecules [20, 33] as well as for dimers, trimers, and other peptides [51, 52].

The Fourier spectra of the intrinsic intramolecular vibrational bands of polyAlaN oligomers were qualitatively similar for different N (N = 1, 2, ..., 18) and for different numbers p (p = 1, 2, ..., 10) of such oligomers in the water box, but they also exhibited several quantitative features. Fig. 4 shows the typical overview and selected window spectra of polyAla12 oligomers, derived from the time-dependent total dipole moment reflecting the intrinsic vibrational motions of the molecules. The spectra were obtained with a trajectory duration of 2 ns, time window of 510 ps, and a time step of 5 fs (T = 298 K).

Comparing the overview Fourier spectra of intrinsic vibrations for single polyAla12 oligomers (p = 1) and for their assemblies with p = 10 (see Fig. 4), we found that the set of spectral components was virtually identical. However, a change in the spectral components was

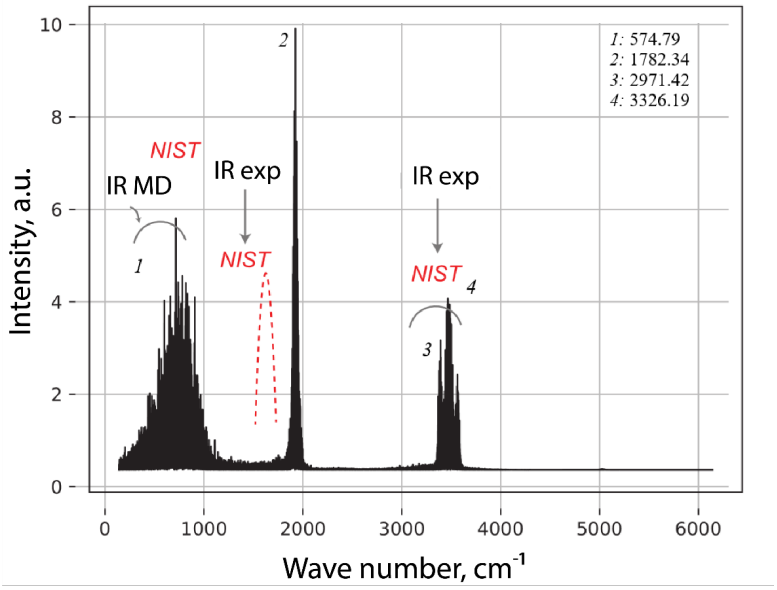


Fig. 3. Fourier spectra of time-dependent dipole moment of water molecules: IR MD corresponds to results obtained with the VMD IR Spectral Density Calculator plugin (t = 1 ns, f_D = 200 THz); IR exp NIST corresponds to the experimental results from the NIST database [48]
The wavenumbers (cm^{-1}) of spectral bands *1–4* are given in the legend

observed as the number of oligomers increased: the structure with two peaks in the center at 3313.5 and 3358.1 cm^{-1} transformed into a structure with two peaks at 3277 and 3394.4 cm^{-1}. This change likely indicates dipole–dipole interactions between oligomers in the assembly. A similar evolution of spectral components was reproduced for other values of the parameters N and p. The differences observed between the typical spectral windows from the overview spectra of polyAla12 oligomer assemblies (see Fig. 4) are likely due to phonon–phonon coupling of local vibrations, as well as to collective mechanisms forming spectral components in the molecular assembly.

The Fourier spectra of forced vibrations for polyAla18 oligomers (p = 1) were calculated from the total dipole moment, with a trajectory duration of 2 ns, under an applied symmetric square-wave electric field. The square-wave amplitude was varied over two orders of magnitude, from 0.004 to 0.400 V/nm, corresponding to local atomic fields within the molecule. The fundamental harmonics showed essentially the same behavior and patterns at different vibrational frequencies with varying excitation parameters. Fig. 5 shows the typical overview spectra of forced vibrations for polyAla18 oligomers at p = 1, computed from the total dipole moment, with a trajectory duration of 2 ns, under an applied symmetric square-wave electric field with a peak-to-peak amplitude of 0.4 V/nm at different fundamental wavenumbers.

Spectra with similar characteristics were obtained at lower fields in the range of 0.01–0.400 V/nm for all three types of electric field.

Comparing the spectra of forced vibrations (see Fig. 5) and intrinsic vibrations, we found that field excitation at wavenumbers of 5555 and 4167 cm^{-1}, as well as at other wavenumbers in the region above the frequencies of intrinsic local vibrations, did not cause any noticeable rearrangement of the spectral components of oligomers for different N(N = 1, 2, ..., 18). When the excitation frequency coincided with an intrinsic local vibration frequency, for example at wavenumbers (in cm^{-1}) of 3333, 1111, 1042, and 980, a strong rearrangement of the spectral components was observed, consistent with resonant pumping of forced vibrations (see Fig. 4). This result is likely due to corresponding changes in the conformational structure and in the total dipole moment. Indeed, the frequency dependences obtained for the time-averaged total dipole moment of polyAla18 oligomers for different values of p at a field strength E= 0.4 V/nm were consistent with this interpretation.

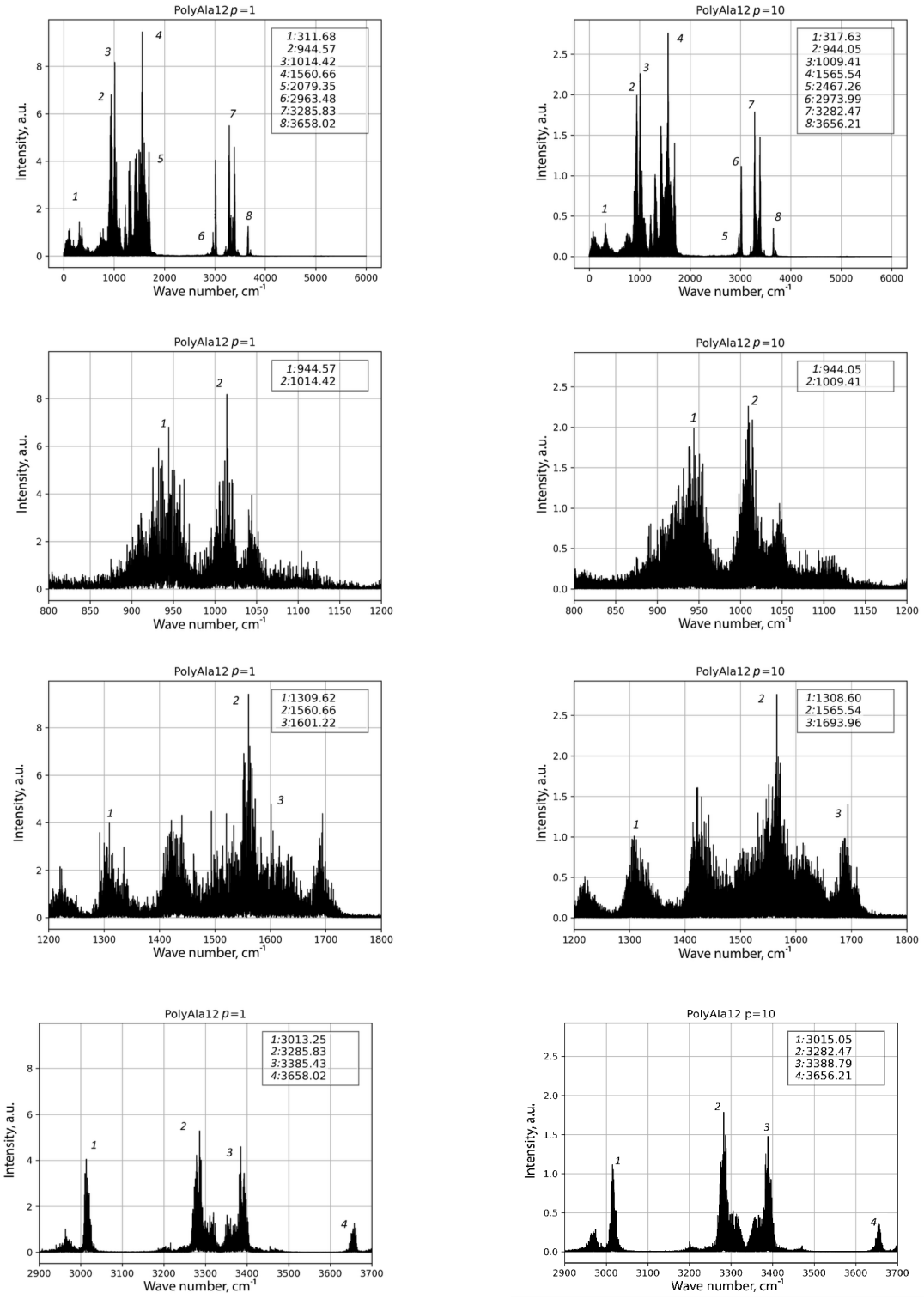
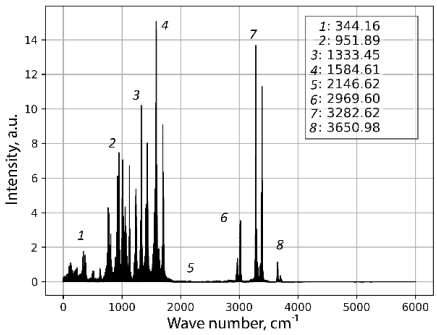
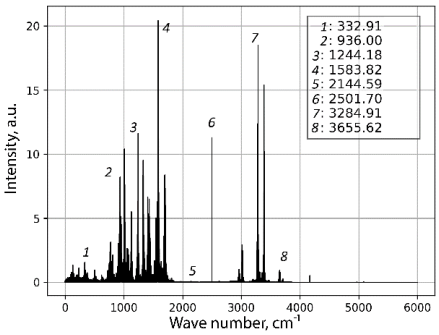


Fig. 4. Overview vibrational spectra of polyAla12 oligomers, computed from the total dipole moment. Selected spectral windows are shown for different numbers p of oligomers
The wavenumbers (cm^{-1}) of spectral bands are given in the legends

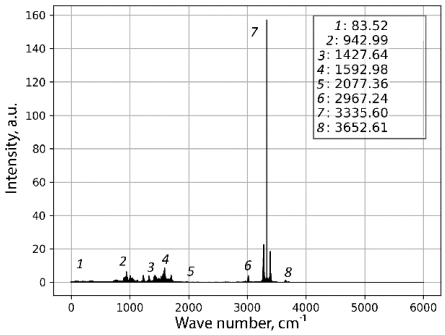
a) WN = 5555 cm^{-1}



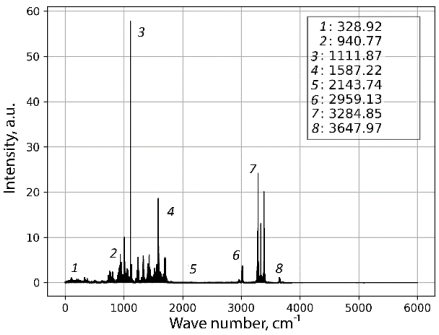
b) WN =4167 cm^{-1}



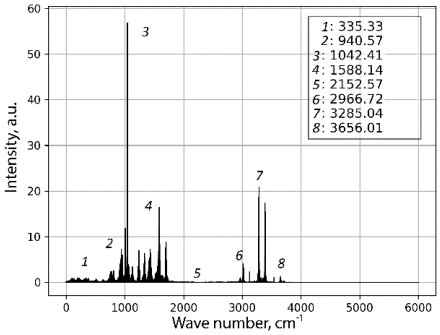
c) WN = 3333 cm^{-1}



d) WN =1111 cm^{-1}



e) WN = 1042cm^{-1}



f) WN = 980cm^{-1}

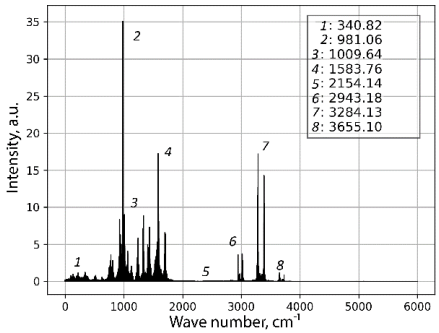


Fig. 5. Fourier spectra of forced vibrations
for polyAla18 oligomers (p = 1), computed from the total dipole moment,
with trajectory duration of 2 ns, under an applied symmetric square-wave electric field
(peak-to-peak amplitude of 0.4 V/nm), at different fundamental wavenumbers (WN)

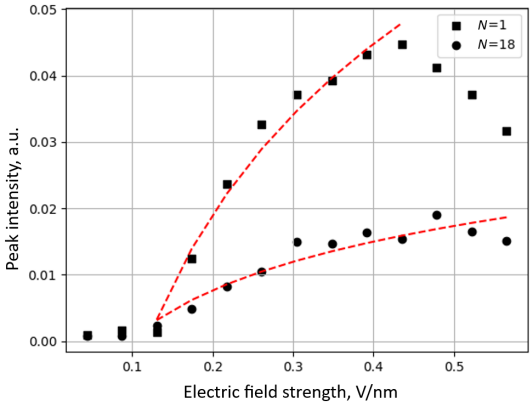


Fig. 6. Resonance peak intensity of polyAlaN molecules at $N = 1$ and $N = 18$ ($p = 1$) as a function of electric field strength under square-wave excitation at WN = 3333 cm^{-1}

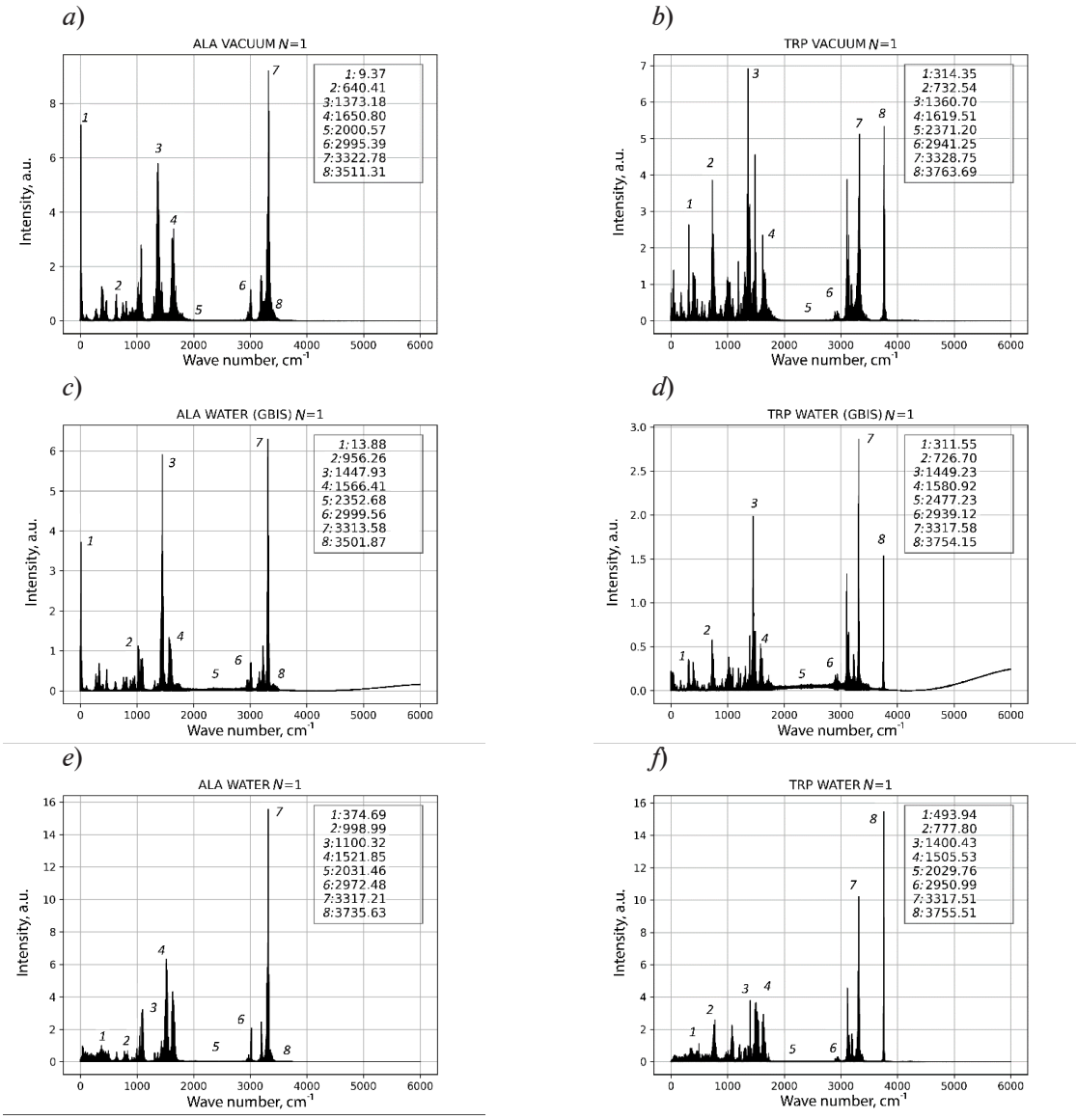


Fig. 7. Simulated Fourier spectra of time-dependent dipole moment for Ala and Trp molecules ($t = 1$ ns) in different environments: Ala in vacuum (*a*); Trp in vacuum (*b*); Ala with GBIS (*c*); Trp with GBIS (*d*); Ala in explicit water solvent (*e*); Trp in explicit water solvent (*f*)

Fig. 6 shows the intensities of the peaks in the resonant spectral bands of polyAlaN molecules at $N = 1$, $N = 18$ and $p = 1$ as a function of the electric field strength under square-wave excitation at a fundamental wavenumber of 3333 cm^{-1}. A nearly linear relationship was observed between the resonance peak intensities and the electric field strength in the region of very small field amplitudes. This linear region extends up to the maximum intensities of the resonant spectral bands, when the field amplitude reaches about 0.4 V/nm, which is consistent with the results known from the literature [53, 54].

The spectral line intensities at different excitation frequencies either remained virtually unchanged or increased linearly with increasing field strength over the given range.

Fig. 7 shows the spectral characteristics of the amplitude-time realization of the electric dipolemoments of Ala and Trp molecules simulated for vacuum conditions and various water-solvent models. The differences revealed in the spectral characteristics, discussed below, allowed us to formulate and justify some significant additions to the description of the vibrational properties of molecules.

Discussion

The results presented above allow analyzing the dynamic properties of the considered set of oligomers in the IR range. Comparing the overview Fourier spectra of intrinsic vibrations for single oligomers and for their assemblies, we found that the set of spectral components was virtually identical for different values of the parameters N and p. The effects of forced vibrations under external electric fields of various types, including harmonic and pulsed periodic fields, observed in the total dipole moments of oligomer assemblies, were found to be similar in energy and spectral characteristics to those observed in single amino acid molecules.

Considering the typical selected spectral windows from the overview vibrational spectra of the oligomer assembly, computed from the total dipole moment, we observe a frequency proximity effect both among the local oscillators themselves and between these oscillators and the applied electric field. We can therefore assume that these windows exhibit effects of mutual coupling of local vibrations; such coupling is likely due to phonon interactions, leading to collective formation of spectral components. As the oligomer size increased, a redistribution of the spectral components was observed: the structure with two peaks in the center (at 3313.5 and 3358.1 cm^{-1}) was transformed into a structure with two peaks at 3277 and 3394.4 cm^{-1}. A similar evolution of spectral components was reproduced for other values of N. In our view, this effect is caused by Fermi resonance of the second harmonic of the vibrations at 1565.7 and 1695.5 cm^{-1} present in the spectrum, with the resonant frequency at 3333 cm^{-1}, which we were able to identify by applying an electric field.

No significant changes in the total dipole moment were observed for a single molecule under an applied electric field in the case of forced local vibrations, which likely points to conformational stability of a single oligomer upon excitation of local (rather than collective) vibrations. However, significant changes appear for larger numbers of oligomers in the assembly, when the parameter $p = 3$, 4, and 5. In this case, the effects of the applied electric field on intermolecular vibrations and dipole–dipole interactions may be observed.

During the simulation, a difference was revealed for the first time in the dependences of the resonance peaks of polyAlaN molecules at $N = 1$ and $N = 18$, on the electric field strength under square-wave excitation at a fundamental wavenumber of 3333 cm^{-1} (see Fig. 5). The resonance peak intensity is significantly higher for a single molecule (see Fig. 6) than for the oligomer, whose conformation and total energy are more stable with respect to excitation of intramolecular local oscillators.

Conclusion

We performed the first supercomputer molecular dynamics simulations of oligomers of several amino acids under electromagnetic fields in the IR range. The supercomputer methods developed here are suitable for applications in nanobiotechnology and microelectronics that incorporate biomolecular components, among which amino acid oligomers play a major role. The methodology has proven to be highly effective and reliable, yielding new results that consistently complement existing theoretical and experimental data. We used three types of amplitude modulation of the applied electric field (harmonic, a periodic sequence of unipolar rectangular pulses, and a symmetric square wave) to lay the groundwork for further practical studies and establish the means to monitor anharmonicity over a broad frequency band in the mid- and far-infrared regions.

The method allowed us to compare the frequency spectra of intrinsic molecular vibrations both in water and in the absence of a water environment, and to identify the common features and peculiarities. Adding water (*in silico*) shifted the frequencies upward by a few percent, i.e., towards higher vibrational energies. This shift likely originates from the specific intrinsic vibrational spectrum of water molecules, whose nonlinear couplings become active simultaneously with the local oscillators of the solutes.

A set of characteristics for both intrinsic local vibrational modes (normal modes) and forced vibrations of oligomers in the far- and mid-infrared ranges was identified for the first time. Interpretation of the obtained patterns allowed us to propose a consistent model of molecular physics, including mutual phonon couplings of local oscillators, satisfying the fundamental physical concepts of the intramolecular and intermolecular dynamics of groups of biomolecules.

The results can be used to determine the functional properties of dehydrated biomolecular films for applications in biophysics, nanobiotechnology, and microelectronics, for example in the design of prototypes of bioelectronic and heterogeneous hybrid microelectronic devices with embedded biomolecular components [55].

REFERENCES

1. **Ruan X., Ruan X., Huang H.,** Application of terahertz spectroscopy in medical microbiological detection, J. Phys. Conf. Ser. 2425 (1) 012045.

2. **Turton D. A., Senn H. M., Harwood T., et al.,** Terahertz underdamped vibrational motion governs protein-ligand binding in solution, Nat. Commun. 5 (03 Jun) (2014) 3999.

3. **Noble B. B., Todorova N., Yarovsky I.,** Electromagnetic bioeffects: A multiscale molecular simulation perspective, Phys. Chem. Chem. Phys. 24 (11) (2022) 6327–6348.

4. **Woods K. N.,** Solvent-induced backbone fluctuations and the collective librational dynamics of lysozyme studied by terahertz spectroscopy, Phys. Rev. E. 81 (3) (2010) 031915.

5. **Niehues G., Heyden M., Schmidt D. A., Havenith M.,** Exploring hydrophobicity by THz absorption spectroscopy of solvated amino acids, Faraday Discuss. 150 (23 May) (2011) 193–207.

6. **Jeong S.-Y., Cheon H., Lee D., Son J.-H.**, Determining terahertz resonant peaks of biomolecules in aqueous environment, Opt. Express. 28 (3) (2020) 3854–3863.

7. **Grechko M., Hasegawa T., D'Angelo F., et al.,** Coupling between intra- and intermolecular motions in liquid water revealed by two-dimensional terahertz-infrared-visible spectroscopy, Nat. Commun. 9 (1) (2018) 885.

8. **Xu J., Galan J., Ramian G., et al.,** Terahertz circular dichroism spectroscopy of biomolecules, In book: Jensen J. O., Theriault J.-M. (Eds.) Proc. SPIE. Vol. 5268: Chemical and Biological Standoff Detection. (27 Febr) (2004) 19–26.

9. **Beyer C., Christen P., Jelesarov I.**, **Fröhlichet J.,** Real-time assessment of possible electromagnetic-field-induced changesin protein conformation and thermal stability, Bioelectromagnetics. 35 (7) (2014) 470–478.

10. **Calabrò E., Magazщ S.,** Resonant interaction between electromagnetic fields and proteins: A possible starting point for the treatment of cancer, Electromagn. Biol. Med. 37 (3) (2018) 155–168.

11. **Harvey A.,** The interaction between electromagnetic fields at megahertz, gigahertz and terahertz frequencies with cells, tissues and organisms: Risks and potential, J. R. Soc. Interface. 14 (2017) 0585.

12. **Wu H., Ghaani M. R., Futera Z., English N. J.,** Effects of externally applied electric fields on the manipulation of solvated-chignolin folding: Static- versus alternating-field dichotomy at play, J. Phys. Chem. B. 126 (2) (2022) 376–386.

13. **Vaden T. D., de Boer T. S. J. A., Simons J. P., et al.,** Vibrational spectroscopy and conformational structure of protonated polyalanine peptides isolated in the gas phase, J. Phys. Chem. A. 112 (20) (2008) 4608–4616.

14. **Matsunaga Y., Koike R., Ota M., et al.,** Influence of structural symmetry on protein dynamics, PLoS One. 7 (11) (2012) e50011.

15. **Wako H., Endo S.,** Dynamic properties of oligomers that characterize low-frequency normal modes, Biophys. Physicobiol. 16 (Nov 29) (2019) 220–231.

16. **Husseini F. S., Robinson D., Hunt N. T., et al.,** Computing infrared spectra of proteins using the exciton model, J. Comput. Chem. 38 (16) (2017) 1362–1375.

17. **Schultheis V., Reichold R., Schropp B., Tavan P.,** A polarizable force field for computing the infrared spectra of the polypeptide backbone, J. Phys. Chem. B. 112 (39) (2008) 12217–12230.

18. **Narayan B., Herbert C., Rodriguez B. J., et al.,** Replica exchange molecular dynamics of diphenylalanine amyloid peptides in electric fields, J. Phys. Chem. B. 125 (20) (2021) 5233–5242.

19. **Bradshaw R. T., Dziedzic J., Skylaris Ch.-K., Essex J. W.,** The role of electrostatics in enzymes: Do biomolecular force fields reflect protein electric fields? J. Chem. Inf. Model. 60 (6) (2020) 3131–3144.

20. **Baranov M. A., Karseeva E. K., Tsybin O. Yu.,** Supercomputer simulation of intramolecular oscillations of glycine, diphenylalanine, and tryptophan in an electric field of the terahertz and infrared ranges, Biophysics. 69 (2) (2024) 179–194.

21. **Wolpert M., Hellwig P.,** Infrared spectra and molar absorption coefficients of the 20 alpha amino acids in aqueous solutions in the spectral range from 1800 to 500 cm^{-1}, Spectrochim. Acta A.: Mol. Biomol. Spectrosc. 64 (4) (2006) 987–1001.

22. **Barth A.,** Infrared spectroscopy of proteins, Biochim. Biophys. Acta Bioenerg. 1767 (9) (2007) 1073–1101.

23. **Zhang F., Tominaga K., Hayashi M., Wang H.-W.**, Low-frequency vibration study of amino acids using terahertz spectroscopy and solid-state density functional theory, In book: Zhang C., Zhang Xi-Ch., Nani M. (Eds.) Proc. SPI. Vol. 9275, Infrared, Millimeter-Wave, and Terahertz Technologies III; Conf.: SPIE/COS Photonics Asia 2014, 11 Nov., Beijing, P. 92750D.

24. **Moon J. H., Oh J. Y., Kim M. S.,** A systematic and efficient method to estimate the vibrational frequencies of linear peptide and protein ions with any amino acid sequence for the calculation of Rice-Ramsperger-Kassel-Marcus rate constant, J. Am. Soc. Mass Spectrom. 17 (12) (2006) 1749–1757.

25. **Baranov M. A., Shariaty F., Tsybin O. Y.** Dynamics of glycine, diphenylalanine, and tryptophan oligomers: Computer simulation in an IR electric field with different forms and polarization, J. Biomol. Struct. Dyn. 44 (5) (2026) 2651–2658.

26. **Barth A.,** The infrared absorption of amino acid side chains, Progr. Biophys. Mol. Biol. 74 (3–5) (2000) 141–173.

27. **Barth A., Zscherp C.,** What vibrations tell us about proteins, Q. Rev. Biophys. 35 (4) (2002) 369–430.

28. **Butyrskaya E. V., Nechaeva L. S., Shaposhnik V. A., Drozdova** E. **I.,** The assignment of the bands in IR spectra of aqueous solutions of glycine on the basis of quantum-chemical calculations, Sorbtsionnyye i Khromatograficheskiye Protsessy [Sorption & Chromatographic Processes]. 12 (4) (2012) 501–512 (in Russian).

29. **Redkov A. V., Osipov A. V., Kukushkin S. A.,** Molecular dynamics simulation of the indentation of nanoscale films on a substrate, Tech. Phys. Lett. 42 (6) (2016) 639–643.

30. **Nepomnyashchaya E. K., Baranov M. A., Tsybin O. Yu.,** Computer resonance dynamics of a glycine molecule in an infrared electric field, Pisma v Zhurnal Tekhnicheskoi Fiziki. 49 (7) (2023) 8 –11 (in Russian).

31. **Baranov M. A., Nepomnyashchaya E. K., Tsybin O. Yu.,** Fourier spectrum of the integral dipole moment of a number of amino acids supercomputer models, St. Petersburg State Polytechnical University Journal. Physics and Mathematics. 15 (4) (2022) 55–68 (in Russian).

32. **Baranov M. A., Tsybin O. Yu., Velichko E. N.,** Free energy relaxation of glycine, tryptophan and albumin molecules in the ionized aqueous solution: Computer analysis, St. Petersburg Polytechnical State University Journal. Physics and Mathematics. 14 (4) (2021) 135–146 (in Russian).

33. **Baranov M. A., Karseyeva E. K., Tsybin O. Yu.,** Supercomputer dynamical models of glycine, tryptophan and diphenyl-L-alanine in the electrical fields of terahertz and infrared spectral ranges, St. Petersburg State Polytechnical University Journal. Physics and Mathematics. 16 (3) (2023) 59–72 (in Russian).

34. **Goodsell D. S., Olson A. J.,** Structural symmetry and protein function, Annu. Rev. Biophys. Biomol. Struct. 29 (1) (2000) 105–153.

35. **Bahar I.**, **Lezon T. R., Bakan A., Shrivastava I. H.,** Normal mode analysis of biomolecular structures: Functional mechanisms of membrane proteins, Chem. Rev. 110 (3) (2010) 1463–1497.

36. **Faridoddin S., Baranov M. A., Tsybin O. Yu.,** Structure of biomolecular films through advanced imaging and statistical analysis, Colloids Surf. A. Physicoch. Eng. Asp. 702 (P. 1– 5 Dec) (2024) 134920.

37. **Kompan M. E., Baranov M. A., Malyshkin** V. G., **Tsybin O.Yu.,** Raman spectra in range 75 − 1200 cm^{-1} of amino acids L-tryptophan, diphenyl-L-alanine and glycine in aqueous solution and in dehydrated films, Phys. Solid State. 66 (8) (2024) 1445−1449 (in Russian).

38. **Löffler G., Schreiber H., Steinhauser O.,** Calculation of the dielectric properties of a protein and its solvent: Theory and a case study, J. Mol. Biol. 270 (3) (1997) 520−534.

39. **Baranov M., Tsybin O.,** Supercomputer simulation of amino acid molecules high-frequency polarizability in THz electric field, Proc. 2023 Int. Conf. on Electrical Engineering and Photonics (EExPolytech), 19−20 Oct., 2023, St. Petersburg, Russian Federation, IEEE (2023) 261−264.

40**. Karplus M.,** Molecular dynamics simulations of biomolecules, Acc. Chem. Res. 35 (6) (2002) 321−323.

41. **Ruiz M. P., Aragonиs A. C., Camarero N., et al.,** Bioengineering a single-protein junction, J. Am. Chem. Soc. 139 (43) (2017) 15337−15346.

42. **Reimann K., Woerner M., Elsaesser T.,** Two-dimensional terahertz spectroscopy of condensed-phase molecular systems, J. Chem. Phys. 154 (12) (2021) 120901.

43. **Solomentsev G. Y., English N. J., Mooney D. A.,** Effects of external electromagnetic fields on the conformational sampling of a short alanine peptide, J. Comput. Chem. 33 (9) (2012) 917−923.

44. **Kelly C. M., Northey T., Ryan K., et al.,** Conformational dynamics and aggregation behavior of piezoelectric diphenylalanine peptides in an external electric field, Biophys. Chem. 196 (Jan) (2015) 16−24.

45. **Hadley K. R., McCabe C.**, Coarse-grained molecular models of water: A review, Mol. Simul. 38 (8−9) (2012) 671−681.

46. **Mao Y., Zhang Y.,** Thermal conductivity, shear viscosity and specific heat of rigid water models, Chem. Phys. Lett. 542 (23 Jul) (2012) 37−41.

47. **MacKerell, Ir., A. D., Bashford D., Bellott M., et al.,** All-atom empirical potential for molecular modeling and dynamics studies of proteins, J. Phys. Chem. B. 102 (18) (1998) 3586−3616.

48**. Linstrom P. J., Mallard W. G.,** NIST standard reference database number 69, NIST (National Institute of Standards and Technologies) Chemistry WebBook. Vol. 1227. No. 69 (2005.) 20899.

49. **Feng J.-Y., Lee Y.-P., Zhu Ch.-Y., et al.,** IR−VUV spectroscopy of pyridine dimers, trimers and pyridine − ammonia complexes in a supersonic jet, Phys. Chem. Chem. Phys. 22 (37) (2020) 21520−21534.

50. **Zhang B.**, **Yu Y., Zhang Zh., et al.,** Infrared spectroscopy of neutral water dimer based on a tunable vacuum ultraviolet free electron laser, J. Phys. Chem. Lett. 11 (3) (2020) 851−855.

51. **Baranov M. A., Karseeva E. K., Tsybin O. Yu.,** Prototypes of devices for heterogeneous hybrid semiconductor electronics with an embedded biomolecular domain, Russian Microelectronics. 2023. Vol. 52 (6) (2023) 517−526.

СПИСОК ЛИТЕРАТУРЫ

1. **Ruan X., Ruan X., Huang H.** Application of terahertz spectroscopy in medical microbiological detection // Journal of Physics: Conference Series. 2022. Vol. 2425. No. 1. P. 012045.

2. **Turton D. A., Senn H. M., Harwood T., Lapthorn A. J., Ellis E. M., Wynne K.** Terahertz underdamped vibrational motion governs protein-ligand binding in solution // Nature Communications. 2014. Vol. 5. 03 June. P. 3999.

3. **Noble B. B., Todorova N., Yarovsky I.** Electromagnetic bioeffects: a multiscale molecular simulation perspective // Physical Chemistry Chemical Physics. 2022. Vol. 24. No. 11. Pp. 6327–6348.

4. **Woods K. N.** Solvent-induced backbone fluctuations and the collective librational dynamics of lysozyme studied by terahertz spectroscopy // Physical Review E. 2010. Vol. 81. No. 3. P. 031915.

5. **Niehues G., Heyden M., Schmidt D. A., Havenith M.** Exploring hydrophobicity by THz absorption spectroscopy of solvated amino acids // Faraday Discussions. 2011. Vol. 150. 23 May. Pp. 193–207.

6. **Jeong S.-Y., Cheon H., Lee D., Son J.-H.** Determining terahertz resonant peaks of biomolecules in aqueous environment // Optics Express. 2020. Vol. 28. No. 3. Pp. 3854–3863.

7. **Grechko M., Hasegawa T., D'Angelo F., Ito H., Turchinovich D., Nagata Y., Bonn M.** Coupling between intra- and intermolecular motions in liquid water revealed by two-dimensional terahertz-infrared-visible spectroscopy // Nature Communications. 2018. Vol. 9. No. 1. P. 885.

8. **Xu J., Galan J., Ramian G., Savvidis P., Scopatz A., Birge R. R., Allen S. J., Plaxco K.** Terahertz circular dichroism spectroscopy of biomolecules // Edited by Jensen J. O., Theriault J.-M. Proceedings SPIE. 2004. Vol. 5268. Chemical and Biological Standoff Detection. 27 February. Pp. 19–26.

9. **Beyer C., Christen P., Jelesarov I., Fröhlichet J.** Real-time assessment of possible electromagnetic-field-induced changesin protein conformationand thermal stability // Bioelectromagnetics. 2014. Vol. 35. No. 7. Pp. 470–478.

10. **Calabrò E., Magazщ S.** Resonant interaction between electromagnetic fields and proteins: A possible starting point for the treatment of cancer // Electromagnetic Biology and Medicine. 2018. Vol. 37. No. 3. Pp. 155–168.

11. **Harvey A.** The interaction between electromagnetic fields at megahertz, gigahertz and terahertz frequencies with cells, tissues and organisms: Risks and potential // Journal of the Royal Society, Interface. 2017. Vol. 14. P. 0585

12. **Wu H., Ghaani M. R., Futera Z., English N. J.** Effects of externally applied electric fields on the manipulation of solvated-chignolin folding: Static- versus alternating-field dichotomy at play // The Journal of Physical Chemistry B. 2022. Vol. 126. No. 2. Pp. 376–386.

13. **Vaden T. D., de Boer T. S. J. A., Simons J. P., Snoek L. C., Suhai S., Paizs B.** Vibrational spectroscopy and conformational structure of protonated polyalanine peptides isolated in the gas phase // The Journal of Physical Chemistry A. 2008. Vol. 112. No. 20. Pp. 4608–4616.

14. **Matsunaga Y., Koike R., Ota M., Tame J. R. H., Kidera A.** Influence of structural symmetry on protein dynamics // PLoS One. 2012. Vol. 7. No. 11. P. e50011.

15. **Wako H., Endo S.** Dynamic properties of oligomers that characterize low-frequency normal modes // Biophysics and Physicobiology. 2019. Vol. 16. November 29. Pp. 220–231.

16. **Husseini F. S., Robinson D., Hunt N. T., Parker A. W., Hirst J. D.** Computing infrared spectra of proteins using the exciton model // Journal of Computational Chemistry. 2017. Vol. 38. No. 16. Pp. 1362–1375.

17. **Schultheis V., Reichold R., Schropp B., Tavan P.** A polarizable force field for computing the infrared spectra of the polypeptide backbone // The Journal of Physical Chemistry B. 2008. Vol. 112. No. 39. Pp. 12217–12230.

18. **Narayan B., Herbert C., Rodriguez B. J., Brooks B. R., Buchete N.-V.**
Replica exchange molecular dynamics of diphenylalanine amyloid peptides in electric fields // The Journal of Physical Chemistry B. 2021. Vol. 125. No. 20. Pp. 5233–5242.

19. **Bradshaw R. T., Dziedzic J., Skylaris Ch.-K., Essex J. W.** The role of electrostatics in enzymes: Do biomolecular force fields reflect protein electric fields? // Journal of Chemical Information and Modeling. 2020. Vol. 60. No. 6. Pp. 3131–3144.

20. **Баранов М. А., Карсеева Э. К., Цыбин О. Ю.** Суперкомпьютерное моделирование внутримолекулярных колебаний глицина, дифенилаланина и триптофана в электрическом поле терагерцового и инфракрасного диапазонов // Биофизика. 2024. Т. 69. № 2. С. 213–229.

21. **Wolpert M., Hellwig P.** Infrared spectra and molar absorption coefficients of the 20 alpha amino acids in aqueous solutions in the spectral range from 1800 to 500 cm^{-1} // Spectrochimica Acta A.: Molecular and Biomolecular Spectroscopy. 2006. Vol. 64. No. 4. Pp. 987–1001.

22. **Barth A.** Infrared spectroscopy of proteins // Biochimica et Biophysica Acta – Bioenergetics. 2007. Vol. 1767. No. 9. Pp. 1073–1101.

23. **Zhang F., Tominaga K., Hayashi M., Wang H.-W.** Low-frequency vibration study of amino acids using terahertz spectroscopy and solid-state density functional theory // Zhang C., Zhang Xi-Ch., Nani M. (Eds.) Proceedings of SPI. Vol. 9275. Infrared, Millimeter-Wave, and Terahertz Technologies III. Conference: SPIE/COS Photonics Asia 2014. 11 November, Beijing, P. 92750D.

24. **Moon J. H., Oh J. Y., Kim M. S.** A systematic and efficient method to estimate the vibrational frequencies of linear peptide and protein ions with any amino acid sequence for the calculation of Rice-Ramsperger-Kassel-Marcus rate constant // Journal of the American Society for Mass Spectrometry. 2006. Vol. 17. No. 12. Pp. 1749–1757.

25. **Baranov M. A., Shariaty F., Tsybin O. Y.** Dynamics of glycine, diphenylalanine, and tryptophan oligomers: Computer simulation in an IR electric field with different forms and polarization // Journal of Biomolecular Structure and Dynamics. 2026. Vol. 44. No. 5. Pp. 2651–2658.

26. **Barth A.** The infrared absorption of amino acid side chains // Progress in Biophysics and Molecular Biology. 2000. Vol. 74. No. 3–5. Pp. 141–173.

27. **Barth A., Zscherp C.** What vibrations tell us about proteins // Quarterly Reviews of Biophysics. 2002. Vol. 35. No. 4. Pp. 369–430.

28. **Бутырская Е. В., Нечаева Л. С., Шапошник В. А., Дроздова В. И.** Отнесение полос в ИК спектрах водных растворов глицина на основе квантовохимического расчета // Сорбционные и хроматографические процессы. 2012. Т. 4 № .12. С. 512–501.

29. **Редьков А. В., Осипов А. В. Кукушкин С.А.** Моделирование процесса индентирования наномасштабных пленок на подложках методом молекулярной динамики // Письма в Журнал технической физики. 2016. Т. 42. № 12. С. 64–72.

30. **Непомнящая Э. К., Баранов М. А., Цыбин О. Ю.** Компьютерная резонансная динамика молекулы глицина в электрическом поле инфракрасного диапазона // Письма в Журнал технической физики. 2023. Т. 49. № 7. С. 8–11.

31. **Баранов М. А., Непомнящая Э. К., Цыбин О. Ю.** Фурье-спектр интегрального дипольного момента суперкомпьютерных моделей ряда аминокислот // Научно-технические ведомости СПбГПУ. Физико-математические науки. 2022. Т. 15. № 4. С. 55–68.

32. **Баранов М. А., Цыбин О. Ю., Величко Е. Н.** Компьютерный анализ релаксации свободной энергии молекул глицина, триптофана и альбумина в ионизованном водном растворе // Научно-технические ведомости СПбПУ. Физико-математические науки. 2021. Т. 14. № 4. С. 135–146.

33. **Баранов М. А., Карсеева Э. К., Цыбин О. Ю.** Суперкомпьютерные динамические модели глицина, триптофана и дифенилаланина в электрических полях терагерцового и инфракрасного спектральных диапазонов // Научно-технические ведомости СПбГПУ. Физико-математические науки. 2023. Т. 16. № 3. С. 59–72.

34. **Goodsell D. S., Olson A. J.** Structural symmetry and protein function // Annual Review of Biophysics and Biomolecular Structure. 2000. Vol. 29. No. 1. Pp. 105–153.

35. **Bahar I., Lezon T. R., Bakan A., Shrivastava I. H.** Normal mode analysis of biomolecular structures: Functional mechanisms of membrane proteins // Chemical Review. 2010. Vol. 110. No. 3. Pp. 1463–1497.

36. **Faridoddin S., Baranov M. A., Tsybin O. Yu.** Structure of biomolecular films through advanced imaging and statistical analysis // Colloids and Surfaces A: Physicochemical and Engineering Aspects. 2024. Vol. 702. Part 1. 5 December. P. 134920.

37. **Компан М. Е., Баранов М. А., Малышкин В. Г., Цыбин О. Ю.** Спектры комбинационного рассеяния в диапазоне 1200 – 75 $см^{-1}$ аминокислот L-триптофана, дифенил-L-аланина и глицина в водном растворе и в гидратированных пленках // Физика твердого тела. 2024. Т. 66. № 8. С. 1445–1449.

38. **Löffler G., Schreiber H., Steinhauser O.** Calculation of the dielectric properties of a protein and its solvent: Theory and a case study // Journal of Molecular Biology. 1997. Vol. 270. No. 3. Pp. 520–534.

39. **Baranov M., Tsybin O.** Supercomputer simulation of amino acid molecules high-frequency polarizability in THz electric field // Proceedings of the 2023 International Conference on Electrical Engineering and Photonics (EExPolytech), 19–20 October 2023. St. Petersburg, Russian Federation. IEEE, 2023. Pp. 261–264.

40**. Karplus M.** Molecular dynamics simulations of biomolecules // Accounts of Chemical Research. 2002. Vol. 35. No. 6. Pp. 321–323.

41. **Ruiz M. P., Aragonиs A. C., Camarero N., Vilhena J. G., Ortega M., Zotti L. A., Pérez R., Cuevas J. C., Gorostiza P., Днez-Pérez I.** Bioengineering a single-protein junction // Journal of the American Chemical Society. 2017. Vol. 139. No. 43. Pp. 15337–15346.

42. **Reimann K., Woerner M., Elsaesser T.** Two-dimensional terahertz spectroscopy of condensed-phase molecular systems // The Journal of Chemical Physics. 2021. Vol. 154. No. 12. P. 120901.

43. **Solomentsev G. Y., English N. J., Mooney D. A.** Effects of external electromagnetic fields on the conformational sampling of a short alanine peptide // Journal of Computational Chemistry. 2012. Vol. 33. No. 9. Pp. 917–923.

44. **Kelly C. M., Northey T., Ryan K., Brooks B. R., Kholkin A. L., Rodriguez B. J., Buchete N.-V.** Conformational dynamics and aggregation behavior of piezoelectric diphenylalanine peptides in an external electric field // Biophysical Chemistry. 2015. Vol. 196. January. Pp. 16–24.

45. **Hadley K. R., McCabe C.** Coarse-grained molecular models of water: A review // Molecular Simulation. 2012. Vol. 38. No. 8–9. Pp. 671–681.

46. **Mao Y., Zhang Y.** Thermal conductivity, shear viscosity and specific heat of rigid water models // Chemical Physics Letters. 2012. Vol. 542. 23 July. Pp. 37–41.

47. **MacKerell, Ir., A. D., Bashford D., M. Bellott M., et al.** All-atom empirical potential for molecular modeling and dynamics studies of proteins // The Journal of Physical Chemistry B. 1998. Vol. 102. No. 18. Pp. 3586–3616.

48**. Linstrom P. J., Mallard W. G.** NIST standard reference database number 69 // NIST (National Institute of Standards and Technologies) Chemistry WebBook. 2005. Vol. 1227. No. 69. P. 20899.

49. **Feng J.-Y., Lee Y.-P., Zhu Ch.-Y., Hsu P.-J., Kuo J.-L., Ebata T.** IR–VUV spectroscopy of pyridine dimers, trimers and pyridine – ammonia complexes in a supersonic jet // Physical Chemistry Chemical Physics. 2020. Vol. 22. No. 37. Pp. 21520–21534.

50. **Zhang B.**, **Yu Y., Zhang Zh., et al.** Infrared spectroscopy of neutral water dimer based on a tunable vacuum ultraviolet free electron laser // The Journal of Physical Chemistry Letters. 2020. Vol. 11. No. 3. Pp. 851–855.

51. **Баранов М. А., Карсеева Е. К., Цыбин О. Ю.** Прототипы приборов гетерогенной гибридной полупроводниковой электроники с встроенным биомолекулярным доменом // Микроэлектроника. 2023. Т. 52. № 6. Р. 497–507.

THE AUTHORS

BARANOV Maksim A.
Peter the Great St. Petersburg Polytechnic University
29 Politechnicheskaya St., St. Petersburg, 195251, Russia
baranovma1993@gmail.com
ORCID: 0000-0003-4555-0009

TSYBIN Oleg Yu.
Peter the Great St. Petersburg Polytechnic University
29 Politechnicheskaya St., St. Petersburg, 195251, Russia
oleg.tsybin@gmail.com
ORCID: 0000-0002-8308-059X

СВЕДЕНИЯ ОБ АВТОРАХ

БАРАНОВ Максим Александрович – *кандидат физико-математических наук, доцент Высшей школы прикладной физики и космических технологий Санкт-Петербургского политехнического университета Петра Великого.*
195251, Россия, г. Санкт-Петербург, Политехническая ул., 29
baranovma1993@gmail.com
ORCID: 0000-0003-4555-0009

ЦЫБИН Олег Юрьевич – *доктор физико-математических наук, профессор Высшей школы прикладной физики и космических технологий Санкт-Петербургского политехнического университета Петра Великого.*
195251, Россия, г. Санкт-Петербург, Политехническая ул., 29
oleg.tsybin@gmail.com
ORCID: 0000-0002-8308-059X

Received 24.04.2025. Approved after reviewing 27.02.2026. Accepted 27.02.2026.
Статья поступила в редакцию 24.04.2025. Одобрена после рецензирования 27.02.2026. Принята 27.02.2026.

© Peter the Great St. Petersburg Polytechnic University, 2026

Original article
DOI: https://doi.org/10.18721/JPM.19205

THE INFLUENCE OF A SILICA TRENCH PROFILE ON THE PHOTOSENSITIVITY OF A CMOS-COMPATIBLE AVALANCHE PHOTODIODE IN THE VISIBLE RANGE

D. I. Dolzhenko✉, *E. D. Letkiman*

Peter the Great St. Petersburg Polytechnic University, St. Petersburg, Russia

✉ ddi.dev.94@gmail.com

Abstract. This work has involved the simulation of technological operations of manufacturing a silicon (Si) avalanche photodiode and calculating its output characteristics. As a result, the values of its multiplication factor (from 49.5 to 62.3) and spectral sensitivity (from 15.8 to 19.6 A/W) depending on the shallow trench insulation defect type are presented for a Si avalanche photodiode. It has been shown that the technological defects causing narrowing of the width of the trench towards its bottom have the greatest impact on these parameters. As a result, the multiplication factor decreases by up to 18%. The dependence of the photodiode gain on the trench's wall inclination angle was established to be described well by a linear function. It was also demonstrated that the trench narrowing led to an increase in the lateral component of the electric field strength near the groove, which reduced the breakdown voltage, but did not lead to an increase in multiplication.

Keywords: avalanche photodiode, multiplication factor, spectral sensitivity, technological defects, STI, TCAD

Citation: Dolzhenko D. I., Letkiman E. D., The influence of a silica trench profile on the photosensitivity of a CMOS-compatible APD in the visible range, St. Petersburg State Polytechnical University Journal. Physics and Mathematics. 19 (2) (2026) 57–67. DOI: https://doi.org/10.18721/JPM.

This is an open access article under the CC BY-NC 4.0 license (https://creativecommons.org/licenses/by-nc/4.0/)

Научная статья
УДК 621.383.523
DOI: https://doi.org/10.18721/JPM.19205

ВЛИЯНИЕ ПРОФИЛЯ ТРАНШЕИ ИЗ ДИОКСИДА КРЕМНИЯ НА ФОТОЧУВСТВИТЕЛЬНОСТЬ КМОП-СОВМЕСТИМОГО ЛАВИННОГО ФОТОДИОДА ВИДИМОГО ДИАПАЗОНА

Д. И. Долженко✉, *Е. Д. Леткиман*

Санкт-Петербургский политехнический университет Петра Великого,
Санкт-Петербург, Россия

✉ ddi.dev.94@gmail.com

Аннотация. В работе проведено моделирование технологических операций изготовления кремниевого лавинного фотодиода и расчет его выходных характеристик. В результате представлены значения его коэффициента умножения (62,3 – 49,5) и спектральной чувствительности (19,6 – 15,8 А/Вт) в зависимости от типа дефекта траншеи из диоксида кремния. Показано, что наибольшим образом на данные параметры влияют технологические дефекты, приводящие к сужению профиля траншеи (узкой щели) по направлению к ее дну, что приводит к снижению коэффициента умножения вплоть до 18%. Установлено, что зависимость усиления фотодиода от угла наклона стенки

© Dolzhenko D. I., Letkiman E. D., 2026. Published by Peter the Great St. Petersburg Polytechnic University.

траншеи хорошо описывается линейной функцией. Показано, что сужение траншеи вызывает увеличение латеральной компоненты напряженности электрического поля вблизи этой траншеи, что снижает значение пробивного напряжения и не увеличивает коэффициент умножения исследуемого фотодиода.

Ключевые слова: лавинный фотодиод, коэффициент умножения, спектральная чувствительность, технологические дефекты, STI, TCAD

Ссылка для цитирования: Долженко Д. И., Леткиман Е. Д. Влияние профиля траншеи из диоксида кремния на фоточувствительность КМОП-совместимого лавинного фотодиода видимого диапазона // Научно-технические ведомости СПбГПУ. Физико-математические науки. 2026. Т. 2 № .19. С. 57–67. DOI: https://doi.org/10.18721/JPM.19205

Статья открытого доступа, распространяемая по лицензии CC BY-NC 4.0 (https://creativecommons.org/licenses/by-nc/4.0/)

Introduction

CMOS-compatible avalanche photodiodes (APDs) are widely used in precision positioning devices, optical communication systems, and LIDAR (light detection and ranging) systems [1–4]. However, forming the cathode and anode on the silicon wafer surface poses several major challenges, the most significant of which are surface effects: non-uniform electric field distribution and surface leakage currents [5]. These factors can cause not only a sharp reduction in the avalanche multiplication factor across the entire spectral range but also premature surface breakdown of the wafer.

One promising solution is to form a narrow trench (a few micrometers wide) between the cathode and anode, filled with silica (SiO_2). This method is known as shallow trench isolation (STI) [6]. There are numerous methods for etching silicon, but as a rule, the stronger the anisotropy of the profile formed, the more complex the process and the higher the equipment requirements.

However, each approach has its drawbacks. This combination of factors does not always guarantee the desired field distribution and impact ionization paths, which affects the current values at a given supply voltage. In addition, different patterns of multiple reflection of light arise when the entire photosensitive area is illuminated (or when part of it is illuminated at an angle). In view of these unfavorable conditions, we can formulate the goal of our study:

to analyze how the profile of a trench filled with silica affects the current–voltage behavior of a CMOS-compatible avalanche photodiode.

Research methodology and description of the silicon avalanche photodiode structure

Calculations of the output characteristics and simulations of the fabrication process of the avalanche photodiode were carried out in the Sentaurus TCAD package. Despite the limitations of real photomask patterns, we treated the structure as axisymmetric in our simulations. This minimizes the edge effects, so that the resulting electric field distribution can be interpreted unambiguously. The donor (N_D) and acceptor (N_A) concentrations, as well as the change rates of these concentrations ΔN_D and ΔN_A near the p–n junction, were chosen so as to provide a sufficient slope of the current–voltage curve in the linear regime [7]. These conditions were chosen to observe the changes in the behavior of the current–voltage curve across all its regions.

The most common trench profiles and associated defects were used in the simulations (see Fig. 2). The corresponding fabrication technologies for these structures are listed in Table 1. Although the set of selected profiles is far from exhaustive, it provides insight into how the avalanche develops and how the field forms near the trench.

It was expected that some STI profile defects would not significantly affect the avalanche development or the multiplication factor. However, no preliminary selection is possible without simulation, since it is unrealistic to account for several simultaneous changes in the electric field distribution, ionization potential, and carrier mobility.

© Долженко Д. И., Леткиман Е. Д., 2026. Издатель: Санкт-Петербургский политехнический университет Петра Великого.

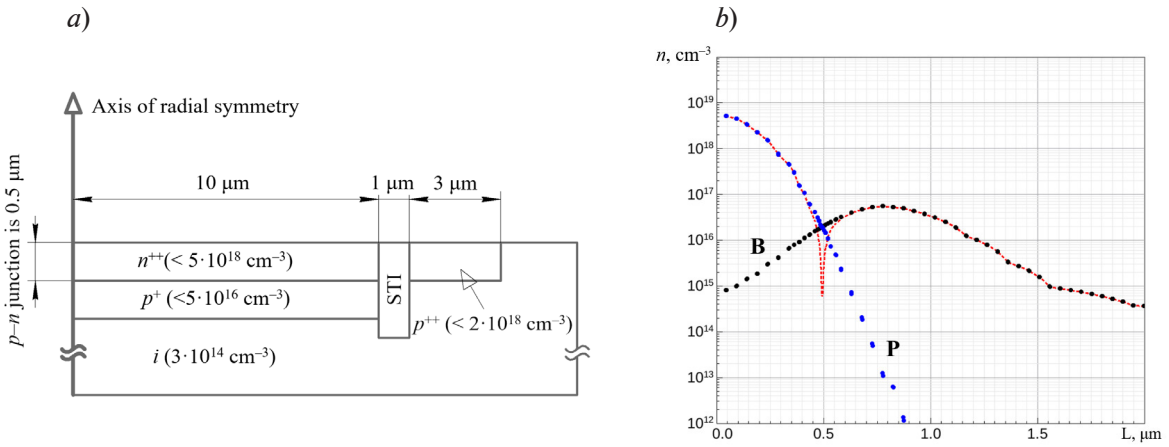


Fig. 1. Schematic of radial cross-section of the structure (*a*);
dopant (boron and phosphorus) concentration profiles versus depth in the photosensitive region (*b*)
The red curve shows the dopant concentration as an absolute value

A mesh convergence study is one of the first stages in simulations of a wide range of structures. We should note that two different mesh types are advisable for simulating fabrication processes and physics of semiconductor devices. An adaptive mesh is convenient for models of fabrication processes: its step a decreases as the change rate of the target quantity N_D with respect to the coordinate x increases, i.e., $1/a \sim dN_D/dx$. This mesh provides high accuracy and saves computational resources.

An adaptive mesh is unsuitable for simulating the physics of the resulting structure, because the cell size grows rapidly with depth, producing a significant error and often leading to a lack of solution convergence, especially in optics. Therefore, a mesh must be rebuilt before the simulation of the output characteristics, with a minimum step determined by a mesh convergence analysis.

Classical drift-diffusion equations and Poisson's equation for electron and hole concentrations, traditionally adopted in TCAD (Technology Computer-Aided Design) simulations of semiconductor structures, were used as the transport model. The standard set of physical models recommended for simulating silicon photodiodes [16] was used to describe generation and recombination mechanisms.

It is essential to discuss how avalanche parameters themselves are estimated for the avalanche photodiode. For the silicon structure, we estimated the breakdown electric field using the well-known ionization model [16, 17]. To this end, we calculated the ionization integrals for electrons and holes, which become equal to unity at silicon breakdown, using the following equations:

$$\int_0^W \alpha_n \exp\left(-\int_x^W (\alpha_n - \alpha_p)dx'\right)dx = 1, \quad \int_0^W \alpha_p \exp\left(-\int_x^W (\alpha_p - \alpha_n)dx'\right)dx = 1, \tag{1}$$

where α_n, α_p are the ionization coefficients for electrons and holes, respectively; W is the width of the space charge region; x, x' are the coordinates for the outer and inner integrals, respectively.

The ionization coefficients, in turn, can be estimated from the Van Overstraeten–De Man model [18] based on the Chynoweth equations [19], accurately describing ionization in the field range $(1–6)\cdot10^5$ V/cm near silicon breakdown:

$$\alpha_n(x) = \gamma\alpha_n \exp\left(-\frac{\gamma b_n}{E(x)}\right), \quad \alpha_p(x) = \gamma\alpha_p \exp\left(-\frac{\gamma b_p}{E(x)}\right), \tag{2}$$

where α_n, α_p, b_n, b_p are empirical model coefficients reflecting the ionization rate; $E(x)$ is the local electric field strength; γ is the phonon temperature correction.

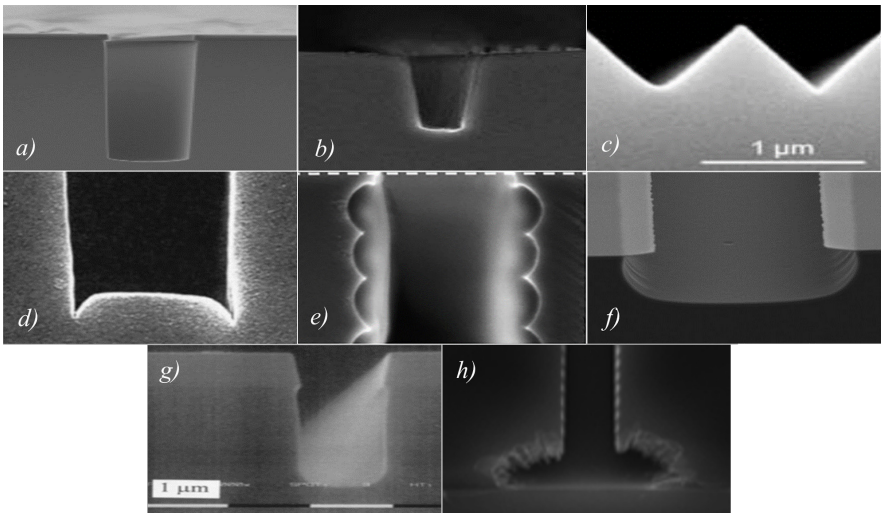


Fig. 2. Doping profiles with different defect types:
vertical, rectangular, anisotropic, with smooth sidewalls (*a*); trapezoidal, sidewall inclination angle ≥ 80° (most common) (*b*); V-shaped, with inclination angle < 80° (*c*); W-shaped, anisotropic, with microtrenching at the sidewall edges (*d*); scalloped (*e*); oval, hemispherical, isotropic (*f*); U-shaped, anisotropic (*g*); profile with undercut at the trench bottom (*h*). See Table 1 for the fabrication technologies

Table 1

Fabrication technologies for the doping profiles shown in Fig. 2

Position in Fig. 2	Technology	Source
a)	Dry etching (ICP-RIE)	[8]
b)	Dry etching	[9]
c)	KOH wet etching	[10]
d)	Reactive ion etching (RIE)	[11]
e)	Cyclic dry etching (BOSCH process)	[12]
f)	Isotropic SF_6 plasma etching	[13]
g)		[14]
h)	Reactive ion etching (RIE)	[15]

We used the following coefficient values:

$$\alpha_n = 7.03 \cdot 10^5 \text{ cm}^{-1},\ \alpha_p = (6.71\text{–}15.82) \cdot 10^5 \text{ cm}^{-1};$$

$$b_n = 1.231 \cdot 10^6 \text{ V/cm},\ b_p = (1.693\text{–}2.036) \cdot 10^6 \text{ V/cm}.$$

The choice of α_p and b_p within these intervals depended on the magnitude of $E(x)$.
The phonon temperature correction follows the expression

$$\gamma = \tanh\left(\frac{\hbar\omega}{2kT_0}\right) \Big/ \tanh\left(\frac{\hbar\omega}{2kT}\right), \tag{3}$$

where $\hbar\omega$ is the phonon energy ($\hbar\omega = 0.063$); T_0 is the temperature for which the empirical parameters are given.

Results and discussion

Simulation of such structures must begin with defining the geometric parameters of the trench profile whose shape is to be analyzed. The profile width typically does not exceed 1 μm [20, 21], while the STI depth is a variable parameter. Therefore, at the first stage, in addition to mesh convergence analysis, we assessed how the depth of the STI profile affects the current–voltage characteristic of the avalanche photodiode for a rectangular trench profile.

Both dependences in Fig. 3 show a significant drop in the multiplication factor M at a trench depth $L < 3$ μm. Despite a decrease in the supply voltage of about %10, M drops by about 72%. This is because when the depth of the STI, which acts as a guard ring, decreases, lateral avalanche processes become possible. The electric field distribution shifts increasingly toward the surface, and the lateral electric field near the surface (at small L) is several times stronger, since it is not confined by the silica trench.

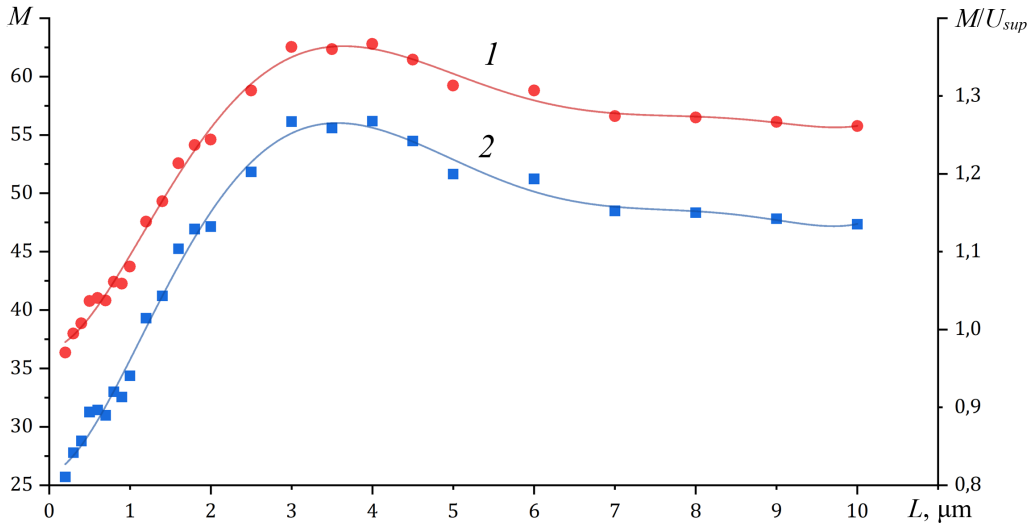


Fig. 3. Multiplication factor M (*1*) and its values normalized to the supply voltage, M/U_{sup} (*2*), as a function of STI profile depth
Supply voltage $U_{sup} = 0.98U_{br}$ (U_{br} is the breakdown voltage)

At $L > 4$ μm, the multiplication factor M begins to decrease gradually. As the depth increases, the field becomes more elongated, and the intensity at a wavelength of about 670 nm drops by about an order of magnitude already at a depth of 10 μm. The field strength decreases only slightly in the depth range below 10 μm, where most of the radiation is absorbed (here it is considerably closer to the STI region). At greater depths, the change rate of M gradually increases. Importantly, however, simulating greater depths is impractical, since it sharply reduces the number of available etching methods, requiring a high aspect ratio for the STI profile.

In the second stage, we turn to simulating profiles (trench width $W = 1$ μm, depth $L = 3$ μm) with different defect types. Note that fully isotropic etching cannot be implemented because of the unfavorable 3 : 1 aspect ratio. Fig. 4 shows the current–voltage curves for the photocurrent and the dark current. The breakdown voltage is predominantly influenced by the degree of narrowing toward the bottom of the STI trench, with a consequent increase in the contribution of the lateral field component to the avalanche process. Although the other defect types alter the field distribution near the edge of the photosensitive region, they have almost no effect on the breakdown voltage.

The resulting values of the multiplication factor and spectral sensitivity are listed in Table 2. Thus, defects associated with trench narrowing can reduce M by up to 18%.

For the W-shaped defect type, the values are almost identical to those of the idealized rectangular profile, because the formation of two depressions near the trench sidewalls can locally increase the trench depth to as much as 4 μm. According to the data in Fig. 3, the multiplication factor M remains essentially unchanged in the 3–4 μm range.

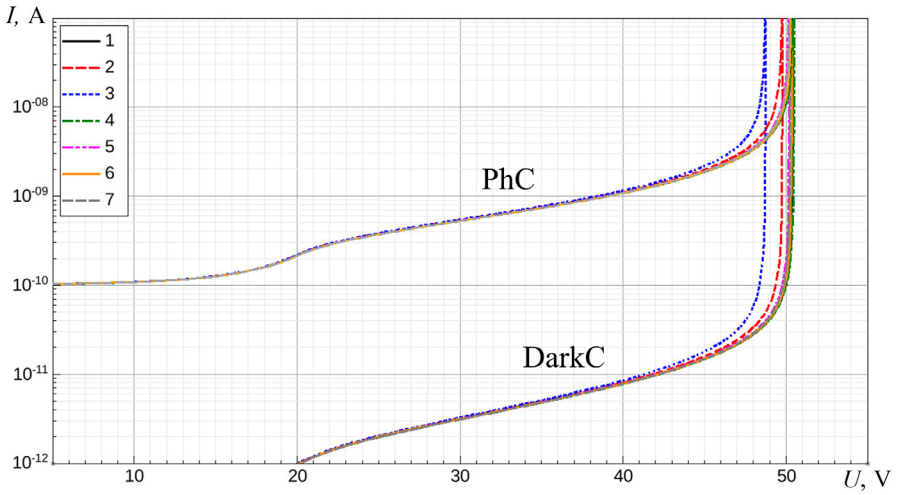


Fig. 4. Calculated I–V curves for the photocurrent (PhC) and dark current (DarkC) for different STI profile types and defects
The curve numbers correspond to the profile types in Table 2

Table 2

Key parameters of STI profile for different types of defects

Profile	S, A/W	M	U_{br}, V	M/U_{sup} (0.98 U_{br})
1. Rectangular	19.0	60.4	50.3	1.23
2. Trapezoidal	18.2	57.3	49.7	1.18
3. V-shaped	15.8	49.5	48.6	1.04
4. W-shaped	19.6	62.3	50.4	1.26
5. Scalloped	18.6	59.0	50.1	1.20
6. U-shaped	18.8	59.6	50.3	1.21
7. Undercut at trench bottom	18.6	59.4	50.2	1.21

Notations: S is the spectral sensitivity at $\lambda = 670$ nm; U_{br} is the breakdown voltage; M and M/U_{sup} are the unnormalized multiplication factor and that normalized to the supply voltage U_{sup}; $U_{sup} = 0.98U_{br}$.

In the third stage, we analyzed how narrowing of the profile at the trench bottom affects the multiplication factor. Fig. 5 shows the multiplication factor and spectral sensitivity versus the trench width, W_b, at the bottom. The dependences are well fitted by straight lines:

$$y = 2.9825x + 16.0922,\ R^2 = 0.9728 \text{ (for } S\text{)},$$

$$y = 10.3498x + 50.2300,\ R^2 = 0.9786 \text{ (for } M\text{)}.$$

The resulting dependences $M(W_b)$ and $S(W_b)$ can be rewritten as linear functions of the change in trench width:

$$M(W_b) = M(W_{b(\max)}) - x_1\Delta W_b,\ S(W_b) = S(W_{b(\max)}) - x_2\Delta W_b, \quad (4)$$

where $W_{b(\max)}$, μm, is the maximum width at the trench bottom (rectangular trench profile); ΔW_b, μm, is the deviation of the trench bottom width from its value for the rectangular profile; x_1 and x_2 are the linearization coefficients for M and S, respectively ($x_1 \approx 10$, $x_2 \approx 3$).

Fig. 6 shows the magnitude of the electric field strength and its lateral component versus the STI profile depth.

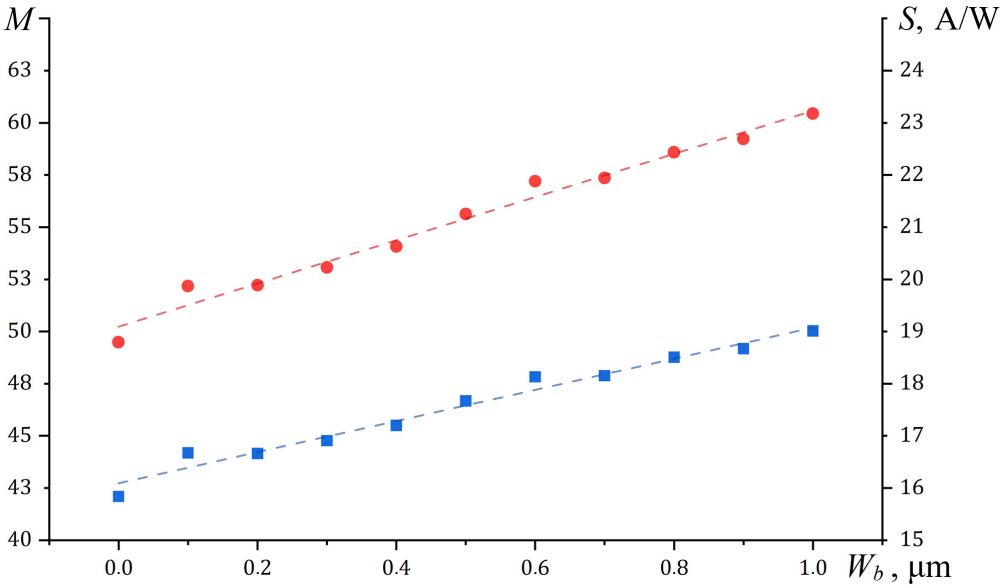


Fig. 5. Multiplication factor M (red symbols) and spectral sensitivity S (blue symbols) versus trench width W_b at the trench bottom. The fitting lines are shown as dashed lines

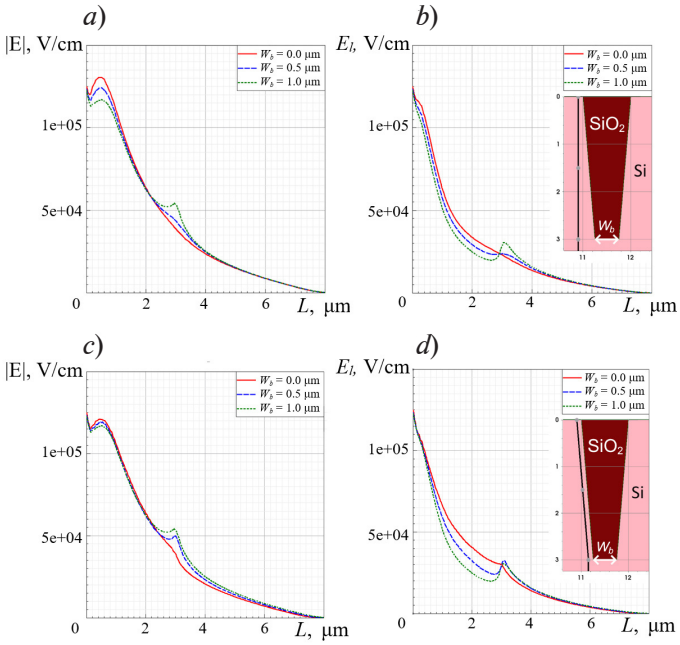


Fig. 6. Magnitude of electric field strength (*a*, *c*) and its lateral component (*b*, *d*) versus STI profile depth for three values of the bottom width W_b and different positions relative to the STI boundaries (the directions are indicated by black segments in the insets): 0.1 μm perpendicular to the upper STI boundary (*b*); along a line parallel to the lateral STI boundary with a 0.1 μm gap (L < 3 μm) and perpendicular to the surface (L > 3 μm) (*d*). U_{sup} = 40 V

The lateral field component along the chosen axis is stronger for the narrowed profile in the depth range below 3 μm, where the light intensity is highest. As a result, ionization processes in the lateral direction contribute more when the electric field reaches a critical value, which triggers premature breakdown of the avalanche photodiode.

Conclusion

We studied CMOS-compatible avalanche photodiode structures with shallow trench isolation (STI) as a guard ring. The following key parameter values were obtained at a supply voltage $U_{sup} = 0.98U_{br}$ ($\lambda = 670$ nm) by simulating the fabrication process and the output characteristics of the avalanche photodiode: a multiplication factor $M = 62.3$ and a spectral sensitivity $S = 19.6$ A/W.

The simulations for a SiO_2 trench width of about 1 μm showed that the optimal depth is about 3–4 μm, which rules out single-step isotropic silicon etching. The drop in M can reach 30% for etching with an aspect ratio of 1:1.

We found that defects causing the STI profile to narrow toward the trench bottom can reduce the multiplication factor M by up to 18%. Deviations of M from the optimum do not exceed 2.5% for the other defect types considered.

The dependences of the multiplication factor and spectral sensitivity on the profile width at the trench bottom are well approximated by linear functions expressed in terms of the deviation from the ideal profile. The decrease in the multiplication factor with the narrowing of the trench is associated with an increased contribution of the lateral component of the electric field in the region with the highest light intensity.

In the future, we plan to analyze the processes leading to a decrease in W_b, address the need to recalibrate the model, study the spectral dependences, and explore ways to minimize the effect of such technological defects and deviations on the multiplication factor of the avalanche photodiode.

REFERENCES

1. **Joo J. E., Lee M. J., Park S. M.,** A CMOS optoelectronic receiver IC with an on-chip avalanche photodiode for home-monitoring LiDAR sensors, Sensors, 21 (13) (2021) 4364.

2. **Wu Q.**, **Li Y., Yang Y., Chen S., Zhao Y.,**The law that guides the development of photolithography technology and the methodology in the design of photolithographic process, Proc. 2020 China Semiconductor Technology International Conference (CSTIC), Jun 26 –Jul 17, 2020, Shanghai, China, IEEE, (2020) 3–8.

3. **Furtado A. S., Diniz J. A., Monteiro D. W. D. L.,** Fabrication and characterization of active pixel sensors (APS) using simple metal gate nMOS technology, ECS Trans. 23 (1) (2009) 461.

4. **Goy J.**, **Courtois B., Karam J. M., Pressecq F.,** Design of an APS CMOS image sensor for low light level applications using standard CMOS technology, Analog Integr. Cir. Sig. Proc. 29 (1) (2001) 95–104.

5. **Kamrani E., Lesage F., Sawan M.,** Efficient premature edge breakdown prevention in SiAPD fabrication using the standard CMOS process, Semicond. Sci. Technol. 28 (4) (2013) 045008.

6. **Zhi W., Quan Q., Yu P., Jiang Y.,** A 45 nm CMOS avalanche photodiode with 8.4-GHz bandwidth, Micromachines. 11 (1) (2020) 65.

7. **Williams G. M., Huntington A. S.,** Probabilistic analysis of linear mode vs. Geiger mode APD FPAs for advanced LADAR enabled interceptors, In book: Howart R. T., Richards R. D. (Eds.) "Spaceborne Sensors III", Proc. SPIE. 6220 (30 May) (2006) 622008.

8. **Zhang Y., Wu Y., Sun Q., et al.,** Inductively coupled plasma dry etching of silicon deep trenches with extremely vertical smooth sidewalls used in micro-optical gyroscopes, Micromachines.14 (4) (2023) 846.

9. **Li L., Zhao X., Wong C. P.,** Charge transport in uniform metal-assisted chemical etching for 3D high-aspect-ratio micro-and nanofabrication on silicon, ECS J. Solid State Sci. Technol. 4 (9) (2015) P337–P346.

10. **Frühauf J., Krönert S.,** Wet etching of silicon gratings with triangular profiles, Microsyst. Technol.11 (12) (2005) 1287–1291.

11. **Hoekstra R. J., Kushner M. J., Sukharev V., Schoenborn P.,** Microtrenching resulting from specular reflection during chlorine etching of silicon, J. Vac. Sci. Technol. B. 16 (4) (1998) 2102–2104.

12. **Chang B., Leussink P., Jensen F.**, **et al.,** DREM: Infinite etch selectivity and optimized scallop size distribution with conventional photoresists in an adapted multiplexed Bosch DRIE process, Microelectron. Eng. 191 (5 May) (2018) 77–83.

13. **Panduranga P., Abdou A., Ren Zh., et al.,** Isotropic silicon etch characteristics in a purely inductively coupled SF6 plasma, J. Vac. Sci. Technol. B. 37 (6) (2019) 061206.

14. **Burtsev A., Li Y. X., Zeijl H. W., Beenakker C. I. M.,** An anisotropic U-shaped SF6-based plasma silicon trench etching investigation, Microelectron. Eng. 40 (2) (1998) 85–97.

15. **Laermer F., Urban A.,** Milestones in deep reactive ion etching, In book: Digest of technical papers of the 13th Int. Conf. on Solid-State Sensors, Actuators & Microsyst., Seoul, Korea (South), 05–09 June, 2005. TRANSDUCERS'05, IEEE, 2 (2005) 1118–1121.

16. **Hofbauer M., Schneider-Hornstein K., Zimmermann H.,** Single-photon detection for data communication and quantum systems, IOP Publishing, 2053–2563, Bristol (UK), 2021.

17. **Sze S. M., Yiming Li, Ng K. K.,** Physics of semiconductor devices, Second Ed., Wiley, New York, 1981.

18. **Van Overstraeten R., De Man H.,** Measurement of the ionization rates in diffused silicon *p–n* junctions, Solid State Electron.13 (5) (1970) 583–608.

19. **Chynoweth A. G.,** Chynoweth, ionization rates for electrons and holes in silicon, Phys. Rev. 109 (5) (1958) 1537–1540.

20. **Lee M. J., Choi W. Y.,** Performance optimization and improvement of silicon avalanche photodetectors in standard CMOS technology, IEEE J. Sel. Top. Quantum Electron. P-P (20 Sept) (2017) 1–1.

21. **Wang W., Zeng H.-A., Wang F., et al.,** A speed-optimized, low-noise APD with 0.18 μm CMOS technology for the VLC applications, Mod. Phys. Lett. B, 34 (29) (2020) 2050321.

СПИСОК ЛИТЕРАТУРЫ

1. **Joo J. E., Lee M. J., Park S. M.** A CMOS optoelectronic receiver IC with an on-chip avalanche photodiode for home-monitoring LiDAR sensors // Sensors. 2021. Vol. 21. No. 13. P. 4364.

2. **Wu Q.**, **Li Y., Yang Y., Chen S., Zhao Y.** The law that guides the development of photolithography technology and the methodology in the design of photolithographic process // Proceedings of the 2020 China Semiconductor Technology International Conference (CSTIC). June 26 –July 17, 2020, Shanghai, China, IEEE, 2020. Pp. 3–8.

3. **Furtado A. S., Diniz J. A., Monteiro D. W. D. L.** Fabrication and characterization of active pixel sensors (APS) using simple metal gate nMOS technology // ECS Transactions. 2009. Vol. 23. No. 1. P. 461.

4. **Goy J.**, **Courtois B., Karam J. M., Pressecq F.** Design of an APS CMOS image sensor for low light level applications using standard CMOS technology // Analog Integrated Circuits and Signal Processing. 2001. Vol. 29. No. 1–2. Pp. 95–104.

5. **Kamrani E., Lesage F., Sawan M.** Efficient premature edge breakdown prevention in SiAPD fabrication using the standard CMOS process // Semiconductor Science and Technology. 2013. Vol. 28. No. 4. P. 045008.

6. **Zhi W., Quan Q., Yu P., Jiang Y.** A 45 nm CMOS avalanche photodiode with 8.4-GHz bandwidth // Micromachines. 2020. Vol. 11. No. 1. P. 65.

7. **Williams G. M., Huntington A. S.** Probabilistic analysis of linear mode vs. Geiger mode APD FPAs for advanced LADAR enabled interceptors // Howart R. T., Richards R. D. (Eds.). Spaceborne Sensors III. Proceedings SPIE. 2006. Vol. 6220. 30 May. P. 622008.

8. **Zhang Y., Wu Y., Sun Q., Shen L., Lan J., Guo L., Shen Zh., Wang X., Xiao J., Xu J.** Inductively coupled plasma dry etching of silicon deep trenches with extremely vertical smooth sidewalls used in micro-optical gyroscopes // Micromachines. 2023. Vol. 14. No. 4. P. 846.

9. **Li L., Zhao X., Wong C.-P.** Charge transport in uniform metal-assisted chemical etching for 3D high-aspect-ratio micro-and nanofabrication on silicon // ECS Journal of Solid State Science and Technology. 2015. Vol. 4. No. 9. Pp. P337–P346.

10. **Frühauf J., Krönert S.** Wet etching of silicon gratings with triangular profiles // Microsystem Technologies. 2005. Vol. 11. No. 12. Pp. 1287–1291.

11. **Hoekstra R. J., Kushner M. J., Sukharev V., Schoenborn P.** Microtrenching resulting from specular reflection during chlorine etching of silicon // Journal of Vacuum Science & Technology B: Microelectronics and Nanometer Structures Processing, Measurement, and Phenomena. 1998. Vol. 16. No. 4. Pp. 2102–2104.

12. **Chang B., Leussink P., Jensen F., Hübner J., Jansen H.** DREM: Infinite etch selectivity and optimized scallop size distribution with conventional photoresists in an adapted multiplexed Bosch DRIE process // Microelectronic Engineering. 2018. Vol. 191. 5 May. Pp. 77–83.

13. **Panduranga P., Abdou A., Ren Zh., Pedersen R. H., Nezhad M. P.** Isotropic silicon etch characteristics in a purely inductively coupled SF6 plasma // Journal of Vacuum Science & Technology B. 2019. Vol. 37. No. 6. P. 061206.

14. **Burtsev A., Li Y. X., Zeijl H. W., Beenakker C. I. M.** An anisotropic U-shaped SF6-based plasma silicon trench etching investigation // Microelectronic Engineering. 1998. Vol. 40. No. 2. Pp. 85–97.

15. **Laermer F., Urban A.,** Milestones in deep reactive ion etching // Digest of technical papers (Vol. 2) of the 13th International Conference on Solid-State Sensors, Actuators and Microsystems (TRANSDUCERS'05), Seoul, Korea (South), 05–09 June, 2005. IEEE. 2005, Pp. 1118–1121.

16. **Hofbauer M., Schneider-Hornstein K., Zimmermann H.**, Single-photon detection for data communication and quantum systems. Bristol (UK): IOP Publishing, 2053–2563, 2021.

17. **Зи С.** Физика полупроводниковых приборов. Пер. с англ. М.: Рипол Классик, 1973. 655 с.

18. **Van Overstraeten R., De Man H.** Measurement of the ionization rates in diffused silicon *p–n* junctions // Solid State Electronics. 1970. Vol. 13. No. 5. Pp. 583–608.

19. **Chynoweth A. G.** Ionization rates for electrons and holes in silicon // Physical Review. 1958. Vol. 109. No. 5. Pp. 1537–1540.

20. **Lee M.-J., Choi W.-Y.** Performance optimization and improvement of silicon avalanche photodetectors in standard CMOS technology// IEEE Journal of Selected Topics in Quantum Electronics. 2017. Vol. P-P. 20 September. Pp. 1–1.

21. **Wang W., Zeng H.-A., Wang F., Wang G., Xie Y., Feng Sh.** A speed-optimized, low-noise APD with 0.18 μm CMOS technology for the VLC applications // Modern Physics Letters B. 2020. Vol. 34. No. 29. P. 2050321.

THE AUTHORS

DOLZHENKO Dmitry I.
Peter the Great St. Petersburg Polytechnic University
29 Politechnicheskaya St., St. Petersburg, 195251, Russia
ddi.dev.94@gmail.com
ORCID: 0000-0002-5707-4145

LETKIMAN Egor D.
Peter the Great St. Petersburg Polytechnic University
29 Politechnicheskaya St., St. Petersburg, 195251, Russia
letkiman.egor@gmail.com

СВЕДЕНИЯ ОБ АВТОРАХ

ДОЛЖЕНКО Дмитрий Игоревич – *кандидат физико-математических наук, старший преподаватель Высшей школы электроники и микросистемной техники Санкт-Петербургского политехнического университета Петра Великого.*
195251, Россия, г. Санкт-Петербург, Политехническая ул., 29
ddi.dev.94@gmail.com
ORCID: 0000-0002-5707-4145

ЛЕТКИМАН Егор Дмитриевич – *студент Института электроники и телекоммуникаций Санкт-Петербургского политехнического университета Петра Великого.*
195251, Россия, г. Санкт-Петербург, Политехническая ул., 29
letkiman.egor@gmail.com

Received 11.12.2025. Approved after reviewing 26.12.2025. Accepted 02.02.2026.
Статья поступила в редакцию 11.12.2025. Одобрена после рецензирования 26.12.2025. Принята 02.02.2026.

© Peter the Great St. Petersburg Polytechnic University, 2026

Original article
DOI: https://doi.org/10.18721/JPM.19206

THE MIXED PARAMETRIC AND SELF-OSCILLATIONS: THE EFFECT OF NONLINEAR PARAMETRIC EXCITATION AND DELAYS ON THEM CAUSING SELF-OSCILLATIONS

A. A. Alifov✉

Mechanical Engineering Research Institute of the RAS, Moscow, Russia

✉ alishir@mail.ru

Abstract. In the paper, the mixed parametric and self-oscillations in the presence of a nonlinear parametric action and a delay in friction causing self-oscillations have been studied. For this purpose, a model of a frictional self-oscillating system interacting with an energy source of limited power was used. The solution of nonlinear differential equations of motion was constructed using the direct linearization method. The relations of nonstationary and stationary oscillation modes were obtained. By application of the Routh – Hurwitz criteria, the conditions for the stability of stationary oscillations were derived. The calculations were carried out in order to gain information about the dynamics of fluctuations. An analysis of the data showed that the amplitude-frequency dependence changed its behavior under the influence of the delay. The latter also led to the appearance of stability regions on the lower branches of the amplitude curves, and a dependence arose on the steepness of the energy source characteristic.

Keywords: nonlinearity, parametric excitation, delay, mixed oscillations, parametric oscillations, self-oscillations, method, linearization, energy source

Citation: Alifov A. A., The mixed parametric and self-oscillations: The effect of nonlinear parametric excitation and delays on them causing self-oscillations, St. Petersburg State Polytechnical University Journal. Physics and Mathematics. 19 (2) (2026) 68–75. DOI: https://doi.org/10.18721/JPM.19206

This is an open access article under the CC BY-NC 4.0 license (https://creativecommons.org/licenses/by-nc/4.0/)

Научная статья
УДК 534.16
DOI: https://doi.org/10.18721/JPM.19206

СМЕШАННЫЕ ПАРАМЕТРИЧЕСКИЕ И АВТОКОЛЕБАНИЯ: ДЕЙСТВИЕ НА НИХ НЕЛИНЕЙНОГО ПАРАМЕТРИЧЕСКОГО ВОЗБУЖДЕНИЯ И ЗАПАЗДЫВАНИЯ, ВЫЗЫВАЮЩЕГО АВТОКОЛЕБАНИЯ

А. А. Алифов✉

Институт машиноведения им. А.А. Благонравова РАН, Москва, Россия

✉ alishir@mail.ru

Аннотация. В работе изучены смешанные параметрические и автоколебания при наличии нелинейного параметрического воздействия и запаздывания в трении, вызывающего автоколебания. Для этого использована модель фрикционной автоколебательной системы, взаимодействующей с источником энергии ограниченной мощности. Решение нелинейных дифференциальных уравнений движения достигнуто методом прямой линеаризации. Получены соотношения между нестационарными и стационарными режимами колебаний. С применением критериев Рауса – Гурвица

© Alifov A. A., 2026. Published by Peter the Great St. Petersburg Polytechnic University.

установлены условия устойчивости стационарных колебаний. Проведены расчеты с целью получения информации о динамике колебаний. Анализ полученных данных показал, что под действием запаздывания амплитудно-частотная зависимость изменяет свое поведение. Запаздывание приводит также к появлению участков устойчивости на нижних ветвях амплитудных кривых, и возникает зависимость от крутизны характеристики источника энергии.

Ключевые слова: нелинейность, параметрическое возбуждение, запаздывание, смешанные колебания, параметрические колебания, автоколебания, линеаризация

Ссылка для цитирования: Алифов А. А. Смешанные параметрические и автоколебания: действие на них нелинейного параметрического возбуждения и запаздывания, вызывающего автоколебания // Научно-технические ведомости СПбГПУ. Физико-математические науки. 2026. Т. 19. № 2. С. 68–75. DOI: https://doi.org/10.18721/JPM.19206

Статья открытого доступа, распространяемая по лицензии CC BY-NC 4.0 (https://creativecommons.org/licenses/by-nc/4.0/)

Introduction

A large number of studies have considered various oscillatory processes. According to the well-known classification, oscillation theory distinguishes four types of oscillations, which form four classes of mixed oscillations (interactions between types) [1–3]. One of these classes comprises mixed parametric oscillations and self-oscillations.

The goal of this study is to analyze mixed parametric oscillations and self-oscillations, accounting for three factors: nonlinear parametric excitation, time delay in friction that causes self-oscillations, and the limited power of the energy source.

Energy consumption has become increasingly important in the modern world, and time delays can occur in many systems [4–10].

Parametric oscillations, described mathematically by differential equations with periodic coefficients, can arise in various systems. A comprehensive study of parametric oscillations under quadratic parametric excitation is provided in [11].

In this paper, the solution of the nonlinear differential equations for mixed parametric oscillations and self-oscillations is constructed using linearization and the change of variables with averaging [17].

Equations of motion

Let us consider mixed parametric oscillations and self-oscillations adopting a commonly used model of a self-oscillating system [1, 2, 15]. In this model, a spring (with fixed ends) and a damper are connected to a body lying on a belt that moves continuously at a certain velocity V. The parameters c_0 and γ are the coefficients of the linear and nonlinear parts of the spring force, respectively; k_0 is the damping coefficient (all three parameters are constants). The velocity V is given by $V = r_0\dot{\varphi}$. The body has mass m and velocity $\dot{x}$ in the direction of motion x. The belt is driven by a motor with rotor angular velocity $\dot{\varphi}$ and torque characteristic $M(\dot{\varphi})$, which includes the resisting torque. A friction force $T(U)$ arises between the body and the belt, causing self-oscillations and depending on the relative velocity $U = r_0\dot{\varphi} - \dot{x}$.

The system of differential equations describing mixed parametric oscillations and self-oscillations under nonlinear parametric excitation and delay takes the following form:

$$\begin{aligned} m\ddot{x} + k_0\dot{x} + c_0 x &= T(U_\Delta) - \gamma x^3 - bx^3\cos\nu t, \\ I\ddot{\varphi} &= M(\dot{\varphi}) - r_0 T(U_\Delta), \end{aligned} \tag{1}$$

where $bx^3\cos(\nu t)$ is the term representing nonlinear parametric excitation (b = const, ν = const); r_0 is the radius at which the friction force is applied (r_0 = const); U_Δ is the relative velocity ($U_\Delta = r_0\dot{\varphi} - \dot{x}_\Delta$, $\dot{x}_\Delta = \dot{x}(t-\Delta)$, Δ = const is the delay); I is the moment of inertia of the motor rotor, I = const.

© Алифов А. А., 2026. Издатель: Санкт-Петербургский политехнический университет Петра Великого.

The characteristic of the friction force $T(U_\Delta)$ is taken in the form

$$T(U_\Delta) = T_0(\operatorname{sgn} U_\Delta - \alpha_1 U_\Delta + \alpha_3 U_\Delta{}^3), \tag{2}$$

where T_0 is the normal reaction force, T_0 = const; the coefficients α_1 and α_3 are constants; $\operatorname{sgn}(U_\Delta) = +1$ for $U_\Delta > 0$, $\operatorname{sgn}(U_\Delta) = -1$ for $U_\Delta < 0$.

If $U_\Delta = 0$, the characteristic $T(0)$ lies in the range

$$-T_0 \le T(0) \le T_0.$$

Interestingly, characteristic (2) also occurred in space experiments [16].

Using the direct linearization method [17–20], we replace expression (2) with a function of the form

$$T(U_\Delta) = T_0[\operatorname{sgn}(U_\Delta) + B_T + k_T \dot{x}],$$

where the linearization coefficients B_T and k_T are determined by the expressions

$$\begin{gathered} B_T = -\alpha_1 u + \alpha_3 u^3 + 3N_2\alpha_3 u p^2 a^2,\ k_{\dot{O}} = -\alpha_3 \bar{N}_3(p^2a^2 - h),\ h = 3(u_0^2 - u^2)/\bar{N}_3, \\ u_0^2 = \alpha_1/3\alpha_3,\ N_2 = (2r+1)/(2r+3),\ \bar{N}_3 = (2r+3)/(2r+5), \\ a = max|x| \text{ is the amplitude.} \end{gathered} \tag{3}$$

Using the direct linearization method, we also replace the nonlinear part of the spring force γx^3 with a linear one $c_f x$ with the linearization coefficient $c_f = \bar{N}_3 \gamma a^2$. After linearization, Eqs. (1) take the form

$$\begin{gathered} m\ddot{x} + k_0\dot{x} + c\,x = T_0(B_{\dot{O}} + \operatorname{sgn} U_\Delta + k_T \dot{x}_\Delta) - bx^3 \cos\ t \\ I\ddot{\varphi} = M(\dot{\varphi}) - r_0 T_0(\operatorname{sgn} U_\Delta + B_T + k_T \dot{x}_\Delta), \end{gathered} \tag{4}$$

where $c = c_0 + c_f$.

Solution of the equations and stability conditions for stationary oscillations

The solutions of Eqs. (4) obtained by change of variables with averaging [17], taking into account the expression

$$\dot{x}_\Delta = -ap\sin(\psi - p\Delta),$$

take the following form:

$$x = a\cos\psi,\ \dot{x}_\Delta = -ap\sin\psi,\ \psi = pt + \xi,\ p = \nu/2,\ \dot{\varphi} = \Omega. \tag{5}$$

The solutions of Eqs. (4) differ for the cases $U_\Delta > 0$ and $U_\Delta < 0$. The equations for determining the nonstationary values of the amplitude a, oscillation phase ξ, and velocity u, given by $u = r_0\Omega$, take the following form.

a) $u \ge ap$:

$$\begin{aligned} \frac{da}{dt} &= -\frac{1}{4pm}(2aG - 0.5ba^3 \sin 2\xi), \\ \frac{d\xi}{dt} &= \frac{1}{4pma}(2aW + ba^3 \cos 2\xi), \\ \frac{du}{dt} &= \frac{r_0}{I}\left[M(\frac{u}{r}) - r_0 T_0(1 + B_{\dot{O}})\right]; \end{aligned} \tag{6a}$$

b) $u < ap$:

$$\frac{da}{dt} = -\frac{1}{4pm}\left[2aG - 0.5ba^3 \sin 2\xi - \frac{8T_0}{\pi ap}\sqrt{a^2p^2 - u^2}\right],$$

$$\frac{d\xi}{dt} = \frac{1}{4pma}(2aW + ba^3 \cos 2\xi), \tag{6b}$$

$$\frac{du}{dt} = \frac{r_0}{I}\left[M(\frac{u}{r}) - r_0T_0(1 + B_{\dot{O}}) - \frac{r_0T_0}{\pi}(3\pi - 2\psi_*)\right],$$

where $\omega_0^2 = c_0/m$, $G = p[k_0 - T_0k_T \cos(p\Delta)]$, $W = m(\omega_0^2 - p^2) + c_{\dot{O}} - pT_0k \sin p\Delta$, $\psi^* = 2\pi - \arcsin(u/ap)$.

The stationary values of the amplitude and phase are determined by the conditions $\dot{a} = 0$, $\dot{\xi} = 0$. For the velocity values $u \geq ap$, they are found from the relations

$$4(4G^2 + W^2) = b^2a^4, \text{ tg}(2\xi) = -2G/W,$$

and for $u < ap$, the stationary amplitude satisfies the relation $a \approx u/p$.

The load on the energy source from the oscillatory system is determined by the condition $\dot{u} = 0$, yielding the relation

$$M(u/r) - S(a, u) = 0,$$

where

a) $u \geq ap$: $S(a,u) = r_0T_0(1 + B_T)$;

b) $u < ap$: $S(a,u) = r_0T_0[(1 + B_T) + \pi^{-1}(3\pi - 2\psi)]$.

The stationary values of the velocity u can be found from the intersection points of the curves $M(u/r)$ and $S(a,u)$.

To derive the stability conditions for stationary oscillations, we compose equations in variations for Eqs. (6) and, using the Routh–Hurwitz criteria, we obtain

$$B_1 > 0,\ B_3 > 0,\ B_1B_2 - B_3 > 0, \tag{7}$$

where $B_1 = -(b_{11} + b_{22} + b_{33})$, $B_2 = b_{11}b_{33} + b_{11}b_{22} + b_{22}b_{33} - b_{23}b_{32} - b_{12}b_{21} - b_{13}b_{31}$, $B_3 = b_{11}b_{23}b_{32} + b_{12}b_{21}b_{33} + b_{22}b_{13}b_{31} - b_{11}b_{22}b_{33} - b_{12}b_{23}b_{31} - b_{13}b_{21}b_{32}$.

For $u \geq ap$, we obtain the following expressions:

$$b_{11} = \frac{r_0}{I}\left(Q - r_0T_0\frac{\partial B_{\dot{O}}}{\partial u}\right),\ b_{12} = -6I^{-1}r_0^2T_0N_2\alpha_3uap^2,\ b_{13} = 0,$$

$$b_{21} = -3m^{-1}T_0a\ \alpha_3u\cdot\cos(p\Delta),$$

$$b_{22} = -\frac{1}{4pm}\left[2p(k_0 + T_0\bar{N}_3\alpha_3(3a^2p^2 - h)\cos p\Delta) - \frac{3}{2}ba^2 \sin 2\xi\right],$$

$$b_{23} = \frac{ba^3}{4pm}\cos 2\xi,\ b_{31} = -3m^{-1}T_0\alpha_3u\cdot\sin(p\Delta),$$

$$b_{32} = \frac{1}{2pm}\left[\bar{N}_3a(\gamma + 2T_0\alpha_3p^3 \sin p\Delta) + ba\cos 2\xi\right],\ b_{33} = -\frac{ba^3}{2pma}\sin 2\xi,$$

$$\frac{\partial B_{\dot{O}}}{\partial u} = -(\alpha_1 - 3\alpha_3u^2 - 3\alpha_3N_2a^2p^2),\ \frac{\partial k_{\dot{O}}}{\partial a} = -2\bar{N}_3\alpha_3ap^2,$$

where $Q = \frac{d}{du}M(\frac{u}{r_0})$.

If $u < ap$, we obtain the following coefficients:

$$b_{11} = \frac{r_0}{I}\left[Q - r_0 T_0 \frac{\partial B_{\dot{O}}}{\partial u} - \frac{2r_0 T_0}{\pi\sqrt{a^2 p^2 - u^2}}\right],$$

$$b_{12} = -\frac{r_0^2 T_0}{I}\left[\frac{\partial B_{\dot{O}}}{\partial a} + \frac{2u}{\pi a\sqrt{a^2 p^2 - u^2}}\right],$$

$$b_{21} = -\frac{auT_0}{m}\left[3\alpha_3 \cos p\Delta - \frac{2}{\pi a^2 p^2\sqrt{a^2 p^2 - u^2}}\right],$$

$$b_{22} = -\frac{1}{4pm}\left[2p(k_0 + T_0\bar{N}_3\alpha_3(3a^2 p^2 - h)\cos p\Delta) - \frac{3}{2}ba^2 \sin 2\xi\right] - \frac{2T_0 u^2}{\pi m a^2 p^2\sqrt{a^2 p^2 - u^2}},$$

while the coefficients b_{13}, b_{23}, b_{31}, b_{33} are unchanged.

Calculations of stationary oscillation regimes

The following parameter values were chosen for the calculations:

$$m = 9.8\ \text{N}\cdot\text{s}^2\cdot\text{cm}^{-1},\ k_0 = 0.196\ \text{N}\cdot\text{s}\cdot\text{cm}^{-1},\ c_0 = \text{N}\cdot\text{cm}^{-1},\ b = 0.686\ \text{N}\cdot\text{cm}^{-1},$$

$$\gamma = \pm 1.96\ \text{N}\cdot\text{cm}^{-3},\ T_0 = 4.9\ \text{N},\ \alpha_1 = 0.84\ \text{s}\cdot\text{cm}^{-1},\ \alpha_3 = 0.18\ \text{s}^3\cdot\text{cm}^{-3},$$

$$r_0 = 1\ \text{cm},\ I = 9.8\ \text{N}\cdot\text{s}\cdot\text{cm}^2,\ p\Delta = \pi/2,\ \pi,\ 3\pi/2.$$

Some calculated results for $u = 1.2\ \text{cm}\cdot\text{s}^{-1}$ and different characteristics of the spring force ($\gamma > 0$, $\gamma < 0$) are shown in Fig. 1. Solid lines correspond to delay cases $p\Delta = \pi/2$, dashed lines to $p\Delta = \pi$, and dotted lines to $p\Delta = 3\pi/2$.

The shaded sectors correspond to values of the energy source characteristic steepness Q for which oscillations are stable. It would be more accurate to plot these sectors on the load curve $S(a,u)$, but for the sake of saving space, they are shown on the amplitude curves.

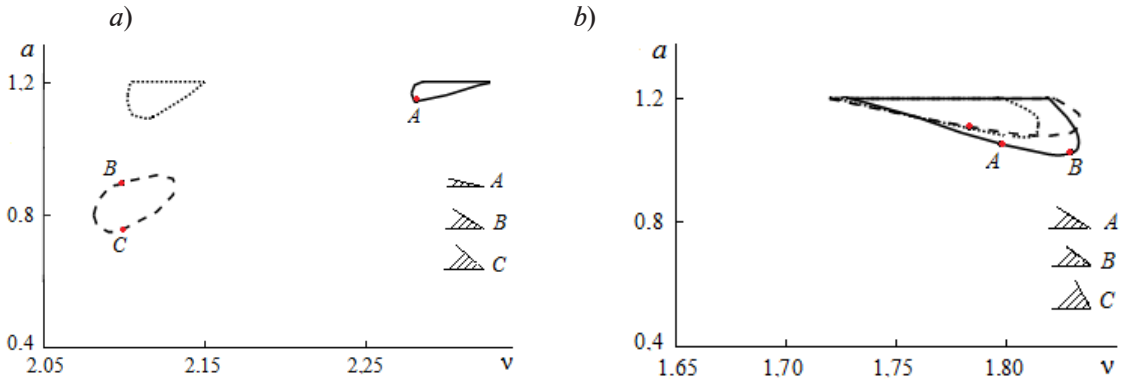


Fig. 1. Results of numerical calculations of the amplitude-frequency characteristics of the system under consideration for elastic forces with

Three cases are shown for the delay $p\Delta$:$\pi/2$: $\pi/2$ (solid lines), π (dashed lines), and $3\pi/2$ (dotted lines). The red points A, B, C correspond to the shaded sectors representing the ranges of the slope Q of the energy source characteristic within which oscillations are stable

Conclusion

We considered dynamics of mixed parametric oscillations and self-oscillations under nonlinear parametric excitation and time delay in friction that causes self-oscillations. A model of a frictional self-oscillating system interacting with a limited-power energy source was used to gain insight into the properties of these oscillations; calculations of stationary oscillations were performed.

Analysis of the obtained data led to the following conclusions.

First, the amplitude curve shifts significantly in the amplitude-frequency plane compared with the no-delay case, and the resonance region expands.

Second, stability regions depending on the slope of the energy source characteristic appear in some sections of the lower branches of the amplitude curves.

A number of effects that occur in the interaction of an oscillatory system with an energy source under linear parametric excitation are described in detail in monograph [1]. As the present study has shown, similar effects also occur under nonlinear parametric excitation.

REFERENCES

1. **Alifov A. A., Frolov K. V.,** Interaction of nonlinear oscillatory systems with energy sources; Hemisphere Publishing Corporation, New York, Washington, Philadelphia, London, 1990.

2. **Chelomey V. N.** (Chairman), Vibratsii v technike: spravochnik [Vibrations in machinery: Handbook], in 6 Vols., Vol. 2; Ed. by Blekhman I. I., Publishing House of Mechanical Engineering, Moscow, 1979 (in Russian).

3. **Andronov A. A., Vitt A. A., Khaikin S. E.,** Theory of vibration, Nauka Publishing, Moscow, 1981 (in Russian).

4. **Krasnoselskiĭ M., Pokrovskiĭ A.,** Systems with hysteresis, Springer-Verlag, Berlin, Heidelberg, New-York, 1989.

5. **Tkhan V. Z., Dementev Yu. N., Goncharov V. I.,** Improving the accuracy calculation of time delay automatic control, Software & Systems. 31 (3) (2018) 521–526 (in Russian).

6. **Keller A. A.,** Time-delay systems with application to mechanical engineering process dynamics and control, Math. Comput. Simul. 12 (2018) 64–73.

7. **Sykora H. T., Sadeghpour M., Ge J. I., et al.,** On the moment dynamics of stochastically delayed linear control systems, Int. J. Robust Nonlin. 30 (18) (2020) 8074–8097.

8. **Gupta S. K., Wang J., Barry O. R.,** Nonlinear vibration analysis in precision motion stage with PID and time-delayed feedback controls, Nonlinear Dyn. 101 (2) (2020) 439–464.

9. **Tsykunov A. M.,** Robust control of object with distributed delay and unknown order of mathematical model, Mekhatronika, Avtomatizatsiya, Upravlenie [Mechatronics., Automatization, Control]. 17 (4) (2016) 219–227 (in Russian).

10. **Rubanik V. P.,** Kolebaniya kvazilineynykh sistem s zapazdyvaniyem [Oscillations of quasilinear systems having delay], Nauka Publishing, Moscow, 1969 (in Russian).

11. **Schmidt G., Schulz R.,** Parametererregte Schwingungen, Deutscher Verlag d. Wiss., VEB, Berlin, 1975.

12. **Bogolyubov N. N., Mitropolsky Y. A.,** Asymptotic methods in the theory of non-linear oscillations, CRC Press, Florida, USA, 1961.

13. **Moiseev N. N.**, Asimptoticheskiye metody nelineynoy mekhaniki [Asymptotic methods of nonlinear mechanics], Nauka, Moscow, 1981 (in Russian).

14. **Butenin N. V., Neymark Yu. I., Fufayev N. A.,** Vvedeniye v teoriyu nelineynykh kolebaniy [Introduction to the theory of nonlinear oscillations], Nauka, Moscow, 1976) (in Russian).

15. **Klimov D. M.,** On one type of self-excited vibrations in a system with dry friction, Mech. Solids. 38 (3) (2003) 1–7.

16. **Bronovets M. A., Zhuravlev V. F.,** On self-excited vibrations in friction source measurement systems, Mech. Solids. 47 (3) (2012) 261–268.

17. **Alifov A. A.,** Metody pryamoy linearizatsii dlya rascheta nelineynykh system [Methods of direct linearization for calculation of nonlinear systems], Research Center "Regular and Chaotic Dynamics", Moscow, 2015 (in Russian).

18. **Alifov A. A.,** Method of the direct linearization of mixed nonlinearities, J. Mach. Manuf. Reliab. 46 (2) (2017) 128–131.

19. **Alifov A. A.,** About direct linearization methods for nonlinearity, Hu Z., Petoukhov S., He M. (Eds.); Conf. proc.: “Advances in Artificial Systems for Medicine and Education III (AIMEE 2019)” (Book Ser. “Advances in Intelligent Systems and Computing”. Vol. 1126). Springer, Cham, Switzerland (2020) 105–114.

20. **Alifov A. A.,** On the calculation by the method of direct linearization of mixed oscillations in a system with limited power-supply, Hu Z., Petoukhov S., Dychka I., He M. (Eds.); Conf. proc.: “Advances in Computer Science for Engineering and Education II (ICCSEEA 2019)” (Book Ser. “Advances in Intelligent Systems and Computing”. Vol. 938). Springer, Cham, Switzerland (2020) 23–31.

СПИСОК ЛИТЕРАТУРЫ

1. **Alifov A. A., Frolov K. V.** Interaction of nonlinear oscillatory systems with energy sources. New York, Washington, Philadelphia, London: Hemisphere Publishing Corporation, 1990. 327 p.

2. Вибрации в технике. Справочник: В 6-ти т. Ред. совет: В. Н. Челомей (пред., гл. ред.) и др. Т. 2. Колебания нелинейных механических систем. Под ред. И. И. Блехмана. М.: Машиностроение, 1979. 351 с.

3. **Андронов А. А., Витт А. А., Хайкин С. Э.** Теория колебаний. М.: Наука. Гл. ред. физ.-мат. лит. 1981. 568 с.

4. **Красносельский М. А., Покровский А. В.** Системы с гистерезисом. М.: Наука, 1983. 272 с.

5. **Тхан В. З., Дементьев Ю. Н., Гончаров В. И.** Повышение точности расчета систем автоматического управления с запаздыванием // Программные продукты и системы. 2018. Т. 31. № 3. С. 521–526.

6. **Keller A. A.** Time-delay systems with application to mechanical engineering process dynamics and control // International Journal of Mathematics and Computers in Simulation. 2018. Vol. 12. Pp. 64–73.

7. **Sykora H. T., Sadeghpour M., Ge J. I., Bachrathy D., Orosz G.** On the moment dynamics of stochastically delayed linear control systems // International Journal of Robust and Nonlinear Control. 2020. Vol. 30. No. 18. Pp. 8074–8097.

8. **Gupta S. K., Wang J., Barry O. R.** Nonlinear vibration analysis in precision motion stage with PID and time-delayed feedback controls // Nonlinear Dynamics. 2020. Vol. 101. No. 2. Pp. 439–464.

9. **Цыкунов А. М.** Робастное управление объектом с распределенным запаздыванием и неизвестным порядком математической модели // Мехатроника, автоматизация, управление. 2016. Т. 17. № 4. С. 219–227.

10. **Рубаник В. П.** Колебания квазилинейных систем с запаздыванием. М.: Наука, 1969. 288 с.

11. **Шмидт Г.** Параметрические колебания. М.: Мир, 1978. 336 с.

12. **Боголюбов Н. Н., Митропольский Ю. А.** Асимптотические методы в теории нелинейных колебаний. М.: Наука, 1974. 504 с.

13. **Моисеев Н. Н.** Асимптотические методы нелинейной механики. М.: Наука, 1981. 400 с.

14. **Бутенин Н. В., Неймарк Ю. И., Фуфаев Н. А.** Введение в теорию нелинейных колебаний. М.: Наука, 1976. 256 с.

15. **Климов Д. М.** Об одном виде автоколебаний в системе с сухим трением // Известия Российской академии наук. Механика твердого тела. 2003. № 3. С. 6–12.

16. **Броновец М. А., Журавлёв В. Ф.** Об автоколебаниях в системах измерения сил трения // Известия Российской академии наук. Механика твердого тела. 2012. № 3. С. 3–11.

17. **Алифов А. А.** Методы прямой линеаризации для расчета нелинейных систем. Москва–Ижевск: НИЦ «Регулярная и хаотическая динамика». 74 .2015 с.

18. **Alifov A. A.** Method of the direct linearization of mixed nonlinearities // Journal of Machinery Manufacture and Reliability. 2017. Vol. 46. No. 2. Pp. 128–131.

19. **Alifov A. A.** About direct linearization methods for nonlinearity // Hu Z., Petoukhov S., He M. (Eds.) Conference proceedings: “Advances in Artificial Systems for Medicine and Education III (AIMEE 2019)” (Book Series “Advances in Intelligent Systems and Computing”. Vol. 1126). Cham, Switzerland: Springer, 2020. Pp. 105–114.

20. **Alifov A. A.** On the calculation by the method of direct linearization of mixed oscillations in a system with limited power-supply // Hu Z., Petoukhov S., Dychka I., He M. (Eds.). Conference proceedings: “Advances in Computer Science for Engineering and Education II (ICCSEEA 2019)” (Book Series “Advances in Intelligent Systems and Computing”. Vol. 938). Cham, Switzerland: Springer, 2020. Pp. 23–31.

THE AUTHOR

ALIFOV Alishir A.
Mechanical Engineering Research Institute of the Russian Academy of Sciences
4 Malij Haritonjevskij lane, Moscow, 101000, Russia
alishir@mail.ru
ORCID: 0000-0003-2327-068X

СВЕДЕНИЯ ОБ АВТОРЕ

АЛИФОВ Алишир Али оглы – *доктор технических наук, главный научный сотрудник Лаборатории динамических процессов Института машиноведения имени А. А. Благонравова Российской академии наук.*
101000, Москва, Малый Харитоньевский переулок, 4
alishir@mail.ru
ORCID: 0000-0003-2327-068X

Received 01.12.2025. Approved after reviewing 06.02.2026. Accepted 06.02.2026.
Статья поступила в редакцию 01.12.2025. Одобрена после рецензирования 06.02.2026. Принята 06.02.2026.

© Peter the Great St. Petersburg Polytechnic University, 2026

EXPERIMENTAL TECHNIQUE AND DEVICES

Original article
DOI: https://doi.org/10.18721/JPM.19207

THICKNESS DETERMINATION OF COATINGS BY X-RAY FLUORESCENT ANALYSIS USING A CALIBRATION CURVE OBTAINED BY CALCULATIONS

S. S. Kozlovskii[1], *P. S. Gunkov*[1]✉,
Ya. A. Berdnikov[1], *V. A. Donskikh-Tyrsa*[2]

[1] Peter the Great St. Petersburg Polytechnic University, St. Petersburg, Russia;

[2] Regional Center for Standardization, Metrology and Testing in St. Petersburg and Leningrad Region (Test-St. Petersburg), St. Petersburg, Russia

✉ gunkov-pavel@yandex.ru

Abstract. When measuring a coating thickness by X-ray fluorescent analysis, the preliminary calibration of the detection system is required using reference samples with a known coating thickness. This operation is quite time-consuming and gives results only for a certain detection system and a pair of elements (the base material and coating). In our study, the calibration curve has been obtained by the Monte Carlo calculation method using the MCC 3D software. In so doing, we calculated the dependences of the ratios of peak intensities of fluorescence lines from Fe K_α (substrate) and Zn K_α (coating), as well as Cu K_α (substrate) and Au L_α (coating) on the values of coating thickness. Moreover, the coating thickness determination errors were obtained. A conclusion was made about the possibility of using the Monte Carlo method to determine the coating thickness without preliminary calibration.

Keywords: X-ray fluorescence analysis, thickness, substrate, thin film, simulation, Monte Carlo method

Citation: Kozlovskiy S. S., Gunkov P. S., Berdnikov Ya. A., Donskikh-Tyrsa V. A., Determination of coating thickness using the Monte Carlo method, St. Petersburg State Polytechnical University Journal. Physics and Mathematics. 19 (2) (2026) 76–83. DOI: https://doi.org/10.18721/JPM.19207

This is an open access article under the CC BY-NC 4.0 license (https://creativecommons.org/licenses/by-nc/4.0/)

© Kozlovskiy S. S., Gunkov P. S., Berdnikov Ya. A., Donskikh-Tyrsa V. A., 2026. Published by Peter the Great St. Petersburg Polytechnic University.

Научная статья
УДК 539.1.075
DOI: https://doi.org/10.18721/JPM.19207

ОПРЕДЕЛЕНИЕ ТОЛЩИНЫ ПОКРЫТИЙ МЕТОДОМ РЕНТГЕНОФЛУОРЕСЦЕНТНОГО АНАЛИЗА С ИСПОЛЬЗОВАНИЕМ ГРАДУИРОВОЧНОЙ ЗАВИСИМОСТИ, ПОЛУЧЕННОЙ РАСЧЕТНЫМ ПУТЕМ

С. С. Козловский[1], *П. С. Гуньков*[1]✉,
Я. А. Бердников[1], *В. А. Донских-Тырса*[2]

[1] Санкт-Петербургский политехнический университет Петра Великого, Санкт-Петербург, Россия;

[2] Государственный региональный центр стандартизации, метрологии и испытаний в г. Санкт-Петербурге и Ленинградской области (ФБУ «Тест-С.-Петербург»), Санкт-Петербург, Россия

✉ gunkov-pavel@yandex.ru

Аннотация. При измерении толщины покрытия методом рентгенофлуоресцентного анализа (РФА) требуется провести предварительную калибровку системы регистрации на эталонных образцах с известной толщиной покрытия. Такая операция занимает довольно много времени и дает результат лишь для определенной системы регистрации и пары элементов (базового материала и его покрытия). В настоящей работе калибровочная кривая определена расчетным методом Монте-Карло с использованием программы MCC 3D. Так были получены зависимости отношения интенсивностей линий флуоресценции Fe K_α (подложка) и Zn K_α (покрытие), а также Cu K_α (подложка) и Au L_α (покрытие) от значений толщины покрытий. Кроме того, рассчитаны погрешности определения толщины покрытий и сделан вывод о возможности применения метода Монте-Карло для расчета толщины покрытия без предварительной градуировки. Помимо этого, были рассчитаны оптимальные углы установки детекторов относительно нормали для расчета толщины покрытия методом РФА.

Ключевые слова: рентгенофлуоресцентный анализ, покрытие, подложка, тонкая пленка, симуляция Монте-Карло, градуировочная зависимость

Ссылка для цитирования: Козловский С. С., Гуньков П. С., Бердников Я. А., Донских-Тырса В. А. Определение толщины покрытий методом рентгенофлуоресцентного анализа с использованием градуировочной зависимости, полученной расчетным путем // Научно-технические ведомости СПбГПУ. Физико-математические науки. 2026. Т. 19. № 2. С. 76–83. DOI: https://doi.org/10.18721/JPM.19207

Статья открытого доступа, распространяемая по лицензии CC BY-NC 4.0 (https://creativecommons.org/licenses/by-nc/4.0/)

Introduction

Applying coatings to various surfaces and controlling their thickness are important challenges for many industries. The composition and thickness of coatings are determined using ultrasonic testing, eddy-current testing, X-ray fluorescence analysis (XRF), and electron microscopy. Each of the methods has its own advantages and disadvantages [1]. For XRF analysis of coating thickness, the layer order must be known and a calibration sample must be available.

The goal of this study is to develop a method for determining the coating thickness by the Monte Carlo method [2]. Using this method, we established the exposure time required for X-ray irradiation of the sample to determine the coating thickness with the required accuracy.

Zinc coatings on iron and gold coatings on copper were chosen as test pairs because they are the most common. Galvanizing steel, i.e., coating the metal with a layer of zinc that blocks

© Козловский С. С., Гуньков П. С., Бердников Я. А., Донских-Тырса В. А., 2026. Издатель: Санкт-Петербургский политехнический университет Петра Великого.

moisture and oxygen, protects steel from corrosion and is widely used to rust-proof steel products. Gold plating is most often applied to copper products in the jewelry industry, as well as for decorative design and for creating and restoring works of art [3]. Although alloys rather than pure metals are used in practice, we considered the simplest systems: Zn–Fe and Au–Cu.

Experimental samples and procedures

The key dependences and exposure times were determined using Monte Carlo simulations performed with the certified MCC 3D software [4–6]. This software has passed metrological certification, so the results obtained with it should be considered reliable.

The source used to irradiate the sample was modeled using the spectrum of an X-ray tube with a transmission rhodium anode and a 127 μm beryllium window operating at 30 kV (an equivalent of the Moxtek Magnum). In contrast to [7–10], where an experimental spectrum of the X-ray tube was used as the irradiation source, we simulated the X-ray spectrum by the Monte Carlo method.

The X-ray tube model used is shown in Fig. 1. The simulation was performed for a tube with a collimator; the diameter of the generated photon beam at the sample was 2 mm, the radiation intensity was $I = 1.26 \cdot 10^7$ photons/(s·μA).

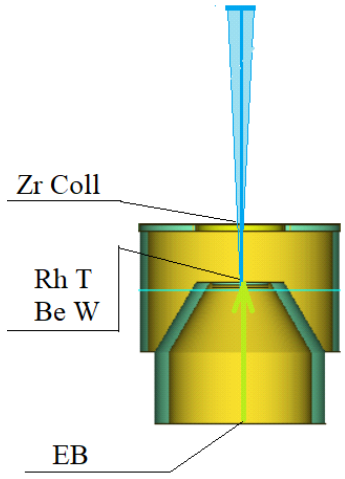


Fig. 1. Model of collimated X-ray tube used in the simulations:
zirconium collimator Zr Coll, rhodium target Rh T, beryllium window Be W, electron beam EB; the generated photon beam is shown as a blue cone

The detector in the study was a simulation model of an Amptek detector with a 500 μm crystal and a 12.7 μm beryllium window.

Determination of optimal detector angle relative to the normal for calculating the coating thickness

To find the optimal detector angle, we considered a system with the following arrangement: X-rays from the source struck the sample at a right angle, and the flux of fluorescence photons was recorded by ring detectors (to accelerate the simulations) positioned at different angles 3 cm from the sample surface. Five positions of the detector were selected. The detectors were positioned at the following angles relative to the sample normal (degrees): 15, 30, 45, 60 and 75. An iron disk with a diameter of 0.5 cm and a thickness of 1 cm was used as a sample. A Zn layer with thickness s (ranging from 0 to 50 μm) was deposited on the sample. The simulation setup is shown in Fig. 2.

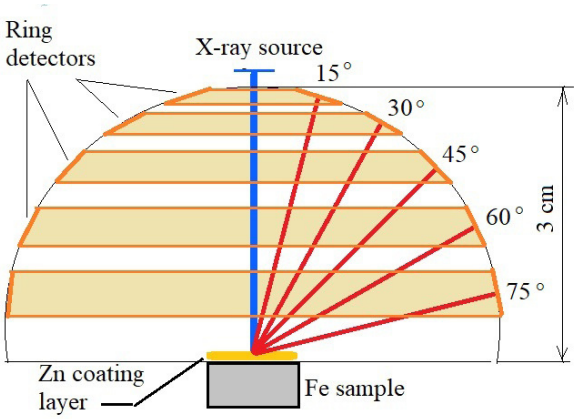


Fig. 2. Simulation model for the Zn–Fe pair:
Fe sample, Zn coating layer; Ring detectors, X-ray source. The incident X-rays are shown as a blue line; fluorescence emitted from the sample at different angles is shown as red rays

The simulations yielded the fluorescence spectra from samples with different Zn coating thicknesses and at different angles. First, the Fe K_α and Zn K_α peak intensities were plotted as a function of coating thickness s for different detector angles. A similar dependence was obtained for gold on copper.

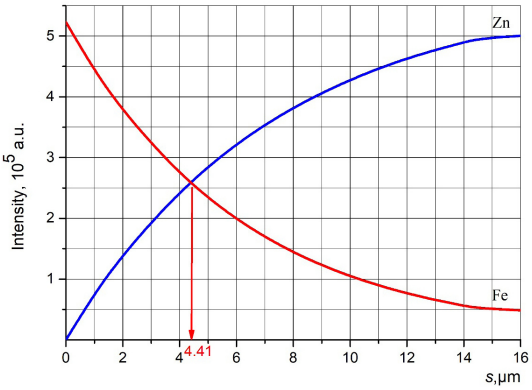


Fig. 3. Calculated Fe K_α and Zn K_α peak intensities versus coating thickness for detector angle of 45°

The value s = 4.41 μm corresponds to equal heights of the fluorescence maxima from the substrate and coating

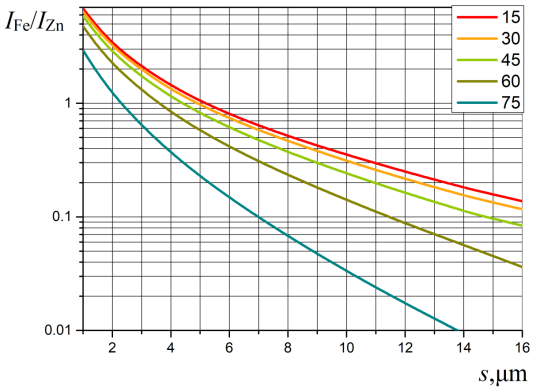


Fig. 4. Calculated Fe K_α/Zn K_α peak intensity ratios versus coating thickness for different detector angles (in degrees)

As an example, Fig. 3 shows the Fe K_α and Zn K_α peak intensities as a function of coating thickness s for a detector angle of 45°. The other dependences have a similar shape, but as the detector angle increases, the intersection point of the curves shifts toward smaller thicknesses. This is because the information depth decreases as the detector angle increases.

The intersection of the curves corresponds to the coating thickness at which the heights of the peaks associated with Fe K_α (substrate) and Zn K_α (coating) are equal.

Fig. 4 shows the Fe K_α/Zn K_α peak intensity ratio as a function of coating thickness for different detector angles.

A family of curves was plotted based on the simulation results, reflecting the dependence of the peak intensity ratio on the coating thickness for various angles. We can conclude from the data in Fig. 4 that the dependences of the Fe K_α/Zn K_α peak intensity ratio on the coating thickness are close for detector angles up to 45°. The behavior of the curves changes above this value: the ratio drops more sharply, and the range of measurable thicknesses narrows considerably. This result indicates that the geometric parameters of the instrument must be precisely known and controlled.

The simulation model of the X-ray fluorescence analyzer is shown in Fig. 5. Fig. 5,*a* shows the model, including the radiation source, the sample, and the detectors. Fig. 5,*b* shows the simulated trajectories of the incident X-ray photons and of the fluorescence photons emitted by the sample.

The simulation setup in Fig. 5 comprises four identical Amptek detectors arranged symmetrically about the vertical axis at 45° to the normal to speed up statistics accumulation.

As a result of the calculations, we obtained a calibration curve for the Fe K_α/Zn K_α peak intensity ratio as a function of coating thickness for a 45° detector angle at a tube voltage of 30 kV and a current of 1 mA. The same dependence was obtained for a Cu substrate coated with Au. The results are shown in Fig. 6. A similar dependence was described in [2].

The accuracy of the thickness measurement based on a calibration curve depends on the number of detected signals used to construct that curve.

The relative uncertainty δ in measuring the n_1/n_2 count ratio, assuming a Poisson distribution for counts n_1 and n_2, is given by the formula:

$$\delta = \sqrt{1/n_1 + 1/n_2}. \qquad (1)$$

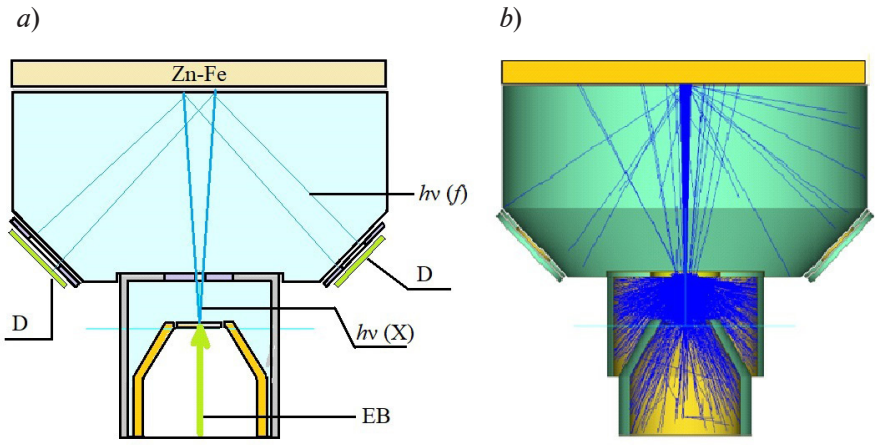


Fig. 5. Simulation model of the X-ray fluorescence analyzer (*a*) and the corresponding simulated photon trajectories (*b*); electron beam EB, generated X-ray photons *hν* (X), Zn-Fe sample, fluorescence photons *hν* (*f*), detectors D

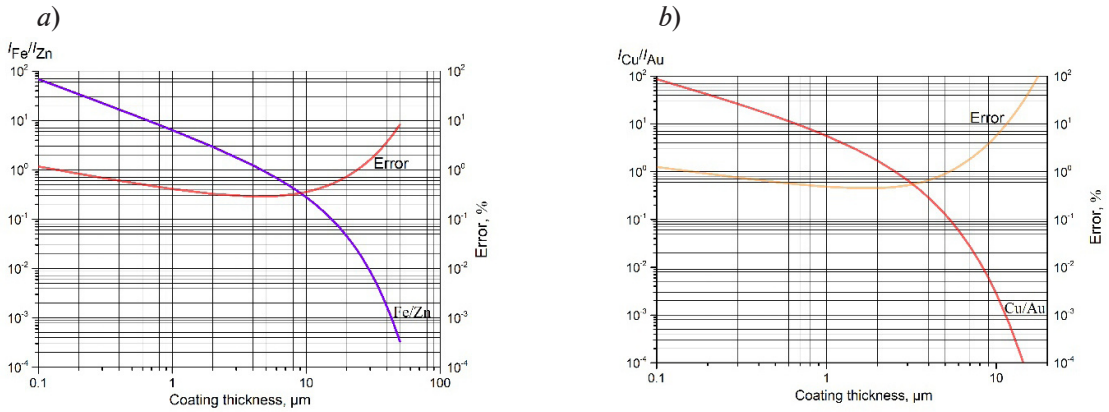


Fig. 6. Fe K_α/Zn K_α (*a*) and Cu K_α/Au L_α (*b*) peak intensity ratios as functions of coating thickness; corresponding uncertainty of coating thickness measurement for the chosen tube radiation intensity ($U = 30$ kV, $I = 1$ mA); the detector angle is 45° in both cases

Fig. 6 shows the substrate-to-coating peak intensity ratios as functions of coating thickness, along with the corresponding thickness measurement uncertainties.

The thickness measurement uncertainty we obtained is comparable to the values reported in [2, 9].

Conclusion

The results presented in this work show that Monte Carlo simulations in X-ray fluorescence analysis of coating thickness make it possible to determine coating thickness without prior calibration and to optimize the measurement process to achieve the required accuracy. However, this naturally requires experimental verification. In this work, we considered the simplest case, where the coating thickness was calculated for a pure element deposited on a pure substrate. Nevertheless, the Monte Carlo method can be used to calculate the thickness of coatings consisting of an arbitrary set of elements.

Once the relationship between coating thickness and the substrate-to-coating peak intensity ratio is known, the exposure time required to measure that thickness with the required accuracy can be found easily. Note that long exposure times are needed to measure gold coatings thicker than 10 μm on copper and zinc coatings thicker than 40 μm on iron with acceptable accuracy. For a practical instrument designed to measure coating thickness by the method described here, the optimal detector angle relative to the normal should not exceed 45°. At larger angles, the range of measurable thicknesses narrows substantially, and the measurement uncertainty increases.

REFERENCES

1. **Li Z., Wang C., Ju H., et al.,** Prediction model of aluminized coating thicknesses based on Monte Carlo simulation by X-ray fluorescence, Coatings. 12 (6) (2022) 764.

2. **Giurlani W., Berretti E., Innocenti M., Lavacchi A.,** Coating thickness determination using X-ray fluorescence spectroscopy: Monte Carlo simulations as an alternative to the use of standards, Coatings. 9 (2) (2019) 79.

3. **Brunetti A., Golosio B., Schoonjans T., Oliva P.,** Use of Monte Carlo simulations for cultural heritage X-ray fluorescence analysis, Spectrochim. Acta B. At. Spectrosc. 108 (1 June) (2015) 15–20.

4. **Bagayev K. A., Kozlovskiy S. S.,** An application of computer simulation to detector calibration in the aqueous medium, St. Petersburg Polytechnic University Journal: Physics and Mathematics. (2(122)) (2011) 106–111 (in Russian).

5. **Gunkov P. S., Kozlovskiy S. S., Berdnikov Ya. A.,** Optimizatsiya parametrov izmereniya na rentgenofluorestsentnom analizatore s pomoshchyu programmy dlya rascheta prokhozhdeniya izlucheniya cherez veshchestvo [Optimization of measurement parameters on an X-ray fluorescence analyzer using a program for calculating the passage of radiation through matter], Proc. X Russian Scientific and Practical Conf. of X-ray equipment manufacturers, Nov. 24, 2023, St. Petersburg, Publishing House of the St. Petersburg State Electrotechnical University ("LETI"), (2023) 52–54 (in Russian).

6. **Repnikova E. A., Dech A. V., Kozlovskiy S. S.,** Modelirovaniye prokhozhdeniya gamma-izlucheniya cherez trekhmernyye mnogosloynyye struktury [Simulation of the gamma-radiation passage through 3D multilayer structures], Proc. the 30-th anniversary of Science Week at SPbGTU, Part 5 (Interuniversity Sci. conf., Nov. 26 – Dec. 1, 2001), Publ. House of SPbGTU (2002) 58–59 (in Russian).

7. **Giurlani W., Berretti E., Lavacchi A., Innocenti M.,** Thickness determination of metal multilayers by ED-XRF multivariate analysis using Monte Carlo simulated standards, Anal. Chim. Acta. 1130 (15 Sept) (2020) 72–79.

8. **Pessanha S., Manso M., Antunes V., et al.,** Monte Carlo simulation of portable XRF setup: Non-invasive determination of gold leaf thickness in indo-Portuguese panel paintings, Spectrochim. Acta B. At. Spectrosc. 156 (June) (2019) 1–6.

9. **Pessanha S., Queralt I., Carvalho M. L., Sampaio J. M.,** Determination of gold leaf thickness using X-ray fluorescence spectrometry: Accuracy comparison using analytical methodology and Monte Carlo simulations, Appl. Radiat. Isot. 152 (1 June) (2019) 6–10.

10. **Lins S. A. B., Gigante G. E., Cesareo R., et al.,** Testing the accuracy of the calculation of gold leaf thickness by MC simulations and MA-XRF scanning, Appl. Sci. 10 (10) (2020) 3582.

СПИСОК ЛИТЕРАТУРЫ

1. **Li Z., Wang C., Ju H., Li X., Qu Y., Yu J.** Prediction model of aluminized coating thicknesses based on Monte Carlo simulation by X-ray fluorescence // Coatings. 2022. Vol. 12. No. 6. P. 764.

2. **Giurlani W., Berretti E., Innocenti M., Lavacchi A.** Coating thickness determination using X-ray fluorescence spectroscopy: Monte Carlo simulations as an alternative to the use of standards // Coatings. 2019. Vol. 9. No. 2. P. 79.

3. **Brunetti A., Golosio B., Schoonjans T., Oliva P.** Use of Monte Carlo simulations for cultural heritage X-ray fluorescence analysis // Spectrochimica Acta. Part B: Atomic Spectroscopy. 2015. Vol. 108. 1 June. Pp. 15–20.

4. **Багаев К. А., Козловский С. С.** Применение компьютерного моделирования для калибровки детекторов в водной среде // Научно-технические ведомости СПбГПУ. Физико-математические науки. 2011. № 2 (122). С. 106–111.

5. **Гуньков П. С., Козловский С. С., Бердников Я. А.** Оптимизация параметров измерения на рентгенофлуоресцентном анализаторе с помощью программы для расчета прохождения излучения через вещество // X Всероссийская научно-практическая конференция производителей рентгеновской техники. Программа и материалы конференции. СПб.: Изд-во СПбГЭТУ «ЛЭТИ», 2023. С. 52–54.

6. **Репникова Е. А., Деч А. В., Козловский С. С.** Моделирование прохождения гамма-излучения через трехмерные многослойные структуры // XXX Юбилейная Неделя науки СПбГТУ. 26 ноября – 1 декабря 2001. Материалы межвузовской научной конференции. Часть V (ФизМех). СПб.: Издательство СПбГТУ, 2002. С. 59–58.

7. **Giurlani W., Berretti E., Lavacchi A., Innocenti M.** Thickness determination of metal multilayers by ED-XRF multivariate analysis using Monte Carlo simulated standards // Analytica Chimica Acta. 2020. Vol. 1130. 15 September. Pp. 72–79.

8. **Pessanha S., Manso M., Antunes V., Carvalho M. L., Sampaio J. M.** Monte Carlo simulation of portable XRF setup: Non-invasive determination of gold leaf thickness in indo-Portuguese panel paintings // Spectrochimica Acta. Part B: Atomic Spectroscopy. 2019. Vol. 156. June. Pp. 1–6.

9. **Pessanha S., Queralt I., Carvalho M. L., Sampaio J. M.** Determination of gold leaf thickness using X-ray fluorescence spectrometry: Accuracy comparison using analytical methodology and Monte Carlo simulations // Applied Radiation and Isotopes. 2019. Vol. 152. 1 June. Pp. 6–10.

10. **Lins S. A. B., Gigante G. E., Cesareo R., Ridolfi S., Brunetti A.** Testing the accuracy of the calculation of gold leaf thickness by MC simulations and MA-XRF scanning // Applied Sciences 2020. Vol. 10. No. 10. P. 3582.

THE AUTHORS

KOZLOVSKIY Stanislav S.
Peter the Great St. Petersburg Polytechnic University
29 Politechnicheskaya St., St. Petersburg, 195251, Russia
skozlovski@phmf.spbstu.ru

GUNKOV Pavel S.
Peter the Great St. Petersburg Polytechnic University
29 Politechnicheskaya St., St. Petersburg, 195251, Russia
gunkov-pavel@yandex.ru
ORCID: 0000-0003-0309-5917

BERDNIKOV Yaroslav A.
Peter the Great St. Petersburg Polytechnic University
29 Politechnicheskaya St., St. Petersburg, 195251, Russia
berdnikov@spbstu.ru
ORCID: 0000-0003-0309-5917

DONSKIKH-TYRSA Victor A.
The Federal Budgetary Institution "State Regional Center for Standardization, Metrology and Testing in St. Petersburg and Leningrad Region" ("Test-St. Petersburg")
1 Kurlyandskaya St., St. Petersburg, 190103, Russia
vdt.test.spb@gmail.com

СВЕДЕНИЯ ОБ АВТОРАХ

КОЗЛОВСКИЙ Станислав Станиславович – *кандидат физико-математических наук, доцент Высшей школы фундаментальных физических исследований Санкт-Петербургского политехнического университета Петра Великого.*
195251, Россия, г. Санкт-Петербург, Политехническая ул., 29
skozlovski@phmf.spbstu.ru

ГУНЬКОВ Павел Сергеевич – *аспирант Высшей школы фундаментальных физических исследований Санкт-Петербургского политехнического университета Петра Великого.*
195251, Россия, г. Санкт-Петербург, Политехническая ул., 29
gunkov-pavel@yandex.ru
ORCID: 0000-0003-0309-5917

БЕРДНИКОВ Ярослав Александрович – *доктор физико-математических наук, профессор Высшей школы фундаментальных физических исследований Санкт-Петербургского политехнического университета Петра Великого.*
195251, Россия, г. Санкт-Петербург, Политехническая ул., 29
berdnikov@spbstu.ru
ORCID: 0000-0003-0309-5917

ДОНСКИХ-ТЫРСА Виктор Александрович – *инженер испытательной лаборатории товаров бытового и промышленного назначения Федерального бюджетного учреждения «Государственный региональный центр стандартизации, метрологии и испытаний в г. Санкт-Петербурге и Ленинградской области» (ФБУ «Тест-С.-Петербург»).*
190103, Россия, г. Санкт-Петербург, Курляндская ул., 1
vdt.test.spb@gmail.com

Received 19.01.2026. Approved after reviewing 09.02.2026. Accepted 09.02.2026.
Статья поступила в редакцию 19.01.2026. Одобрена после рецензирования 09.02.2026. Принята 09.02.2026.

© Peter the Great St. Petersburg Polytechnic University, 2026

PHYSICAL ELECTRONICS

Original article
DOI: https://doi.org/10.18721/JPM.19208

THE INFLUENCE OF AR^+ AND CD^+ ION IMPLANTATION ON THE COMPOSITION AND ELECTRONIC STRUCTURE OF MONOCRYSTALLINE ZINC TELLURIDE

J. B. Khujaniyozov[1]✉, B. E. Umirzakov[1], D. A. Tashmukhamedova[1], V. V. Loboda[2], A. A. Abduvayitov[1]

[1] Tashkent State Technical University Named after Islam Karimov,

Tashkent, Republic of Uzbekistan;

[2] Peter the Great St. Petersburg Polytechnic University, St. Petersburg, Russia

✉ KhujaniyozovJB@mail.ru

Abstract. The effect of Ar^+ and Cd^+ ion implantation and subsequent thermal annealing has been studied on a single-crystal ZnTe (111) using a whole range of spectroscopy methods: ultraviolet photoelectron one (UPS), light absorption one, and Auger electron one (AES). The results showed that bombardment of the surface with Ar^+ and Cd^+ ions with an energy of E_0 = 1 keV until a saturation dose of of D_{sat} = (6–8)·10^{16}cm^{-2} was reached resulted in the destruction of the crystal structure of the ion-implanted layers and, as a consequence, in surface metallization. In particular, after implantation with Cd^+ ions and subsequent annealing at T = 850 K, the formation of a homogeneous continuous $Zn_{0.5}Cd_{0.5}Te$ film 30–35 Å thick was observed, which indicated the redistribution of components and the formation of a new phase state on the ZnTe surface. The results of the study of $Zn_{0.5}Cd_{0.5}Te$ thin films demonstrate the presence of two clearly defined maxima in the valence electron spectra corresponding to binding energies of −1.4 eV and −5.2 eV.

Keywords: heterostructure, photoelectron spectroscopy, implantation, molecular beam epitaxy, saturation dose, thin film, zinc telluride

Citation: Khujaniyozov J. B., Umirzakov B. E., Tashmukhamedova D. A., Loboda V. V., Abduvayitov A. A., The influence of $Ar^+$and Cd^+ ion implantation on the composition and electronic structure of monocrystalline zinc telluride, St. Petersburg State Polytechnical University Journal. Physics and. 19 (2) (2026) 84–97. DOI: https://doi.org/10.18721/JPM.19208

This is an open access article under the CC BY-NC 4.0 license (https://creativecommons.org/ Mathematics licenses/by-nc/4.0/)

© Khujaniyozov J. B., Umirzakov B. Y., Tashmukhamedova D. A., Loboda V. V., Abduvayitov A. A., 2026. Published by Peter the Great St. Petersburg Polytechnic University.

Научная статья
УДК 538.971:621.315.592
DOI: https://doi.org/10.18721/JPM.19208

ВЛИЯНИЕ ИМПЛАНТАЦИИ ИОНОВ AR^+ И CD^+ НА СОСТАВ И ЭЛЕКТРОННУЮ СТРУКТУРУ МОНОКРИСТАЛЛИЧЕСКОГО ТЕЛЛУРИДА ЦИНКА

Ж. Б. Хужаниёзов[1]✉, *Б. Е. Умирзаков*[1], *Д. А. Ташмухамедова*[1], *В. В. Лобода*[2], *А. А. Абдувайитов*[1]

[1] Ташкентский государственный технический университет им. Ислама Каримова, г. Ташкент, Узбекистан;

[2] Санкт-Петербургский политехнический университет Петра Великого, Санкт-Петербург, Россия

✉ KhujaniyozovJB@mail.ru

Аннотация. Влияние ионной имплантации Ar^+ и Cd^+, а также последующего термического отжига было изучено на монокристаллическом образце ZnTe(111) с применением комплекса методов спектроскопии: ультрафиолетовой фотоэлектронной, поглощения света в УФ-. ИК-, видимой областях и Оже-электронной. Результаты исследований показали, что бомбардировка поверхности ионами Ar^+ и Cd^+ с энергией E_0 = 1 кэВ до достижения дозы насыщения D_{sat} = (6−8)·10^{16} $см^{-2}$ приводит к разрушению кристаллической структуры ионно-имплантированных слоев и, как следствие, к металлизации поверхности. В частности, после имплантации ионами Cd^+ и последующего отжига при температуре T = 850 K наблюдается формирование гомогенной сплошной пленки $Zn_{0,5}Cd_{0,5}Te$ толщиной 30 − 35 Å, что свидетельствует о перераспределении компонентов и образовании нового фазового состояния на поверхности ZnTe. Результаты исследования тонких пленок $Zn_{0,5}Cd_{0,5}Te$ демонстрируют наличие двух отчетливо выраженных максимумов в спектрах валентных электронов, соответствующих энергиям связи −1,4 эВ и −5,2 эВ.

Ключевые слова: гетероструктура, фотоэлектронная спектроскопия, имплантация, молекулярно-лучевая эпитаксия, доза насыщения, тонкая пленка, теллурид цинка

Ссылка для цитирования: Хужаниёзов Ж. Б., Умирзаков Б. Е., Ташмухамедова Д. А., Лобода В. В., Абдувайитов А. А. Влияние имплантации ионов Ar^+ и Cd^+ на состав и электронную структуру монокристаллического теллурида цинка // Научно-технические ведомости СПбГПУ. Физико-математические науки. 2026. Т. 19. № 2. С. 84–97. DOI: https://doi.org/10.18721/JPM.19208

Статья открытого доступа, распространяемая по лицензии CC BY-NC 4.0 (https://creativecommons.org/licenses/by-nc/4.0/)

Introduction

$A^{II}B^{VI}$ semiconductors such as cadmium and zinc tellurides (CdTe, ZnTe) have long served as model objects for fundamental research; however, their practical application remained relatively limited, being mainly confined to X-ray detectors and luminophores. Nevertheless, these compounds are characterized by high structural perfection and possess unique optical properties.

In recent years, $A^{II}B^{VI}$ compounds have attracted increasing attention as promising materials for efficient conversion of solar energy into electricity, owing to their high quantum yield in the green spectral region [1–5].

One of the factors hindering the widespread use of heterostructures based on CdTe and ZnTe is the significant mismatch in their lattice parameters. The resulting mechanical stresses at interfaces can lead to degradation and failure of the structures. The lattice mismatch also introduces

© Хужаниёзов Ж. Б., Умирзаков Б. Е., Ташмухамедова Д. А., Лобода В. В., Абдувайитов А. А., 2026. Издатель: Санкт-Петербургский политехнический университет Петра Великого.

uncertainties in the accurate determination of the band offset, reflected in a substantial scatter (up to ±10% of the average bandgap) in the published data on the valence band offset of CdTe/ZnTe heterostructures [6–9].

Studies on heterostructures based on binary semiconductors [10–18], in particular, the CdTe/ZnTe system with identical nominal thickness of the narrow-gap layer, demonstrate a significant discrepancy in the energy position and shape of the emission band. This points to a pronounced dependence of the actual structure of the thin layer on the specific growth conditions. For the CdTe/ZnTe system, this aspect is of particular importance in the context of developing CdTe quantum dots doped with a precisely controlled amount of Mn^{2+} magnetic ions [19].

Stresses arising during growth and their subsequent relaxation play a key role for heteroepitaxial structures. These processes have a decisive influence on the crystalline perfection of the structure, which, in turn, directly affects the electronic properties of the material and, consequently, the parameters of fabricated infrared detectors [20–28]. A wide range of optical [24] and X-ray diffraction [25, 26] methods are used for high-precision measurements of residual strains occurring in the bulk of the material, providing valuable information on the mechanical state of the structure.

Ref. [28] reports on an experimental study of weak strains in the near-surface regions of amorphous chromium (Cr) and mercury-cadmium telluride (HgCdTe) layers using an innovative null method. The study yielded quantitative data demonstrating the dependence of the second-harmonic amplitude on the magnitude of applied stresses. In addition, precision measurements of residual stresses in the surface layer of a multilayered HgCdTe/CdTe/ZnTe/GaAs structure grown by molecular beam epitaxy were performed, which made it possible to establish the parameters of the structure's stressed state.

The method of low-energy ion implantation has proven to be an effective tool for targeted modification of the composition, structure and properties of various materials [29–37], opening new prospects in materials science and surface engineering.

The present work reports on the surface modification of monocrystalline zinc telluride (ZnTe) films by implantation of argon Ar^+ and cadmium Cd^+ ions combined with thermal treatment.

The goal of this study is a detailed investigation of the mechanisms leading to changes in the elemental composition and electronic structure of zinc telluride films as a result of a complex treatment.

Experimental procedure

The film samples were studied using an ultra-high-vacuum system (Fig. 1) consisting of two functionally separated chambers.

Annealing, thermal oxidation and ion bombardment procedures were carried out in the first chamber; these procedures prepared the materials for further analysis.



Fig. 1. Experimental setup

The second chamber was used for detailed analysis of the composition, density of states of valence electrons, band structure, as well as emission and optical characteristics of the samples.

Polished and chemically etched monocrystalline ZnTe(111) samples and epitaxial *n*-type ZnTe/Si(111) films grown by magnetron sputtering were used for the study.

The experiments were performed under high vacuum (pressure down to 10^{-7} Pa) using a combination of spectroscopic methods: Auger electron spectroscopy (AES), ultraviolet photoelectron spectroscopy (UPS), optical absorption spectroscopy in the UV, IR and visible ranges, and elastic peak electron spectroscopy (EPES).

Depth profiles of atomic distributions were determined by AES combined with precision layer-by-layer sputtering of the surface with Ar^+ ions at an energy E_0 ranging from 2 to 3 keV. Prior to ion implantation,

the ZnTe samples were degassed by heating to $T = 900$ K for three hours. This process was combined with Ar^+ ion sputtering at a pressure of 10^{-7} Pa to remove surface contaminants.

After cleaning, the Auger peaks corresponding to carbon (C), sulfur (S) and oxygen (O) completely disappeared, indicating a high degree of surface purity. The concentrations of zinc (Zn) and tellurium (Te) atoms stabilized within the range of about 49–50 at.%, which indicated the restoration of the stoichiometric composition.

Cd^+ ions were implanted at an energy $E_0 = 3–1$ keV with a dose $D = 8 \cdot 10^{16}$ cm^{-2}; this value corresponded to the saturation dose, at which further increase in dose did not lead to significant changes in the material properties. The Cd^+ ions were generated by electron bombardment, which provided high precision control of the ion beam parameters.

Experimental results and discussion

Fig. 2 shows the change in the surface concentration of zinc in ZnTe under bombardment with Ar^+ ions at an energy $E_0 = 1$ keV at room temperature.

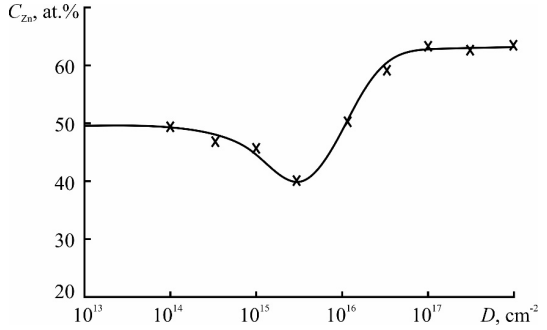


Fig. 2. Dependence of the surface zinc concentration in ZnTe/Si(111) film on the irradiation dose after bombardment with 1 keV Ar^+ ions at room temperature

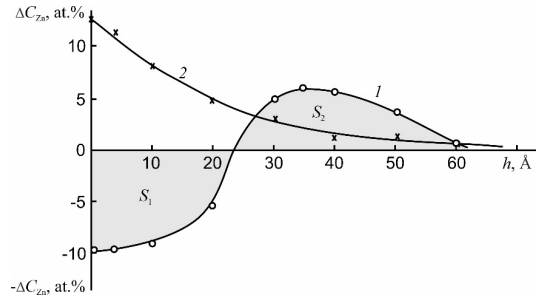


Fig. 3. Dependences of deviation ДΔC_{Zn} on depth of ZnTe/Si(111) film bombarded with 1 keV Ar^+ ions at doses D (cm^{-2}): $5 \cdot 10^{15}$ (curve *1*) and $6 \cdot 10^{16}$ (curve *2*)

It can be seen that the surface Zn concentration C_{Zn} remains practically unchanged up to a dose $D = 10 \cdot 2^{14}$ cm^{-2}, indicating the stability of the material surface at the initial stage of ion exposure. Then, a decrease in the Zn concentration by 7–8 at.% is observed in the dose range from $2 \cdot 10^{14}$ to $5 \cdot 10^{15}$ cm^{-2}. A further increase in the ion dose leads to an increase in C_{Zn}, reaching 65–66 at.% at $D = (6–4) \cdot 10^{16}$ cm^{-2}. After that, further irradiation causes stabilization of the zinc concentration, which then undergoes virtually no changes.

To comprehensively analyze the modification of the surface concentration of Zn and Te atoms during Ar^+ ion bombardment, the depth dependence of the deviation ΔC_{Zn} of Zn concentration from the stoichiometric composition was studied at two different irradiation doses: $5 \cdot 10^{15}$ and $6 \cdot 10^{16}$ cm^{-2} (Fig. 3).

It follows from the data in Fig. 3 that a decrease in the Zn concentration by 8–10 at.% is observed at a dose of $D = 5 \cdot 10^{15}$ cm^{-2} in the near-surface layers, remaining almost unchanged down to a depth $h = 5–6$ Å. An increase in ΔC_{Zn} to about 6 at.% is observed in the range $h = 10–40$ Å. With a further increase in depth, ΔC_{Zn} decreases monotonically, tending to zero at $h = 60–65$ Å, which indicates the restoration of the stoichiometric composition characteristic of ZnTe. The decrease in Zn concentration in the range $h = 0–20$ Å is presumably due to the diffusion of Zn atoms deeper into the target or (less likely) to the diffusion of Te atoms to the surface (taking into account the significant difference in the masses of Te and Zn atoms). It is evident that the areas S_1 and S_2 under curve *1* differ only slightly, which suggests that there is no appreciable evaporation of Zn (or Te) atoms. At higher bombardment doses ($D \geq 6 \cdot 10^{16}$ cm^{-2}, see curve *2* in Fig. 3), the value of ΔC_{Zn} in the near-surface layers increases to 10–12 at.%, then decreases monotonically with increasing h. At a depth of 50–60 Å, the value of ΔC_{Zn} is about 1–2 at.%, remaining practically unchanged at $h \geq 60$ Å.

In all probability, desorption of Te atoms from the surface layers occurs at high ion bombardment doses along with their diffusion to the surface, leading to metallization of the surface layers of the ZnTe film. In this case, the surface layers become completely disordered.

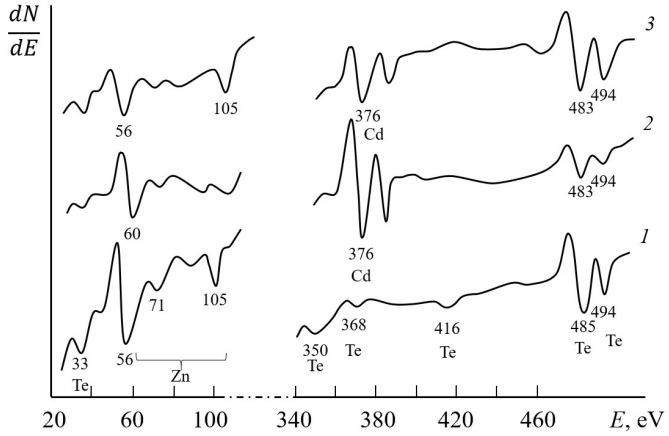


Fig. 4. Auger spectra of samples at different stages of the study:
as-grown ZnTe(111) sample (curve *1*); sample after implantation with Cd^+ (E_0 = 1 keV, $D_s = 8 \cdot 10^{16}$ cm^{-2}) (curve *2*); sample after ion implantation and annealing at T = 850 K for 40 min (curve *3*). The numbers correspond to the positions of the peaks (eV)

Fig. 4 shows the Auger spectra of ZnTe samples implanted with Cd^+ ions at an energy E_0 = 1 keV and a dose $D_s = 8 \cdot 10^{16}$ cm^{-2}, recorded before and after annealing at T = 850 K for 40 min. It is known that analysis of the shift and shape of low-energy peaks induced by the participation of valence electrons provides data on the formation of new compounds.

The atomic concentration C_x in the near-surface layers can be estimated from the intensities of the high-energy peaks using the following formula [38]:

$$C_x = \frac{I_x / S_x}{\sum_{i=1} \frac{I_i}{S_i}},$$

where I_i, I_x are the intensities of the Auger peaks, S_i, S_x are the Auger sensitivity factors.

The following Auger peaks were used to determine the atomic concentrations:

Zn: E = 994 eV; Te: E = 483 eV; Cd: E = 376 eV.

The characteristic Zn and Te peaks are clearly observed in the Auger spectrum of the unimplanted ZnTe film. Quantitative analysis of the spectra showed that the surface concentration of Zn was about 49 at.%, and that of Te about 51 at.%. Implantation of Cd^+ ions causes decomposition of the ZnTe compound with simultaneous incorporation of Cd atoms into the ZnTe lattice. Distinct Zn and Cd peaks are observed in the Auger spectrum after ion implantation, while the intensity of Te peaks decreases significantly, so that low-intensity peaks disappear completely, which indicates predominant desorption of Te atoms from the sample surface. The main low-energy peak (56 eV) characteristic of ZnTe shifts by 4 eV towards higher energies. This is because Cd^+ ion implantation induces decomposition of the original ZnTe sample and a sharp decrease in Te concentration; as a result, the peak energy approaches the value characteristic of pure Zn. Analysis of the high-energy peaks of the full Auger spectrum revealed that the surface concentrations of Cd, Zn and Te atoms were approximately 48, 40, and 12 at.%, respectively.

After annealing at 850 K for 40 min, the 60 eV peak shifts back towards lower energies. The concentrations of Cd and Zn atoms decrease to 23–25 at.%, while that of Te increases to 50–52 at.%, indicating the formation of a monocrystalline film with an approximate composition $Zn_{0.5}Cd_{0.5}Te$ (see curve *3* in Fig. 4).

The electronic structure of the surface layers, including the density of electronic states and band parameters, was studied by ultraviolet photoelectron spectroscopy (UPS) and optical absorption spectroscopy [39].

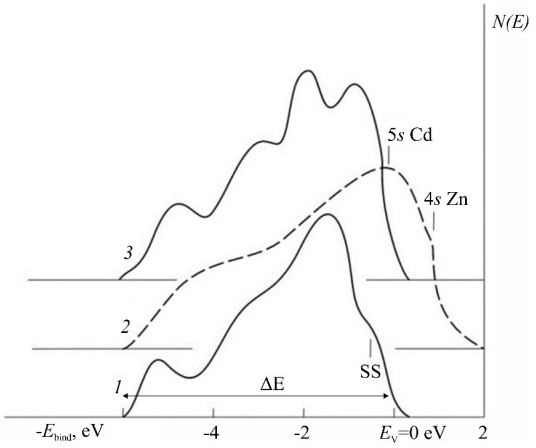


Fig. 5. UPS spectra recorded at different stages of the study: as-grown ZnTe(111) sample (curve *1*); sample after implantation with Cd^+ ions (E_0 = 1 keV, D_s = $8 \cdot 10^{16}$ cm^{-2}) (curve 2); sample after ion implantation and annealing at T = 850 K for 40 min (curve *3*); SS denotes surface states

Fig. 5 shows photoelectron spectra recorded at a photon energy $h\nu$ = 10.8 eV for a ZnTe sample implanted with Cd^+ ions at an energy E_0 = 1 keV and a dose $D = 8 \cdot 10^{16}$ cm^{-2}, before and after thermal annealing at T = 850 K.

Two well-defined peaks are clearly observed in the spectrum of pure ZnTe at binding energies of about −1.4 and −5.2 eV, as well as a characteristic feature at E_{SS} = −0.5 eV, presumably related to the existence of surface states. Detailed information on the possible mechanisms behind the formation of these peaks is given in Table 1.

Analysis of the data in Table 1 shows that the spectral peaks of pure ZnTe originate from the excitation of electrons from hybridized 4*s* Zn + 5*p* Te states and 5*s* Te states. Ion implantation leads to a shift of the leading edge of the spectrum towards higher energies, reaching about 1.8 eV. In addition, an increase in the spectral width (ΔE) is observed, the main peaks characteristic of ZnTe(111) disappear, and new peaks appear, which are likely associated with the formation of Zn, Cd inclusions and their compounds (see Table 1). In this case, the positions of the valence band top E_v and the Fermi level E_F coincide completely, indicating the metallic character of the ion-implanted layers. A characteristic spectral feature, accompanied by the appearance of four distinct peaks, is observed in the spectrum of the $Zn_{0.5}Cd_{0.5}Te$ film obtained after thermal annealing of the ion-implanted ZnTe at T = 850 K. A detailed interpretation of these peaks is also given in Table 1. Importantly, the position of the E_v level shifts towards lower energies by about 2 eV.

The bandgap width of the studied samples was estimated from the optical absorption (transmittance) spectra.

Table 1

Stages of UPS analysis of samples subjected to Cd^+ ion bombardment and annealing; interpretation of the results

Stage	Sample	UPS result	
		E_{bind}, eV	Peak formation mechanism
1. Initial	ZnTe (111)	–0.5	Surface state (SS)
		–1.4	4*s* Zn + 5*p* Te
		–5.2	5*s* Te
2. Implantation E_0 = 1 keV, $D_s = 8 \cdot 10^{16}$ cm^{-2}	ZnTe	+0.2	5*s* Cd
		+0.8	4*s* Zn
		–3.8	5*s* Te
3. Annealing at T = 850 K	$Zn_{0.5}Cd_{0.5}Te$/ZnTe	–0.3	Surface state (SS)
		–0.8	4*s* Zn + 5*p* Te
		–1.8	5*s* Cd + 5*p* Te
		–2.8	4*s* Zn + 5*p* Te
		–4.6	5*s* Te

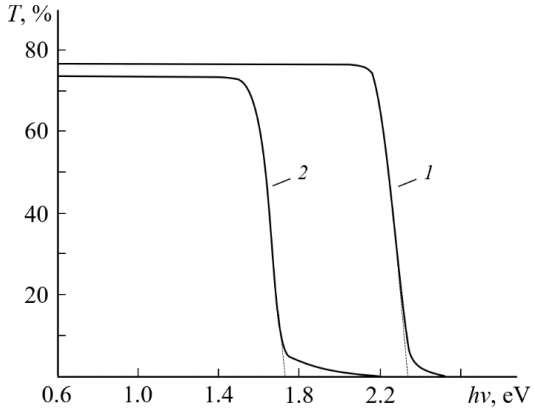


Fig. 6. Dependences of optical transmittance on photon energy for the as-grown ZnTe sample (curve *1*) and the final $Zn_{0.5}Cd_{0.5}Te$/ZnTe(111) film (curve *2*).
Film thickness was 30–35 Å, room temperature

Fig. 6 shows the dependences of the transmittance T_{ph} on the photon energy $h\nu$ for pure ZnTe(111) and for the $Zn_{0.5}Cd_{0.5}Te$/ZnTe(111) film obtained by post-implantation annealing at $T = 850$ K. Analysis of Fig. 6 shows that the transmittance of the pure ZnTe sample remains practically unchanged up to a photon energy of about 2.1 eV, indicating the absence of noticeable light absorption in this spectral region. A sharp drop in transmittance to zero is observed in the energy range $h\nu = 2.1$–2.3 eV, caused by intense light absorption. Extrapolation of this segment of the curve to the $h\nu$ axis allows approximately estimating the bandgap width E_g. Similarly, the E_g value for the $Zn_{0.5}Cd_{0.5}Te$ film was found to be approximately 1.75 eV. It should be noted that in the second case, the sharp decrease in T_{ph} begins already at about 1.7 eV, but complete absorption is reached only at about 2.2 eV. Apparently, ultra-thin films (less than 40 Å) exhibit some residual transparency even at $h\nu > E_g$, transmitting low-intensity light.

Table 2 presents the band and optical parameters derived from the photoelectron and optical absorption spectra for the initial and final samples (ZnTe and $Zn_{0.5}Cd_{0.5}Te$/ZnTe, respectively).

The energy of the valence band top E_v was determined as the difference between the photon energy and the width of the photoelectron spectrum:

$$E_v = h\nu - \Delta E.$$

The optical parameters of the samples were determined at a photon energy $h\nu = 1.2$ eV. Analyzing the data in Table 2, we find significant differences in the band and optical parameters of the $Zn_{0.5}Cd_{0.5}Te$ film and the ZnTe substrate. In particular, the bandgap width for the three-component film is about 1.75 eV, while for the substrate it is 2.35 eV. Subsequent studies revealed that the value of x in the $Zn_{1-x}Cd_x$ system reached 0.6 upon increasing the annealing temperature to 900 K, and grew to 0.8 at 950 K Upon a further increase in temperature in the range of 1000–1050 K, complete evaporation of cadmium atoms from the film occurred. Variation of the Cd^+ bombardment energy in the range from 1 to 10 keV will allow for controllable modifications in the thickness of the $Zn_{1-x}Cd_xTe$ film from 30–35 Å to 900–1000 Å, which opens up attractive prospects for precise tuning of material properties.

Table 2

Band and optical parameters of the films obtained from UPS and optical transmittance spectra

Experimental sample	Band energy parameters (eV)			Optical parameters at $h\nu = 1.2$ eV		
	E_v	E_g	X	R	T_{ph}	K
ZnTe	5.30	2.35	2.95	22	78	0
$Zn_{0.5}Cd_{0.5}Te$	5.35	1.75	3.6	26	74	

Notations: E_v is the energy of the valence band top, E_g is the bandgap width; χ is the electron affinity; R, T_{ph}, K are the reflectance, transmittance and absorptance, respectively; $h\nu$ is the photon energy.

Conclusion

For the first time, we comprehensively analyzed the effect of bombardment of the surface of zinc telluride (ZnTe) films with low-energy argon (Ar^+) and cadmium (Cd^+) ions on changes in the elemental composition and electronic structure of the near-surface layers.

It was found that irradiation with Ar^+ ions in the low-dose range ($D \leq 10 \cdot 5^{15}$ cm^{-2}) led to enrichment of the ZnTe surface with tellurium atoms, while a predominance of zinc atoms was observed with at higher doses ($D \geq 5 \cdot 10^{15}$ cm^{-2}); implantation of Cd^+ ions caused accumulation of Zn and Cd atoms on the ZnTe surface.

Thin films of the $Zn_{0.5}Cd_{0.5}Te$ solid solution with a uniform thickness in the range of 30–35 Å were formed by implanting Cd^+ ions into monocrystalline ZnTe followed by controlled annealing at 850 K.

Photoelectron spectroscopy and optical transmittance spectroscopy were used to obtain the distribution of the density of states of valence electrons, the energy band parameters and the optical characteristics of the grown $Zn_{0.5}Cd_{0.5}Te$ thin films. Two distinct maxima in the density of states were observed in the valence electron spectra of $Zn_{0.5}Cd_{0.5}Te$ at binding energies of −1.4 and −5.2 eV. These maxima correspond to specific features of the electron density distribution in the valence band of the material under study.

REFERENCES

1. **Iniewski K.,** CdTe and CdZnTe materials: Material properties and applications, Springer, Cham, Switzerland, 2024.

2. **Suthar D., Chuhadiya S., Sharma R., et al.,** An overview on the role of ZnTe as an efficient interface in CdTe thin film solar cells: A review, Mater. Adv. 3 (22) (2022) 8081–8107.

3. **Zhao Y., Jia Z., Lin Q.,** Optoelectronic properties and charge carrier dynamics of polycrystalline ZnTe thin films, J. Phys. Chem. Lett. 16 (24) (2025) 5979–5985.

4. **Yılmaz S., Başol B. M., Olğar M. A., et al.,** Comparative analysis of chloride-treated ZnTe films in photodetector devices, Mat. Sci. Semicond. Process. 198 (1 Nov) (2025) 109733.

5. **Zhang L., Liu C., Yang Q., et al.,** Growth and characterization of highly Nitrogen doped ZnTe films on GaAs (001) by molecular beam epitaxy, Mat. Sci. Semicond. Process. 29 (Jan) (2015) 351–356.

6. **Ergashov Y. S., Tashmukhamedova D. A., Djurabekova F. G., Umirzakov B. E.,** Effect of surface microroughness on the composition and electronic properties of CdTe/Mo(111) films, Bull. Russ. Acad. Sci., Phys. 80 (2) (2016) 138.

7. **Bagaev V. S., Zaytsev V. V., Kalinin V. V., et al.,** Excitonic luminescence of CdTe and $Cd_{0.87}Zn_{0.13}Te$ submonolayers in ZnTe films grown by molecular beam epitaxy, Solid State Commun. 88 (10) (1993) 777-780.

8. **Karczewski G., Maćkowski S., Kutrowski M., et al**., Photoluminescence study of CdTe/ZnTe self-assembled quantum dots, Appl. Phys. Lett. 74 (20) (1999) 3011–3013.

9. **Moger S. N., Mahesha M. G.,** Investigation on ZnTe/$Cd_xZn_{1-x}Te$ heterostructure for photodetector applications, Sens. Actuat. A-Phys. 315 (1 Nov) (2020) 112294.

10. **Hernández C. V.,** Introduction to Raman spectroscopy and its applications, Springer Cham, Switzerland, 2025.

11. **Kapitonov A. M., Woggon U., Kayser D., et al.,** Luminescence of epitaxial sub-monolayer CdSe nanostructures in ZnSe, J. Lumin. 112 (1–4) (2005) 177–180.

12. **Kim J. S., Kim H. M., Park H. L., Choi J. C.,** Growth and optical characterization of single quantum well structure of submonolayer ZnS/ZnTe, Solid State Commun. 137 (3) (2006) 115–119.

13. **Umirzakov B. E., Tashmukhamedova D. A., Boltaev E. U., Dzhurakhalov A. A., O**btaining of epitaxial films of metal silicides by ion implantation and molecular beam epitaxy, Mater. Sci. Eng. B. 101 (1–3) (2003) 124–127.

14. **Kryshtab T., Andraca J. A., Borkovska L. V., et al.,** Effect of CdTe monolayer insertion on CdZnTe/ZnTe quantum well characteristics, Microelectron. J. 39 (3–4) (2008) 418–422.

15. **Fan J., Ouyang L., Liu X., et al,** Growth and material properties of ZnTe on GaAs, InP, InAs and GaSb (001) substrates for electronic and optoelectronic device applications. J. Cryst. Growth. 323 (1) (2011) 127–131.

16. **Umirzakov B. E., Donaev S. B.,** On the creation of ordered nuclei by ion bombardment for obtaining nanoscale Si structures on the surface of CaF_2 films, J. Surf. Invest.: X-Ray, Synchrotron Neutron Tech. 11 (4) (2017) 746–748.

17. **Agekyan V., Chukeev M.**, **Karczewski G., et al.,** Exciton spectra and energy transfer in CdTe/ZnTe double quantum wells grown by atomic-layer epitaxy, Semiconductors. 53 (16) (2019) 2060–2063.

18. **Abduvayitov A. A., Boltaev Kh. Kh., Umirzakov B. E., et al.,** Analyzing the change in the composition of a CdTe surface upon implanting ions O^{2+} and subsequent annealing. Bull. Russ. Acad. Sci.: Phys. 88 (11) (2024) 1850–1854.

19. **Sawicki K., Malinowski F. K., Galkowski K., et al.,** *Single-color*, *in situ* photolithography marking of individual CdTe/ZnTe quantum dots containing a single Mn^{2+} ion, Appl. Phys. Lett. 106 (1) (2015) 012101.

20. **Samin A. J., Petrosky J. C.,** An analysis of point defects in ZnTe using density functional theory calculations, J. Alloys Compnd. 921 (15 Nov) (2022) 166017.

21. **Ryzhkov M. S., Kozlov D. A., Khudaiberdiev D. A., et al.,** Interference transport in a two-dimensional topological insulator in a CdHgTe quantum well, JETP Letters. 117 (1) (2023) 44–47.

22. **Shcherbakov I. P., Dunaev A. A., Eron'ko S. B., Chmel' A. E.,** Spectroscopic investigation of impurity and intrinsic distortions of the crystallite structure in ZnTe ceramics during mechanical treatment, Tech. Phys. Lett. 47 (2) (2021) 181–183.

23. **Tarasov A. S., Mikhailov N. N., Dvoretsky S. A., et al.,** Preparation of atomically clean and structurally ordered surfaces of epitaxial CdTe films for subsequent epitaxy, Semiconductors. 55 (1) (2021) S62–S66.

24. **Martinez A. M., Giudici P., Trigubo A. B., et al.,** Crystalline quality, composition homogeneity, tellurium precipitates/inclusions concentration, optical transmission, and energy band gap of Bridgman grown single-crystalline $Cd_{1-x}Zn_xTe$ ($0 \le x \le 0.1$), Materials. 14 (15) (2021) 4207.

25. **Dvoretsky S. A., Stupak M. F., Mikhailov N. N., et al.,** Study of the crystalline state of MBE (013)HgCdTe/CdTe/ZnTe/GaAs heterostructure layers by the second harmonic generation method, Semiconductors. 56 (8) (2022) 562–569.

26. **Stupak M. F., Mikhailov N. N., Dvoretskii S. A., et al.,** Possibilities of characterizing the crystal parameters of $Cd_xHg_{1-x}Te$ structures on GaAs substrates by the method of generation of the probe-radiation second harmonic in reflection geometry, Physics of the Solid State. 62 (2) (2020) 252–259.

27**. Ushakov V. V., Klevkov Yu. V.,** Microphotoluminescence of undoped single-crystal zinc telluride produced by nonequilibrium vapor-phase growth techniques, Semiconductors. 39 (9) (2005) 993–997.

28. **Stupak M. F., Dvoretsky S. A., Mikhailov N. N., et al.,** Measurement of local stresses in the surface layers of multilayer structures by the null method using phase matching, Tech. Phys. Lett. 50 (1) (2024) 32–35.

29. **Chemam R., Bouabellou A., Grob J. J., et al.,** ZnTe formed by ion implantation in a SiO_2 layer on silicon, Nucl. Instrum. Methods Phys. Res. B. 216 (Febr) (2004) 116–120.

30. **Umirzakov B. E., Tashmukhamedova D. A., Ruzibaeva M. K., et al.,** Investigation of change of the composition and structure of the CaF_2/Si films surface at the low-energy bombardment, Nucl. Instrum. Methods Phys. Res. B. 326 (1 May) (2014) 322–325.

31. **Isakhanov Z. A., Mukhtarov Z. E., Umirzakov B. E., Ruzibaeva M. K.,** Optimum ion implantation and annealing conditions for stimulating secondary negative ion emission, Tech. Phys. 56 (4) (2011) 546–549.

32. **Hassan A. M., Diab F., Kotp E. F., et al.,** Implantation of Cu onto ZnTe thin film using plasma focus device for optoelectronic applications, Opt. Mater. 117 (Jul) (2021) 111182.

33. **Abduvayitov A. A., Tashmukhamedova D. A., Umirzakov B. E., et al.,** Effect of argon ion bombardment on the composition, electronic structure and physical properties of cadmium fluoride, St. Petersburg State Polytechnical University Journal. Physics and Mathematics. 17 (3) (2024) 87–96.

34. **Tashmukhamedova D. A.,** Study of composition and electronic structure of $CoSi_2$/Si interface, Bull. Russ. Acad. Sci., Phys. 70 (8) (2006) 1409–1411.

35. **Mahmood W., Awan S.U., Din A.U., et al.,** Pronounced impact of *p*-type carriers and reduction of bandgap in semiconducting ZnTe thin films by Cu doping for intermediate buffer layer in heterojunction solar cells, Materials. 12 (8) (2019) 1359.

36. **Donaev S. B., Tashatov A. K., Umirzakov B. E.,** Effect of Ar+-ion bombardment on the composition and structure of the surface of $CoSi_2$/Si(111) nanofilms, J. Surf. Invest.: X-Ray, Synchrotron Neutron Tech. 9 (2) (2015) 406–409.

37. **Abduvayitov A. A., Boltaev Kh. Kh., Rozikov G. A.,** Study of the composition of uncontrolled impurities and the profiles of their distribution at the Ni–CdS interface, J. Surf. Invest.: X-Ray, Synchrotron Neutron Tech. 16 (5) (2022) 860–863.

38. **Ghosh K., Ghorai G., Sahoo P. K.,** Cathodoluminescence and structural properties of ZnTe nanocrystals synthesized from Te/ZnO thin films, J. Alloys Compnd. 960 (15 Oct) (2023) 170655.

39. **Davis L. E., MacDonald N.C., Palmberg P.W., et al.,** Handbook of Auger electron spectroscopy, 2-nd ed., Physical Electronics Industry Inc., Minnesota (USA), 1976.

40. **Boltaev Kh. Kh., Tashmukhamedova D. A., Umirzakov B. E.,** Structure and electronic properties of nanoscale phases and nanofilms of metal silicides produced by ion implantation in combination with annealing, J. Surf. Invest.: X-ray, Synchrotron Neutron Tech. 8 (2) (2014) 326–331.

СПИСОК ЛИТЕРАТУРЫ

1. **Iniewski K.** CdTe and CdZnTe materials: Material properties and applications. Cham, Switzerland: Springer, 2024. 259 p.

2. **Suthar D., Chuhadiya S., Sharma R., Himanshu, Dhaka M. S.** An overview on the role of ZnTe as an efficient interface in CdTe thin film solar cells: A review // Materials Advances. 2022. Vol. 3. No. 22. Pp. 8081–8107.

3. **Zhao Y., Jia Z., Lin Q.** Optoelectronic properties and charge carrier dynamics of polycrystalline ZnTe thin films // The Journal of Physical Chemistry Letters. 2025. Vol. 16. No. 24. Pp. 5979–5985.

4. **Yılmaz S., Başol B. M., Olğar M. A., Bayazıt T., Küzükömeroğlu T., Bacaksız E.** Comparative analysis of chloride-treated ZnTe films in photodetector devices // Materials Science in Semiconductor Processing, 2025. Vol. 198. 1 November. P. 109733.

5. **Zhang L., Liu C., Yang Q., Cui L., Zeng Y.** Growth and characterization of highly nitrogen doped ZnTe films on GaAs (001) by molecular beam epitaxy // Materials Science in Semiconductor Processing. 2015. Vol. 29. January. Pp. 351–356.

6. **Эргашов Е. С., Ташмухамедова Д. А., Джурабекова Ф. Г., Умирзаков Б. Е.** Влияние микронеоднородностей поверхности на состав и электронные свойства пленок CdTe/Mo(111) // Известия Российской академии наук. Серия физическая. 2016. Т. 80. № 2. Ст. 157.

7. **Bagaev V. S., Zaytsev V. V., Kalinin V. V., Oktyabrskii S. R., Plotnikov A. F.** Excitonic luminescence of CdTe and $Cd_{0.87}Zn_{0.13}Te$ submonolayers in ZnTe films grown by molecular beam epitaxy // Solid State Communications. 1993. Vol. 88. No. 10. Pp. 777–780.

8. **Karczewski G., Maćkowski S., Kutrowski M., Wojtowicz T., Kossut J.** Photoluminescence study of CdTe/ZnTe self-assembled quantum dots // Applied Physics Letters. 1999. Vol. 74. No. 20. Pp. 3011–3013.

9. **Moger S. N., Mahesha M. G.** Investigation on ZnTe/$Cd_xZn_{1-x}Te$ heterostructure for photodetector applications // Sensors and Actuators A: Physical. 2020. Vol. 315. 1 November. P. 112294.

10. **Hernández C. V.** Introduction to Raman spectroscopy and its applications. Cham, Switzerland: Springer, 2025. 244 p.

11. **Kapitonov A. M., Woggon U., Kayser D., Hommel D., Itoh T.** Luminescence of epitaxial sub-monolayer CdSe nanostructures in ZnSe // Journal of Luminescence. 2005. Vol. 112. No. 1–4. Pp. 177–180.

12. **Kim J. S., Kim H. M., Park H. L., Choi J. C.** Growth and optical characterization of single quantum well structure of submonolayer ZnS/ZnTe // Solid State Communications. 2006. Vol. 137. No. 3. Pp. 115–119.

13. **Umirzakov B. E., Tashmukhamedova D. A., Boltaev E. U., Dzhurakhalov A. A. O**btaining of epitaxial films of metal silicides by ion implantation and molecular beam epitaxy // Materials Science and Engineering: B –Solid State Materials for Advanced Technology. 2003. Vol. 101. No. 1–3. Pp. 124–127.

14**. Kryshtab T., Andraca J. A., Borkovska L. V., Korsunska N. O., Venger Ye. F., Sadofyev Yu. G**. Effect of CdTe monolayer insertion on CdZnTe/ZnTe quantum well characteristics // Microelectronics Journal. 2008. Vol. 39. No. 3–4. Pp. 418–422.

15. **Fan J., Ouyang L., Liu X., Ding D., Furdyna J. K., Smith D. J., Zhang Y. H.** Growth and material properties of ZnTe on GaAs, InP, InAs and GaSb (001) substrates for electronic and optoelectronic device applications // Journal of Crystal Growth. 2011. Vol. 323. No. 1. Pp. 127–131.

16. **Умирзаков Б. Е., Донаев С. Б.** Создание ионной бомбардировкой упорядоченных зародышей для получения наноразмерных структур Si на поверхности пленок CaF_2 // Поверхность. Рентгеновские, синхротронные и нейтронные исследования. 2017. № 7. С. 70–73.

17. **Agekyan V., Chukeev M., Karczewski G., Serov A., Filosofov N., Reznitski A.** Exciton spectra and energy transfer in CdTe/ZnTe double quantum wells grown by atomic-layer epitaxy // Semiconductors. 2019. Vol. 53. No. 16. Pp. 2060–2063.

18. **Абдуваитов А. А., Болтаев Х. Х., Умирзаков Б. Е., Ташмухамедова Д. А., Абдурахманов Г.** Изучение изменения состава поверхности CdTe при имплантации ионов O^{2+} и последующего отжига // Известия Российской академии наук. Серия физическая. 2024. Т. 88. № 11. С. 1830–1834.

19. **Sawicki K., Malinowski F. K., Galkowski K., Jakubczyk T., Kossacki P., Pacuski W., Suffczinski J.** Single-color, *in situ* photolithography marking of individual CdTe/ZnTe quantum dots containing a single Mn^{2+} ion // Applied Physics Letters. 2015. Vol. 106. No. 1. P. 012101.

20. **Samin A. J., Petrosky J. C.** An analysis of point defects in ZnTe using density functional theory calculations // Journal of Alloys and Compounds. 2022. Vol. 921. 15 November. P. 166017.

21. **Рыжков М. С., Козлов Д. А., Худайбердиев Д. А., Квон З. Д., Михайлов Н. Н.** Интерференционный транспорт в двумерном топологическом изоляторе в CdHgTe квантовой яме // Письма в ЖЭТФ. 2023. Т. 117. № 1–2 (1). С. 50–54.

22. **Щербаков И. П., Дунаев А. А., Еронько С. Б., Чмель А. Е.** Спектроскопическое исследование примесных и собственных нарушений строения кристаллитов в керамике ZnTe при механической обработке // Письма в ЖТФ. Т. 47. № 4. С. 26–28.

23. **Тарасов А. С., Михайлов Н. Н., Дворецкий С. А., Менщиков Р. В., Ужаков И. Н., Кожухов А. С., Федосенко Е. В., Терещенко О. Е.** Получение атомарно-чистых и структурно-упорядоченных поверхностей эпитаксиальных пленок CdTe для последующей эпитаксии // Физика и техника полупроводников. 2021. Т. 55. № 9. С. 748–753.

24. **Martinez A. M., Giudici P., Trigubo A. B., D'Elia R., Heredia E., Ramelli R., Gonzalez R., Aza F., Gilabert U.** Crystalline quality, composition homogeneity, tellurium precipitates/inclusions concentration, optical transmission, and energy band gap of Bridgman grown single-crystalline $Cd_{1-x}Zn_xTe$ ($0 \le x \le 0.1$) // Materials. 2021. Vol. 14. No. 15. P. 4207.

25. **Дворецкий С. А., Ступак М Ф., Михайлов Н. Н., Макаров С. Н., Елесин А. Г., Верхогляд А. Г.** Исследование кристаллического состояния слоев молекулярно-лучевой эпитаксии гетероструктур (013)HgCdTe/CdTe/ZnTe/GaAs методом генерации второй гармоники // Физика и техника полупроводников. 2022. Т. 8 № .56. С. 787–780.

26. **Ступак М Ф., Михайлов Н. Н., Дворецкий С. А., Якушев М. В., Икусов Д. Г., Макаров С. Н., Елесин А. Г., Верхогляд А. Г.** Возможности характеризации кристаллических параметров структур $Cd_xHg_{1-x}Te$ на подложке из GaAs методом генерации на отражение второй гармоники зондирующего излучения // Физика твердого тала. 2020. Т. 62. № 2. С. 252–259.

27. **Ушаков В. В., Клевков Ю. В.** Микрофотолюминесценция нелегированного монокристаллического теллурида цинка, полученного неравновесными парофазными методами // Физика и техника полупроводников. 2005. Т. 39. № 9. С. 1029–1033.

28. **Ступак М Ф., Дворецкий С. А., Михайлов Н. Н., Макаров С. Н., Елесин А. Г.** Измерение локальных напряжений в поверхностных слоях многослойных структур нуль-методом с использованием фазового синхронизма // Письма в Журнал технической физики. 2024. Т. 50. № 1. С. 32–35.

29. **Chemam R., Bouabellou A., Grob J. J., Muller D., Schmerber G.** ZnTe nanoparticles formed by ion implantation in a SiO_2 layer on silicon // Nuclear Instruments and Methods in Physics Research B: Beam Interactions with Materials and Atoms. 2004. Vol. 216. February. Pp. 116–120.

30. **Umirzakov B. E., Tashmukhamedova D. A., Ruzibaeva M. K., Djurabekova F. G., Danaev S. B.** Investigation of change of the composition and structure of the CaF_2/Si films surface at the low-energy bombardment // Nuclear Instruments and Methods in Physics Research B: Beam Interactions with Materials and Atoms. 2014. Vol. 326. 1 May. Pp. 322–325.

31. **Исаханов З. А., Мухтаров З. Э., Умирзаков Б. Е., Рузибаева М. К.** Оптимальные режимы ионной имплантации и отжига для стимулирования вторичной отрицательной ионной эмиссии // Журнал технической физики. 2011. Т. 8. № 4. С. 117–120.

32. **Hassan A. M., Diab F., Kotp E. F., Al-Kashef G., Shaaban E. R., Metawa A. E.** Implantation of Cu onto ZnTe thin film using plasma focus device for optoelectronic applications // Optical Materials. 2021. Vol. 117. July. P. 111182.

33. **Abduvayitov A. A., Tashmukhamedova D. A., Umirzakov B. E., Khujaniyozov J. B., Bekpulatov I. R., Loboda V. V.** Effect of argon ion bombardment on the composition, electronic structure and physical properties of cadmium fluoride // St. Petersburg State Polytechnical University Journal. Physics and Mathematics. 2024. Vol. 17. No. 3. Pp. 87–96.

34. **Ташмухамедова Д. А.** Исследование состава и электронной структуры границы раздела $CoSi_2$/Si // Известия Российской академии наук. Серия физическая. 2006. Т. 70. № 8. С. 1228–1230.

35. **Mahmood W., Awan S.U., Din A.U., et al.** Pronounced impact of *p*-type carriers and reduction of bandgap in semiconducting ZnTe thin films by Cu doping for intermediate buffer layer in hetero-junction solar cells // Materials. 2019. Vol. 12. No. 8. P. 1359.

36. **Донаев С. Б., Ташатов А. К., Умирзаков Б. Е.** Влияние бомбардировки ионами Ar^+ на состав и структуру поверхности нанопленок $CoSi_2$/Si(111) // Поверхность. Рентгеновские, синхротронные и нейтронные исследования. 2015. № 4. С. 95–98.

37. **Абдувайитов А. А., Болтаев Х. Х., Розиков Г. А.** Изучение состава неконтролируемых примесей и профиля их распределения на границе раздела Ni–CdS // Поверхность. Рентгеновские, синхротронные и нейтронные исследования. 2022. № 10. С. 48–51.

38. **Ghosh K., Ghorai G., Sahoo P. K.** Cathodoluminescence and structural properties of ZnTe nanocrystals synthesized from Te/ZnO thin films // Journal of Alloys and Compounds. 2023. Vol. 960. 15 October. P. 170655.

39. **Davis L. E., MacDonald N.C., Palmberg P.W., Riach G.E., Weber R.E.** Handbook of Auger electron spectroscopy. Second edition. Minnesota (USA): Physical Electronics Industry Inc., 1976. 252 p.

40. **Болтаев Х. Х., Ташмухамедова Д. А., Умирзаков Б. Е.** Состав и электронные свойства наноразмерных фаз и нанопленок силицидов металлов, созданных методом ионной имплантации в сочетании с отжигом // Поверхность. Рентгеновские, синхротронные и нейтронные исследования. 2014. № 4. С. 24–29.

THE AUTHORS

KHUJANIYOZOV Jumanazar B.
Tashkent State Technical University Named after Islam Karimov
2 Universitet St., Almazar, Tashkent, 100095, Republic of Uzbekistan
KhujaniyozovJB@mail.ru
ORCID: 0000-0001-6067-8196

UMIRZAKOV Baltokhodja E.
Tashkent State Technical University Named after Islam Karimov
2 Universitet St., Almazar, Tashkent, 100095, Republic of Uzbekistan
be.umirzakov@gmail.com
ORCID: 0000-0002-9815-2111

TASHMUKHAMEDOVA Dilnoza A.
Tashkent State Technical University Named after Islam Karimov
2 Universitet St., Almazar, Tashkent, 100095, Republic of Uzbekistan
ftmet@mail.ru
ORCID: 0000-0001-5813-7518

LOBODA Vera V.
Peter the Great St. Petersburg Polytechnic University
29 Politechnicheskaya St., St. Petersburg, 195251, Russia
vera_loboda@mail.ru
ORCID: 0000-0003-3103-7060

ABDUVAYITOV Akbarjon A.
Tashkent State Technical University Named after Islam Karimov
2 Universitet St., Almazar, Tashkent, 100095, Republic of Uzbekistan
akbarjon.abduvayitov@gmail.com
ORCID: 0000-0002-5732-6103

СВЕДЕНИЯ ОБ АВТОРАХ

ХУЖАНИЁЗОВ Жуманазар Бобокулович – *кандидат физико-математических наук, доцент кафедры общей физики Ташкентского государственного технического университета имени Ислама Каримова.*
2100095, *Республика* Узбекистан, г. Ташкент, Университетская ул., 2
KhujaniyozovJB@mail.ru
ORCID: 0000-0001-6067-8196

УМИРЗАКОВ Балтоходжа Ерматович – *доктор физико-математических наук, профессор кафедры общей физики Ташкентского государственного технического университета имени Ислама Каримова.*
2100095, Республика Узбекистан, г. Ташкент, Университетская ул., 2
be.umirzakov@gmail.com
ORCID: 0000-0002-9815-2111

ТАШМУХАМЕДОВА Дилноза Артикбаевна – *доктор физико- математических наук, профессор кафедры технологий производства электронных аппаратов Ташкентского государственного технического университета имени Ислама Каримова.*
2100095, Республика Узбекистан, г. Ташкент, Университетская ул., 2
ftmet@mail.ru
ORCID: 0000-0001-5813-7518

ЛОБОДА Вера Владимировна – *кандидат физико-математических наук, директор Высшей школы электроники и микросистемной техники Санкт-Петербургского политехнического университета Петра Великого.*
195251, Россия, г. Санкт-Петербург, Политехническая ул., 29
vera_loboda@mail.ru
ORCID: 0000-0003-3103-7060

АБДУВАЙИТОВ Акбаржон Абдумаджитович – *доктор физико-математических наук, профессор кафедры общей физики Ташкентского государственного технического университета имени Ислама Каримова.*
2100095, Республика Узбекистан, г. Ташкент, Университетская ул., 2
akbarjon.abduvayitov@gmail.com
ORCID: 0000-0002-5732-6103

Received 14.01.2026. Approved after reviewing 12.02.2026. Accepted 13.02.2026.
Статья поступила в редакцию 14.01.2026. Одобрена после рецензирования 12.02.2026. Принята 13.02.2026.

© Peter the Great St. Petersburg Polytechnic University, 2026

Original article
DOI: https://doi.org/10.18721/JPM.19209

RADIATION DEFECT FORMATION DURING SEQUENTIAL ION BOMBARDMENT OF ALPHA-GALLIUM OXIDE

A. I. Klevtsov[1,2]✉, *P. A. Karaseov*[1], *A. I. Titov*[1]

[1] Peter the Great St. Petersburg Polytechnic University, St. Petersburg, Russia;

[2] Joint-Stock Company "Research and Production Enterprise «ELAR»", St. Petersburg, Russia

✉ klevtsovanton@rambler.ru

Abstract. This paper presents the results of a study of radiation damage accumulation in α-Ga_2O_3 under sequential bombardment with fluorine and phosphorus ions with varying energies of the keV range. A significant effect of the ion irradiation sequence on both the number and depth distribution profile of stable defects was established. The physical nature of this noncommutativity is discussed.

Keywords: gallium oxide, ion implantation, sequential irradiation, radiation defects, Rutherford backscattering

Citation: Klevtsov A. I., Karaseov P. A., Titov A. I., Radiation defect formation during sequential ion bombardment of alpha-gallium oxide, St. Petersburg State Polytechnical University Journal. Physics and Mathematics. 19 (2) (2026) 98–106. DOI: https://doi.org/10.18721/JPM.19209

This is an open access article under the CC BY-NC 4.0 license (https://creativecommons.org/licenses/by-nc/4.0/)

Научная статья
УДК 539.1.043
DOI: https://doi.org/10.18721/JPM.19209

ОБРАЗОВАНИЕ УСТОЙЧИВЫХ РАДИАЦИОННЫХ ПОВРЕЖДЕНИЙ ПРИ ПОСЛЕДОВАТЕЛЬНОЙ ИОННОЙ БОМБАРДИРОВКЕ АЛЬФА-ОКСИДА ГАЛЛИЯ

А. И. Клевцов[1,2]✉, *П. А. Карасев*[1], *А. И. Титов*[1]

[1] Санкт-Петербургский политехнический университет Петра Великого, Санкт-Петербург, Россия;

[2] Акционерное общество «Научно-производственное предприятие «ЭЛАР»», Санкт-Петербург, Россия

✉ klevtsovanton@rambler.ru

Аннотация. В работе представлены результаты исследования накопления радиационных повреждений в α-Ga_2O_3 при последовательной бомбардировке ионами фтора и фосфора с различной энергией кэВ-диапазона. Установлено заметное влияние последовательности ионного облучения как на количество, так и профиль распределения устойчивых дефектов по глубине. Обсуждается физическая природа подобной некоммутативности.

Ключевые слова: оксид галлия, ионная имплантация, последовательное облучение, радиационный дефект, резерфордовское обратное рассеяние

© Klevtsov A. I., Karaseov P. A., Titov A. I., 2026. Published by Peter the Great St. Petersburg Polytechnic University.

Ссылка для цитирования: Клевцов А. И., Карасев П. А., Титов А. И. Образование устойчивых радиационных повреждений при последовательной ионной бомбардировке альфа-оксида галлия // Научно-технические ведомости СПбГПУ. Физико-математические науки. 2026. Т. 2 № .19. С.98 –106. DOI: https://doi.org/10.18721/JPM.19209

Статья открытого доступа, распространяемая по лицензии CC BY-NC 4.0 (https://creativecommons.org/licenses/by-nc/4.0/)

Introduction

Ion implantation is a key process in modern semiconductor technology for selectively modifying material properties. It is well known that irradiation of semiconductors with accelerated ions always produces stable damage to the crystal lattice [1]. The extent of this radiation damage depends on several parameters, including ion mass and energy, flux density, temperature, and target composition [2, 3].

Sequential bombardment with ions of different energies and/or different chemical elements is widely used for fabricating semiconductor devices. A common example of this approach is forming a required depth distribution of dopant atoms [4]. Even though this approach is widespread, the mechanisms that determine the final degree of structural disorder in the target under sequential bombardment remain poorly understood for many semiconductors. In fact, they are virtually unexplored for such promising materials as gallium oxide.

Furthermore, it is known from the literature that defect accumulation under sequential bombardment with ions of different energies and/or types can be both non-additive and non-commutative [5–7]. Non-additivity means that the final damage profile is not simply the sum of the profiles produced by each individual irradiation with its energy and dose. Non-commutativity means that the final damage distribution can depend dramatically on the sequence in which irradiation is applied (see, e.g., data for silicon [5, 6] and gallium nitride [7]). Moreover, the second irradiation can even reduce the damage level introduced by the first implantation for certain ion combinations and bombardment sequences [8–14].

Wide-bandgap oxide semiconductors are attracting increasing attention for power electronics and optoelectronics, offering new opportunities but also calling for a deeper understanding of their radiation resistance and defect formation under accelerated ion implantation.

One of the most promising representatives of this family is gallium oxide [15–19], which exists in several polymorphic modifications [15]. The monoclinic β-phase of gallium oxide (β-Ga_2O_3), with a bandgap of about 4.8 eV, is already actively studied and introduced in the fabrication of Schottky diodes [20] and field-effect transistors [21]. The metastable rhombohedral α-phase of gallium oxide (α-Ga_2O_3) with a corundum structure has unique properties, such as

a large bandgap (up to ~5.3 eV),

and a high critical breakdown field (up to ~8 MV/cm);

moreover, it can be grown epitaxially on relatively inexpensive sapphire substrates [22, 23].

Practical devices based on α-Ga_2O_3 require reliable methods for local doping and isolation; ion implantation is the primary technique for this purpose. Thus, to lay the foundations for ion-beam modification of α-Ga_2O_3, the mechanisms of radiation defect accumulation and annealing in this material must be understood, in particular under sequential irradiation. However, while the formation of structural disorder and radiation resistance of β-Ga_2O_3 have been studied actively in recent years [15–22, 24], data for α-Ga_2O_3 remain limited [25–27], and studies of sequential bombardment with different ion types and energies were virtually absent until recently [28].

In this work, we present the first study of radiation damage accumulation in α-Ga_2O_3 under sequential bombardment with light fluorine (F^+) and phosphorus (P^+) ions at keV energies typical of industrial applications.

© Клевцов А. И., Карасев П. А., Титов А. И., 2026. Издатель: Санкт-Петербургский политехнический университет Петра Великого.

Experimental procedure

We studied epitaxial α-Ga_2O_3 layers with a corundum structure, about 2 μm thick and with (0001) orientation, grown on the *c*-plane of a sapphire substrate by hydride vapour-phase epitaxy (HVPE) at Perfect Crystals LLC (St. Petersburg) [29]. The samples were irradiated with fluorine and phosphorus ions at room temperature using a 500 kV ion implanter (HVEE-500) at Research and Production Enterprise ELAR JSC (St. Petersburg). Irradiation was performed at an angle of 7° with respect to the [0001] crystallographic direction to minimize channeling effects in the crystal.

To ensure a valid comparison of the experimental data, radiation damage was evaluated at equal displacements per atom (DPA) generated in the target. The ion doses Φ_{DPA} were determined in the binary collision approximation as the ratio of the vacancy concentration at the maximum of the elastic energy loss profile (n_v) for a given ion fluence, calculated using the TRIM code [30], to the atomic concentration of α-Ga_2O_3 ($n_{at} = 1.03 \cdot 10^{23}$ atoms/cm^3), so that $\Phi_{DPA} = (n_v \cdot \Phi)/n_{at}$, where Φ is the fluence in cm^{-2}.

The ion flux density, defined as $F_{DPA} = d\Phi_{DPA}/dt$, was also kept constant in units of DPA/s. All irradiation parameters are given in the table.

Table

Parameters of ion irradiation used

Ion	Energy		R_p	R_{pd}	1 DPA	Ion current density		
	keV	keV/u	nm	nm	10^{14} cm^{-2}	μA/cm^2	10^{11} cm$^{-2}\cdot$s^{-1}	10^{-3} DPA/s
F^+	25	1.3	30	17	10.61	0.41	25.4	2.4
	50	2.6	55	36	12.15	0.47	29.2	
	60	3.0	74	48	12.72	0.49	30.6	
P^+	40	1.3	30	17	6.28	0.24	15.1	
	80	2.6	55	36	6.48	0.25	15.6	

Notations: R_p is the projected range of impurity ions (position of the maximum of the implanted impurity concentration); R_{pd} is the maximum of the primary defect generation function; DPA is the number of displacements per atom.

Note. Singly charged positive ions were used in all cases. The dose was 1.5 DPA in all cases.

The degree of disorder in the crystal structure of the samples after irradiation was measured by Rutherford backscattering spectrometry in channeling mode (RBS/C). The measurements used a probing beam of 0.7 MeV He^{++} ions along the [0001] crystallographic direction. The scattered particle detector was positioned at 170° relative to the incident beam direction.

Experimental results and discussion

Fig. 1 shows the generation functions of primary point defects and the corresponding elastic energy losses (solid lines), calculated with TRIM [30]. The values of the maxima of the implanted impurity concentration profile R_p and of the primary defect generation function R_{pd} are also summarized in the table. The ion energies were chosen so that the primary point defect distributions for F^+ (25 keV) and P^+ (40 keV) ions, as well as for F^+ (50 keV) and P^+ (80 keV) ions, were similar to each other (see Fig. 1). The ion energy for the second (high-energy) irradiation was chosen so that the maximum of the defect generation function was located at a depth corresponding to the position of defects formed in the bulk during the first (low-energy) irradiation.

Fig. 2 shows experimental RBS/C spectra for single irradiation with 25 and 50 keV fluorine ions at a dose of 1.5 DPA. The spectra represent the number of detected backscattered helium ions as a function of the channel number of the multichannel analyzer. In both cases, two maxima are observed in the spectra: one in the bulk of the sample, the bulk defect peak (BDP); the other in the surface region, the surface defect peak (SDP), associated with the formation of an amorphous surface layer due to diffusion of primary point defects from the bulk to the surface owing to their mobility [25]. For 25 keV fluorine ions, the BDP is located in the region of channel 246,

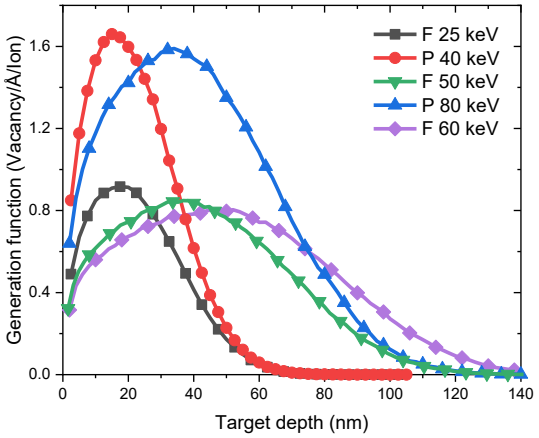


Fig. 1. Dependences of primary point defect generation function in α-Ga_2O_3 on the sample depth, calculated with TRIM for fluorine ions with energies of 25–60 keV and phosphorus ions with energies of 40 and 80 keV

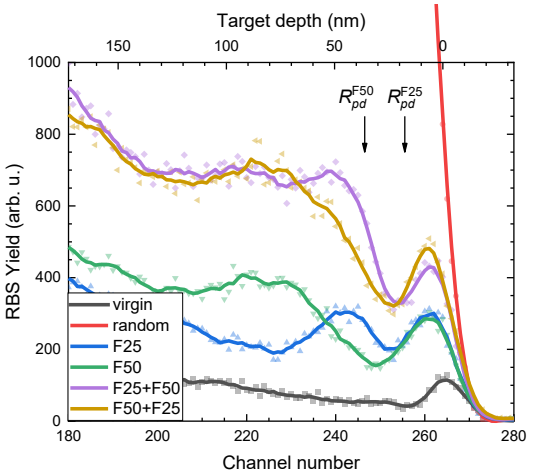


Fig. 2. Experimental RBS/C spectra for α-Ga_2O_3 samples irradiated with 25 and 50 keV fluorine ions under different conditions: single and double irradiations in different sequences (see legend). The spectra of unirradiated samples recorded in the aligned (virgin) and random directions of the probing beam

The dose was 1.5 DPA for each individual irradiation. The arrows mark the maxima of the primary point defect generation functions. Each maximum corresponds to irradiation with fluorine ions at one of the energies considered

which corresponds to a depth of about 35 nm and to the maximum of the generation function for 50 keV fluorine ions, for which, in turn, the BDP is located in the region of channel 229, equivalent to a depth of about 62 nm.

Fig. 2 also shows the results of sequential irradiation with fluorine ions for two sequences: low energy (25 keV) followed by high energy (50 keV), and the reverse, high energy (50 keV) followed by low energy (25 keV). Each irradiation step was performed with the same dose: 1.5 DPA. It follows from the data in Fig. 2 that the final shape of the spectrum and consequently the defect distribution strongly depend on the irradiation sequence, despite identical DPA and DPA/s values. Indeed, when the first irradiation is performed with low-energy fluorine ions, i.e., when the total energy is 25+50 keV, an increase in the BDP is observed after the second irradiation. Conversely, the BDP value is lower for the reverse irradiation order.

Therefore, irradiation with 25 and 50 keV fluorine ions is a non-commutative process [28].

Next, experiments were carried out to test the commutativity of ion irradiation of α-Ga_2O_3 samples with phosphorus ions. As noted above, the irradiation energies for phosphorus ions were chosen so that the primary point defect generation functions were similar to the corresponding functions for F^+ ions. The irradiation was performed with the same dose: 1.5 DPA. Fig. 3 shows the RBS/C spectra for single irradiations with 40 and 80 keV phosphorus ions; their BDP positions are also in the region of channels 246 (depth of ~35 nm) and 229 (~62 nm), respectively [25, 26]. The results of irradiation with phosphorus ions in different sequences, namely 40+80 keV and 80+40 keV, are also shown in Fig. 3. A significant increase in the signal is observed for the low-energy → high-energy sequence, with consequently a more intense accumulation of stable radiation damage. As in the case of fluorine ions, irradiation with 40 and 80 keV phosphorus ions is also a non-commutative process.

Finally, in the concluding experiment, the energy of the second fluorine irradiation was chosen to be 60 keV, so that the generation maximum lay somewhat deeper than the BDP position for 25 keV ions. The doses of each irradiation step were also 1.5 DPA. The resulting RBS/C spectra for the cases F^+ 25 + 60 keV and 60 + 25 keV are shown in Fig. 4. It can be seen that the generation maximum is shifted deeper into the sample by about 13 nm relative to the BDP position for F^+ 25 keV, and the BDP for F 60 keV is located in the region of channel 220 (~90 nm). As in the other cases, more intense defect formation was observed for the low-energy → high-energy irradiation sequence. Despite the increase in the energy of the second ion, irradiation with 25+60 keV fluorine ions also proved to be non-commutative.

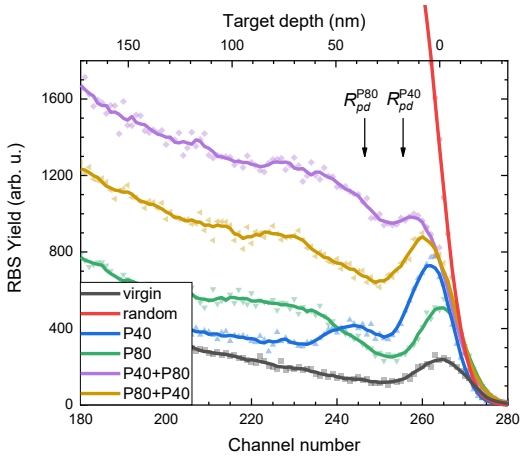


Fig. 3. RBS/C spectra similar to those in Fig. 2, but for irradiation with 40 and 80 keV phosphorus ions (see legend)

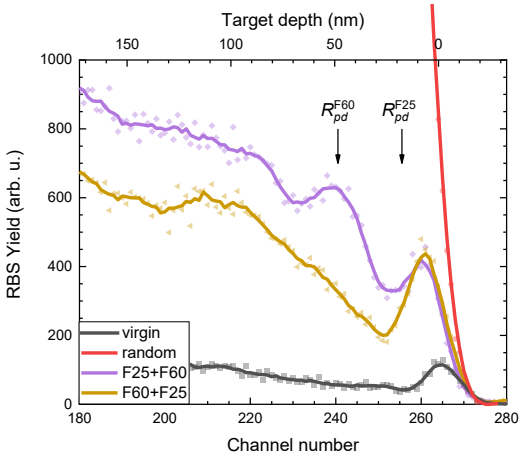


Fig. 4. Spectra similar to those in Fig. 2, but corresponding only to double irradiation with 25 and 60 keV fluorine ions in different sequences

To date, two mechanisms of ion implantation in semiconductors that lead to non-commutativity of structural damage accumulation have been proposed. Both have been confirmed to be valid.

The *first mechanism* [25] is the non-linearity of dose dependence of structural damage at different depths for each type of bombarding ion.

The *second mechanism* [7, 31] is the formation of a higher concentration of stable damage at depth upon irradiation with lower-energy ions, which leads to more efficient formation of stable defects involving mobile point defects during subsequent high-energy irradiation.

It is the second mechanism that we observed experimentally. In the case when high-energy irradiation was applied first, the concentration of stable damage in the bulk was lower (compared to low-energy irradiation) and mobile point defects were less efficiently trapped at depth and diffused to the interface between the amorphous surface layer and the crystalline layer. Further studies are clearly needed to elucidate the physical nature of non-commutativity under sequential ion implantation into α-Ga_2O_3 samples.

Conclusion

We studied radiation damage accumulation in gallium alpha oxide under sequential bombardment with fluorine ions and, separately, with phosphorus ions at different energies. It was found that the process is non-commutative: the final damage depends on the sequence of irradiation. We proposed possible mechanisms for this effect. Understanding the mechanisms and physical origin of the stable defect accumulation rate as a function of the ion implantation sequence can make it possible to predict and control the final defect profile in electronic devices based on α-Ga_2O_3. Further experimental and theoretical studies of this phenomenon are clearly necessary.

REFERENCES

1. **Feldman L. C., Mayer J. W.,** Fundamentals of surface and thin film analysis, North-Holland, Amsterdam, Netherlands, 1986.

2. **Davies J. A.,** High energy density collision cascades and spike effects (Ch. 4), In book: J. S. Williams, J. M. Poate (Eds.). Ion implantation and beam processing, Academic Press, Sydney, Australia (1984) 81–97.

3. **Thompson D. A.,** High density cascade effects, Radiat. Eff. 56 (3–4) (1981) 105–150.

4. **Taube A., Kaminska E., Kozubal M., et al.,** Ion implantation for isolation of AlGaN/GaN HEMTs using C or Al, Phys. Status Solidi A. 212 (5) (2015) 1162–1169.

5. **Abroyan I. A., Titov A. I., Khlebalkin A. V.,** Obrazovaniye defektov v kremnii pri kombinirovannom obluchenii ionami [The formation of defects in silicon under combined ion irradiation], Fiz. Tekh. Poluprovodn. (USSR). 13 (2) (1979) 227–233 (in Russian).

6. **Abroyan A. I., Konyshev V. V., Titov A. I., Khlebalkin A. V.,** Vliyaniye sostoyaniya kristallicheskoy struktury kremniya na nakopleniye defektov pri ionnom obluchenii [The influence of the state of the Si crystalline structure on the accumulation of defects during ion irradiation], Fiz. Tekh. Poluprovodn. (USSR). 15 (1) (1981)166–168 (in Russian).

7. **Titov A. I., Karaseov P. A., Karabeshkin K. V., Struchkov A. I.,** The formation of radiation damage in GaN during successive bombardment by light ions of various energies, Vacuum. 2020. 173 (March) (2020) 109149.

8. **Bai Q., Li L., Cheng F. F., et al.,** Study on microstructure and mechanical properties of He and H ion irradiated 6H-SiC, Nucl. Instrum. Meth. Phys. Res. B. 365 (Part A, 15 Dec) (2015) 347–351.

9. **Bogh E., Hogild P., Stensgaard I.,** Spatial distribution of defects in ion bombarded silicon and germanium, Rad. Eff. 7 (1–2) (1971) 115–121.

10. **Kool W.H., Roosendaal H. E., Wiggers L.W., Saris F. W.,** Production and beam annealing of damage in carbon implanted silicon. II, Rad. Eff. 36 (1–2) (1978) 41–48.

11. **Abroyan I. A., Nikulina L. M., Titov A. I.,** Ionically stimulated ordering of previously irradiated silicon, Fiz. Tekh. Poluprovodn. (USSR). 19 (6) (1985) 1030–1034 (in Russian).

12. **Abroyan I. A., Nikulina L. M.,** Molecular effect during light ion implantation in semiconductors, Fiz. Tekh. Poluprovodn. (USSR). 31 (10) (1997) 1164 –1167 (in Russian).

13. **Jiang W., Weber W. J., Zhang Y., et al.,** Ion beam analysis of irradiation effects in 6H–SiC, Nucl. Instrum. Meth. Phys. Res. B. 207 (1) (2003) 92–99.

14. **Pelaz L., Marqués L. A., Barbolla J.,** Ion-beam-induced amorphization and recrystallization in silicon, J. Appl. Phys. 96 (11) (2004) 5947–5976.

15. **Stepanov S. I., Nikolaev V. I., Bougrov V. E., Romanov A. E.,** Gallium oxide: properties and application – A review, Rev. Adv. Mater. Sci. 44 (1) (2016) 63–86.

16. **Pearton S. J., Ren F., Mastro M. (Eds.),** Gallium oxide. Technology, devices and applications, Elsevier Inc., Amsterdam (Netherlands), 2019.

17. **Pearton S. J., Ren F., Tadjer M., Kim J.,** Perspective: Ga_2O_3 for ultra-high power rectifiers and MOSFETS, J. Appl. Phys. 124 (22) (2018) 220901.

18. **Wellmann P. J.,** Power electronic semiconductor materials for automotive and energy saving applications – SiC, GaN, Ga_2O_3, and diamond, Z. Anorg. Allg. Chem. 643 (21) (2017) 1312–1322.

19. **Nikolskaya A., Okulich E., Korolev D., et al.,** Ion implantation in β-Ga_2O_3: Physics and technology, J. Vac. Sci. Technol. A. 39 (3) (2021) 030802.

20. **Cai Y., Feng Z., Wang Z., et al.,** Demonstration of the normally off β-Ga_2O_3 MOSFET with high threshold voltage and high current density, Appl. Phys. Lett. 123 (19) (2023) 193501.

21. **Farzana E., Roy S., Hendricks N. S., et al.,** Vertical PtO_x/Pt/β-Ga_2O_3 Schottky diodes with high permittivity dielectric field plate for low leakage and high breakdown voltage, Appl. Phys. Lett. 123 (19) (2023) 192102

22. **Ahmadi E., Oshima Y.,** Materials issues and devices of α-and β-Ga_2O_3, J. Appl. Phys. 126 (16) (2019) 160901.

23. **Polyakov S. J., Nikolaev S. J., Yakimov S. J., et al.,** Deep level defect states in β-, α-, and ε-Ga_2O_3 crystals and films: Impact on device performance, J. Vac. Sci. Technol. A. 40 (2) (2022) 020804.

24. **Azarov A., Galeckas A., Mikhaylov A. et al.,** Defect evolution and nitrogen incorporation in ion-implanted β-Ga_2O_3, Appl. Phys. Lett. 125 (19) (2024) 192107.

25. **Klevtsov A., Karaseov P., Azarov A., et al.,** Non-linear effects in α-Ga_2O_3 radiation phenomena, APL Mater. 12 (11) (2024) 111121.

26. **Klevtsov A. I., Karaseov P. A., Karabeshkin K. V., Titov A. I.,** Peculiarities of structure damage accumulation under the implantation of ions of different masses into alpha-gallium oxide at low damage levels, St. Petersburg State Polytechnical University Journal. Physics and Mathematics. 16 (4) (2023) 42–49 (in Russian).

27. **Titov A., Klevtsov A., Fedorenko E., et al.,** Density and fractality of collision cascades in α-Ga_2O_3, Appl. Phys. Lett. 127 (15) (2025) 152107.

28. **Klevtsov A. I., Kleimanov R. V., Azarov A., et al.,** Damage accumulation in alpha gallium oxide during sequential keV light ion implantations, Proc. 2024 Int. Conf. on Electrical Engineering and Photonics (EExPolytech), Oct. 17–18, St. Petersburg, Russia, IEEE (2024) 339–342.

29. **Pechnikov A. I., Stepanov S. I., Chikiryaka A.V., et al.,** Thick α-Ga_2O_3 layers on sapphire substrates grown by halide epitaxy, Semicond. 53 (6) (2019) 780–783.

30. **Ziegler J. F., Biersack J. P., Littmark U.,** The stopping and range of ions in solids, Pergamon Press, New York, 1985.

31. **Titov A. I., Karaseov P. A., Kataev A. Yu., et al.,** Model for radiation damage buildup in GaN, Nucl. Instrum. Meth. Phys. Res. B. 277 (15 Apr) (2012) 80–83.

СПИСОК ЛИТЕРАТУРЫ

1**. Фелдман Л., Майер Д.** Основы анализа поверхности и тонких пленок. Пер. с англ. М.: Мир, 1989. 342 с.

2. **Davies J. A.** High energy density collision cascades and spike effects (Chapter 4) // J. S. Williams, J. M. Poate (Eds.). Ion implantation and beam processing. Sydney, Australia: Academic Press, 1984. Pp. 81–97.

3. **Thompson D. A.** High density cascade effects // Radiation Effects. 1981. Vol. 56. No. 3–4. Pp. 105–150.

4. **Taube A., Kaminska E., Kozubal M. et al.** Ion implantation for isolation of AlGaN/GaN HEMTs using C or Al // Physica Status Solidi A. 2015. Vol. 212. No. 5. Pp. 1162–1169.

5. **Аброян И. А., Титов А. И., Хлебалкин А. В.** Образование дефектов в кремнии при комбинированном облучении ионами // Физика и техника полупроводников. 1979. Т. 13. № 2. С. 227–233.

6. **Аброян А. И., Конышев В. В., Титов А. И., Хлебалкин А. В**. Влияние состояния кристаллической структуры кремния на накопление дефектов при ионном облучении // Физика и техника полупроводников. 1981. Т. 15. № 1. С. 166–168.

7. **Titov A. I., Karaseov P. A., Karabeshkin K. V., Struchkov A. I.** The formation of radiation damage in GaN during successive bombardment by light ions of various energies // Vacuum. 2020. Vol. 173. March. P. 109149.

8. **Bai Q., Li L., Cheng F. F., Bin R., Fa T., Fu E., Yao S. D.** Study on microstructure and mechanical properties of He and H ion irradiated 6H-SiC // Nuclear Instruments and Methods in Physics Research B. 2015. Vol. 365. Part A, 15 December. Pp. 347–351.

9. **Bogh E., Hogild P., Stensgaard I.** Spatial distribution of defects in ion bombarded silicon and germanium // Radiation Effects. 1971. Vol. 7. No. 1–2. Pp. 115–121.

10. **Kool W. H., Roosendaal H. E., Wiggers L. W., Saris F. W.** Production and beam annealing of damage in carbon implanted silicon. II // Radiation Effects. 1978. Vol. 36. No. 1–2. Pp. 41–48.

11. **Аброян И. А., Никулина Л. М., Титов А. И.** Ионно-стимулированное упорядочение структуры предварительно облученного кремния // Физика и техника полупроводников. 1985. Т. 19. № 6. С. 1030–1034.

12. **Аброян И. А., Никулина Л. М.** Молекулярный эффект при имплантации легких ионов в полупроводники // Физика и техника полупроводников. 1997. Т. 31. № 10. С. 1164–1167.

13. **Jiang W., Weber W. J., Zhang Y., Thevuthasan S., Shutthanandan V.** Ion beam analysis of irradiation effects in 6H–SiC // Nuclear Instruments and Methods in Physics Research B. 2003. Vol. 207. No. 1. Pp. 92–99.

14. **Pelaz L., Marqués L. A., Barbolla J.** Ion-beam-induced amorphization and recrystallization in silicon //Journal of Applied Physics. 2004. Vol. 96. No. 11. Pp. 5947–5976.

15. **Stepanov S. I., Nikolaev V. I., Bougrov V. E., Romanov A. E.** Gallium oxide: properties and application – A review // Reviews on Advanced Materials Science. 2016. Vol. 44. No. 1. Pp. 63–86.

16. **Pearton S. J., Ren F., Mastro M.** (Eds.). Gallium oxide. Technology, devices and applications. Amsterdam, Netherlands: Elsevier Inc., 2019. 479 p.

17. **Pearton S. J., Ren F., Tadjer M., Kim J.** Perspective: Ga_2O_3 for ultra-high power rectifiers and MOSFETS // Journal of Applied Physics. 2018. Vol. 124. No. 22. P. 220901.

18. **Wellmann P. J.** Power electronic semiconductor materials for automotive and energy saving applications – SiC, GaN, Ga2O3, and diamond // Zeitschrift für anorganische und allgemeine Chemie. 2017. Vol. 643. No. 21. Pp. 1312–1322.

19. **Nikolskaya A., Okulich E., Korolev D., et al.** Ion implantation in β-Ga_2O_3: Physics and technology // Journal of Vacuum Science & Technology A. 2021. Vol. 39. No. 3. P. 030802.

20. **Cai Y., Feng Z., Wang Z., et al.** Demonstration of the normally off β-Ga2O3 MOSFET with high threshold voltage and high current density // Applied Physics Letters. 2023. Vol. 123. No. 19. P. 193501.

21. **Farzana E., Roy S., Hendricks N. S., Krishnamoorthy S., Speck J. S.** Vertical PtO_x/Pt/β-Ga_2O_3 Schottky diodes with high permittivity dielectric field plate for low leakage and high breakdown voltage // Applied Physics Letters. 2023. Vol. 123. No. 19. P. 192102.

22. **Ahmadi E., Oshima Y.** Materials issues and devices of α-and β-Ga_2O_3 //Journal of Applied Physics. 2019. Vol. 126. No. 16. P. 160901.

23. **Polyakov A. Y., Nikolaev V. I., Yakimov E. B., Ren F., Pearton S. J., Kim J.** Deep level defect states in β-, α-, and ε-Ga_2O_3 crystals and films: Impact on device performance // Journal of Vacuum Science & Technology A. 2022. Vol. 40. No. 2. P. 020804.

24. **Azarov A., Galeckas A., Mikhaylov A., Nikolskaya A., Tetelbaum D., Korolev D., Monakhov E., Kuznetsov A.** Defect evolution and nitrogen incorporation in ion-implanted β-Ga_2O_3 // Applied Physics Letters. 2024. Vol. 125. No. 19. P. 192107.

25. **Klevtsov A., Karaseov P., Azarov A., Karabeshkin K., Fedorenko E., Titov A., Kuznetsov A.** Non-linear effects in α-Ga_2O_3 radiation phenomena // APL Materials. 2024. Vol. 12. No. 11. P. 111121.

26. **Клевцов А. И., Карасев П. А., Карабешкин К. В., Титов А. И.** Особенности накопления структурных нарушений при имплантации ионов разных масс в альфа-оксиде галлия при малых уровнях повреждения // Научно-технические ведомости СПбГПУ. Физико-математические науки. 2023. Т. 16. № 4. С. 42–49.

27. **Titov A., Klevtsov A., Fedorenko E., Azarov A., Kuznetsov A., Karaseov P.** Density and fractality of collision cascades in α-Ga_2O_3 // Applied Physics Letters. 2025. Vol. 127. No. 15. P. 152107.

28. **Klevtsov A. I., Kleimanov R. V., Azarov A., Karaseov P. A., Karabeshkin K. V., Titov A. I.** Damage accumulation in alpha gallium oxide during sequential keV light ion implantations // Proceedings of the 2024 International Conference on Electrical Engineering and Photonics (EExPolytech). October 17–18, St. Petersburg, Russia. IEEE: 2024. Pp. 339–342.

29. **Печников А. И., Степанов С. И., Чикиряка А. В., Щеглов М. П., Одноблюдов М. А., Николаев В. И.** Толстые слои alpha-Ga_2O_3 на сапфировых подложках, полученные методом хлоридной эпитаксии // Физика и техника полупроводников. 2019. Т. 53. № 6. С. 789–792.

30. **Ziegler J. F., Biersack J. P., Littmark U.** The stopping and range of ions in solids. New York: Pergamon Press, 1985. 321 p.

31. **Titov A. I., Karaseov P. A., Kataev A. Yu, Azarov A. Yu, Kucheyev S. O.** Model for radiation damage buildup in GaN // Nuclear Instruments and Methods in Physics Research B. 2012. Vol. 277. 15 April. Pp. 80–83.

THE AUTHORS

KLEVTSOV Anton I.
Peter the Great St. Petersburg Polytechnic University,
Joint-Stock Company "Research and Production Enterprise «ELAR»»,
29 Politechnicheskaya St., St. Petersburg, 195251, Russia
klevtsovanton@rambler.ru
ORCID: 9685-6988-0004-0009

KARASEOV Platon A.
Peter the Great St. Petersburg Polytechnic University
29 Politechnicheskaya St., St. Petersburg, 195251, Russia
platon.karaseov@spbstu.ru
ORCID: 0000-0003-2511-0188

TITOV Andrei I.
Peter the Great St. Petersburg Polytechnic University
29 Politechnicheskaya St., St. Petersburg, 195251, Russia
ATitov@spbstu.ru
ORCID: 0000-0003-4933-9534

СВЕДЕНИЯ ОБ АВТОРАХ

КЛЕВЦОВ Антон Игоревич – *ассистент кафедры физики Института физики и математики Санкт-Петербургского политехнического университета Петра Великого, инженер-технолог 1 категории Акционерного общества "Научно-производственное предприятие «ЭЛАР»".*
195251, Россия, г. Санкт-Петербург, Политехническая ул., 29
klevtsovanton@rambler.ru
ORCID: 0009-0004-6988-9685

КАРАСЕВ Платон Александрович – *доктор физико-математических наук, профессор Высшей инженерно-физической школы Санкт-Петербургского политехнического университета Петра Великого.*
195251, Россия, г. Санкт-Петербург, Политехническая ул., 29
platon.karaseov@spbstu.ru
ORCID: 0000-0003-2511-0188

ТИТОВ Андрей Иванович – *доктор физико-математических наук, профессор Высшей инженерно-физической школы Санкт-Петербургского политехнического университета Петра Великого.*
195251, Россия, г. Санкт-Петербург, Политехническая ул., 29
ATitov@spbstu.ru
ORCID: 0000-0003-4933-9534

Received 20.05.2026. Approved after reviewing 03.06.2026. Accepted 03.06.2026.
Статья поступила в редакцию 20.05.2026. Одобрена после рецензирования 03.06.2026. Принята 03.06.2026.

© Peter the Great St. Petersburg Polytechnic University, 2026

PHYSICAL MATERIALS TECHNOLOGY

Overview article
DOI: https://doi.org/10.18721/JPM.19210

PLASMONIC NANOMATERIALS FORMED BY ION EXCHANGE IN GLASS: PROPERTIES AND APPLICATIONS

V. V. Zhurikhina[1,2]✉, *E. S. Babich*[2], *A. N. Terpitskiy*[2], *I. Nuritdinov*[3], *M. A. Rakhmatov*[4], *A. A. Eshbekov*[4]

[1] Peter the Great St. Petersburg Polytechnic University, St. Petersburg, Russia;

[2] Alferov University, RAS, St. Petersburg, Russia;

[3] Institute of Nuclear Physics, Academy of Sciences of the Republic of Uzbekistan, Tashkent, Uzbekistan;

[4] Sharof Rashidov Samarkand State University, Samarkand, Uzbekistan

✉ zhurihina_vv@spbstu.ru

Abstract. Plasmonic materials based on noble metal nanostructures exhibit unique optical properties in the visible range. Currently, plasmons supported by metal nanoparticles or propagating along metal interfaces are attracting increasing attention in sensorics, medicine, imaging, nanophotonics, and optoelectronic technologies. This article has provided a brief overview of two main plasmonic modes: surface plasmon polaritons at metal interfaces and localized plasmons in nanostructures. It also discussed the physical principles of plasmon-enhanced sensors, such as colorimetric, plasmon-enhanced fluorescence, and surface enhanced Raman scattering ones. These sensors are widely used in healthcare, security, food processing, and environmental monitoring. The fabrication of plasmonic nanostructures in glasses using ion exchange and their application for detecting chemical compounds and biological objects was discussed.

Keywords: localization of light, nanostructure, ion exchange, plasmon, electromagnetic field amplification, sensor

Funding: The research was supported by the Ministry of Science and Higher Education of the Russian Federation (Project FSRM-2026-0005)

C**itation:** Zhurikhina V. V., Babich E. S., Terpitskiy A. N., Nuritdinov I., Rakhmatov M. A., Eshbekov A. A., Plasmonic nanomaterials formed by ion exchange in glass: properties and applications, St. Petersburg State Polytechnical University Journal. Physics and Mathematics. 19 (2) (2026) 107–135. DOI: https://doi.org/10.18721/JPM.19210

This is an open access article under the CC BY-NC 4.0 license (https://creativecommons.org/licenses/by-nc/4.0/)

© Zhurikhina V. V., Babich E. S., Terpitskiy A. N., Nuritdinov I., Rakhmatov M. A., Eshbekov A. A., 2026. Published by Peter the Great St. Petersburg Polytechnic University.

Обзорная статья
УДК 538.9 + 538.975
DOI: https://doi.org/10.18721/JPM.19210

ПЛАЗМОННЫЕ НАНОМАТЕРИАЛЫ, ФОРМИРУЕМЫЕ МЕТОДОМ ИОННОГО ОБМЕНА В СТЕКЛЕ: СВОЙСТВА И ПРИМЕНЕНИЕ

В. В. Журихина[1,2]✉, Е. С. Бабич[2], А. Н. Терпицкий[2], И. Нуритдинов[3], М. А. Рахматов[4], А. А. Эшбеков[4]

[1] Санкт-Петербургский политехнический университет Петра Великого, Санкт-Петербург, Россия;

[2] Академический университет им. Ж. И. Алфёрова РАН, Санкт-Петербург, Россия;

[3] Институт ядерной физики Академии наук Республики Узбекистан, г. Ташкент, Республика Узбекистан;

[4] Самаркандский государственный университет имени Шарофа Рашидова, г. Самарканд, Республика Узбекистан

✉ zhurihina_vv@spbstu.ru

Аннотация. Плазмонные материалы на основе наноструктур благородных металлов обладают уникальными оптическими свойствами в видимом диапазоне. В настоящее время плазмоны, которые поддерживаются металлическими наночастицами или распространяются вдоль металлических интерфейсов, привлекают все большее внимание в сенсорике, медицине, визуализации, нанофотонных и оптоэлектронных технологиях. В статье представлен краткий обзор двух основных плазмонных мод: поверхностных плазмонных поляритонов на металлических интерфейсах и локализованных плазмонов в наноструктурах, а также физических основ плазмонно-усиленных датчиков, таких как колориметрические сенсоры, сенсоры на основе плазмонно-усиленной флуоресценции и сенсоры на основе гигантского комбинационного рассеяния. Такие датчики широко используются в здравоохранении, безопасности, пищевой промышленности и мониторинге окружающей среды. Рассмотрено получение плазмонных наноструктур в стеклах методом ионного обмена и их применение для детектирования химических соединений и биообъектов.

Ключевые слова: локализация световой волны, наноструктура, ионный обмен, плазмон, усиление электромагнитного поля, сенсор

Финансирование: Работа выполнена при поддержке Министерства науки и высшего образования Российской Федерации (проект FSRM-2026-0005).

Ссылка для цитирования: Журихина В. В., Бабич Е. С., Терпицкий А. Н., Нуритдинов И., Рахматов М. А., Эшбеков А. А. Плазмонные наноматериалы, формируемые методом ионного обмена в стекле: свойства и применение // Научно-технические ведомости СПбГПУ. Физико-математические науки. 2026. Т. 19. № 2. С. 107–135. DOI: https://doi.org/10.18721/JPM.19210

Статья открытого доступа, распространяемая по лицензии CC BY-NC 4.0 (https://creativecommons.org/licenses/by-nc/4.0/)

Introduction

It is well known that the electromagnetic properties of noble metals, such as gold, silver and copper, at optical wavelengths closely resemble those of an electron gas. Classical electron theory predicts and numerous experiments confirm a negative real part of the dielectric permittivity for these metals at or near optical wavelengths [1]. Consequently, charge oscillations can propagate along the surface of noble and several other metals at optical frequencies. Surface charge oscillations dominate the electromagnetic response of nanoparticles with sizes of the order of several nanometers.

© Журихина В. В., Бабич Е. С., Терпицкий А. Н., Нуритдинов И., Рахматов М. А., Эшбеков А. А., 2026. Издатель: Санкт-Петербургский политехнический университет Петра Великого.

A surface plasmon arises from collective oscillations of conduction electrons in nanostructured metal systems [2]. A unique property of such systems is that they can concentrate optical energy at the nanoscale via surface plasmons. If the external excitation frequency matches the surface plasmon frequency, surface plasmon resonance (SPR) occurs.

Both the intensity and the position of the SPR depend strongly on the size, shape, and composition of the nanostructures, as well as on the dielectric properties of the surrounding medium [5]. This sensitivity opens the avenue for spectroscopic methods for monitoring the interactions between the analyte and the sensor surface in real time [6]. Moreover, SPR-based sensors require only minute amounts of analyte and use label-free techniques, making it possible to forgo any preliminary preparation [7]. As a result, this approach offers a highly sensitive, versatile, and efficient technology that has been rapidly developing over the past two decades.

Surface plasmon polaritons and plasmons in nanoparticles

Plasmon resonance typically takes two distinct forms (Fig. 1):
surface plasmon polaritons (SPPs) propagating along metal–dielectric interfaces;
localized surface plasmon resonance (LSPR) in metal nanoparticles [8].

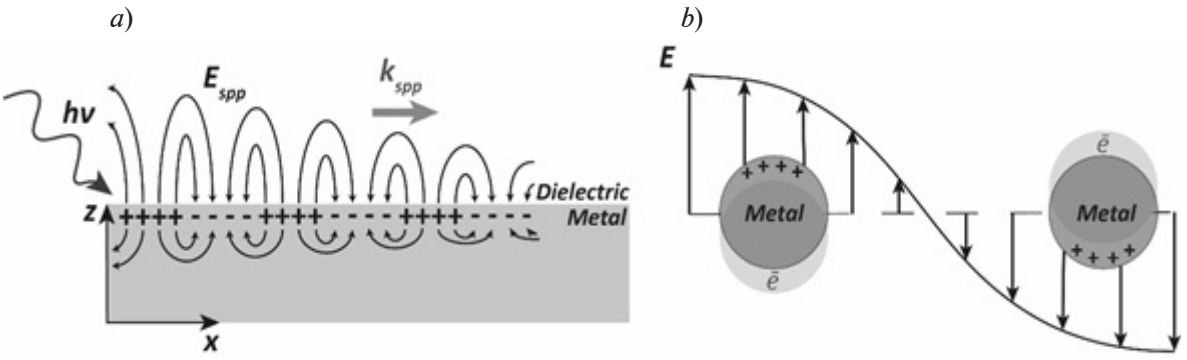


Fig. 1. Schematic of two types of plasmon resonance:
surface plasmon polariton (SPP) propagating along a metal–dielectric interface (*a*);
localized surface plasmon resonance (LSPR) in nanoparticles excited
by an incident electromagnetic wave (*b*)

LSPR occurs when the metal nanostructure is much smaller than the wavelength of incident light. Optimal nanoparticle sizes for the optical range are from 10 to 15 nm [9]. The interaction with an external electromagnetic wave excites collective non-propagating oscillations of the surface electrons in the metal nanostructure. The plasmon oscillation frequency depends on the nanoparticle morphology and the wave polarization. For an ellipsoidal nanoparticle, the LSPR frequency ω_α along the axis α is given by the following formula [10]:

$$\omega_\alpha = \omega_p \Big/ \sqrt{1+\varepsilon_d\left(1/L_\alpha - 1\right)}, \qquad (1)$$

where ω_p is the Drude plasma frequency, ε_d is the relative permittivity of the surrounding medium, L_α is the geometric factor for the given axis ($L_\alpha = 1/3$ for a sphere).

As follows from Eq. (1), the resonance frequency depends on the dielectric permittivity of the surrounding medium; this dependence is the basis for plasmonic sensors. Moreover, plasmon resonance concentrates the electromagnetic field strongly around the nanostructure. Molecules in the near field of the nanoparticle participate in radiative and non-radiative processes, whose efficiency is increased by enhanced local fields. This effect, often called the nanoantenna effect [11], underlies surface-enhanced fluorescence [12] and surface-enhanced Raman scattering [13]. Both phenomena can be exploited in sensing applications.

In contrast to LSPR, SPPs involve electron oscillations along metal–dielectric interfaces, in particular, on thin metal films. These waves are polarized in the direction normal to the surface (TM-polarization) and can exist only at interfaces between materials whose real parts of the dielectric permittivity have opposite signs (the real part of the dielectric permittivity in metals is negative at optical frequencies). At optical frequencies, waves propagating along a metal–dielectric interface take the form of electromagnetic fields coupled to surface plasma oscillations, i.e., oscillations of conduction electrons in the metal [14]. This is essentially a two-dimensional excitation whose electromagnetic field decays exponentially with distance from the interface [14].

The SPP wavevector Q at frequency ω can be written as [10]:

$$Q = \frac{\omega}{c}\sqrt{\frac{\varepsilon_m \varepsilon_d}{\varepsilon_m + \varepsilon_d}}, \tag{2}$$

where ε_m is the dielectric function of the metal.

Because the wavevector of incident light does not match that of the propagating SPP (the SPP wavevector is always larger), SPPs cannot be excited by radiation in free space. Excitation requires momentum matching, which can be achieved, for instance, via attenuated total reflection or by using a periodic structure.

The classic setup for SPP excitation is the Kretschmann configuration [15], where a metal film (typically a noble metal, most often gold) deposited on a prism reflects the incident light almost completely, except at a specific angle called the SPP excitation angle. As follows from Eq. (2), this angle depends on the refractive index of the medium, a property that sensors exploit.

Propagating SPPs or a mixed SPP/LSPR regime can be used to detect changes in the dielectric permittivity of the surrounding medium. When analyte molecules in an aqueous solution bind to the plasmonic metal film, the SPP excitation angle shifts, and the SPP wavelength increases because the molecules have a higher refractive index [16, 17].

SPP-based optical fiber sensors were also fabricated [18, 19]. These sensors rely on single-mode tapered fibers coated with a thin metal layer on one side. The optical mode propagating in the fiber can excite various hybrid surface plasmon modes in the metal layer. Consequently, the transmission spectrum of the metal-coated fiber exhibits several SPP peaks whose positions depend on the system parameters and the refractive index of the surrounding medium [18]. SPP-based fiber-optic sensors offer several advantages, including light weight, capabilities for remote sensing and multiplexing.

Sensors based on plasmons in nanoparticles

Noble-metal nanoparticles, such as gold, silver and copper, exhibit LSPR in the optical range and serve as the basis for plasmonic sensors [20]. According to Eq. (1), the LSPR position depends on the shape of the nanoparticle and its dielectric environment: the resonance wavelength shifts when analyte molecules bind to the nanoparticle surface (sometimes prior functionalization of the nanoparticle is required to achieve this), changing the local refractive index (Fig. 2).

A change in the refractive index n of the surrounding medium by Δn shifts the position of the LSPR peak λ_{res} (in wavelength units) or E_{res} (in energy units). The corresponding proportionality constant, or sensitivity, can be expressed in wavelength (S_λ) or energy (S_E) units [21]:

$$S_\lambda = d\lambda_{res}/dn,\ S_E = dE_{res}/dn = -1.240\ S_\lambda/\lambda^2\ (\text{nm/eV}).$$

The relatively large linewidth Γ complicates analysis, because this parameter can vary by more than an order of magnitude among nanostructures with different geometries. Clearly, it is easier to detect a resonance shift for narrow lines, so the ratio of the resonance shift to the linewidth

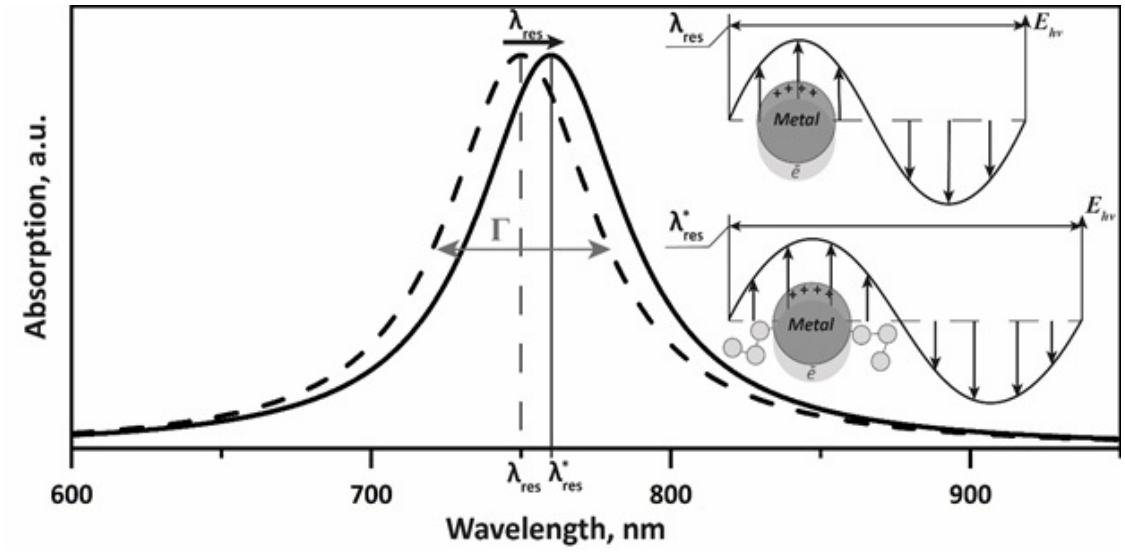


Fig. 2. Shift of LSPR peak in response to changes in the surrounding medium; key parameters are resonance linewidth Γ (full width at half maximum) and peak position λ_{res} on the wavelength axis

serves as a more accurate measure of a plasmon-based sensor's performance. This dimensionless quantity is the figure of merit (FOM) of the resonance structure [21]:

$$\text{FOM} = S/\Gamma.$$

FOM can be easily determined experimentally; it provides a convenient basis for comparing the plasmonic characteristics of different structures. Earlier studies found [22] that the FOM for small metal nanoparticles depends only on the nature of the metal itself. It reaches its highest value when damping is low (i.e., when the imaginary part of the dielectric function is small) and at frequencies where the real part of the dielectric function exhibits the strongest dependence on frequency. The resonance frequency and in turn the FOM of plasmonic sensors can be fine-tuned by adjusting the nanoparticle geometry. Among all noble-metal sensors, those based on silver nanoparticles exhibit the highest FOM, owing to silver's low losses in the optical frequency range.

Colorimetric plasmonic sensors, relying on shifts of the LSPR peak in colloidal nanoparticle solutions, offer a simple and convenient approach to detecting analytes in solution, often allowing direct visualization of analyte concentration. For example, functionalized gold nanoparticles were used for colorimetric detection of heavy metals, small biological molecules and biomacromolecules [23–25].

A new colorimetric assay was proposed in [26] for ultrasensitive visual glucose detection based on gold bipyramids. This glucose assay achieved a detection limit of 0.02 mM. Moreover, the proposed sensor can be used to estimate glucose levels by the naked eye from the color change, thus distinguishing between healthy individuals and diabetic patients without any sophisticated instrumentation.

Enhancement of the electromagnetic field near nanoparticle surfaces due to LSPR can be used in plasmon-enhanced fluorescence spectroscopy. LSPR-based sensors can achieve enhanced fluorescence by increasing either the excitation efficiency of the analyte or its emission efficiency [27]. In both cases, stronger local electromagnetic fields lead to greater enhancement. According to Eq. (1), field enhancement near sharp features is higher because of the geometric factor (often called the 'lightning rod' or 'tip' effect). Thus nanorods, elongated ellipsoids, and dendrites exhibit stronger plasmon-enhanced fluorescence than nanospheres. The enhancement factor for plasmonic fluorescence typically lies in the range of 10–100, though optimized nanostructures can yield values as high as 10^3 in some cases [28].

In particular, Xie et al. used arrays of silver nanotriangles to enhance the fluorescence of near-infrared dyes [29], finding that the low quantum yield (4%) of the dye's NIR fluorescence could be increased by two orders of magnitude if a silver nanotriangle array was used.

Surface-enhanced Raman scattering (SERS) is one of the most powerful and promising analytical techniques for biological and chemical sensing, offering several key advantages [30–33]:

high selectivity, owing to the unique spectral fingerprints of analytes;

high sensitivity, down to single-molecule detection;

operational simplicity;

capability to detect multicomponent mixtures with a single excitation laser, thanks to narrow spectral bands.

Raman scattering (RS) by itself has low efficiency because of its small scattering cross-section (on the order of 10^{-28}–10^{-30} cm^2/molecule). However, the enhanced local electromagnetic field near plasmonic nanostructures can boost the Raman signal by factors of 10^4 to 10^8 [34]. The magnitude of this local field enhancement near the plasmonic nanostructures determines the performance of SERS-based sensors; consequently, considerable research effort has been focused on developing effective SERS substrates [35–37].

An effective technique for fabricating plasmonic structures, notable for its relative simplicity and low cost, is ion exchange in glass, which can produce plasmonic structures both in the bulk and on the surface [38–41]. Combining ion exchange with glass polarization and etching makes it possible to create microchannels with plasmonic nanoparticles inside the glass, which holds promise for microfluidics applications [42, 43].

Plasmonic structures formed by ion exchange in glasses

Glasses are unique materials with properties critical to many technologies. They are transparent and hard at room temperature, mechanically strong, and highly chemically resistant. In 1752, the great Russian scientist Mikhail Lomonosov wrote in a letter to Ivan Shuvalov, the curator of Moscow University [44]:

They're wrong about it, Shuvalov: wrong to class
The gaudy look of minerals higher than our glass.
. . . . . .
When I sit before you, and to ecstasy will pass,
It's not the precious stones I praise, nor gold, but glass[1].

Ion exchange from molten salts is a well-established technology for modifying the physicochemical properties of glass. Craftsmen used this method during the Renaissance to produce ceramics coated with a thin glass film containing silver and copper nanoparticles of various sizes, formed through ion exchange between metal ions and alkali ions in the glass, followed by reduction of the metal ions and their aggregation into nanoparticles [45].

Optical glass is typically an amorphous material composed of several types of oxides [46]:

network formers (SiO_2, GeO_2 or P_2O_5);

intermediate network formers (Al_2O_3, TiO_2), which cannot form glass by themselves but can be combined with network formers;

network modifiers (Na_2O, K_2O, CaO, or BaO), which are less strongly bound to the glass network.

Ion exchange is essentially a chemical reaction where mobile ions in a solid are exchanged for ions of similar charge from a solution. Because alkali modifier ions are weakly bound to the glass matrix, they are the most suitable for ion exchange. For optical and photonic applications, the vast majority of cases involve exchanging Na^+ or K^+ ions in the glass for Ag^+, K^+, or Tl^+ ions from a molten salt bath (Fig. 3).

[1] M. V. Lomonosov, "A Letter on the Uses of Glass" (excerpt), trans. by Colin John Holcombe, Ocaso Press, accessed 20.06.2026, https://www.ocasopress.com/lomonosov-use-of-glass.html.

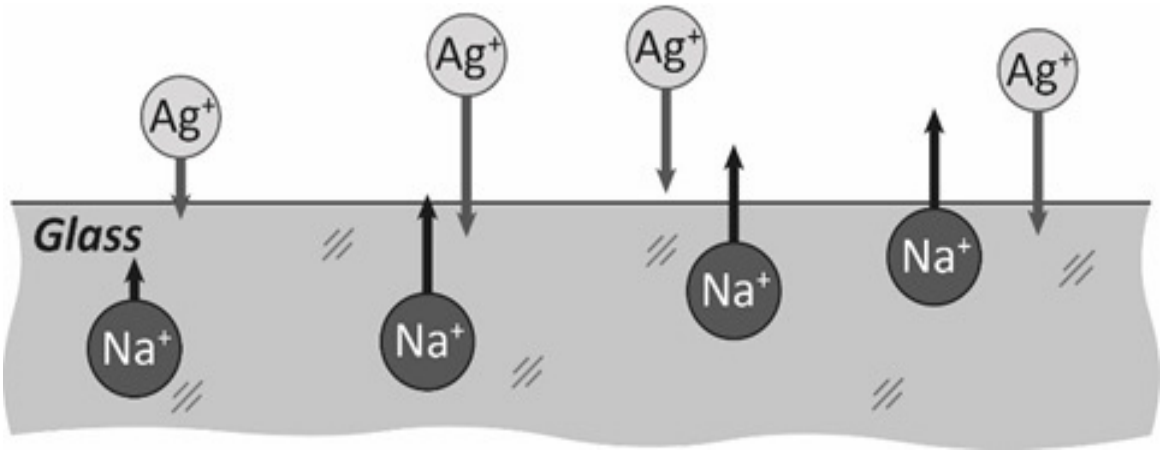


Fig. 3. Schematic representation of ion exchange in glass

Ion exchange technology is successfully used for glass strengthening [47], fabricating optical waveguides and active optical devices [48, 49], and forming metal nanostructures in glass [50]. Let us focus in more detail on the last of these applications.

Formation of metal nanoparticles in the bulk and on the glass surface. Among the many types of metal nanoparticles, silver nanoparticles appear particularly interesting for synthesis and study because silver exhibits the highest electrical and thermal conductivity of all metals [51]. The electronic and optical properties of silver nanoparticles can be controlled by choosing appropriate synthesis conditions.

Common methods for producing metal nanoparticles in glasses include rapid synthesis by quenching from the melt [52], the sol-gel technique [53], ion implantation [54], and ion exchange [55].

Ion exchange offers several advantages:

it can introduce relatively high concentrations of metal ions into the glass;

the glass remains undamaged after the exchange (unlike ion implantation, which introduces substantial defects into the glass matrix);

it allows producing large volumes of glass with metal nanoparticles.

After silver ions are introduced into the glass matrix by ion exchange, the next step is to induce phase decomposition of the supersaturated glass–metal solid solution and bring about precipitation of the second phase, metal nanoparticles. This is achieved either by annealing (thermal treatment) the ion-exchanged glass in air or in a hydrogen atmosphere, or by ionizing radiation, with or without subsequent thermal treatment. Alternatively, nanoparticles can be obtained by ion exchange in glass containing reducing agents, that is, variable-valency ions.

The main limitation of the method is that it is difficult to produce monodisperse nanoparticle ensembles with a narrow size distribution. This limitation stems from the nature of the process itself, which consists of two stages: ion diffusion and subsequent aggregation. Ion exchange produces polydisperse nanoparticles due to stochastic nucleation and diffusion-controlled growth [56]. Even after the process parameters are optimized, the size distribution remains wide [57]. The depth at which the nanoparticles are located ranges from hundreds of nanometers to several micrometers, depending on the process duration and temperature, as well as on the charge of the diffusing ion. The penetration depth is significantly smaller for multiply charged ions (e.g., Cu^{2+}) than for singly charged ions (Ag^{+}, Na^{+}) [58]. Thermal treatment at temperatures above the glass transition temperature can induce the formation of core–shell structures [59].

The glass composition critically affects ion diffusion and reduction. Adding ions of variable valence, e.g., cerium, iron, or antimony, promotes the reduction of silver during ion exchange and the growth of photoluminescent molecular silver clusters and plasmonic silver nanoparticles [60].

Subjecting glasses doped with halides (such as chlorine or bromine) to $Na^+ \leftrightarrow Ag^+$ ion exchange and thermal treatment produces photo- and thermochromic AgCl or AgBr nanocrystals [61]. The method for forming nanoparticles by ion exchange is reproducible, with only minor deviations in glass composition or process parameters.

When thermal treatment is carried out in air at temperatures below a certain threshold, molecular clusters (smaller than 1 nm) form in the glass; these likely represent silver dimers [62]. The processes occurring can be written as follows [62]:

$$2(\equiv Si - O - Ag^+) \leftrightarrow \equiv Si - O - Si\equiv + O^- + (Ag_2)^+,$$

$$O^- + (Ag_2)^+ \rightarrow 2\,Ag^0 + (1/2)\,O_2.$$

Increasing the annealing time at temperatures below the threshold increases only the number of clusters, not their size. Annealing above the threshold temperature causes the silver nanoparticles to grow in size [62]. The electronic structure of molecular clusters differs substantially from that of metal nanoparticles; in particular, molecular clusters exhibit luminescence in the visible range under UV excitation, making them useful for various sensing applications [63, 64]. However, because of their small size, molecular clusters lack the collective electron oscillation, i.e., the plasmon resonance, that characterizes larger nanoparticles.

An alternative thermal treatment method for forming metal nanoparticles in ion-exchanged glass is annealing of the sample in a reducing hydrogen (H_2) atmosphere. This approach produces a glass-metal nanocomposite inside the glass and a metal nanoisland film on the glass surface, driven by diffusion of metal atoms reduced due to hydrogen penetration into the glass [56]. The reduction of metal ions is described by the reaction [65]:

$$\equiv Si - O - Ag^+ + (1/2)\,H_2 \rightarrow \equiv Si - O - H^+ + Ag^0.$$

Under certain conditions, annealing of ion-exchanged glass in hydrogen can favor nanoparticle formation either on the surface or in the bulk of the glass [66], and can create ordered ensembles of metal nanoparticles on the surface [67].

Ionizing radiation, such as gamma rays, electrons, heavy ions, X-rays, or laser beams, can be used in combination with thermal treatment, or as a substitute for it, to produce silver nanoparticles in ion-exchanged glass [68–70]. Ionizing radiation creates excitons in the dielectric glass matrix, leading to stable defects and changes in the valence state of dopant and impurity ions in the glass.

Gamma irradiation of the dielectric glass matrix produces electron–hole pairs in the matrix. Some of the electrons reduce silver ions to the neutral state [71]:

$$\text{glass} \xrightarrow{\gamma\text{-rays}} h^+ + e^-,$$

$$Ag^+ + e^- \rightarrow Ag^0$$

Subsequent formation of nanoparticles occurs when thermal treatment activates the diffusion of neutral silver atoms in the glass matrix by the following reaction [71] (Fig. 4):

$$nAg^0 \rightarrow Ag_n.$$

The formation of silver nanoparticles manifests as peaks at plasmon resonance wavelengths of 400–420 nm in the optical absorption spectra, and the initially transparent glass turns pale yellow or intense yellow, depending on the volume fraction of nanoparticles. The formation of silver nanoparticles depends on the irradiation dose; gamma irradiation accelerates this rate compared to thermal annealing because it raises the diffusion coefficient of silver in the glass by several orders of magnitude [71, 72].

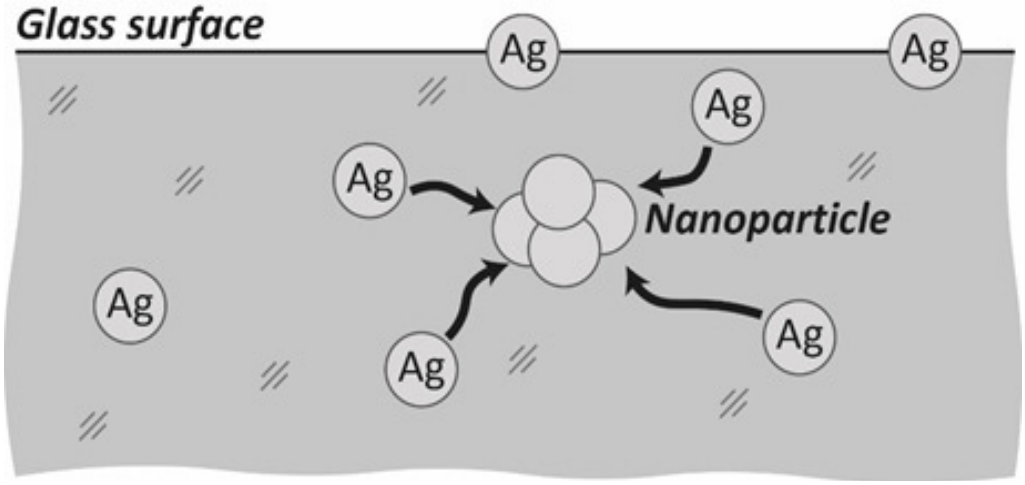


Fig. 4. Schematic of silver nanoparticle formation in glass

Nanoparticles can also be formed in the glass by laser irradiation without additional thermal annealing. Laser irradiation heats the irradiated region of the glass and softens it [73]; in ion-exchanged glass, it breaks the bonds between silver and non-bridging oxygen, after which the silver ions are reduced by electrons from negatively charged non-bridging oxygen atoms [66]. Additionally, laser irradiation at 355 nm produces free electrons in the glass through multiphoton absorption [74]. This in turn leads to reduction of silver ions to the metallic state through trapping of electrons. Supersaturation of the near-surface region of the glass with silver atoms drives phase decomposition and precipitation of metal nanoparticles [75].

Dendritic metal structures in glass. Dendritic (or fractal) nanostructures have attracted considerable interest because of their branched morphology and large surface area, making them attractive for many practical applications, particularly SERS and catalysis [76, 77]. Studies investigated the production of silver dendrites using various methods:

photoreduction in the presence of polyvinyl alcohol [78];

reduction with ascorbic acid in the presence of sodium polyacrylate [79];

galvanic displacement [80] using pulsed sonolectrochemical techniques [81], and others.

However, most methods of wet chemistry for producing dendritic nanostructures rely on surfactants or polymer templates, which complicates the synthesis procedure and the sample purification. In some cases, contamination of the final product is difficult to avoid because undesirable side products form in the reaction medium, rendering the dendrites unsuitable for further use. Therefore, developing template-free methods for synthesizing dendritic nanostructures remains a major challenge.

A promising method for synthesizing silver dendrites, requiring no complex equipment and no wet chemistry, is ion exchange in glass combined with DC poling applied to opposite sides [82] or to the same side [40] of the glass substrate. Fig. 5 shows the structures obtained by this technique.

The mechanism of dendrite formation with a voltage applied to ion-exchanged glass containing metal ions can be described as follows [82].

In the first stage, silver ions drift in an electric field and are reduced at the cathode, forming nuclei of the metallic phase on the glass surface. In the second stage, these nuclei grow by diffusion and form metal islands in contact with the cathode; some of these islands act as secondary cathodes and thus become sources of dendrite growth. Because the silver ions are concentrated in the near-surface region of the glass after ion exchange, dendrite growth occurs mainly in the plane parallel to the sample surface, within the glass. Subsequent etching of the glass in a dilute hydrofluoric acid/ammonium fluoride (HF/NH_4F) solution causes needle-like structures with heights up to ~100 nm and finer dendrite branches to emerge on the glass surface [40]. The resulting metal nanostructures hold promise for applications in catalysis and SERS sensors.

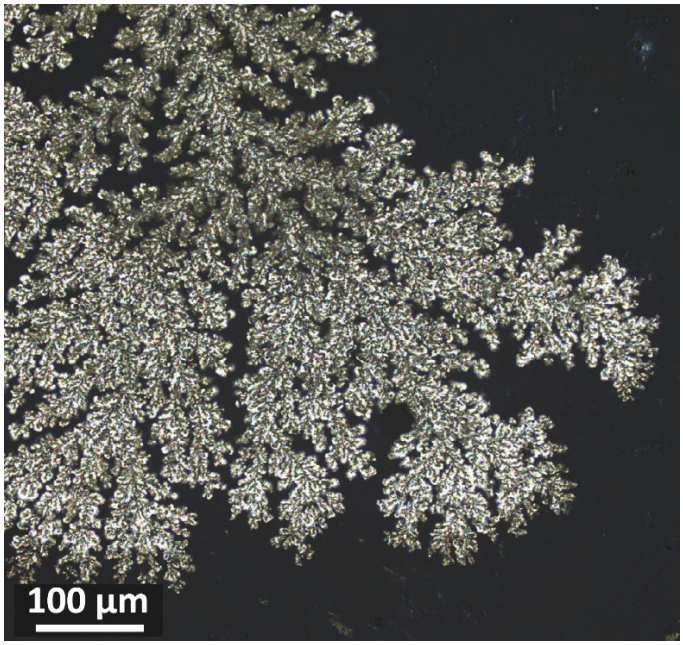


Fig. 5. Optical image of silver dendrites
in ion-exchanged glass

Plasmonic nanostructures as substrates for SERS sensors

The interaction between light and noble metal nanostructures is the key to one of the most effective optical detection methods, SERS. Metal nanostructures act as 'hot spots' for the electric field of the incident light wave, due to LSPR [83]. When an analyte molecule lies close to one of these hot spots, its Raman signal increases by several orders of magnitude due to enhancement of the electric field acting on the molecule. This effect gives LSPR-based sensors ultralow detection limits combined with the high selectivity inherent in Raman spectroscopy [84].

Optimization of the substrates is required to develop high-performance SERS sensors. Ideal SERS substrates should provide high signal enhancement, reproducible response, reusability, stable metal nanoparticles, low cost, and a simple fabrication method [85].

Comparison of ion exchange with other fabrication methods for SERS

The main parameters characterizing plasmonic structures used as SERS substrates are the nanoparticle size distribution, the density of hot spots, and the enhancement factor of the Raman signal. Below we briefly compare methods for fabricating metal nanostructures for SERS.

Ion exchange in glass. Nanoparticles obtained by ion exchange in glass have a rather wide polydisperse size distribution, which results from the diffusion-controlled mechanism of their formation [86]. The particle size can be varied from 2 to 250 nm by controlling the ion exchange times and annealing conditions [87, 88]. The RMS deviation in size can reach 30–40% [86]. The hot-spot density is moderate, but it can be varied, for example, by combining ion exchange with thermal poling of the glass [66]. Combining these two methods also makes it possible to form hot spots in a predetermined pattern. The SERS enhancement factor is moderate (up to 10^7 [89]).

Femtosecond laser writing with reduction. In this approach, intense femtosecond laser pulses are focused into the bulk of glass or a precursor solution. Multiphoton absorption triggers local reduction of metal ions (e.g., Ag^+ or Au^{3+}) to the neutral state, producing nanoparticles in the focal region. This method makes it possible to obtain particles of controllable size (typically 20–200 nm) by adjusting the laser power and scanning speed, and forming structures

with designed geometries [91]. The size dispersion is about 10% [92]. The hot-spot density is high. Arrays of dimers or particle chains with gaps below 10 nm can be created, including 3D structures inside the material [92]. The high SERS enhancement factor (up to 10^{10} [93]) is achieved by precisely controlling nanoparticle size and by creating ensembles with tailored characteristics [91, 94].

Nanoimprint lithography with metal deposition. This technique involves applying a polymer resist to the substrate and embossing a pattern (holes or pillars) into it with a mechanical stamp. A metal layer (Ag, Au) is then deposited by thermal or electron-beam evaporation; after the resist is removed, highly ordered metal structures remain on the substrate [95, 96]. The resulting size distribution is extremely narrow (virtually monodisperse). This method also provides the best reproducibility of shape and size (from 10 nm to several micrometers), matching the stamp pattern [97]. Nanoimprint lithography offers the highest hot-spot density and makes it possible to design arrays with field enhancement in precisely defined narrow regions (e.g., in gaps between nanodisks) [97]. This yields high SERS enhancement factors (up to 10^7 [97]) for structures with sub-nanometer gaps.

Chemical etching with metallization. In this approach, a surface (e.g., silicon, copper, or aluminum foil) is treated with a chemical etchant to create roughness. Next, a noble metal layer is deposited on this rough surface chemically or galvanically [98, 99]. The process is difficult to control and often produces dendritic structures. The resulting size distribution is wide and fractal, with sizes ranging from nano- to microscale [100]; the hot-spot density is rather high, providing a sufficiently high SERS enhancement factor (up to 10^8 for metallized mesoporous silicon [101]).

The table compares the methods described above in terms of these three key characteristics.

Table

Comparison of plasmonic structure parameters for different fabrication methods

Method	Size distribution	Hot-spot density	SERS enhancement factor
Ion exchange in glass	Wide (polydisperse) [86]	Medium/low (random distribution) [88]	10^3–10^7 [89, 90]
Femtosecond laser writing + reduction	Narrow (controlled) [91, 92]	High [92]	10^8–10^{10} [93, 102]
Nanoimprint lithography + metal deposition	Very narrow (monodisperse) [10]	Very high (deterministic placement) [96]	10^6–10^7 [97]
Chemical etching + metallization	Wide (random, dendritic) [100]	Very high (sub-nanometer gaps) [14]	10^7–10^8 [101]

Despite the relatively low hot-spot density and moderate SERS enhancement factor compared to other techniques, ion exchange offers several unique advantages making it attractive for SERS substrates:

1. Technological simplicity and scalability. The process is simple and inexpensive, suitable for large-scale production of SERS-active substrates. It requires neither complex lithographic equipment nor high vacuum.

2. Low cost of starting materials. The substrate is multicomponent glass, which is inexpensive and technologically convenient. The ion exchange procedure itself also requires no costly equipment or consumables.

3. Nanoparticles are protected from the environment. Unlike many other methods where nanoparticles lie directly on the surface and are susceptible to oxidation and sulfidation, a thin glass layer covers the metal nanoparticles within the bulk of ion-exchanged glass. This ensures durability and preservation of the substrate without loss of properties, and allows multiple uses by successive etching, which exposes fresh layers with intact nanoparticles for reuse.

4. A high enhancement factor (up to 10^5-10^6) is sufficient for many analytical applications, including biomedical ones.

5. Flexibility and controllability. The process allows varying both composition and structure of the nanoparticles. For example, sequentially introducing different metal ions (copper and silver) and controlling the annealing temperature makes it possible to form core–shell nanostructures and nanostructures of mixed composition whose plasmon resonance position depends on the metal concentration ratio. Combining ion exchange with laser irradiation also allows writing the structures of a required shape.

6. Integration into optical circuits. Forming nanoparticles in glass is ideal for developing integrated sensor chips that combine optical waveguides and microfluidics.

7. Well-studied and amenable to modeling. The processes of ion exchange and subsequent nanoparticle formation are well understood and can be mathematically modeled, allowing prediction of the properties of the final nanostructures.

Thus, while the method has numerous advantages, the most important are the unique combination of simplicity and cost-effectiveness, and the potential for improved durability of SERS substrates due to natural protection of the nanoparticles by the glass matrix. This makes the technology particularly attractive for practical and stable sensors suitable even for field conditions. Although the method has some limitations in controlling the nanoparticle size dispersion, these do not pose a serious obstacle to its application.

Silver nanoparticles provide the best SERS enhancement among all noble metal nanostructures, although they are prone to oxidation and sulfidation.

Given the parameters of substrates fabricated by different methods (see above), SERS substrates based on ion-exchanged glasses with silver nanostructures appear the most promising for the following reasons:

silver nanostructures provide high SERS signal enhancement;

silver nanoisland films can be removed from the surface after use, and new nanoparticles can be formed on the surface by simply heating the glass substrate with silver ions; in other words, the substrate is reusable [38];

when silver nanostructures lie in the bulk of the glass, they remain undamaged; they can be brought to the surface directly before use by etching the glass [40];

the method is simple, low-cost, and the results are highly reproducible.

Substance detection with SERS on substrates with silver nanostructures formed by ion exchange

Ref. [39] reports on SERS enhancement provided by silver nanoisland films formed on the glass surface by ion exchange and thermal annealing, as well as the effect from the arrangement of hot spots in ensembles of self-assembled silver nanoislands. Raman spectra were measured for an aqueous solution of 1,2-di(4-pyridyl)ethylene (BPE) at a concentration of 10^{-3} M under non-resonant excitation. Comparison of SERS characteristics of nanoisland films at different growth stages showed that enhancement dominated at the nanoisland coalescence stage due to increased electric field in closely spaced groups

of nanoislands. A linear dependence between the SERS signal and the surface density of nanoislands was observed at earlier growth stages. The maximum enhancement occurred at the onset of coalescence.

Silver nanoisland films formed on the surface of ion-exchanged glass by thermal annealing are stable in biocompatible buffers, which opens new opportunities for applications in SERS diagnostics of biological objects dissolved in buffers. It was found in [41] that silver nanoisland films are stable in phosphate-buffered saline (PBS), one of the most common buffers in biological research, in PBS diluted 1:100 with water, in PBS-based buffer where sodium chloride (NaCl) is replaced by the same amount of sodium perchlorate ($NaClO_4$), and in acidic phosphate buffer. The nanoisland films provided a good SERS signal from a BPE monolayer (concentration of 10^{-4} M) after exposure to PBS, making them promising for biosensor applications.

SERS has been successfully applied to diagnose amino acids and proteins. SERS spectra of D-alanine and DL-serine were observed in [103] using substrates prepared from silver nanoisland films immersed in standard PBS solutions with millimolar concentrations of these amino acids. The resulting spectra differ significantly in peak intensity and position from the Raman spectra of bulk solutions and from SERS spectra of crystallites of the corresponding amino acids on substrates not immersed in buffer, as well as from Raman spectra on pure glass. This effect is presumably due to electrostatic orientation of zwitterionic amino acids by the silver nanoparticles, which acquire a negative charge due to desorption of Ag(I) chloride in the solution.

Thus, despite sufficient signal enhancement from metal nanoislands, the interaction of the amino acids with the metallic substrate should be taken into account in the detection of amino acids in various biocompatible buffers.

A comparative study [104] evaluated SERS and enzyme-linked immunosorbent assay (ELISA) for detecting SARS-CoV-2 virus nucleoproteins. SERS substrates were silver nanoisland films on the surface of ion-exchanged glass. The SERS spectra can be used to distinguish between the features of antigens, antibodies, and the features indicating the binding between them. The SERS method exhibited a much lower detection limit (1 pg/mL) compared to ELISA (approximately 50–100 pg/mL), and significantly reduced the analysis time: ELISA requires about two hours, whereas SERS measurements take only a few seconds.

The branched structure of dendrites makes them highly attractive for sensing applications. Several studies explored the use of dendrites for SERS diagnostics [105–107]. For example, dendritic nanostructures formed by electrolysis in silver-enriched glass for SERS detection of low concentrations of hazardous substances were analyzed in [108]. The detection limit for the thiram pesticide corresponded to a surface concentration of $4.6 \cdot 10^{-10}$ g/mm^2 (a monolayer). The Raman enhancement factor provided by the dendrites was $4 \cdot 10^5$.

Silver is well known for its antibacterial properties, making it valuable for medicine and pharmacology [109]. However, the toxic effects of silver on living cells can hinder the use of silver nanoparticle substrates for SERS analysis of biological objects. Nanoparticles of other metals, particularly gold, can be used in such cases. Bimetallic nanoparticles (e.g., silver-gold) are also promising: they could combine the advantages of each metal, i.e., the high LSPR figure of merit provided by silver, and the chemical and biological inertness of gold for biological diagnostics.

Ion exchange and back-diffusion were used in [110] to produce ensembles of biocompatible Au–Ag alloy nanoparticles with varying silver contents, suitable for use as SERS substrates. The bimetallic Au–Ag nanoparticles were grown by silver-to-sodium ion exchange in silicate glass, followed by deposition of a depercolated gold film on the sample surface and subsequent heat treatment. Varying the heat treatment regime made it possible to control the fraction of silver in the nanoparticles and adjust the spectral position of their LSPR between the resonances of gold and silver nanoparticles.

Cell viability assays on pure glass and on glass substrates with nanoparticles of different compositions showed that cells grown on control slides, on slides with gold nanoparticles, and on slides with nanoparticles containing 40–50 wt.% silver exhibited similar viability within the reference limits. In contrast, substrates with pure silver nanoparticles showed a noticeable decrease in viability and approximately 100% loss of functionality/adhesion [110].

Future directions

The versatility of ion exchange in glass opens new prospects for its application in plasmonics and photonics; some of these are already under way, while others are just beginning to be explored.

Integrated photonic platform. Ion exchange in glass is one of the primary technological platforms for producing low-cost, high-performance planar waveguides [111]. The process, which typically involves exchanging K^+ or Ag^+ ions for Na^+ ions in the glass, induces a local increase in the refractive index, forming the basis for light guiding. This technology has evolved over the past 30 years, enabling a wide range of devices for telecommunications, optical information processing, and sensing [112]. Waveguide structures include both passive and active components. Passive devices, such as directional couplers, gratings, and optical splitters, have been successfully constructed many times [113]. Active devices, such as integrated optical amplifiers and lasers, are fabricated by doping the glass with rare-earth ions (e.g., Nd^{3+}), with subsequent formation of waveguides by ion exchange [114]. One of the most interesting directions is the application of this technology to quantum photonics. In the future, ion-exchanged waveguides could be used to implement quantum circuits for cryptography and quantum processing, integrating them with ion-exchanged glass lasers on a single chip. This positions ion-exchanged glass as a promising platform for quantum integrated optics [115].

Flexible glass-based photonics. The concept of "flexible photonics" is a new stage for ion-exchanged glass devices [116]. This direction is seen as an alternative to polymer-based flexible photonics, which has its drawbacks: a limited range of refractive indices, NIR absorption, and low chemical stability. Although glass is traditionally considered a rigid material, using thin ion-exchanged layers makes it possible to fabricate photonic components on flexible glass substrates. The idea is that the ion exchange technology can be adapted to create flexible photonic structures based on commercial glass, simultaneously retaining low optical losses and chemical stability.

Ultra-thin sheets of commercial glass (e.g., Willow Glass from Corning, less than 100 μm thick [117]) with high surface quality and paper-like flexibility could be used for flexible photonic devices. Ion exchange has been proposed for strengthening these ultra-thin glasses. For alkali-containing glasses, conventional ion exchange (e.g., $Na^+ \leftrightarrow K^+$) generates compressive stress on the surface that counteracts microcracks under bending, so that smaller bending radii can be achieved without fracture. This paves the way for fully glass-based flexible devices for portable electronics.

Photonic devices with noble metal ions/nanoparticles. Another benefit offered by growing metal nanoparticles and clusters via ion exchange lies in creating low-cost photonic systems with improved performance for a wide range of applications. In particular, introducing noble metal ions (Ag, Au) by ion exchange into the bulk or onto the surface of microcavities (microspheres, microdisks) with whispering gallery modes (WGM), made of multicomponent glasses, can impart new properties to these devices. The luminescence efficiency and emission of the rare-earth ions can be enhanced by nucleating and growing noble-metal nanostructures (dimer clusters and/or metal nanoparticles several nanometers in size) inside the gain medium of a resonator made of glass doped with rare-earth ions, after by ion exchange and thermal post-treatment. This enhancement arises from surface plasmon resonance and/or energy transfer mechanisms, as observed for planar substrates [118, 119]. Moreover, signal enhancement at the converted frequency occurs within the same microresonator, which, supporting high optical energy density, allows photons to interact repeatedly with both the rare-earth ions and the metal nanostructures, typically located a few tens/hundreds of nanometers below the resonator surface, within the range of the waveguide modes. If these nanostructures are small plasmonic nanoparticles (e.g., a few nanometers in size), a combination of two resonant phenomena, waveguide modes of the microresonator and the plasmonic response of the nanoparticles, could lead to further significant enhancement of the signal.

The presence of noble-metal nanoparticles embedded in the waveguide cavity in glass could also enhance the nonlinear optical response of the medium due to plasmonic effects. For example, silver nanoparticles, with their high third-order nonlinearity, are prime candidates for developing all-optical signal processing devices, such as efficient optical limiters that require materials with a high nonlinear refractive index $n^{(2)}$ [120].

Quantum and coherent plasmonics. Research efforts in this field are shifting from simple field enhancement by plasmonic nanoparticles to exploiting quantum phenomena such as phase coherence and strong coupling between plasmons and other quasiparticles (excitons, electron-hole pairs). This opens new avenues for creating elements for quantum computers based on graphene plasmons and new types of nanophotonic devices [121]. Quantum plasmonics makes it possible to fabricate single-photon sources, transistors via photon blockade, and thresholdless nanolasers (spasers). Hybrid plasmonic-photonic circuits support on-chip generation, manipulation, and detection of single plasmons [122, 123].

Conclusion

Nanostructures that exhibit plasmon resonances have a wide range of practical applications, from visualizing glucose concentrations in blood to detecting toxic substances and diagnosing viral infections. The performance of plasmon-enhanced sensors depends directly on the geometry of the plasmonic structures and on the methods used to fabricate them. Importantly, the parameters of the nanostructures can be readily adjusted to different applications by choosing the material and the morphology of the structure. The distinct benefits of fabricating plasmonic nanostructures in glasses via ion exchange are their simplicity and low cost. All these factors provide the flexibility necessary for developing various sensors based on plasmonic field enhancement, opening up broad opportunities for using such devices. Further advances in plasmonics will enable even more efficient signal enhancement and imaging of analytes, as well as improved designs for new devices detecting chemical and biological compounds via fluorescence and SERS.

Acknowledgment

The authors would like to express their deep gratitude to Andrey Alexandrovich Lipovskii (Doctor of Physical and Mathematical Sciences, Professor, Head of Department of Functional Micro- and Nanomaterials at Alferov University) for fruitful discussions that improved the manuscript.

REFERENCES

1. **Bass M.,** Handbook of optics, Vol. I: Geometrical and physical optics, polarized light, components and instruments. McGraw-Hill, Inc., New York, 1996.

2. **Bohm D., Pines D.,** A collective description of electron interactions: III. Coulomb interactions in a degenerate electron gas, Phys. Rev. 92 (3) (1953) 609–625.

3. **Albella P., Garcia-Cueto B., González F., et al.,** Shape matters: Plasmonic nanoparticle shape enhances interaction with dielectric substrate, Nano Lett. 11 (9) (2011) 3531–3537.

4. **Jain P. K., El-Sayed M. A.,** Surface plasmon resonance sensitivity of metal nanostructures: Physical basis and universal scaling in metal nanoshells, J. Phys. Chem. C. 111 (47) (2007) 17451–17454.

5. **Scherbak S. A., Shustova O. V., Zhurikhina V. V., Lipovskii A. A.,** Electric properties of hemispherical metal nanoparticles: Influence of the dielectric cover and substrate, Plasmonics. 10 (3) (2015) 519–527.

6. **Rich R.,** Advances in surface plasmon resonance biosensor analysis, Curr. Opin. Biotechnol. 11 (1) (2000) 54–61.

7. **Écija-Arenas Б., Kirchner E.-M., Hirsch T., Fernández-Romero J. M.,** Development of an aptamer-based SPR-biosensor for the determination of kanamycin residues in foods, Anal. Chim. Acta. 1169. (18 Jul) (2021) 338631.

8. **Zayats A. V., Smolyaninov I. I.,** Near-field photonics: surface plasmon polaritons and localized surface plasmons, J. Opt. A: Pure Appl. Opt. 5 (4) (2003) S16–S50.

9. **Kosubukin V. A.,** Size dependence of light-field enhancement caused by surface plasmon excitation, Phys. Lett. A. 160 (6) (1991) 584–588.

10. **Klimov V.,** Nanoplasmonics, Jenny Stanford Publishing, Singapore, 2014.

11. **Novotny L.,** Effective wavelength scaling for optical antennas, Phys. Rev. Lett. 98 (26) (2007) 266802.

12. **Russell K. J., Liu T.-L., Cui S., et al.,** Large spontaneous emission enhancement in plasmonic nanocavities, Nat. Photonics. 6 (7) (2012) 459–462.

13. **Fan M., Andrade G. F. S., Brolo A. G.,** A review on the fabrication of substrates for surface enhanced Raman spectroscopy and their applications in analytical chemistry, Anal. Chim. Acta. 693 (1–2) (2011) 7–25.

14. **Agranovich V. M., Mills D. L.,** Surface polaritons: Electromagnetic waves at surfaces and interfaces, Elsevier, New York, 2012.

15. **Zayats A. V., Smolyaninov I. I., Maradudin A. A.,** Nano-optics of surface plasmon polaritons, Phys. Rep. 408 (3–4) (2005) 131–314.

16. **Bolduc O. R., Pelletier J. N., Masson J.-F.,** SPR biosensing in crude serum using ultralow fouling binary patterned peptide SAM, Anal. Chem. 82 (9) (2010) 3699–3706.

17. **Homola J., Yee S. S., Gauglitz G.,** Surface plasmon resonance sensors: Review, Sens. Actuator B – Chem. 54 (1–2) (1999) 3–15.

18. **Monzyn-Hernández D., Villatoro J., Talavera D., et al.,** Optical-fiber surface-plasmon resonance sensor with multiple resonance peaks, Appl. Opt. 43 (6) (2004) 1216.

19. **Днez A., Andrés M. V., Cruz J. L.,** In-line fiber-optic sensors based on the excitation of surface plasma modes in metal-coated tapered fibers, Sens. Actuator B – Chem. 73 (2–3) (2001) 95–99.

20. **Mayer K. M., Hafner J. H.,** Localized surface plasmon resonance sensors, Chem. Rev. 111 (6) (2011) 3828–3857.

21. **Becker J., Trügler A., Jakab A., et al.,** The optimal aspect ratio of gold nanorods for plasmonic bio-sensing, Plasmonics. 5 (2) (2010) 161–167.

22. **Hohenester U.** Nano and quantum optics: Graduate texts in physics. Cham: Springer International Publishing, 2020.

23. **Daniel W. L., Han M.S., Lee J.-S., et al.,** Colorimetric nitrite and nitrate detection with gold nanoparticle probes and kinetic end points, J. Am. Chem. Soc. 131 (18) (2009) 6362–6363.

24. **Zhang J.**, **Wang L., Pan D., et al.,** Visual cocaine detection with gold nanoparticles and rationally engineered aptamer structures, Small. 4 (8) (2008) 1196–1200.

25. **Storhoff J. J., Elghanian R., Mucic R. C., et al.,** One-pot colorimetric differentiation of polynucleotides with single base imperfections using gold nanoparticle probes, J. Am. Chem. Soc. 120 (9) (1998) 1959–1964.

26. **Qin X., Yuan C.-L., Shi R., et al.,** Colorimetric detection of dopamine based on iodine-mediated etching of gold nanorods, Chin. J. Anal. Chem. 49 (1) (2021) 60–67.

27. **Li M., Cushing S. K., Wu N.,** Plasmon-enhanced optical sensors: A review, Analyst. 140 (2) (2015) 386–406.

28. **Kinkhabwala A., Yu Z., Fan S., et al.,** Large single-molecule fluorescence enhancements produced by a bowtie nanoantenna, Nat. Photon. 3 (11) (2009) 654–657.

29. **Xie F., Pang J. S., Centeno A., et al.,** Nanoscale control of Ag nanostructures for plasmonic fluorescence enhancement of near-infrared dyes, Nano Res. 6 (7) (2013) 496–510.

30. **Vo-Dinh T.,** SERS chemical sensors and biosensors: new tools for environmental and biological analysis, Sens. Actuator B – Chem. 29 (1–3) (1995) 183–189.

31. **Zhurikhina V., Skvortsov A., Babich E., et al.,** Raman spectroscopy of amino acids using metal nanoisland films on glass, Proc. the 2021 Int. Conf. on Electrical Engineering and Photonics (EExPolytech), IEEE, 14–15 Oct., St. Petersburg, Russian Federation (I2021) 168–170.

32. **Li M., Cushing S.K., Zhang J., et al.,** Shape-dependent surface-enhanced Raman scattering in gold–Raman-probe–silica sandwiched nanoparticles for biocompatible applications, Nanotechnol. 23 (11) (2012) 115501.

33. **Zong S., Wang Z., Chen H., et al.,** Surface enhanced Raman scattering traceable and glutathione responsive nanocarrier for the intracellular drug delivery, Anal. Chem. 85 (4) (2013) 2223–2230.

34. **Ko E., Hwang J., Kim J. H., et al.,** Electrochemical fabrication of nanostructures on porous silicon for biochemical sensing platforms, Anal. Sci. 32 (6) (2016) 681–686.

35. **Babich E., Scherbak S., Lubyankina E., et al.,** Power spectral density analysis for optimizing SERS structures, Sensors. 22 (2) (2022) 593.

36. **Batista E., Dos Santos D. P., Andrade G. F. S., et al.,** Using polycarbonate membranes as templates for the preparation of au nanostructures for surface-enhanced Raman scattering, J. Nanosci. Nanotechnol. 9 (5) (2009) 3233–3238.

37. **Miller E. N., Palm D.C., De Silva D., et al.,** Microsphere lithography on hydrophobic surfaces for generating gold films that exhibit infrared localized surface plasmon resonances, J. Phys. Chem B. 117 (49) (2013) 15313–15318.

38. **Zhurikhina V. V., Brunkov P. N., Melehin V. G., et al.,** Self-assembled silver nanoislands formed on glass surface via out-diffusion for multiple usages in SERS applications, Nanoscale Res. Lett. 7 (17 Dec) (2012) 676.

39. **Babich E., Scherbak S., Asonkeng F., et al.,** Hot spot statistics and SERS performance of self-assembled silver nanoisland films, Opt. Mater. Express. 9 (10) (2019) 4090.

40. **Babich E., Raskhodchikov D., Redkov A., et al.,** Dendritic structures by glass electrolysis: Studies and SERS capability, Curr. Appl. Phys. 24 (Apr) (2021) 54–59.

41. **Skvortsov A., Babich E., Redkov A., et al.,** Stable in biocompatible buffers silver nanoisland films for SERS, Biosensors. 11 (11) (2021) 448.

42. **Babich E., Reduto I., Redkov A., et al.,** Thermal poling of glasses to fabricate masks for ion exchange, J. Phys.: Conf. Ser. 1695 (28 Dec) (2020) 012107.

43. **Babich E. S., Gangrskaia E. S., Reduto I. V., et al.,** Self-assembled silver nanoparticles in glass microstructured by poling for SERS application, Curr. Appl. Phys. 19 (10) (2019) 1088–1095.

44. **Lomonosov M. V.,** Izbrannyye filosofskiye proizvedeniya [Selected philosophical works], Gospolitizdat Publishing, Moscow, 1950 (in Russian).

45. **Padovani S., Sada C., Mazzoldi P., et al.,** Copper in glasses of Renaissance luster pottery: Nanoparticles, ions, and local environment, J. Appl. Phys. 93 (12) (2003) 10058–10063.

46. **Zachariasen W. H.,** The atomic arrangement in glass, J. Am. Chem. Soc. 54 (10) (1932) 3841–3851.

47. **Gy R.,** Ion exchange for glass strengthening, Mater. Sci. Eng. B. 149 (2) (2008) 159–165.

48. **Giallorenzi T. G., West E. J., Kirk R., et al.,** Optical waveguides formed by thermal migration of ions in glass, Appl. Opt. 12 (6) (1973) 1240.

49. **Ashley P. R., Bloemer M. J., Davis J. H.,** Measurement of nonlinear properties in Ag-ion exchange waveguides using degenerate four-wave mixing, Appl. Phys. Lett. 57 (15) (1990) 1488–1490.

50. **Berger A.,** Concentration and size depth profile of colloidal silver particles in glass surfaces produced by sodium-silver ion-exchange, J. Non-Cryst. Solids. 151 (1–2) (1992) 88–94.

51. **Cheng Z., Liu L., Xu S., et al.,** Temperature dependence of electrical and thermal conduction in single silver nanowire, Sci. Rep. 5 (02 Jun) (2015) 10718.

52. **Singh S. P., Karmakar B.,** Single-step synthesis and surface plasmons of bismuth-coated spherical to hexagonal silver nanoparticles in dichroic Ag: Bismuth glass nanocomposites, Plasmonics. 6 (3) (2011) 457–467.

53. **Epifani M., Giannini C., Tapfer L., et al.,** Sol–gel synthesis and characterization of Ag and Au nanoparticles in SiO_2, TiO_2, and ZrO_2 thin films, J. Am. Cer. Soc. 83 (10) (2000) 2385–2393.

54. **De Marchi G., Mattei G., Mazzoldi P., et al.,** Two stages in the kinetics of gold cluster growth in ion-implanted silica during isothermal annealing in oxidizing atmosphere, J. Appl. Phys. 92 (8) (2002) 4249–4254.

55. **Chen Y., Jaakola J. J., Säynätjoki A., et al.,** Glass-embedded silver nanoparticle patterns by masked ion-exchange process for surface-enhanced Raman scattering, J. Raman Spectrosc. 42 (5) (2011) 936–940.

56. **Redkov A. V., Zhurikhina V. V., Lipovskii A. A.,** Formation and self-arrangement of silver nanoparticles in glass via annealing in hydrogen: The model, J. Non-Cryst. Solids. 376 (15 Sept) (2013) 152–157.

57. **Abdel-Hameed S. A. M., Fathi A. M.,** Preparation and characterization of silver nanoparticles within silicate glass ceramics via modification of ion exchange process, J. Alloys Compnd. 498 (1) (2010) 71–76.

58. **Gonella F., Quaranta A., Cattaruzza E., et al.,** Cu-alkali ion exchange in glass: a model for the copper diffusion based on XAFS experiments, Comput. Mater. Sci. 33 (1–3) (2005) 31–36.

59. **Demichev I. A., Sidorov A. I., Nikonorov N. V.,** Features of the optical properties of diffusion layers obtained by successive replacement of sodium ions with copper and silver ions in silicate glass, J. Opt. Technol. 82 (11) (2015) 767.

60. **Sgibnev Y. M., Nikonorov N. V., Ignatiev A. I.,** Luminescence of silver clusters in ion-exchanged cerium-doped photo-thermo-refractive glasses, J. Luminesc. 176 (Aug) (2016) 292–297.

61. **Sgibnev Y., Nikonorov N., Ignatiev A.** Governing functionality of silver ion-exchanged photo-thermo-refractive glass matrix by small additives, Appl. Sci. 11 (9) (2021) 3891.

62. **Simo A., Polte J., Pfänder N., et al.,** Formation mechanism of silver nanoparticles stabilized in glassy matrices, J. Am. Chem. Soc. 134 (45) (2012) 18824–18833.

63. **Qu X., Li Y., Li L., et al.,** Fluorescent gold nanoclusters: Synthesis and recent biological application, J. Nanomater. 2015 (13 Aug) (2015) 84097.

64. **Saratovskiy A. S., Girsova M. A., Anfimova I. A., Antropova T. V.,** Formation of molecular clusters of silver by polymer-salt method in porous glasses, Opt. Spectrosc. 131 (1) (2023) 92–94 (in Russian).

65. **Kaganovskii Y., Lipovskii A., Rosenbluh M., et al.,** Formation of nanoclusters through silver reduction in glasses: The model, J. Non-Cryst. Solids. 353 (22–23) (2007) 2263–2271.

66. **Redkov A., Chervinskii S., Baklanov A., et al.,** Plasmonic molecules via glass annealing in hydrogen, Nanoscale Res. Lett. 9 (08 Nov) (2014) 606.

67. **Chervinskii S., Sevriuk V., Reduto I., et al.,** Formation and 2D-patterning of silver nanoisland film using thermal poling and out-diffusion from glass, J. Appl. Phys. 114 (22) (2013) 224301.

68. **Hofmeister H., Thiel S., Dubiel M., et al.,** Synthesis of nanosized silver particles in ion-exchanged glass by electron beam irradiation, Appl. Phys. Lett. 70 (13) (1997) 1694–1696.

69. **Espiau de Lamaestre R., Béa1 H., Bernas H., et al.,** Irradiation-induced Ag nanocluster nucleation in silicate glasses: Analogy with photography, Phys. Rev. B. 76 (20) (2007) 205431.

70. **Zhang J., Dong W., Qiao L., et al.,** Silver nanocluster formation in soda-lime silicate glass by X-ray irradiation and annealing, J. Cryst. Growth. 305 (1) (2007) 278–284.

71. **Farah K., Hosni F., Mejri A., et al.,** Effect of gamma rays absorbed doses and heat treatment on the optical absorption spectra of silver ion-exchanged silicate glass, Nucl. Instrum. Methods. Phys. Res. B. 323 (15 Mar) (2014) 36–41.

72. **Evstropiev S. K., Nikonorov N. V., Salimov Sh,, et al.,** Spektry EPR shchelochnosilikatnykh stekol, podvergnutykh ionnomu obmenu i gamma-oblucheniyu [ESR spectra of alkali-silicate glasses subjected to ion exchange and gamma irradiation], Fizika i Khimiya Stekla [Physics and Chemistry of Glass]. 17 (1) (1991) 126–129 (in Russian).

73. **Kaganovsky Y. S., Antonov I., Ianetz D., et al.,** Mass transfer in optical nanocomposites induced by pulsed laser irradiation // Solid State Phenomena. 2003. Vol. 94. Pp. 105–114.

74. **Marquestaut N., Petit Y., Royon A., et al.,** Three-dimensional silver nanoparticle formation using femtosecond laser irradiation in phosphate glasses: Analogy with photography, Adv. Funct. Mater. 24 (37) (2014) 5824–5832.

75. **Rosenbluh M., Antonov I., Ianetz D., et al.,** Microfabrication of structures by laser light in metal-doped glasses, Opt. Mater. 24 (1–2) (2005) 401–410.

76. **Lo Faro M. J., D'Andrea C., Leonardi A. A., et al.,** Fractal silver dendrites as 3D SERS platform for highly sensitive detection of biomolecules in hydration conditions, Nanomater. 9 (11) (2019) 1630.

77. **Wang D., Astruc D.,** Dendritic catalysis – Basic concepts and recent trends, Coord. Chem. Rev. 257 (15–16) (2013) 2317–2334.

78. **Zhou Y., Yu S. H., Wang C. Y., et al.,** A novel ultraviolet irradiation photoreduction technique for the preparation of single-crystal Ag nanorods and Ag dendrites, Adv. Mater. 11 (10) (1991) 850–852.

79. **Lee G.-J., Shin S.-I., Oh S.-G.**, Preparation of silver dendritic nanoparticles using sodium polyacrylate in aqueous solution, Chem. Lett. subjected to ion exchange and gamma irradiation

80. **Gutés A., Carraro C., Maboudian R.,** Silver dendrites from galvanic displacement on commercial aluminum foil as an effective SERS substrate, J. Am. Chem. Soc. 132 (5) (2010) 1476–1477.

81. **Zhu J., Liu S., Palchik O., et al.,** Shape-controlled synthesis of silver nanoparticles by pulse sonoelectrochemical methods, Langmuir. 16 (16) (2000) 6396–6399.

82. **Brunkov P. N., Lipovskii A. A., Melekhin V. G., et al.,** Formation of silver fractal structures in ion-exchange glasses under poling, Tech. Phys. 60 (2) (2015) 270–274.

83. **Grand J., De la Chapelle M. L., Bijeon J.-L., et al.,** Role of localized surface plasmons in surface-enhanced Raman scattering of shape-controlled metallic particles in regular arrays, Phys. Rev. B: Condens. Matter. 72 (3) (2005) 033407.

84. **Li P., Long F., Chen W., et al.,** Fundamentals and applications of surface-enhanced Raman spectroscopy–based biosensors, Current Opinion in Biomedical Engineering. 13 (2020) 51–59.

85. **Mosier-Boss P.,** Review of SERS substrates for chemical sensing, Nanomater. 7 (6) (2017) 142.

86. **Cheng W. D., Wu Z.J., Gu X.H., et al.,** GISAXS study on the size and distribution evolutions of Ag nanoparticles in ion-exchange glass during annealing, Mater. Chem. Phys. 152 (2015) 48–53.

87. **Inozemtsev V. A., Dokukin M. E., Sgibnev Y. M., et al.,** Na-Ag ion-exchanged glass substrates for plasmon-enhanced fluorescence imaging of neutrophils, Sensors. 25 (7) (2025) 2278.

88. **Kolobkova E., Kuznetsova M. S., Nikonorov N.,** Ag/Na ion exchange in fluorophosphate glasses and formation of Ag nanoparticles in the bulk and on the surface of the glass, ACS Appl. Nano Mater. 2 (11) (2019) 6928–6938.

89. **Simo A., Joseph V., Fenger R., et al.,** Long-term stable silver subsurface ion-exchanged glasses for SERS applications, ChemPhysChem. 12 (9) (2011) 1683–1688.

90. **Zhao J., Lin J., Zhang W., et al.,** SERS-active Ag nanoparticles embedded in glass prepared by a two-step electric field-assisted diffusion, Opt. Mater. 39 (Jan) (2015) 97–102.

91. **Huang H., Hu A., Sivayoganathan M., et al.,** Femtosecond laser fabrication of silver plasmonic structures for application as single particle SERS detectors, Mater. Res. Express. 1 (2) (2014) 025022.

92. **Yao Y., Zhao Y., Zhang H., et al.,** Ultrafast laser-induced 1T′/2H-MoTe2 nanopattern with Au-nanoclusters for Raman monitoring of cellular drug metabolism, ACS Nano. 19 (17) (2025) 16732–16743.

93. **Lun Y., Zhao B., Geng Y., et al.,** Reusable SERS platform of femtosecond laser processed substrate for detection of malachite green, Molecules. 29 (21) (2024) 5053.

94. **Ushkov A., Belozerova N., Dyubo D., et al.,** Laser-synthesized amorphous $PdSe_{2-x}$ nanoparticles: A defect-ich platform for high-efficiency SERS, photocatalysis, and photothermal conversion, Adv. Mater. Interfaces. (7 Dec) (2026) e00902.

95. **Chou S. Y., Krauss P. R., Renstrom P. J.,** Nanoimprint lithography, J. Vac. Sci. Technol. B. 14 (6) (1996) 4129–4133.

96. **Guo L. J.,** Nanoimprint lithography: Methods and material requirements, Adv. Mater. 19 (4) (2007) 495–513.

97. **Cottat M., Lidgi-Guigui N., Tijunelyte I., et al.,** Soft UV nanoimprint lithography-designed highly sensitive substrates for SERS detection, Nanoscale Res. Lett. 9 (21 Nov) (2014) 623.

98. **Malekian B., Xiong K., Emilsson G., et al.,** Fabrication and characterization of plasmonic nanopores with cavities in the solid support, Sensors. 17 (6) (2017) 1444.

99. **Gonзalves M. R., Makaryan T., Enderle F., et al.,** Plasmonic nanostructures fabricated using nanosphere-lithography, soft-lithography and plasma etching, Beilstein J. Nanotechnol. 2 (2011) 448–458.

100. **Bandarenka H. V., Girel K. V., Zavatski S. A., et al.,** Progress in the development of SERS-active substrates based on metal-coated porous silicon, Materials. 11 (5) (2018) 852.

101. **Lai Y., Wang J., He T., et al.,** Improved surface enhanced Raman scattering for nanostructured silver on porous silicon for ultrasensitive determination of 2,4,6-Trinitrotoluene, Anal. Lett. 47 (5) (2014) 833–842.

102. **Hu Y., Zhou Y., Luo G., et al.,** Femtosecond laser-induced nanoparticle implantation into flexible substrate for sensitive and reusable microfluidics SERS detection, Int. J. Extrem. Manuf. 6 (4) (2024) 045005.

103. **Skvortsov A., Babich E., Lipovskii A., et al.,** Raman scattering study of amino acids adsorbed on a silver nanoisland film, Sensors. 22 (14) (2022) 5455.

104. **Fatkhutdinova L. I., Babich E., Boldyrev K., et al.,** Rapid and sensitive detection of nucleoprotein SARS-CoV-2 virus: SERS vs ELISA, Photonic. Nanostruct. 57 (Dec) (2023) 101172.

105. **Yakimchuk D. V., Kaniukov E. Yu., Lepeshov S., et al.,** Self-organized spatially separated silver 3D dendrites as efficient plasmonic nanostructures for surface-enhanced Raman spectroscopy applications, J. Appl. Phys. 126 (23) (2019) 233105.

106. **He L., Lin M., Li H., et al.,** Surface-enhanced Raman spectroscopy coupled with dendritic silver nanosubstrate for detection of restricted antibiotics, J. Raman Spectrosc. 41 (7) (2010) 739–744.

107. **Dies H., Raveendran J., Escobedo C., et al.,** In situ assembly of active surface-enhanced Raman scattering substrates via electric field-guided growth of dendritic nanoparticle structures, Nanoscale. 9 (23) (2017) 7847–7857.

108. **Babich E. S., Lipovskii A. A., Lubyankina E. A.,** Pesticides detection by SERS using dendritic structures grown in glass, St. Petersburg Polytechnic University Journal. Physics and Mathematics. 16 (1.1) (2023) 374–379.

109. **Antsiferova A. A., Kashkarov P. K., Koval'chuk M. V.,** Effect of different forms of silver on biological objects, Nanobiotechnol. Rep. 17 (2) (2022) 155–164.

110. **Babich E., Scherbak S., Kirilenko D., et al.,** Glasses with biocompatible Au/Ag NPs of governed composition, J. Phys. D: Appl. Phys. 57 (13) (2024) 135302.

111. **Broquin J.-E., Honkanen S.,** Integrated photonics on glass: A review of the ion-exchange technology achievements, Appl. Sci. 11 (10) (2021) 4472.

112. **Righini G. C., Licares J.,** Active and quantum integrated photonic elements by ion exchange in glass, Appl. Sci. 11 (11) (2021) 5222.

113. **Yinlei H., Minghua W., Xihua L., et al.,** Recent development of ion-exchanged glass waveguide technology, 2006 Asian Optical Fiber Commun. & Optoelectronic Exposition & Conf., 24 – 27 Oct., Shanghai, China, IEEE (2006) 1–10.

114. **Conti G. N., Peyghambarian N., Ferrari M., et al.,** Rare-earth-doped glasses and ion-exchanged integrated optical amplifiers and lasers, Phil. Mag. B. 82 (6) (2002) 721–734.

115. **Prieto-Blanco X., Montero-Orille C., Linares J., et al.,** Quantum projectors implemented with optical directional couplers in ion-exchanged glasses, J. Lightwave Technol. 40 (23) (2022) 7676–7684.

116. **Berneschi S., Righini G. C., Pelli S.,** Towards a glass new world: The role of ion-exchange in modern technology, Appl. Sci. 11 (10) (2021) 4610.

117. **Righini G. C., Ferrari M., Lukowiak A., et al.,** Flexible glass: Myth and photonic technology, Materials. 18 (9) (2025) 2010.

118. **Huang Y., Zhuang S., Peng L., et al.,** Efficiency improvement of up–conversion luminescence of Yb^{3+}/Tm^{3+} co-doped tellurite glass microsphere, J. Alloys Compnd. 748 (5 Jun) (2018) 93–99.

119. **Singh S. K., Giri N.K., Rai D.K., et al.,** Enhanced upconversion emission in Er^{3+}-doped tellurite glass containing silver nanoparticles, Solid State Sci. 12 (8) (2010) 1480–1483.

120. **Mai H. H., Kaydashev V. E., Tikhomirov V. K., et al.,** Nonlinear optical properties of Ag nanoclusters and nanoparticles dispersed in a glass host, J. Phys. Chem. C. 118 (29) (2014) 15995–16002.

121. **Alonso Calafell I., Cox J. D., Radonjić M., et al.,** Quantum computing with graphene plasmons, npj Quantum Inf. 5 (02 May) (2019) 37.

122. **Bozhevolnyi S. I., Mortensen N. A.,** Plasmonics for emerging quantum technologies, Nanophotonics. 6 (5) (2017) 1185–1188.

123. **Tame M. S., McEnery K. R., Özdemir Ş. K., et al.,** Quantum plasmonics, Nat. Phys. 9 (6) (2013) 329–344.

СПИСОК ЛИТЕРАТУРЫ

1. **Bass M.** Handbook of optics. Vol. I: Geometrical and physical optics, polarized light, components and instruments. New York: McGraw-Hill, Inc., 1996. 1628 p.

2. **Bohm D., Pines D.** A collective description of electron interactions: III. Coulomb interactions in a degenerate electron gas // Physical Review. 1953. Vol. 92. No. 3. Pp. 609–625.

3. **Albella P., Garcia-Cueto B., González F., Moreno F., Wu P. C., Kim T.-H., Brown A., Yang Y., Everitt H. O., Videen G.** Shape matters: Plasmonic nanoparticle shape enhances interaction with dielectric substrate // Nano Letters. 2011. Vol. 11. No. 9. Pp. 3531–3537.

4. **Jain P. K., El-Sayed M. A.** Surface plasmon resonance sensitivity of metal nanostructures: Physical basis and universal scaling in metal nanoshells // The Journal of Physical Chemistry C. 2007. Vol. 111. No. 47. Pp. 17451–17454.

5. **Scherbak S. A., Shustova O. V., Zhurikhina V. V., Lipovskii A. A.** Electric properties of hemispherical metal nanoparticles: Influence of the dielectric cover and substrate // Plasmonics. 2015. Vol. 10. No. 3. Pp. 519–527.

6. **Rich R.** Advances in surface plasmon resonance biosensor analysis // Current Opinion in Biotechnology. 2000. Vol. 11. No. 1. Pp. 54–61.

7. **Écija-Arenas Б., Kirchner E.-M., Hirsch T., Fernández-Romero J. M.** Development of an aptamer-based SPR-biosensor for the determination of kanamycin residues in foods // Analytica Chimica Acta. 2021. Vol. 1169. 18 July. P. 338631.

8. **Zayats A. V., Smolyaninov I. I.** Near-field photonics: surface plasmon polaritons and localized surface plasmons // Journal of Optics A: Pure and Applied Optics. 2003. Vol. 5. No. 4. Pp. S16–S50.

9. **Kosubukin V. A.** Size dependence of light-field enhancement caused by surface plasmon excitation // Physics Letters A. 1991. Vol. 160. No. 6. Pp. 584–588.

10. **Климов В. В.** Наноплазмоника. 2-е изд. М.: Физматлит, 2010. 480 с.

11. **Novotny L.** Effective wavelength scaling for optical antennas // Physical Review Letters. 2007. Vol. 98. No. 26. P. 266802.

12. **Russell K.J., Liu T.-L., Cui S., Hu E.L.** Large spontaneous emission enhancement in plasmonic nanocavities // Nature Photonics. 2012. Vol. 6. No. 7. Pp. 459–462.

13. **Fan M., Andrade G. F. S., Brolo A. G.** A review on the fabrication of substrates for surface enhanced Raman spectroscopy and their applications in analytical chemistry // Analytica Chimica Acta. 2011. Vol. 693. No. 1–2. Pp. 7–25.

14. Поверхностные поляритоны. Электромагнитные волны на поверхностях и границах раздела сред. Сб. статей под ред. Аграновича В. М. и Миллса Д. Л. М.: Наука, 1985. 525 с.

15. **Zayats A. V., Smolyaninov I. I., Maradudin A. A.** Nano-optics of surface plasmon polaritons // Physics Reports. 2005. Vol. 408. No. 3–4. Pp. 131–314.

16. **Bolduc O. R., Pelletier J. N., Masson J.-F.** SPR biosensing in crude serum using ultralow fouling binary patterned peptide SAM // Analytical Chemistry. 2010. Vol. 82. No. 9. Pp. 3699–3706.

17. **Homola J., Yee S. S., Gauglitz G.** Surface plasmon resonance sensors: Review // Sensors and Actuators B: Chemical. 1999. Vol. 54. No. 1–2. Pp. 3–15.

18. **Monzyn-Hernández D., Villatoro J., Talavera D., Luna-Moreno D.** Optical-fiber surface-plasmon resonance sensor with multiple resonance peaks // Applied Optics. 2004. Vol. 43. No. 6. P. 1216.

19. **Днез А., Andrés M. V., Cruz J. L.** In-line fiber-optic sensors based on the excitation of surface plasma modes in metal-coated tapered fibers // Sensors and Actuators B: Chemical. 2001. Vol. 73. No. 2–3. Pp. 95–99.

20. **Mayer K. M., Hafner J. H.** Localized surface plasmon resonance sensors // Chemical Reviews. 2011. Vol. 111. No. 6. Pp. 3828–3857.

21. **Becker J., Trügler A., Jakab A., Hohenester U., Sönnichsen C.** The optimal aspect ratio of gold nanorods for plasmonic bio-sensing // Plasmonics. 2010. Vol. 5. No. 2. Pp. 161–167.

22. **Hohenester U.** Nano and quantum optics: An introduction to basic principles and theory (Book series "Graduate texts in physics"). Cham, Switzerland: Springer International Publishing, 2020. 665 p.

23. **Daniel W.L., Han M.S., Lee J.-S., Mirkin C.A.** Colorimetric nitrite and nitrate detection with gold nanoparticle probes and kinetic end points // Journal of the American Chemical Society. 2009. Vol. 131. No. 18. Pp. 6362–6363.

24. **Zhang J., Wang L., Pan D., Song S., Boey F. Y. C., Zhang H., Fan C.** Visual cocaine detection with gold nanoparticles and rationally engineered aptamer structures // Small. 2008. Vol. 4. No. 8. Pp. 1196–1200.

25. **Storhoff J.J., Elghanian R., Mucic R. C., Mirkin C. A., Letsinger R. L.** One-pot colorimetric differentiation of polynucleotides with single base imperfections using gold nanoparticle probes // Journal of the American Chemical Society. 1998. Vol. 120. No. 9. Pp. 1959–1964.

26. **Qin X., Yuan C.-L., Shi R., Wang S.-Z., Wang Y.-L.** Colorimetric detection of dopamine based on iodine-mediated etching of gold nanorods // Chinese Journal of Analytical Chemistry. 2021. Vol. 49. No. 1. Pp. 60–67.

27. **Li M., Cushing S. K., Wu N.** Plasmon-enhanced optical sensors: a review // The Analyst. 2015. Vol. 140. No. 2. Pp. 386–406.

28. **Kinkhabwala A., Yu Z., Fan S., Avlasevich Y., Müllen K., Moerner W. E.** Large single-molecule fluorescence enhancements produced by a bowtie nanoantenna // Nature Photonics. 2009. Vol. 3. No. 11. Pp. 654–657.

29. **Xie F., Pang J. S., Centeno A., Ryan M. P., Riley D. J., Alford N. M.** Nanoscale control of Ag nanostructures for plasmonic fluorescence enhancement of near-infrared dyes // Nano Research. 2013. Vol. 6. No. 7. Pp. 496–510.

30. **Vo-Dinh T.,** SERS chemical sensors and biosensors: new tools for environmental and biological analysis // Sensors and Actuators B: Chemical. 1995. Vol. 29. No. 1–3. Pp. 183–189.

31. **Zhurikhina V., Skvortsov A., Babich E., Redkov A.** Raman spectroscopy of amino acids using metal nanoisland films on glass // Proceedings of the 2021 International Conference on Electrical Engineering and Photonics (EExPolytech). IEEE, 14–15 October, St. Petersburg, Russian Federation, 2021. Pp. 168–170.

32. **Li M., Cushing S.K., Zhang J., Lankford J., Aguilar Z.P., Ma D., Wu N.** Shape-dependent surface-enhanced Raman scattering in gold–Raman-probe–silica sandwiched nanoparticles for biocompatible applications // Nanotechnology. 2012. Vol. 23. No. 11. P. 115501.

33. **Zong S., Wang Z., Chen H., Yang J., Cui Y.** Surface enhanced Raman scattering traceable and glutathione responsive nanocarrier for the intracellular drug delivery // Analytical Chemistry. 2013. Vol. 85. No. 4. Pp. 2223–2230.

34. **Ko E., Hwang J., Kim J. H., Lee J. H., Lee S. H., Tran V.-K., Chung W. S., Park C. H., Choo J., Seong G. H.** Electrochemical fabrication of nanostructures on porous silicon for biochemical sensing platforms // Analytical Sciences. 2016. Vol. 32. No. 6. Pp. 681–686.

35. **Babich E., Scherbak S., Lubyankina E., Zhurikhina V., Lipovskii A.** Power spectral density analysis for optimizing SERS structures // Sensors. 2022. Vol. 22. No. 2. P. 593.

36. **Batista E., Dos Santos D. P., Andrade G. F. S., Sant'Ana A. C., Brolo A. G., Temperini M. L. A.** Using polycarbonate membranes as templates for the preparation of au nanostructures for surface-enhanced Raman scattering // Journal of Nanoscience and Nanotechnology. 2009. Vol. 9. No. 5. Pp. 3233–3238.

37. **Miller E.N., Palm D.C., De Silva D., Parbatani A., Meyers A.R., Williams D. L., Thompson D. E.** Microsphere lithography on hydrophobic surfaces for generating gold films that exhibit infrared localized surface plasmon resonances // The Journal of Physical Chemistry B. 2013. Vol. 117. No. 49. Pp. 15313–15318.

38. **Zhurikhina V. V., Brunkov P. N., Melehin V. G., Kaplas T., Svirko Y., Rutckaia V. V., Lipovskii A. A.** Self-assembled silver nanoislands formed on glass surface via out-diffusion for multiple usages in SERS applications // Nanoscale Research Letters. 2012. Vol. 7. 17 December. P. 676.

39. **Babich E., Scherbak S., Asonkeng F., Maurer T., Lipovskii A.** Hot spot statistics and SERS performance of self-assembled silver nanoisland films // Optical Materials Express. 2019. Vol. 9. No. 10. P. 4090.

40. **Babich E., Raskhodchikov D., Redkov A., Hmima A., Nashchekin A., Lipovskii A.** Dendritic structures by glass electrolysis: Studies and SERS capability // Current Applied Physics. 2021. Vol. 24. April. Pp. 54–59.

41. **Skvortsov A., Babich E., Redkov A., Lipovskii A., Zhurikhina V.** Stable in biocompatible buffers silver nanoisland films for SERS // Biosensors. 2021. Vol. 11. No. 11. P. 448.

42. **Babich E., Reduto I., Redkov A., Reshetov I., Zhurikhina V., Lipovskii A.** Thermal poling of glasses to fabricate masks for ion exchange // Journal of Physics: Conference Series. 2020. Vol. 1695. 28 December. P. 012107.

43. **Babich E. S., Gangrskaia E. S., Reduto I. V., Béal J., Redkov A. V., Maurer T., Lipovskii A. A.** Self-assembled silver nanoparticles in glass microstructured by poling for SERS application // Current Applied Physics. 2019. Vol. 19. No. 10. Pp. 1088–1095.

44. **Ломоносов М. В.** Избранные философские произведения. М.: Госполитиздат, 1950. 759 с.

45. **Padovani S., Sada C., Mazzoldi P., Brunetti B., Borgia I., Sgamellotti A., Giulivi A., D'Acapito F., Battaglin G.** Copper in glazes of Renaissance luster pottery: Nanoparticles, ions, and local environment // Journal of Applied Physics. 2003. Vol. 93. No. 12. Pp. 10058–10063.

46. **Zachariasen W. H.,** The atomic arrangement in glass // Journal of the American Chemical Society. 1932. Vol. 54. No. 10. Pp. 3841–3851.

47. **Gy R.,** Ion exchange for glass strengthening // Materials Science and Engineering: B. 2008. Vol. 149. No. 2. Pp. 159–165.

48. **Giallorenzi T. G., West E. J., Kirk R., Ginther R., Andrews R. A.** Optical waveguides formed by thermal migration of ions in glass // Applied Optics. 1973. Vol. 12. No. 6. P. 1240.

49. **Ashley P. R., Bloemer M. J., Davis J. H.** Measurement of nonlinear properties in Ag-ion exchange waveguides using degenerate four-wave mixing // Applied Physics Letters. 1990. Vol. 57. No. 15. Pp. 1488–1490.

50. **Berger A.** Concentration and size depth profile of colloidal silver particles in glass surfaces produced by sodium-silver ion-exchange // Journal of Non-Crystalline Solids. 1992. Vol. 151. No. 1–2. Pp. 88–94.

51. **Cheng Z., Liu L., Xu S., Lu M., Wang X.** Temperature dependence of electrical and thermal conduction in single silver nanowire // Scientific Reports. 2015. Vol. 5. 02 June. P. 10718.

52. **Singh S. P., Karmakar B.** Single-step synthesis and surface plasmons of bismuth-coated spherical to hexagonal silver nanoparticles in dichroic Ag: Bismuth glass nanocomposites // Plasmonics. 2011. Vol. 6. No. 3. Pp. 457–467.

53. **Epifani M., Giannini C., Tapfer L., Vasanelli L.** Sol–gel synthesis and characterization of Ag and Au nanoparticles in SiO_2, TiO_2, and ZrO_2 thin films // Journal of the American Ceramic Society. 2000. Vol. 83. No. 10. Pp. 2385–2393.

54. **De Marchi G., Mattei G., Mazzoldi P., Sada C., Miotello A.** Two stages in the kinetics of gold cluster growth in ion-implanted silica during isothermal annealing in oxidizing atmosphere // Journal of Applied Physics. 2002. Vol. 92. No. 8. Pp. 4249–4254.

55. **Chen Y., Jaakola J. J., Säynätjoki A., Tervonen A., Honkanen S.** Glass-embedded silver nanoparticle patterns by masked ion-exchange process for surface-enhanced Raman scattering // Journal of Raman Spectroscopy. 2011. Vol. 42. No. 5. Pp. 936–940.

56. **Redkov A. V., Zhurikhina V. V., Lipovskii A. A.** Formation and self-arrangement of silver nanoparticles in glass via annealing in hydrogen: The model // Journal of Non-Crystalline Solids. 2013. Vol. 376. 15 September. Pp. 152–157.

57. **Abdel-Hameed S. A. M., Fathi A. M.** Preparation and characterization of silver nanoparticles within silicate glass ceramics via modification of ion exchange process // Journal of Alloys and Compounds. 2010. Vol. 498. No. 1. Pp. 71–76.

58. **Gonella F., Quaranta A., Cattaruzza E., Padovani S., Sada C., D'Acapito F., Maurizio C.** Cu-alkali ion exchange in glass: a model for the copper diffusion based on XAFS experiments // Computational Materials Science. 2005. Vol. 33. No. 1–3. Pp. 31–36.

59. **Дёмичев И. А., Сидоров А. И., Никоноров Н. В.** Особенности оптических свойств диффузионных слоев, полученных при последовательном обмене ионов натрия на ионы меди и серебра в силикатном стекле // Оптический журнал. 2015. Т. 82. № 11. С. 66–70.

60. **Sgibnev Y. M., Nikonorov N. V., Ignatiev A. I.** Luminescence of silver clusters in ion-exchanged cerium-doped photo-thermo-refractive glasses // Journal of Luminescence. 2016. Vol. 176. August. Pp. 292–297.

61. **Sgibnev Y., Nikonorov N., Ignatiev A.** Governing functionality of silver ion-exchanged photo-thermo-refractive glass matrix by small additives // Applied Sciences. 2021. Vol. 11. No. 9. P. 3891.

62. **Simo A., Polte J., Pfänder N., Vainio U., Emmerling F., Rademann K.** Formation mechanism of silver nanoparticles stabilized in glassy matrices // Journal of the American Chemical Society. 2012. Vol. 134. No. 45. Pp. 18824–18833.

63. **Qu X., Li Y., Li L., Wang Y., Liang J., Liang J.** Fluorescent gold nanoclusters: synthesis and recent biological application // Journal of Nanomaterials. 2015. Vol. 2015. 13 August. P. 84097.

64. **Саратовский А. С., Гирсова М. А., Анфимова И. Н., Антропова Т. В.** Формирование молекулярных кластеров серебра полимерно-солевым методом в пористых стеклах // Оптика и спектроскопия. 2023. Т. 131. № 1. С. 92–94.

65. **Kaganovskii Yu., Lipovskii A., Rosenbluh M., Zhurikhina V.** Formation of nanoclusters through silver reduction in glasses: The model // Journal of Non-Crystalline Solids. 2007. Vol. 353. No. 22–23. Pp. 2263–2271.

66. **Redkov A., Chervinskii S., Baklanov A., Reduto I., Zhurikhina V., Lipovskii A.** Plasmonic molecules via glass annealing in hydrogen // Nanoscale Research Letters. 2014. Vol. 9. 08 November. P. 606.

67. **Chervinskii S., Sevriuk V., Reduto I., Lipovskii A.** Formation and 2D-patterning of silver nanoisland film using thermal poling and out-diffusion from glass // Journal of Applied Physics. 2013. Vol. 114. No. 22. P. 224301.

68. **Hofmeister H., Thiel S., Dubiel M., Schurig E.** Synthesis of nanosized silver particles in ion-exchanged glass by electron beam irradiation // Applied Physics Letters. 1997. Vol. 70. No. 13. Pp. 1694–1696.

69. **Espiau de Lamaestre R., Béa1 H., Bernas H., Belloni J., Marignier J. L.** Irradiation-induced Ag nanocluster nucleation in silicate glasses: Analogy with photography // Physical Review B. 2007. Vol. 76. No. 20. P. 205431.

70. **Zhang J., Dong W., Qiao L., Li J., Zheng J., Sheng J.** Silver nanocluster formation in soda-lime silicate glass by X-ray irradiation and annealing // Journal of Crystal Growth. 2007. Vol. 305. No. 1. Pp. 278–284.

71. **Farah K., Hosni F., Mejri A., Boizot B., Hamzaoui A. H., Ben Ouada H.** Effect of gamma rays absorbed doses and heat treatment on the optical absorption spectra of silver ion-exchanged silicate glass // Nuclear Instruments and Methods in Physics Research Section B: Beam Interactions with Materials and Atoms. 2014. Vol. 323. 15 March. Pp. 36–41.

72. **Евстропьев С. К., Никоноров Н. В., Салимов Ш. К., Эшбеков А. А., Юдин Д. М.** Спектры ЭПР щелочносиликатных стекол, подвергнутых ионному обмену и гамма-облучению // Физика и химия стекла. 1991. Т. 17. № 1. С. 126–129.

73. **Kaganovsky Y. S., Antonov I., Ianetz D., Rosenbluh M., Ihlemann J., Müller S. G., Marowsky G., Lipovskii A.A.** Mass transfer in optical nanocomposites induced by pulsed laser irradiation // Solid State Phenomena. 2003. Vol. 94. June. Pp. 105–114.

74. **Marquestaut N., Petit Y., Royon A., Mounaix P., Cardinal T., Canioni L.** Three-dimensional silver nanoparticle formation using femtosecond laser irradiation in phosphate glasses: Analogy with photography // Advanced Functional Materials. 2014. Vol. 24. No. 37. Pp. 5824–5832.

75. **Rosenbluh M., Antonov I., Ianetz D., Kaganovskii Yu., Lipovskii A. A.** Microfabrication of structures by laser light in metal-doped glasses // Optical Materials. 2003. Vol. 24. No. 1–2. Pp. 401–410.

76. **Lo Faro M.J., D'Andrea C., Leonardi A. A., Morganti D., Irrera A., Fazio B.** Fractal silver dendrites as 3D SERS platform for highly sensitive detection of biomolecules in hydration conditions // Nanomaterials. 2019. Vol. 9. No. 11. P. 1630.

77. **Wang D., Astruc D.** Dendritic catalysis – Basic concepts and recent trends // Coordination Chemistry Reviews. 2013. Vol. 257. No. 15–16. Pp. 2317–2334.

78. **Zhou Y., Yu S. H., Wang C. Y., Li X. G., Zhu Y. R., Chen Z. Y.** A novel ultraviolet irradiation photoreduction technique for the preparation of single-crystal Ag nanorods and Ag dendrites // Advanced Materials. 1999. Vol. 11. No. 10. Pp. 850–852.

79. **Lee G.-J., Shin S.-I., Oh S.-G.** Preparation of silver dendritic nanoparticles using sodium polyacrylate in aqueous solution // Chemistry Letters. 2004. Vol. 33. No. 2. Pp. 118–119.

80. **Gutés A., Carraro C., Maboudian R.** Silver dendrites from galvanic displacement on commercial aluminum foil as an effective SERS substrate // Journal of the American Chemical Society. 2010. Vol. 132. No. 5. Pp. 1476–1477.

81. **Zhu J., Liu S., Palchik O., Koltypin Y., Gedanken A.** Shape-controlled synthesis of silver nanoparticles by pulse sonoelectrochemical methods // Langmuir. 2000. Vol. 16. No. 16. Pp. 6396–6399.

82. **Брунков П. Н., Липовский А. А., Мелехин В. Г., Редьков А. В., Стаценко В. В.** Формирование серебряных фрактальных структур в ионообменных стеклах при полинге // Журнал технической физики. 2015. Т. 85. № 2. С. 112–117.

83. **Grand J., de la Chapelle M. L., Bijeon J.-L., Adam P.-M., Vial A., Royer P.** Role of localized surface plasmons in surface-enhanced Raman scattering of shape-controlled metallic particles in regular arrays // Physical Review B: Condensed Matter and Materials Physics. 2005. Vol. 72. No. 3. P. 033407.

84. **Li P., Long F., Chen W., Chen J., Chu P. K., Wang H.** Fundamentals and applications of surface-enhanced Raman spectroscopy – based biosensors // Current Opinion in Biomedical Engineering. 2020. Vol. 13. March. Pp. 51–59.

85. **Mosier-Boss P.** Review of SERS substrates for chemical sensing // Nanomaterials. 2017. Vol. 7. No. 6. P. 142.

86. **Cheng W. D., Wu Z.J., Gu X.H., Lin F., Xing X.Q., Mo G., Wu Z.H.** GISAXS study on the size and distribution evolutions of Ag nanoparticles in ion-exchange glass during annealing // Materials Chemistry and Physics. 2015. Vol. 152. 15 February. Pp. 48–53.

87. **Inozemtsev V. A., Dokukin M. E., Sgibnev Y. M., Sherstyukova E. A., Kandrashina S. S., Shvedov M. A., Shelaev, A. V., Nikonorov N. V., Sergunova V. A., Baryshev A. V.** Na-Ag ion-exchanged glass substrates for plasmon-enhanced fluorescence imaging of neutrophils // Sensors. 2025. Vol. 25. No. 7. P. 2278.

88. **Kolobkova E., Kuznetsova M. S., Nikonorov N.** Ag/Na ion exchange in fluorophosphate glasses and formation of Ag nanoparticles in the bulk and on the surface of the glass // ACS Applied Nano Materials. 2019. Vol. 2. No. 11. Pp. 6928–6938.

89. **Simo A., Joseph V., Fenger R., Kneipp J., Rademann K.** Long-term stable silver subsurface ion-exchanged glasses for SERS applications // ChemPhysChem. 2011. Vol. 12. No. 9. Pp. 1683–1688.

90. **Zhao J., Lin J., Zhang W., Wei H., Chen Y.** SERS-active Ag nanoparticles embedded in glass prepared by a two-step electric field-assisted diffusion // Optical Materials. 2015. Vol. 39. January. Pp. 97–102.

91. **Huang H., Hu A., Sivayoganathan M., Duley W. W., Huang Z. H., Zhou Y.** Femtosecond laser fabrication of silver plasmonic structures for application as single particle SERS detectors // Materials Research Express. 2014. Vol. 1. No. 2. P. 025022.

92. **Yao Y., Zhao Y., Zhang H., Pan W., Liang W., Jiang Y., Yan X., Yan Y.** Ultrafast laser-induced 1T′/2H-MoTe2 nanopattern with Au-nanoclusters for Raman monitoring of cellular drug metabolism // ACS Nano. 2025. Vol. 19. No. 17. Pp. 16732–16743.

93. **Lun Y., Zhao B., Geng Y., Du W., Zhao X., Wang X.** Reusable SERS platform of femtosecond laser processed substrate for detection of malachite green // Molecules. 2024. Vol. 29. No. 21. P. 5053.

94. **Ushkov A., Belozerova N., Dyubo D., et al.** Laser-synthesized amorphous $PdSe_{2-x}$ nanoparticles: A defect-rich platform for high-efficiency SERS, photocatalysis, and photothermal conversion // Advanced Materials Interfaces. 2026. 7 December. P. e00902.

95. **Chou S. Y., Krauss P. R., Renstrom P. J.** Nanoimprint lithography // Journal of Vacuum Science & Technology B: Microelectronics and Nanometer Structures Processing, Measurement, and Phenomena. 1996. Vol. 14. No. 6. Pp. 4129–4133.

96. **Guo L. J.** Nanoimprint lithography: Methods and material requirements // Advanced Materials. 2007. Vol. 19. No. 4. Pp. 495–513.

97. **Cottat M., Lidgi-Guigui N., Tijunelyte I., Barbillon G., Hamouda F., Gogol P., Aassime A., Lourtioz J.-M., Bartenlian B., de la Chapelle M. L.** Soft UV nanoimprint lithography-designed highly sensitive substrates for SERS detection // Nanoscale Research Letters. 2014. Vol. 9. 21 November. P. 623.

98. **Malekian B., Xiong K., Emilsson G., Andersson J., Fager C., Olsson E., Larsson-Langhammer E., Dahlin A.** Fabrication and characterization of plasmonic nanopores with cavities in the solid support // Sensors. 2017. Vol. 17. No. 6. P. 1444.

99. **Gonзalves M. R., Makaryan T., Enderle F., Wiedemann S., Plettl A., Marti O., Ziemann P.** Plasmonic nanostructures fabricated using nanosphere-lithography, soft-lithography and plasma etching // Beilstein Journal of Nanotechnology. 2011. Vol. 2. Pp. 448–458.

100. **Bandarenka H. V., Girel K. V., Zavatski S. A., Panarin A., Terekhov S. N.** Progress in the development of SERS-active substrates based on metal-coated porous silicon // Materials. 2018. Vol. 11. No. 5. P. 852.

101. **Lai Y., Wang J., He T., Sun S.** Improved surface enhanced Raman scattering for nanostructured silver on porous silicon for ultrasensitive determination of 2,4,6-Trinitrotoluene // Analytical Letters. 2014. Vol. 47. No. 5. Pp. 833–842.

102. **Hu Y., Zhou Y., Luo G., Li D., Qu M.** Femtosecond laser-induced nanoparticle implantation into flexible substrate for sensitive and reusable microfluidics SERS detection // International Journal of Extreme Manufacturing. 2024. Vol. 6. No. 4. P. 045005.

103. **Skvortsov A., Babich E., Lipovskii A., Redkov A., Yang G., Zhurikhina V.** Raman scattering study of amino acids adsorbed on a silver nanoisland film // Sensors. 2022. Vol. 22. No. 14. P. 5455.

104. **Fatkhutdinova L.I., Babich E., Boldyrev K., et al.** Rapid and sensitive detection of nucleoprotein SARS-CoV-2 virus: SERS vs ELISA // Photonics and Nanostructures – Fundamentals and Applications. 2023. Vol. 57. December. P. 101172.

105. **Yakimchuk D. V., Kaniukov E. Yu., Lepeshov S., et al.** Self-organized spatially separated silver 3D dendrites as efficient plasmonic nanostructures for surface-enhanced Raman spectroscopy applications // Journal of Applied Physics. 2019. Vol. 126. No. 23. P. 233105.

106. **He L., Lin M., Li H., Kim N.-J.** Surface-enhanced Raman spectroscopy coupled with dendritic silver nanosubstrate for detection of restricted antibiotics // Journal of Raman Spectroscopy. 2010. Vol. 41. No. 7. Pp. 739–744.

107. **Dies H., Raveendran J., Escobedo C., Docoslis A.** In situ assembly of active surface-enhanced Raman scattering substrates via electric field-guided growth of dendritic nanoparticle structures // Nanoscale. 2017. Vol. 9. No. 23. Pp. 7847–7857.

108. **Lubyankina E. A., Babich E. S., Lipovskii A. A.,** Pesticides detection by SERS using dendritic structures grown in glass // St. Petersburg Polytechnic University Journal: Physics and Mathematics. 2023. Vol. 16. No. 1.1. Pp. 374–379.

109. **Antsiferova A. A., Kashkarov P. K., Koval'chuk M. V.** Effect of different forms of silver on biological objects // Nanobiotechnology Reports. 2022. Vol. 17. No. 2. Pp. 155–164.

110. **Babich E., Scherbak S., Kirilenko D., Kondratev V., Stupin D., Lipovskii A.** Glasses with biocompatible Au/Ag NPs of governed composition // Journal of Physics D: Applied Physics. 2024. Vol. 57. No. 13. P. 135302.

111. **Broquin J.-E., Honkanen S.** Integrated photonics on glass: A review of the ion-exchange technology achievements // Applied Sciences. 2021. Vol. 11. No. 10. P. 4472.

112. **Righini G. C., Licares J.** Active and quantum integrated photonic elements by ion exchange in glass // Applied Sciences. 2021. Vol. 11. No. 11. P. 5222.

113. **Yinlei H., Minghua W., Xihua L., Jianyi Y., Xiaoqing J., Qiang Z.** Recent development of ion-exchanged glass waveguide technology // 2006 Asian Optical Fiber Communication & Optoelectronic Exposition & Conference. 24–27 October, Shanghai, China, IEEE, 2006. Pp. 1–10.

114. **Conti G. N., Peyghambarian N., Ferrari M., Montagna M., Righini G. C., Brenci M., Forastiere M. A., Pelli S., Ricci G.** Rare-earth-doped glasses and ion-exchanged integrated optical amplifiers and lasers // Philosophical Magazine B. 2002. Vol. 82. No. 6. Pp. 721–734.

115. **Prieto-Blanco X., Montero-Orille C., Linares J., Gonzalez-Nunez H., Balado D.** Quantum projectors implemented with optical directional couplers in ion-exchanged glasses // Journal of Lightwave Technology. 2022. Vol. 40. No. 23. Pp. 7676–7684.

116. **Berneschi S., Righini G.C., Pelli S.** Towards a glass new world: The role of ion-exchange in modern technology // Applied Sciences. 2021. Vol. 11. No. 10. P. 4610.

117. **Righini G. C., Ferrari M., Lukowiak A., Macrelli G.** Flexible glass: Myth and photonic technology // Materials. 2025. Vol. 18. No. 9. P. 2010.

118. **Huang Y., Zhuang S., Peng L., Wu J., Liao T., Xu C., Duan Y.** Efficiency improvement of up-conversion luminescence of Yb^{3+}/Tm^{3+} co-doped tellurite glass microsphere // Journal of Alloys and Compounds. 2018. Vol. 748. 5 June. Pp. 93–99.

119. **Singh S. K., Giri N.K., Rai D.K., Rai S.B.** Enhanced upconversion emission in Er^{3+}-doped tellurite glass containing silver nanoparticles // Solid State Sciences. 2010. Vol. 12. No. 8. Pp. 1480–1483.

120. **Mai H. H., Kaydashev V. E., Tikhomirov V. K., Janssens E., Shestakov M. V., Meledina M., Turner S., Van Tendeloo G., Moshchalkov V. V., Lievens P.** Nonlinear optical properties of Ag nanoclusters and nanoparticles dispersed in a glass host // The Journal of Physical Chemistry C. 2014. Vol. 118. No. 29. Pp. 15995–16002.

121. **Alonso Calafell I., Cox J. D., Radonjić M., Saavedra J. R. M., Garcна de Abajo F. J., Rozema L. A., Walther P.** Quantum computing with graphene plasmons // npj Quantum Information. 2019. Vol. 5. 02 May. P. 37.

122. **Bozhevolnyi S. I., Mortensen N. A.** Plasmonics for emerging quantum technologies // Nanophotonics. 2017. Vol. 6. No. 5. Pp. 1185–1188.

123. **Tame M. S., McEnery K. R., Özdemir Ş. K., Lee J., Maier S. A., Kim M. S.** Quantum Plasmonics // Nature Physics. 2013. Vol. 9. No. 6. Pp. 329–344.

THE AUTHORS

ZHURIKHINA Valentina V.
Peter the Great St. Petersburg Polytechnic University
Alferov University, RAS
29 Politechnicheskaya St., St. Petersburg, 195251, Russia
zhurihina_vv@spbstu.ru
ORCID: 0000-0003-0685-9409

BABICH Ekaterina S.
Alferov University, RAS
8/3 Khlopin St., St. Petersburg, 194021, Russia
babich.katherina@gmail.com
ORCID: 0000-0003-4970-2591

TERPITSKIY Alexey N.
Alferov University, RAS
8/3 Khlopin St., St. Petersburg, 194021, Russia
terpiczkij@mail.ru
ORCID: 0000-0002-1744-5976

NURITDINOV Izzatillo
Institute of Nuclear Physics, Academy of Sciences of the Republic of Uzbekistan
Ulugbek settlement, Tashkent, 100214, Republic of Uzbekistan
izzatilloh@yahoo.com
ORCID: 0000-0002-9749-8751

RAKHMATOV Mashrab A. ogly
Sharof Rashidov Samarkand State University
15 University Blvd., Samarkand, 140100, Republic of Uzbekistan
mashrab-r@gmail.com

ESHBEKOV A'zamkul A.
Sharof Rashidov Samarkand State University
15 University Blvd, Samarkand, 140100, Republic of Uzbekistan
eshbekov-a@mail.ru
ORCID: 0000-0001-8283-791X

СВЕДЕНИЯ ОБ АВТОРАХ

ЖУРИХИНА Валентина Владимировна – *доктор физико-математических наук, профессор Высшей школы фундаментальных физических исследований Санкт-Петербургского политехнического университета Петра Великого, ведущий научный сотрудник лаборатории оптики гетерогенных структур и оптических материалов Академического университета имени Ж. И. Алфёрова РАН.*
195251, Россия, г. Санкт-Петербург, Политехническая ул., 29
zhurihina_vv@spbstu.ru
ORCID: 0000-0003-0685-9409

БАБИЧ Екатерина Сергеевна – *кандидат физико-математических наук, старший научный сотрудник лаборатории оптики гетерогенных структур и оптических материалов Академического университета имени Ж. И. Алфёрова РАН.*
194021, Россия, г. Санкт-Петербург, ул. Хлопина, 8, к. 3
babich.katherina@gmail.com
ORCID: 0000-0003-4970-2591

ТЕРПИЦКИЙ Алексей Николаевич – *инженер лаборатории оптики гетерогенных структур и оптических материалов Академического университета имени Ж. И. Алфёрова РАН.*
194021, Россия, г. Санкт-Петербург, ул. Хлопина, 8, к. 3
terpiczkij@mail.ru
ORCID: 0000-0002-1744-5976

НУРИТДИНОВ Иззатилло – доктор физико-*математических наук, профессор, главный научный сотрудник Института ядерной физики Академии наук Республики Узбекистан.*
100214, Республика Узбекистан, г. Ташкент, поселок Улугбек
izzatilloh@yahoo.com
ORCID: 0000-0002-9749-8751

РАХМАТОВ Машраб Анвар оглы – *аспирант кафедры физики твердого тела Самаркандского государственного университета имени Шарофа Рашидова.*
140100, Республика Узбекистан, г. Самарканд, Университетский б-р, 15
mashrab-r@gmail.com

ЭШБЕКОВ Азамкул Анорбоевич – *доктор физико-математических наук, доцент кафедры физики твердого тела Самаркандского государственного университета имени Шарофа Рашидова.*
140100, Республика Узбекистан, г. Самарканд, Университетский б-р, 15
eshbekov-a@mail.ru
ORCID: 0000-0001-8283-791X

Received 21.11.2025. Approved after reviewing 03.03.2026. Accepted 03.03.2026.
Статья поступила в редакцию 21.11.2025. Одобрена после рецензирования 03.03.2026. Принята 03.03.2026.

© Peter the Great St. Petersburg Polytechnic University, 2026

Original article
UDC 54.057
DOI: https://doi.org/10.18721/JPM.19211

STRUCTURAL PROPERTIES OF SOME NANOCRYSTALLINE SPINEL CHROMITES PREPARED BY SOLID-STATE REACTION METHOD

R. Yousef [1], A. Yousef [2], A. Nassif [3] ✉, Sh. A. Kadhim [4]

[1] Homs University, Homs, Syrian Arab Republic;
[2] Al-Hawash Private University, Homs, Syrian Arab Republic;
[3] Al-Wataniya Private University, Hama, Syrian Arab Republic;
[4] University of Kufa, An Najaf, Republic of Iraq
✉ nassifalaa85@gmail.com

Abstract. Chromium nanocomposites MCr_2O_4 have been synthesized by a solid-state reaction. The synthesized samples were characterized using X-ray powder diffraction technology (XRD). The temperature of synthesis was 1000°C for $NiCr_2O_4$ and 900°C for Zn Cr_2O_4. Miller indices (*hkl*) were calculated for the production, and the compounds were shown to have cubic structure FCC. The lattice parameters were as follows: $a = 8.26$ Å, $Z = 8$, $V = 564.26$Å^3 and $a = 8.2650$ Å, $Z = 8$, $V = 564.58$ Å^3 for $NiCr_2O_4$ and $ZnCr_2O_4$ respectively. The space group of symmetry is F*d*3*m* for the both. The grain sizes were calculated by the Debye − Scherrer formula for the two compounds and were 31.92 nm and 32.78 nm, respectively. The $ZnCr_2O_4$ and $NiCr_2O_4$ nanoparticles' morphology was examined using scanning electron microscopy (SEM). The SEM images showed the agglomeration of the nanoparticles, which were formed of square-shaped nanocrystallites.

Keywords: MCr_2O_4, spinel, solid-state reaction method, grain size

For citation: Nassif A., Yousef R., Yousef A., Kadhim Sh. A., Structural properties of some nanocrystalline spinel chromites prepared by solid-state reaction method, St. Petersburg State Polytechnical University Journal. Physics and Mathematics. 19 (2) (2026) 136–146. DOI: https://doi.org/10.18721/JPM.19211

This is an open access article under the CC BY-NC 4.0 license (https://creativecommons.org/licenses/by-nc/4.0/)

Научная статья
УДК 54.057
DOI: https://doi.org/10.18721/JPM.19211

СТРУКТУРНЫЕ СВОЙСТВА ДВУХ НАНОКРИСТАЛЛИЧЕСКИХ ХРОМШПИНЕЛЕЙ, ПОЛУЧЕННЫХ МЕТОДОМ ТВЕРДОФАЗНЫХ РЕАКЦИЙ

Р. Юсеф [1], А. Юсеф [2], А. Н ссиф [3] ✉, Ш. А. К дхим [4]

[1] Университет Хомса, г. Хомс, Сирийская Арабская Республика;
[2] Частный университет Аль-Хаваш, г. Хомс, Сирийская Арабская Республика;
[3] Частный университет Аль-Ватания, г. Хама, Сирийская Арабская Республика;
[4] Университет Куфы, г. Эн-Наджаф, Республика Ирак
✉ nassifalaa85@gmail.com

Аннотация. В работе были синтезированы нанокомпозиты хрома MCr_2O_4 методом твердофазных реакций. Значения температуры синтеза составили 1000°C для $NiCr_2O_4$ и 900°C для Zn Cr_2O_4. Были рассчитаны индексы Миллера (*hkl*) и показано, что соединения обладают гранецентрированной кубической структурой. Параметры решетки составили: $a = 8{,}26$ Å, $Z = 8$, $V = 564{,}26$ Å ($NiCr_2O_4$) и $a = 8{,}2650$ Å, $Z = 8$, $V = 564{,}58$ Å^3 ($ZnCr_2O_4$).

© Yousef R., Yousef A., Nassif A., Kadhim Sh. A., 2026. Published by Peter the Great St. Petersburg Polytechnic University.

Для обоих хромитов пространственная группа симметрии – F*d*3*m*. Размеры зерен, рассчитанные по формуле Дебая – Шеррера, составили 31,92 нм ($NiCr_2O_4$) и 32,78 нм ($ZnCr_2O_4$). Морфология наночастиц двух синтезированных хромитов была изучена с помощью сканирующей электронной микроскопии. На полученных изображениях была видна агломерация наночастиц, состоящая из квадратных нанокристаллитов.

Ключевые слова: MCr_2O_4, шпинель, метод твердофазных реакций, размер зерна

Для цитирования: Нассиф А., Юсеф Р., Юсеф А., Кадхим Ш. А. Структурные свойства двух нанокристаллических хромшпинелей, полученных методом твердофазной реакции // Научно-технические ведомости СПбГПУ. Физико-математические науки. 2026. Т. 19. № 2. С. 136–146. DOI: https://doi.org/10.18721/JPM.19211

Статья открытого доступа, распространяемая по лицензии CC BY-NC 4.0 (https://creativecommons.org/licenses/by-nc/4.0/)

Introduction

Mixed oxides of chromium with transition metals MCr_2O_4 where M = Ni, Zn, having a spinel structure [1], have attracted a lot of attention due to their great importance in many technical fields and their desirable industrial properties such as their high melting point, high resistance to acids and alkalis, high activity, and low production cost [2]. In recent years this fact has prompted researchers to improve and develop methods for synthesizing these materials. It is possible that the most common method for obtaining these oxides is the solid-state reaction [3], which depends on mechanical mixing of solid oxides and annealing them, in addition to many other chemical techniques that allow obtaining nanometer materials with a high degree of purity and greater homogeneity. Among them, such as the sol-gel method [2], the hydrothermal synthesis method [4], the co-precipitation method [5], and the combustion reaction method [6] are widely used.

In this research, the solid-state reaction method was adopted to synthesize a chromite – transition metal system, as the transition metal chromite has distinctive magnetic properties and is used as a catalyst in many reactions and is also used in the manufacture of gas sensors [6 – 9]. The solid-state reaction method is one of the most important ones for obtaining these compounds because of its ease of preparation, as it does not require special skills. Since some materials are difficult to dissolve in water, this method provides a solution to this problem in terms of preparing the desired compounds without the need to dissolve them in any solution. On the other hand, this advantage constitutes a high economic feasibility for the solid-state method, as the only material used in most of its reactions is acetone, which is used to facilitate the mixing of the solid compounds during the sample preparation process and in relatively small quantities.

This method is characterized by giving a high-purity mixture of what it requires of high-purity oxides without any impurities from different materials for synthesis when mixing compared to other synthesis methods. Stoichiometric ratios of the raw materials are taken in their pure form to ensure the completion of the reaction and obtain a single phase of the new pure material without the presence of other phases of impurities or raw materials [10, 11].

Experimental part

The samples of nickel chromite and zinc chromite were prepared by the solid-state reaction (SSR) method as powders by mixing appropriate amounts of nickel, zinc and chromium oxides $NiO : Cr_2O_3 = 1 : 1$ and $ZnO : Cr_2O_3 = 1 : 1$ in the presence of air. The primary nano oxides were ZnO (99% VWR International Ltd.), NiO (99% Chem-Lab.), and Cr_2O_3 (99.1% Genral Purpose Reagent). The chemical reactions between these oxides were as follows:

$$NiO + Cr_2O_3 \rightarrow NiCr_2O_4, \quad (1)$$

$$ZnO + Cr_2O_3 \rightarrow ZnCr_2O_4. \quad (2)$$

The previous materials were ground and mixed using an agate mortar to ensure obtaining a homogeneous mixture after adding an amount of acetone to improve the homogeneous mixing

© Юсеф Р., Юсеф А., Нассиф А., Кадхим Ш. А., 2026. Издатель: Санкт-Петербургский политехнический университет Петра Великого.

Table 1

The calculated masses of raw materials (oxides) used in the preparation of 10 g of each chromite

Oxide	*M*, g/mol	*m*, g
NiO : Cr_2O_3 = 1 : 1 (see Eq. (1))		
NiO	74.71	3.2951
Cr_2O_3	151.99	6.7048
ZnO : Cr_2O_3 = 1 : 1 (see Eq. (2))		
ZnO	81.37	3.487
Cr_2O_3	151.99	6.513
Cromites		
$NiCr_2O_4$	226.645	9.9999
$ZnCr_2O_4$	233.332	10.0000

Notations: *M*, *m* are respectively the molar mass and mass.

process for approximately 15 min until the acetone dried. This process was repeated three times in succession for each sample. After that, the resulting mixture was dried by heating it to a temperature of 100°C for a sufficient period of time to ensure the elimination of moisture. The raw materials' masses were calculated according to Eqs. (1) and (2) and are presented in Table 1. The required masses were estimated to get a 10 g amount of the resulting compound.

Subsequently, the powder was put inside a porcelain crucible and heated at various temperatures within the range from 600 to 1100°C for nickel chromite and from 600 to 900°C for zinc chromite. Six hours passed throughout the annealing process. After the preparation of zinc- and nickel-chromite nanoparticles the powder was compressed using a hydraulic press to create pellets with a radius of 0.5 cm and a thickness of 0.2 cm under a pressure of 10 t/m^2. The pressing process increased the interaction between the particles by bringing them closer to one another.

Results and discussion

X-ray diffraction (XRD) analysis. The prepared samples were characterised by the X-ray diffraction (XRD) technique (Philips-PW-1840, $\lambda_{CoK\alpha}$ = 1.7889 Å). By XRD technique the optimum temperature for synthesis was determined, which was the temperature that indicated the appearance of a single phase, i.e. obtaining the desired compound. In this investigation, it was 1000°C for the nickel chromite compound and 900°C for the zinc chromite compound, at which a single compound was obtained and all diffraction peaks indicated the raw materials NiO, ZnO, Cr_2O_3 being absent.

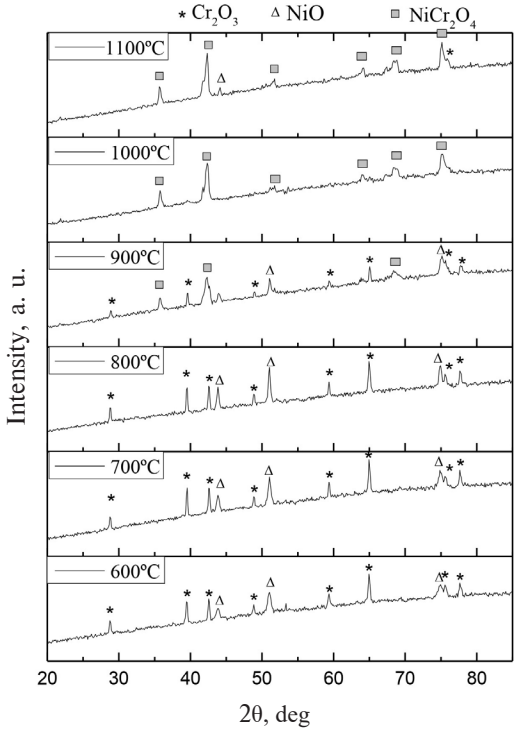


Fig. 1. XRD patterns of the prepared nickel chromite annealed at different temperatures for six hours

The scanning process was carried out using angles within the range 2θ = (20 − 85)° with an angle step of 0.02° and a time step of 2 s. The same angular range was used for all scanning processes. For the measurement procedure, the powder samples were placed on special substrates to eliminate background radiation, while the pellet samples were placed directly on the sample holder, aligned correctly with the substrate used for the powder. After collecting the diffraction data (peak positions and their intensities), the intensity values were plotted against the Bragg diffraction angle 2θ. The crystal lattice constants were then calculated from the positions of the characteristic peaks of the compound.

Nickel chromite $NiCr_2O_4$. Fig. 1 shows the XRD patterns of $NiCr_2O_4$ samples which were annealed in the temperature range from 600°C to 1100°C for 6 hrs. This data exhibited that the initial annealing process did not lead to any reaction between the raw materials, as the resulting peaks indicated a mixture of raw materials, and there was no peak indicating the desired compound.

Therefore, 600ºC could not be considered an optimum temperature for the synthesis of nickel chromite compound, and the resulting mixture was the one of thermally uncombined primary oxides only. For this reason, we gradually raised the annealing temperature while monitoring the synthesis through the resulting pattern, and we found that the primary oxides did not react with each other at all, and the peaks' locations or their intensities did not change until 900ºC. At this temperature, we noticed a clear decrease in the intensities of the peaks that were due to the raw materials, but they did not disappear, in addition to the appearance of three new peaks indicating the nickel chromite compound at the angles 2θ = 35.6º, 42.2º, 68.3º which prompted us to raise the annealing temperature to 1000ºC to ensure that the synthesis was completed perfectly at this temperature or higher temperatures were required to obtain better results. When the resulting compound was annealed at 1000ºC, we noticed that the peaks due to the primary oxides disappeared completely and that all intensive diffraction peaks were attributed to the $NiCr_2O_4$ compound. Therefore, it could be considered that a pure phase of the $NiCr_2O_4$ compound was obtained that did not contain any intermediate phases or any phases of the starting materials from which the synthesis process was finished at 1000ºC. When the annealing temperature was raised to 1100ºC, we noticed the appearance of some peaks due to the starting materials again. Consequently, it became clear to us that the $NiCr_2O_4$ compound began to decompose at 1100ºC and that 1000ºC was the optimal temperature for the synthesis of the $NiCr_2O_4$ compound. The result we reached is consistent with the published practical work [12].

All the diffraction peaks were indexed and compared with the standard JCPDS, ICSD data of the starting NiO, Cr_2O_3 oxides and $NiCr_2O_4$ compound of the numbers 04-0835, 38-1479 and 23-1271 respectively. Fig. 2 shows the XRD pattern of $NiCr_2O_4$, which was annealed at 1000ºC for 6 hrs because that was the optimal temperature for $NiCr_2O_4$ compound synthesis.

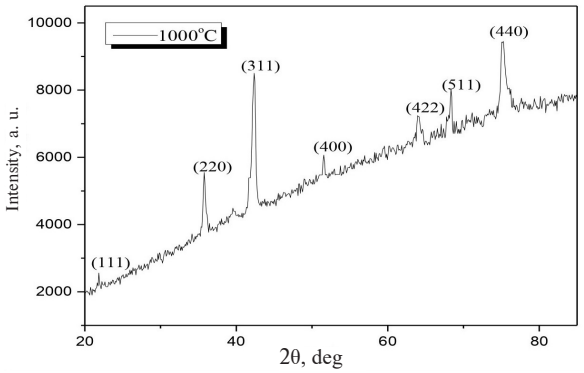


Fig. 2. XRD patterns of the prepared nickel chromite $NiCr_2O_4$ annealed at 1000°C for six hours

Miller indices of diffraction peaks were determined for the $NiCr_2O_4$ compound. These peaks indicate that the $NiCr_2O_4$ has a cubic structure and belongs to the F*d*3*m* space group. From X-ray diffraction measurements of $NiCr_2O_4$, the distance between crystal lattices *d* were calculated using the Bragg law [12]:

$$n\lambda = 2d\cdot\sin\theta,$$

where λ = 1.7889 Å is the X-ray wavelength and θ is the diffraction angle.

Then the values of the lattice constant were determined using the relation of the distance between parallel crystal plans in the case of the cubic crystal structure that is given by the formula [14]:

$$(d_{hkl})^2 = a^2/(h^2 + k^2 + l^2), \qquad (3)$$

where *a* is the lattice constant.

The values of the distance between parallel crystal plans and the lattice constant of $NiCr_2O_4$ for each diffracting peak are listed in Table 2.

An analysis of the data in Table 2 allows us to conclude that the peaks belonging to the Miller indexes (400), (311), (220) are the most intensive, and we find that they meet the conditions:

$$h + k = 2k,\ k + 1 = 2n,\ h + 1 = 2n.$$

Table 2

The results of X-ray diffraction (XRD) analysis for $NiCr_2O_4$ compound annealed at 1000ºC

2θ, dg	I/I_0, %	d_{hkl}, Å	*a*, Å	(*hkl*)
35.668	55	2.919	8.256	(220)
42.210	100	2.483	8.234	(311)
51.380	22	2.062	8.249	(400)
63.901	22	1.689	8.276	(422)
68.363	35	1.591	8.268	(511)
75.122	50	1.467	8.296	(440)

Notations: I/I_0 is the normalized intensity of diffraction peaks, d_{hkl} is the interplanar distance, *a* is the lattice constant, (*hkl*) are the Miller indices

That is, the basic cell is face-centered and therefore the compound crystallizes in Face-Centered Cubic (FCC) type. The average lattice constant of $NiCr_2O_4$ is presented in Table 3. The unit cell volume was also calculated by the following formula:

$$V = a^3 \quad (4)$$

and given in Table 3.

Table 3

Additional structural data for $NiCr_2O_4$ compound

a, Å	V, Å^3	ρ, g/cm^3		Z
		Theoretical	Experimental	
8.2634	564.26	5.3006	5.331	8

Notations: a is the average value of the lattice constant, V is the unit cell volume, ρ is the compound density, Z is the number of formulae in the unit cell.

The experimental density ρ_{exp} of $NiCr_2O_4$ was measured by the pycnometer method (distilled water was used for immersion; its density was 0.99705 g/cm^3 at 25°C). To ensure reproducibility of the results, we repeated each measurement at least 3 times for each sample. The average value is given in Table 3. The theoretical X-ray density for prepared nickel chromite was calculated as follows [11]:

$$\rho_{th} = ZM/N_A V, \quad (5)$$

where Z is the number of formula units in the unit cell ($Z = 8$ for the spinel lattice), M is the molecular mass of the nickel chromite, N_A is the Avogadro number, V is the unit cell volume.

Regarding $Z = 8$, we can write the general formula for the content of the basic cell as follows: $Ni_8Cr_{16}O_{32}$. Thus, one cell contains eight nickel atoms, sixteen chromium ones, and 32 oxygen ones. Substituting the value of Z as an integer in Eq. 5 gives us the value of the theoretical density (see Table 3). The calculated result is very close to the experimental value, which proves the accuracy of our theoretical calculations and the accuracy of our choice of the basic cell unit. The crystallite size of the $NiCr_2O_4$ compound was calculated using Scherrer's formula [14, 15]:

$$L = 0.9\lambda/(\beta \cdot \cos\theta), \quad (6)$$

where β, rad, is the full width at half-maximum (FWHM) of diffraction peaks; λ is the X-ray wavelength (λ = 1.78897); θ is the Bragg reflection angle.

The estimated values of crystallite size for each diffracting peak of $NiCr_2O_4$ compound were calculated using X'pert HighScore software and listed in Table 4. The average crystallite size was 31.92 nm, so the prepared compound had a nanostructure.

Table 4

The broadening of diffraction peaks and average grain size of $NiCr_2O_4$ compound annealed at 1000°C

Peak number	Peak position	β_{obs}	β_{std}	Grain size L, nm	
	degrees			Peak	Averaged
1	35.668	0.295	0.001	33.0	31.92
2	42.210	0.394		25.2	
3	51.380	0.295		34.8	
4	63.900			37.0	
5	68.363	0.296		37.8	
6	75.122	0.492		23.7	

Zinc chromite $ZnCr_2O_4$. Fig. 3 shows the X-ray diffraction patterns of the annealed nickel chromite compound $ZnCr_2O4$ within the temperature range from 600 to 900°C, where it appears that annealing at temperatures of 600°C to 800°C led to the formation of the zinc chromite compound, but with the presence of other peaks that refer to the raw materials, indicating that the thermal reaction is incomplete. It was found from Fig. 3 that all intensive diffraction peaks were attributed to the $ZnCr_2O_4$ compound for the sample annealed at 900°C, where the reaction between primary materials was completed. This indicates that the optimum temperature for $ZnCr_2O_4$ compound synthesis is 900°C which is lower than the temperature of nickel chromite formation.

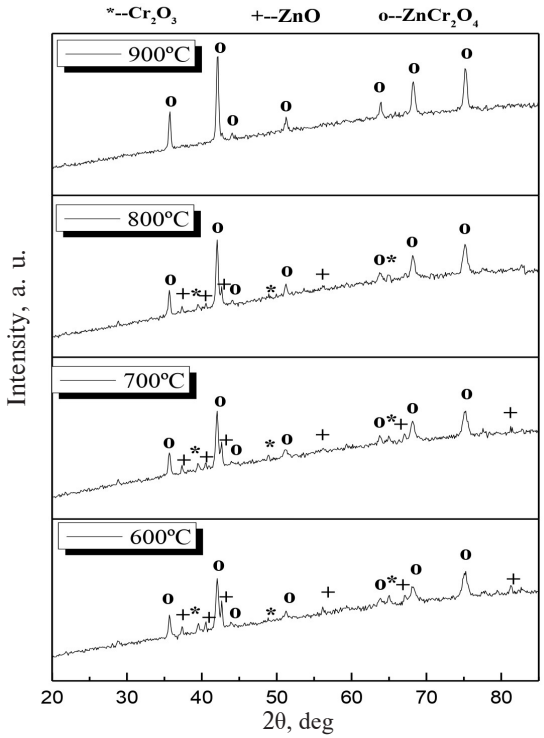


Fig. 3. XRD patterns of the prepared zinc chromite $ZnCr_2O_4$ annealed at different temperatures for six hours

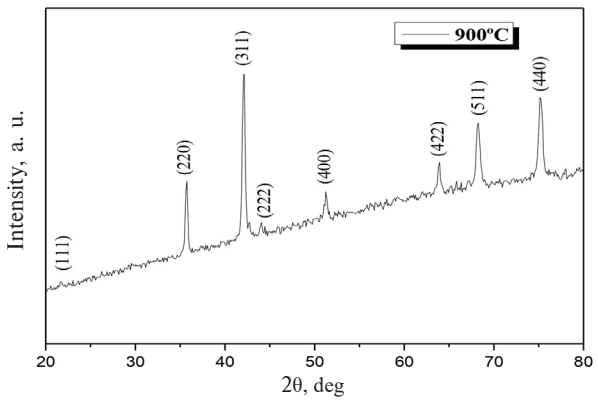


Fig. 4. XRD patterns of the prepared zinc chromite $ZnCr_2O_4$ annealed at 900°C for six hours

All the diffraction peaks were indexed and compared with the standard JCPDS, ICSD data of the starting ZnO and Cr_2O_3 oxides and $ZnCr_2O_4$ compound of the numbers 36-1451, 38-1479 and 24-495 respectively. Fig. 4 shows the XRD pattern of $ZnCr_2O_4$, which was annealed at 900 °C for 6 hrs because that is the optimal temperature for the $ZnCr_2O_4$ compound synthesis.

Miller indices of diffraction peaks were determined for $ZnCr_2O_4$ cromite. These peaks indicated that $ZnCr_2O_4$ had a cubic structure and belonged to the space group F*d3m*. From X-ray diffraction measurements of $ZnCr_2O_4$, the distance between crystal lattices and the values of the lattice constant were determined using the Bragg law and Eq. 3 for cubic crystal structure. The calculated result is listed in Table 5. The results show that the compound belongs to the cubic symmetry pattern, and all the Miller index values for all peaks agree with this crystallization pattern, which is consistent with Eq. 3.

Table 5

The results of X-ray diffraction (XRD) analysis for $ZnCr_2O_4$ compound annealed at 900°C

2θ, dg	I/I_0, %	d_{hkl}, Å	*a*, Å	(*hkl*)
21.704	6	4.7484	8.2245	(111)
35.675	45	2.9186	8.2549	(220)
42.066	100	2.4909	8.2614	(311)
44.031	7	2.3849	8.2615	(222)
51.246	16	2.0674	8.2692	(400)
63.8476	13	1.6906	8.2824	(422)
68.2505	35	1.5936	8.2804	(511)
75.2356	40	1.4646	8.2852	(440)

All notations are identical to those used in Table 2

The unit cell volume of $ZnCr_2O_4$ was calculated by Eq. 4. This value and other structural calculations such as the average lattice constant, the experimental density, the theoretical X-ray

Table 6

Additional structural data for $ZnCr_2O_4$ compound

a, Å	*V*, Å^3	ρ, g/cm^3		*Z*
		Theoretical	Experimental	
8.2650	564.58	5.49	5.45	8

All notations are identical to those used in Table 3

density, and the number of formula units in the single crystal cell are listed in Table 6. Regarding $Z = 8$, we can write the general formula for the content of the basic cell as follows: $Zn_8Cr_{16}O_{32}$. The crystallite size of the $ZnCr_2O_4$ compound was calculated using Eq. 6. The estimated values of crystallite size for each diffracting peak of $ZnCr_2O_4$ compound were calculated using X'pert HighScore software (see Table 7). The average crystallite size was 32.78 nm. Hence, the prepared compound is characterized by a nanostructure.

Table 7

The broadening of diffraction peaks and average grain size of $ZnCr_2O_4$ compound annealed at 900°C

Peak number	Peak position	β_{obs}	β_{std}	Grain size *L*, nm	
	degrees			Peak	Averaged
1	21.704	0.295	0.001	31.9	32.78
2	35.675	0.295		33.0	
3	42.066	0.295		33.6	
4	44.031			33.8	
5	51.246	0.295		34.8	
6	63.848	0.295		37.0	
7	68.251	0.394		28.4	
8	75.236	0.394		29.7	

Table 8

A comparison of the results of structural calculations for $NiCr_2O_4$ and $ZnCr_2O_4$

Compound	*a*, Å	*V*, Å^3	ρ, g/cm^3		*Z*	*L*
			Experimental	Calculated		
$NiCr_2O_4$	8.2634	564.26	5.331	5.30	8	31.92
$ZnCr_2O_4$	8.2650	564.58	5.450		8	32.78

Table 9

A comparison of our results with those obtained from literature

Compound	*a*, Å		*V*, Å^3	
	Our work	Other authors	Our work	Other authors
$NiCr_2O_4$	8.263	8.32 [17, 16]	564.26	575.96 [17, 16]
		8.27 [19, 18]		566.66 [19, 18]
$ZnCr_2O_4$	8.265	8.280 [17, 16]	564.58	567.66 [17, 16]
		8.325 [19, 18]		576.96[19, 18]

The results obtained from the previous calculations for both nickel chromite and zinc chromite compounds are arranged in Table 8. Based on those mentioned earlier, we conclude that the solid synthesis method, a straightforward and reasonably priced preparation technique, can create chromium-based spinels at temperatures between 800 and 1000°C. Furthermore, the nanoscale particle size produced by this preparation technique makes these compounds suitable for use in gas sensitivity applications, electrodes, and other fields.

Table 9 shows a comparison of the results we obtained with some other scientific works.

Scanning electron microscopy (SEM). The morphology of the $ZnCr_2O_4$ and $NiCr_2O_4$ nanoparticles was investigated using scanning electron microscopy (SEM). Fig. 5 displays the SEM images of $ZnCr_2O_4$ and $NiCr_2O_4$ nanoparticles synthesized by solid-state reactions. They show the agglomeration of the nanoparticles, which are formed up of square-shaped nanofine crystallites.

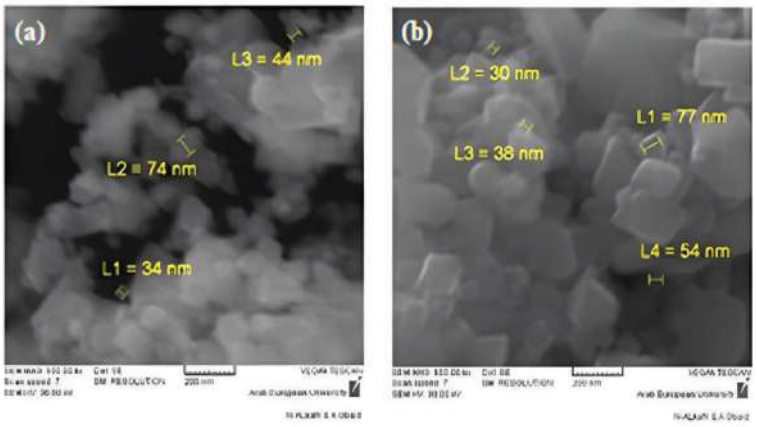


Fig. 5. SEM images of $NiCr_2O_4$ (*a*) and $ZnCr_2O_4$ (*b*) nanoparticles prepared by the solid-state method at 1000°C (*a*) and 900°C (*b*) for 6 hours

Summary

This work has shown that the straightforward and economical solid-state reaction approach can be used to synthesize nickel chromite and zinc chromite nanoparticles successfully, with the optimal synthesis temperatures of 1000°C and 900°C, respectively. Both compounds had nanoscale grain sizes of about 32 nm and crystallized in a face-centered cubic (F*d3m*) structure. The solid-state reaction approach is an effective method to create chromium-based nanocomposites since it can yield highly pure, nanostructured spinel phases at comparatively low synthesis temperatures. The produced compounds are excellent prospects for technical uses including gas sensors, electrodes, and other cutting-edge functional materials because of these structural features.

Acknowledgment

The authors would like to thank the technical team in XRD Lab at Homs University for financial support.

REFERENCES

1. **Fairooz N. Y., Imran A. R.,** Wet commixing synthesis, physical properties and photocatalytical activity of nickel oxide chromite spinel, J. Appl. Chem. 2 (Jan) (2013) 129–136.

2. **Habibi M., Fakhri F.,** Fabrication and characterization of $CuCr_2O_4$ nanocomposite by XRD, FESEM, FTIR and DRS, Synth. React. Inorg. Met.-Org. Nano-Met. Chem. 46 (6) (2016) 847–851.

3. **Ishibashi H., Yasumi T.,** Structural transition of spinel compound $NiCr_2O_4$ at ferrimagnetic transition temperature, J. Magn. Magn. Mater. 310 (2, P. 2) (2007) e610–e612.

4. **Durrani S. K., Hussain S. Z., Saeed K., et al.,** Hydrothermal synthesis and characterization of nanosized transition metal chromite spinels, Turk. J. Chem. 36 (1) (2012) 111–120.

5. **Safaei-Ghomi J., Akbarzadeh Z., Khojastehbakht-Koopaei B.,** C–N cross-coupling reaction catalysed by reusable $CuCr_2O_4$ nanoparticles under ligand-free conditions: a highly efficient synthesis of triarylamines, RSC Adv. 5 (37) (2015) 28879–28884.

6. **Abu Bakar S., Ahad N., Bin Saion E.,** Thermal treatment synthesis and characterization of nanosized nickel chromite spinels, Proc. 2012 Int. Conf. of Solid State Sci & Technol. (ICSSST-2012), Dec. 18 − 20, 2012. Holiday Inn, Malacca, Malaysia; JEOL. Serving Advanced Technology (2013) 47−54.

7. **Barros B., Costa A. C. F. M., Kiminami R. H. G. A., da Gama L.,** Preparation and characterization of spinel MCr_2O_4 (M = Zn, Co, Cu and Ni) by combustion reaction, J. Metastab. Nanocryst. Mater. 20−21 (07 Jul) (2004) 325−332.

8. **Tomiyasu K., Kagomiya I.,** Magnetic structure of $NiCr_2O_4$ studied by neutron scattering and magnetization measurements, J. Phys. Soc. Jpn. 73 (9) (2004) 2539−2542.

9. **Ptak M., Maczka M., Gągor A., et al.**, Temperature-dependent XRD, IR, magnetic, SEM and TEM studies of Jahn − Teller distorted $NiCr_2O_4$ powders, J. Solid State Chem. 201 (May) (2013) 270−279.

10. **West A. R.,** Solid state chemistry and its applications. Second edition, student edition, John Wiley & Sons, Ltd; Chichester, New York, 2022.

11. **Gao H., Guo J., Li Y., et al.,** Highly selective and sensitive xylene gas sensor fabricated from $NiO/NiCr_2O_4$ p-p nanoparticles, Sens. Actuator. B. Chem. 284 (1 Apr) (2019) 305−315.

12. **Muhammed S. A., Abbas N. K.,** Synthesis and investigation of structural and optical properties of CdO:Ag nanoparticles of various concentrations, Baghdad Sci. J. 20 (5) (2023) 32.

13. **Noshahi N. A., Nadeem K., Kamran M.,** Role of Mn doping on magnetic properties of multiferroic $NiCr_2O_4$ nanoparticles, Ceram. Int. 47 (8) (2021) 10643−10649.

14. **Bakar S. A., Soltani N., Yunus W. M. M., et al.,** Structural and paramagnetic behavior of spinel $NiCr_2O_4$ nanoparticles synthesized by thermal treatment method: Effect of calcination temperature, Solid State Commun. 192 (Aug) (2014) 15−19.

15. **Enhessari M., Salehabadi A., Khanahmadzadeh S., et al.,** Modified sol-gel processing of $NiCr_2O_4$ nanoparticles; structural analysis and optical band gap, High Temp. Mater. Process. 36 (22 Jun) (2017) 121−125.

16. **Joshi P., Saxena P., Choudhary P., et al.,** Structural and vibrational response in Al modified $NiCr_2O_4$, AIP Conf. Proc. 2100 (Apr) (2019) 020174.

17. **Yazdanbakhsh M., Khosravi I., Goharshadi E. K., Youssefi A.,** Fabrication of nanospinel $ZnCr_2O_4$ using sol-gel method and its application on removal of azo dye from aqueous solution, J. Hazard. Mater. 184 (1−3) (2010) 684−689.

18. **Kumar K. V., Bhavani S. D.,** Influence of calcination temperature on physical and optical properties of nickel chromite nanoparticles, Sci. Sinter. 54 (4) (2022) 457−468.

19. **Ghosh D., Dutta U., Haque A., et al.,** Ultra-high sensitivity of luminescent $ZnCr_2O_4$ nanoparticles toward nitroaromatic explosives sensing, Dalton Trans. 47 (14) (2018) 5011−5018.

СПИСОК ЛИТЕРАТУРЫ

1. **Fairooz N. Y., Imran A. R.** Wet commixing synthesis, physical properties and photocatalytical activity of nickel oxide chromite spinel // Journal of Applied Chemistry. 2013. Vol. 2. January. Pp. 129−136.

2. **Habibi M., Fakhri F.** Fabrication and characterization of $CuCr_2O_4$ nanocomposite by XRD, FESEM, FTIR and DRS // Synthesis and Reactivity in Inorganic, Metal-Organic and Nano-Metal Chemistry. 2016. Vol. 46. No. 6. Pp. 847−851.

3. **Ishibashi H., Yasumi T.** Structural transition of spinel compound $NiCr_2O_4$ at ferrimagnetic transition temperature // Journal of Magnetism and Magnetic Materials. 2007. Vol. 310. No. 2. Part 2. Pp. e610−e612.

4. **Durrani S. K., Hussain S. Z., Saeed K., Khan Y., Arif M., Akhmed N.** Hydrothermal synthesis and characterization of nanosized transition metal chromite spinels // Turkish Journal of Chemistry. 2012. Vol. 36. No. 1. Pp. 111−120.

5. **Safaei-Ghomi J., Akbarzadeh Z., Khojastehbakht-Koopaei B.** C−N cross-coupling reaction catalysed by reusable $CuCr_2O_4$ nanoparticles under ligand-free conditions: A highly efficient synthesis of triarylamines // RSC Advances. 2015. Vol. 5. No. 37. Pp. 28879−28884.

6. **Abu Bakar S., Ahad N., Bin Saion E.** Thermal treatment synthesis and characterization of nanosized nickel chromite spinels // Proceedings of 2012 International Conference of Solid State Sciences and Technology (ICSSST-2012). December 18 – 20, 2012. Holiday Inn, Malacca, Malaysia. JEOL. Serving Advanced Technology. 2013. Pp. 47–54.

7. **Barros B., Costa A. C. F. M., Kiminami R. H. G. A., da Gama L.** Preparation and characterization of spinel MCr_2O_4 (M = Zn, Co, Cu and Ni) by combustion reaction // Journal of Metastable and Nanocrystalline Materials. 2004. Vol. 20–21. 07 July. Pp. 325–332.

8. **Tomiyasu K., Kagomiya I.** Magnetic structure of $NiCr_2O_4$ studied by neutron scattering and magnetization measurements // Journal of the Physical Society of Japan. 2004. Vol. 73. No. 9. 2539–2542.

9. **Ptak M., Maczka M., Gągor A., Pikul A., Macalik L., Hanuza J.** Temperature-dependent XRD, IR, magnetic, SEM and TEM studies of Jahn – Teller distorted $NiCr_2O_4$ powders // Journal of Solid State Chemistry. 2013. Vol. 201. May. Pp. 270–279.

10. **Вест А.** Химия твердого тела. Теория и приложения. В 2-х ч. Пер. с англ. М.: Мир, 1988. Ч. 1 – 558 с. Ч. 2 – 334 с.

11. **Gao H., Guo J., Li Y., et al.** Highly selective and sensitive xylene gas sensor fabricated from $NiO/NiCr_2O_4$ p-p nanoparticles // Sensors and Actuators B: Chemical. 2019. Vol. 284. 1 April. Pp. 305–315.

12. **Muhammed S. A., Abbas N. K.** Synthesis and investigation of structural and optical properties of CdO:Ag nanoparticles of various concentrations // Baghdad Science Journal. 2023. Vol. 20. No. 5. P. 32.

13. **Noshahi N. A., Nadeem K., Kamran M.** Role of Mn doping on magnetic properties of multiferroic $NiCr_2O_4$ nanoparticles // Ceramics International. 2021. Vol. 47. No. 8. Pp. 10643–10649.

14. **Bakar S. A., Soltani N., Yunus W. M. M., Saion E., Bahrami A.** Structural and paramagnetic behavior of spinel $NiCr_2O_4$ nanoparticles synthesized by thermal treatment method: Effect of calcination temperature // Solid State Communications. 2014. Vol. 192. August. Pp. 15–19.

15. **Enhessari M., Salehabadi A., Khanahmadzadeh S., Arkat K., Nouri J.** Modified sol-gel processing of $NiCr_2O_4$ nanoparticles; structural analysis and optical band gap // High Temperature Materials and Processes. 2017. Vol. 36. 22 June. Pp. 121–125.

16. **Joshi P., Saxena P., Choudhary P., Varshney M. D., Mishra A.** Structural and vibrational response in Al modified $NiCr_2O_4$ // AIP Conference Proceedings. 2019. Vol. 2100. No. 1. April. P. 020174.

17. **Yazdanbakhsh M., Khosravi I., Goharshadi E. K., Youssefi A.** Fabrication of nanospinel $ZnCr_2O_4$ using sol-gel method and its application on removal of azo dye from aqueous solution // Journal of Hazardous Materials. 2010. Vol. 184. No. 1–3. Pp. 684–689.

18. **Kumar K. V., Bhavani S. D.** Influence of calcination temperature on physical and optical properties of nickel chromite nanoparticles // Science of Sintering. 2022. Vol. 54. No. 4. Pp. 457–468.

19. **Ghosh D., Dutta U., Haque A., Mordvinova N. E., Lebedev O. I., Pal K., Gayen A., Seikh M. M., Mahata P.** Ultra-high sensitivity of luminescent $ZnCr_2O_4$ nanoparticles toward nitroaromatic explosives sensing // Dalton Transactions. 2018. Vol. 47. No. 14. Pp. 5011–5018.

THE AUTHORS

YOUSEF Rasha
Homs University
PP75+5VC, Damascus – Aleppo Highway, Homs, Syrian Arab Republic
ryousef@homs-univ.edu.sy

YOUSEF Areej
Al-Hawash Private University
Q8HJ+RMH, Al-Mouzeina, Homs, Syrian Arab Republic
areejyousef@hpu.edu.sy

NASSIF Alaa
Al-Wataniya Private University
XQ92+PMC, Hama, Syrian Arab Republic
nassifalaa85@gmail.com
ORCID: 0000-0001-6190-4642

KADHIM Shaymaa Awad
University of Kufa
P.O. Box 21, Kufa, Najaf Governorate, 540011, Republic of Iraq
shaymaa.alshebly@uokufa.edu.iq
ORCID: 0000-0002-3991-5318

СВЕДЕНИЯ ОБ АВТОРАХ

ЮСЕФ Раша – *PhD в области физики конденсированного состояния, преподаватель Университета Хомса, г. Хомс, Сирийская Арабская Республика.*
PP75+5VC, Syrian Arab Republic, Homs, Damascus – Aleppo Highway, Homs University
ryousef@homs-univ.edu.sy

ЮСЕФ Аридж – *PhD, преподаватель Частного университета Аль-Хаваш, г. Хомс, Сирийская Арабская Республика.*
Q8HJ+RMH, Syrian Arab Republic, Homs, Al-Mouzeina, Al-Hawash University
areejyousef@hpu.edu.sy

НАССИФ Алаа – *доктор военных наук, профессор инженерного факультета Частного университета Аль-Ватания, г. Хама, Сирийская Арабская Республика.*
XQ92+PMC, Syrian Arab Republic, Hama, Al-Wataniya Private University
nassifalaa85@gmail.com
ORCID: 0000-0001-6190-4642

КАДХИМ Шаймаа Авад – *PhD, профессор кафедры физики Университета Куфы, г. Эн-Наджаф, Республика Ирак.*
P.O. Box 21, Republic of Iraq, Kufa, Najaf Governorate, 540011, Kufa University
shaymaa.alshebly@uokufa.edu.iq
ORCID: 0000-0002-3991-5318

Received 30.09.2025. Approved after reviewing 08.12.2025. Accepted 08.12.2025.
Статья поступила в редакцию 30.09.2025. Одобрена после рецензирования 08.12.2025. Принята 08.12.2025.

© Санкт-Петербургский политехнический университет Петра Великого, 2026

BIOPHYSICS AND MEDICAL PHYSICS

Original article
DOI: https://doi.org/10.18721/JPM.19212

DIFFERENCES IN THE INTERACTION OF RAD51 AND UvsX RECOMBINASES WITH DNA REVEALED BY SINGLE-MOLECULE EXPERIMENTS

I. D. Goncharov, A. I. Sadova, I. M. Nuzhin, P. A. Tenitskaya, I. V. Kurdyumova, A. A. Gorkovskaia, M. A. Khodorkovskiy✉, A. A. Alekseev

Peter the Great St. Petersburg Polytechnic University

✉ khodorkovskii@gmail.com

Abstract. Nucleoprotein filaments formed by recombinase proteins on DNA are key structures of the homologous recombination process, which ensures the maintenance of the genome stability. Filament formation on DNA leads to a significant change in the mechanical properties of the complex, in particular to DNA lengthening, while the kinetics of filament assembly depends on mechanical tension. Using optical tweezers, this study has obtained data on the assembly dynamics of human RAD51 recombinase and bacteriophage T6 UvsX recombinase filaments on double-stranded DNA under varying mechanical tension. In the range between 3 and 12 pN, RAD51 efficiently bound to DNA, forming filaments with a high coverage. In contrast to RAD51, an efficient UvsX filament formation occurred only under high tension (12 pN), whereas UvsX binding to DNA was severely restricted at 3–6 pN. The different tendency of the two recombinases to interact with DNA reflected their adaptation to cellular environments and regulatory mechanisms governing homologous recombination.

Keywords: homologous recombination, RAD51, UvsX, RecA, cancer treatment, recombinase polymerase amplification, optical tweezers, nucleoprotein filament

Funding: The reported study was funded by Russian Science Foundation (Grant No. 24-74-00107, “Conformational states of RAD51 recombinase”).

Citation: Goncharov I. D., Sadova A. I., Nuzhin I. M., Tenitskaya P. A., Kurdyumova I. V., Gorkovskaia A. A., Khodorkovskiy M. A., Alekseev A. A., Differences in the interaction of recombinases RAD51 and UvsX with DNA revealed by single-molecule experiments, St. Petersburg State Polytechnical University Journal. Physics and Mathematics. 19 (2) (2026) 147–159. DOI: https://doi.org/10.18721/JPM.19212

This is an open access article under the CC BY-NC 4.0 license (https://creativecommons.org/licenses/by-nc/4.0/)

© Goncharov I. D., Sadova A. I., Nuzhin I. M., Tenitskaya P. A., Kurdyumova I. V., Gorkovskaia A. A., Khodorkovskiy M. A., Alekseev A. A., 2026. Published by Peter the Great St. Petersburg Polytechnic University.

Научная статья
УДК 577.24
DOI: https://doi.org/10.18721/JPM.19212

РАЗЛИЧИЯ ВО ВЗАИМОДЕЙСТВИИ РЕКОМБИНАЗ RAD51 И UvsX С ДНК, ВЫЯВЛЕННЫЕ В ЭКСПЕРИМЕНТАХ НА УРОВНЕ ОДИНОЧНЫХ МОЛЕКУЛ

И. Д. Гончаров, А. И. Садова, И. М. Нужин, П. А. Теницкая, И. В. Курдюмова, А. А. Горьковская, М. А. Ходорковский✉, А. А. Алексеев

Санкт-Петербургский политехнический университет Петра Великого, Санкт-Петербург, Россия

✉ khodorkovskii@gmail.com

Аннотация. Нуклеопротеиновые филаменты, формируемые белками-рекомбиназами на ДНК, являются ключевыми структурами процесса гомологичной рекомбинации, обеспечивающей поддержание стабильности генома. Формирование филамента на ДНК приводит к значительному изменению механических свойств комплекса, в частности к удлинению ДНК, при этом кинетика сборки филамента зависит от механического натяжения. В работе с помощью метода оптического захвата получены данные о динамике сборки филаментов RAD51 человека и UvsX бактериофага T6 на двухцепочечной ДНК при различных силах механического натяжения. В диапазоне 3–12 пН RAD51 эффективно связывается с ДНК, формируя филаменты с высокой степенью покрытия. В отличие от RAD51, эффективное формирование филаментов UvsX происходит только при высоком натяжении (12 пН), тогда как при значениях 3–6 пН связывание UvsX с ДНК существенно ограничено. Различная склонность двух рекомбиназ к взаимодействию с ДНК отражает адаптацию к клеточным условиям и механизмам регуляции гомологичной рекомбинации.

Ключевые слова: гомологичная рекомбинация, RAD51, UvsX, RecA, онкотерапия, рекомбиназная полимеразная амплификация, метод оптического захвата, нуклеопротеиновый филамент

Финансирование: Исследование выполнено при финансовой поддержке Российского научного фонда (грант № 24-74-00107: «Конформационные состояния рекомбиназы RAD51»).

Ссылка для цитирования: Гончаров И. Д., Садова А. И., Нужин И. М., Теницкая П. А., Курдюмова И. В., Горьковская А. А., Ходорковский М. А., Алексеев А. А. Различия во взаимодействии рекомбиназ RAD51 и UvsX с ДНК, выявленные в экспериментах на уровне одиночных молекул // Научно-технические ведомости СПбГПУ. Физико-математические науки. 2026. Т. 2 № .19. С. 147–159. DOI: https://doi.org/10.18721/JPM.19212

Статья открытого доступа, распространяемая по лицензии CC BY-NC 4.0 (https://creativecommons.org/licenses/by-nc/4.0/)

Introduction

Homologous recombination is a key mechanism for maintaining genome stability, enabling cells to repair DNA double-strand breaks, restart stalled replication forks, and exchange genetic material during meiosis [1, 2]. Recombinases play a central role in homologous recombination; they are highly conserved DNA-binding proteins that coat single-stranded DNA (ssDNA), forming a nucleoprotein filament. This filament searches for a homologous sequence on another DNA molecule and promotes strand invasion [3, 4].

© Гончаров И. Д., Садова А. И., Нужин И. М., Теницкая П. А., Курдюмова И. В., Горьковская А. А., Ходорковский М. А., Алексеев А. А., 2026. Издатель: Санкт-Петербургский политехнический университет Петра Великого.

The eukaryotic recombinase RAD51, the bacterial recombinase RecA, and the phage recombinase UvsX belong to the same superfamily, which is represented in all domains of life [5, 6]. The phage recombinase UvsX is functionally closer to the bacterial RecA protein, participating in homologous recombination, recombination-dependent replication, and DNA repair in infected host cells [7, 8]. All members of the superfamily contain a conserved RecA-like ATPase domain with Walker A and Walker B motifs, which are involved in ATP binding and hydrolysis, regulating the assembly, stability, and dissociation of the nucleoprotein filament [5, 9–12].

RecA is the most thoroughly studied member of the family. The structure of its helical filament, intermonomer contacts, and monomer structure are known at near-atomic resolution owing to XRD analysis and cryo-electron microscopy [3, 9]. The functions of RecA in the SOS response, homologous recombination, replication fork restart, horizontal gene transfer, and biofilm formation are well characterized [13–18]. The DNA-dependent ATPase activity of RecA was measured: its k_{cat} values are 30 min^{-1} for the RecA filament on ssDNA and 20 min^{-1} on double-stranded DNA (dsDNA) [19].

Human RAD51 is the focus of considerable attention because increased expression of this recombinase in tumors confers resistance to DNA-damaging chemotherapeutic agents, making this protein a promising candidate for targeted therapy [20–22]. The ATPase activity of human RAD51 was characterized in [23], where it was shown that the catalytic constant k_{cat} is 0.21 min^{-1} in the presence of ssDNA and 0.07–0.11 min^{-1} in the presence of dsDNA.

The UvsX recombinase of T-even phages is substantially less studied than bacterial or eukaryotic homologs, although interest in its properties has increased considerably in recent years due to its use in recombinase polymerase amplification (RPA) [24, 25]. During RPA, UvsX forms nucleoprotein filaments on single-stranded primers and mediates their invasion into a double-stranded DNA template, allowing DNA polymerase to begin synthesis of a new strand without thermal denaturation of the duplex. The highest activity of UvsX among homologs makes this enzyme preferable for use in RPA. For example, according to the literature, the catalytic constant k_{cat} of hydrolysis for UvsX reaches 240–500 min^{-1}, which is an order of magnitude higher than the corresponding value for the bacterial RecA protein [26, 27].

The nucleoprotein filament formed by recombinases is a key structural unit of homologous recombination, providing homology search and strand invasion into donor DNA [28]. Binding of recombinases to DNA leads to significant lengthening of the molecule (approximately 1.5-fold) compared with B-form DNA and to changes in its mechanical properties, including stiffness and elasticity [9, 29–31].

Optical tweezers allow these structural transformations to be monitored in real time at the level of single DNA molecules, since changes in their length are measured under controlled external tension.

This work presents data on the assembly kinetics of nucleoprotein filaments of human RAD51 and bacteriophage T6 UvsX on dsDNA at different applied tensions. The results were obtained using optical tweezers.

Materials and methods

DNA construct. Linear dsDNA, 11,100 base pairs (bps) long, was used for single-molecule DNA experiments. The molecules had an identical natural sequence and carried biotin modifications at both ends for specific attachment to streptavidin-functionalized microspheres. A detailed procedure for obtaining and purifying such DNA constructs is described in [12, 32].

Preparation of purified proteins. Recombinant human RAD51 and bacteriophage T6 UvsX proteins were obtained by expression in *Escherichia coli* strains BLR(DE3)pLysS for RAD51 and Rosetta(DE3) for UvsX. Plasmids encoding the corresponding proteins fused to a polyhistidine tag were used. Cells were grown in Lysogeny broth (LB) medium to an optical density of 0.6, induced with isopropyl-D-1-thiogalactopyranoside (IPTG), and additionally incubated at 37 °C for 3 h. The target protein was purified from the resulting cell biomass by affinity chromatography on Ni-NTA agarose (NTA is nitrilotriacetic acid). The cell lysate was loaded onto the column in a buffer with 50 mM imidazole, after which the protein was eluted with a stepwise imidazole gradient. The resulting preparations had a purity of at least 95%, as confirmed by sodium dodecyl sulfate–polyacrylamide gel electrophoresis (SDS–PAGE). Purified proteins were stored at −80°C in a buffer supplemented with 10% glycerol. A detailed protein purification procedure is described in [33, 34].

Laser tweezers setup. The unique Laser Tweezers setup, assembled based on a non-inverted Axio Imager.Z1 microscope (Carl Zeiss), was used for the experiments. The setup allows for optical trapping with two independent traps simultaneously by splitting the laser radiation (Nd:YAG, $\lambda = 1064$ nm, Spectra Physics, model BL-106C) by a polarizing beam splitter into two components polarized in mutually perpendicular directions. The beams were focused using an immersion objective with a high numerical aperture (NA = 1.25). To move the trap across the sample plane, the beam was directed through a mirror mounted on a piezoelectric positioning stage.

The experimental setup was supplemented with a u-Flux multi-channel microfluidics system (LUMICKS B.V.) for laminar flow and buffer exchange around the sample. The microfluidic chamber was mounted on a motorized microscope stage with three-axis positioning. Images were recorded with an iXon Ultra 897 camera (Andor Technology) with an electron-multiplying CCD array. Video data processing to determine the distance between microspheres and the corresponding DNA stretching force was performed in real time by specialized software we developed in the LabVIEW environment. The stiffness of the optical traps was calibrated from the viscous drag force experienced by a trapped microsphere moving at a given speed in a liquid medium of known viscosity.

Single-molecule DNA experiments

To perform DNA manipulations, microspheres and the DNA molecule attached between them were transferred between channels with laminar flows. Streptavidin-functionalized polystyrene microspheres 2.1 μm in diameter were captured in two independent optical traps in the first channel of the microfluidic system. These microspheres were then transferred to the second channel containing a DNA solution at a concentration of 30 pM. Under these conditions, one DNA molecule was attached to the microspheres via biotin–streptavidin bonds at its ends, thus fixing the DNA between two microspheres. After such fixation, this system was pre-stretched to a force of 10–20 pN in a channel containing only buffer solution to check the integrity of the molecule and exclude multiple attachments. Next, the DNA fixed between the microspheres was transferred to the fourth channel of the microfluidic system containing RAD51 or UvsX recombinase at a concentration of 300 nM.

The buffer solution used had the following composition:

40 mM Tris-HCl (pH 7.5); 0.02% BSA; 1 mM DTT; 5 mM $MgCl_2$; 2 mM ATP.

The assembly of the nucleoprotein filament on the DNA molecule was recorded under these conditions. Measurements were performed in force-clamp mode in the range of 3–12 pN at 22 °C. Nucleoprotein filament assembly was monitored in real time by the increase in the length of the DNA molecule upon complex formation.

The optical trapping method used in this work allows manipulating single biomolecules and monitoring changes in their mechanical properties by controlling the tension force (in the range from fractions of a piconewton to hundreds of piconewtons) and recording the extension of the molecule with nanometer resolution.

Results and discussion

The binding kinetics of RAD51 and UvsX recombinases to DNA was studied using 11,100 bps long dsDNA. A single DNA molecule was trapped by combining the optical tweezers method with the microfluidic system (Fig. 1,*a*). At a fixed tension force, the DNA molecule has an almost constant length determined by entropic and enthalpic contributions to the elastic response. The experimentally obtained dependence of tension force on extension for the DNA construct used is shown in Fig. 1,*b*.

Transfer of the trapped DNA molecule into the channel containing RAD51 recombinase led to nucleoprotein filament assembly. A constant tension force was applied to the sample during incubation, and a change in length was recorded. Fig. 2 shows representative assembly curves of the RAD51 filament obtained at tension forces $F = 3$ pN, 6 pN and 12 pN. The assembly kinetics of the RAD51 filament were only weakly sensitive to variations in the applied tension. In all cases, the complex length reached saturation within 60–80 s.

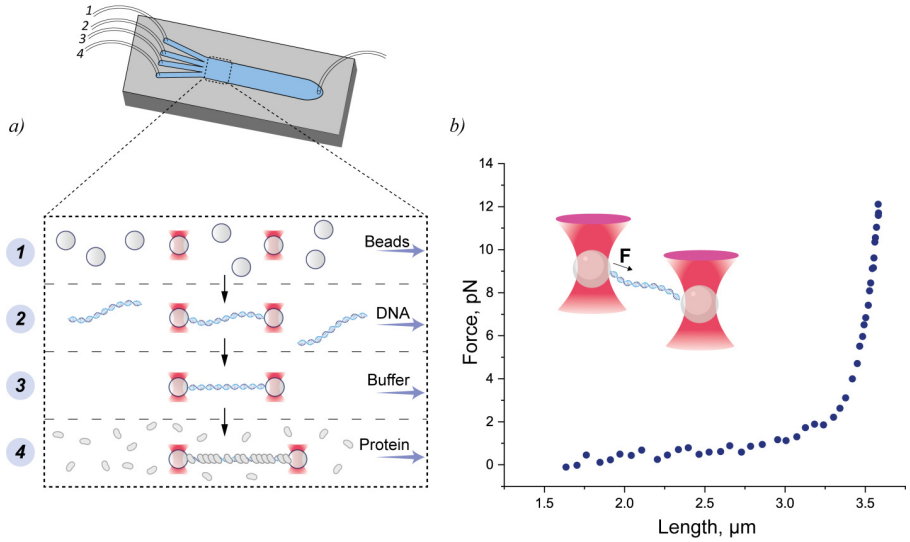


Fig. 1. Graphical representation of single-molecule DNA experiments: schematic image of microfluidic chamber with four laminar flows *1–4* (*a*); example of obtained dependence of tension *F* (pN) on the length of the DNA molecule used in this work (*b*)

The final values of the filament length were

4.82 ± 0.09 μm ($N = 4$) for $F = 3$ pN;

5.02 ± 0.04 μm ($N = 6$) for $F = 6$ pN;

4.99 ± 0.11 μm ($N = 4$) for $F = 12$ pN.

It is useful to compare the results obtained on the final DNA elongation upon assembly of the RAD51–DNA filament with data known from structural studies. According to structural data, DNA in the primary site of the nucleoprotein filament is elongated approximately 1.5-fold relative to the contour length of B-form DNA [5, 35]. The contour length of the DNA molecules used (11,000 bps) is about 3.7 μm. Due to entropic factors, the DNA length recorded as the end-to-end distance was shorter than the contour length and amounted to approximately 3.5 μm at $F = 6$ pN. A 1.5-fold increase of this value gives an estimate of 5.25 μm for the length of filaments formed on the double-stranded DNA used, which agrees with the final DNA elongation of 1.5 μm recorded in the experiments. This result indicates a fairly high degree of DNA coverage by RAD51 recombinase in the formed nucleoprotein filaments.

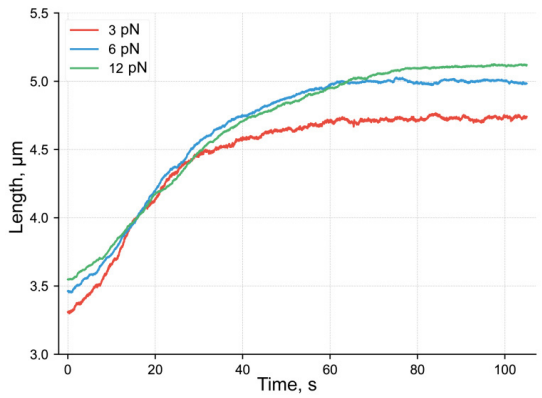


Fig. 2. Representative kinetic curves of RAD51 filament assembly on double-stranded DNA (dsDNA) at three different tension forces

Similarly, the assembly kinetics of UvsX filaments were studied. In contrast to RAD51, complete assembly of the nucleoprotein filament was observed only upon application of force $F = 12$ pN (Fig. 3,*a*). At $F = 3$ pN, no DNA elongation was observed during incubation in the UvsX channel, whereas at $F = 6$ pN only a limited increase in length was recorded, which did not reach a stationary value (during the observation time) corresponding to a 1.5-fold DNA elongation (Fig. 3,*b*).

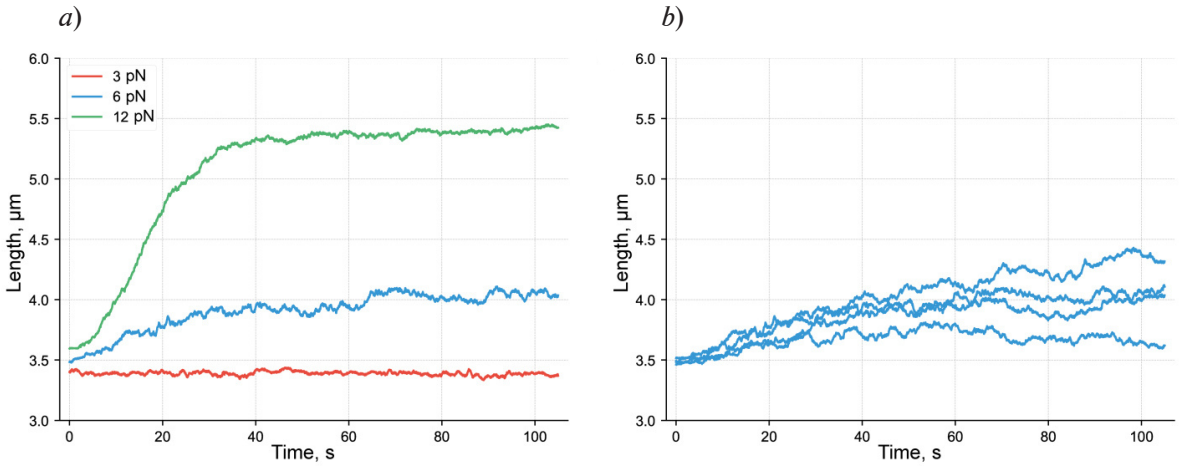


Fig. 3. Observations of UvsX filament assembly on dsDNA:
representative assembly curves at three F values, pN: 3, 6, and 12 (*a*);
UvsX filament assembly curves at $F = 6$ pN (*b*)

At $F = 12$ pN, the complex length reached saturation within 30–40 s, and the final length was 5.4 ± 0.1 μm ($N = 5$). This value is slightly higher than those observed at the same force for RAD51, but it also agrees with an approximately 1.5-fold DNA elongation. The exact filament length recorded in experiments using optical tweezers is determined, in addition to the tension force, by a number of factors, including the degree of DNA coverage by protein, the helix pitch of the filament, the number of monomers per helix turn, the persistence length, and the local presence of regions in an inactive conformation associated with ATP hydrolysis. Nevertheless, structural studies show that filaments formed by recombinases are characterized by DNA elongation of approximately 1.5-fold compared with the length of B-form DNA [9, 30, 31]. The observation of complexes with a greater length, for example at $F = 12$ pN, may indicate the assembly of UvsX filaments with a higher degree of DNA coverage than that of RAD51 filaments under these conditions.

Despite the prevailing opinion about the lower activity of RAD51 recombinase compared with RecA and UvsX, the results obtained indicate its ability to efficiently bind to dsDNA.

It is known from the literature that such binding is difficult for RecA recombinase from the Gram-negative bacterium *Escherichia coli*, typically observed only upon application of a sufficiently high external tension force exceeding 20 pN [32].

The activity of RAD51 recombinase in the cell is controlled by a number of mediator proteins, primarily at the stage of assembly of the nucleoprotein filament on ssDNA [5]. *In vitro*, RAD51 demonstrates increased efficiency of invasion of the 5′-terminal ssDNA fragment during catalysis of strand exchange, compared with the 3′-terminal fragment, which contrasts with the behavior of RecA, for which the 3′-terminal region is preferred [36]. It was shown that the efficiency of 3′-terminal fragment invasion is restored for RAD51 recombinase with duplex DNA with a single-stranded overhang.

In most models of homologous recombination, the assembly of the nucleoprotein filament on ssDNA in the presence of additional proteins, both competing for binding to ssDNA and stimulating the loading of the recombinase onto ssDNA, is considered the key initial stage. However, the natural substrate formed as a result of DNA processing and available for interaction with the recombinase is a hybrid DNA including a dsDNA region transitioning into a 3′-terminal single-stranded fragment. It can therefore be assumed that the assembly of a stable RAD51 filament on dsDNA can further increase (through cooperative interactions) the conformational stability of the RAD51 filament on ssDNA, promoting homologous recombination. The relationship between the conformational states of different regions of the filament formed on hybrid DNA was previously demonstrated for RecA recombinase [37].

UvsX recombinase is considered the most active and therefore the most popular choice for recombinase polymerase amplification systems. The catalytic constant of ATP hydrolysis for UvsX exceeds the corresponding value for RAD51 by three orders of magnitude. During infection of a cell by T-even bacteriophages, UvsX recombinase ensures recombination-dependent replication of multiple copies of the viral genome at late stages of infection, making it possible to synthesize hundreds of copies of phage DNA in a compressed time frame [38]. Uncontrolled binding of UvsX to dsDNA could interfere with replication processes under conditions of intensive phage DNA synthesis, as well as lead to unnecessary ATP consumption. In the case of RAD51, such interaction of the recombinase with dsDNA seems more likely and is not accompanied by significant ATP overconsumption due to the substantially lower ATPase activity of this recombinase. Moreover, RAD51 activity in eukaryotic cells is additionally controlled by a significantly wider set of regulatory proteins.

Conclusion

This work reports on the binding kinetics of RAD51 and UvsX recombinases at different external tensions in the range of 3–12 pN. The observed absence of UvsX binding to double-stranded DNA (dsDNA) without application of sufficient tension apparently reflects the evolutionary adaptation of the phage replication system. The different propensity of RAD51 and UvsX recombinases to bind dsDNA indicates possible alternative pathways for organizing recombination complexes *in vivo*.

The optical tweezers technique opened up the possibility for quantitatively characterizing the influence of mechanical stress on the formation and stability of recombinase complexes.

Single-molecule DNA studies allow direct testing of the influence of the type of DNA substrate and physical conditions on the assembly and stability of nucleoprotein filaments and provide a basis for a more detailed description of the molecular mechanisms of homologous recombination.

Acknowledgment

The authors express their deep gratitude to Yuri Vladimirovich Kil (Senior Researcher at the Laboratory of Molecular and Cellular Biophysics, NRC "Kurchatov Institute" – Petersburg Nuclear Physics Institute) for providing the BLR(DE3)pLysS strain and the expression vector for RAD51 isolation, as well as for fruitful discussion of the manuscript, which contributed to improving its quality.

REFERENCES

1. **Stewart M. D., Merino Vega D., Arend R. C., et al.,** Homologous recombination deficiency: concepts, definitions, and assays, Oncologist. 27 (3) (2022) 167–174.

2. **Ito M., Shinohara A.,** Chromosome architecture and homologous recombination in meiosis, Front. Cell Dev. Biol. 10 (Jan 6) (2023) 1097446.

3. **Yang H., Pavletich N. P.,** Insights into homology search from cryo-EM structures of RecA-DNA recombination intermediates, Curr. Opin. Genet. Dev. 71 (Dec) (2021) 188–194.

4. **McIlwraith M. J., Van Dyck E., Masson J.-Y., et al.,** Reconstitution of the strand invasion step of double-strand break repair using human Rad51 Rad52 and RPA proteins, J. Mol. Biol. 304 (2) (2000) 151–164.

5. **Bonilla B., Hengel S. R., Grundy M. K., Bernstein K. A.,** RAD51 gene family structure and function, Annu. Rev. Genet. 54 (Nov) (2020) 25–46.

6. **Pan Y., Xie N., Zhang X., et al.,** Computational insights into the dynamic structural features and binding characteristics of recombinase UvsX compared with RecA, Molecules. 28 (8) (2023) 3363.

7. **Yang S., VanLoock M. S., Yu X., Egelman E. H.,** Comparison of bacteriophage T4 UvsX and human Rad51 filaments suggests that RecA-like polymers may have evolved independently, J. Mol. Biol. 312 (5) (2001) 999–1009.

8. **Bleuit J. S., Xu H., Ma Y., et al.,** Mediator proteins orchestrate enzyme–ssDNA assembly during T4 recombination-dependent DNA replication and repair, Proc. Natl. Acad. Sci. 98 (15) (2001) 8298–8305.

9. **Chen Z., Yang H., Pavletich N. P.,** Mechanism of homologous recombination from the RecA–ssDNA/dsDNA structures, Nature. 453 (7194) (2008) 489–494.

10. **Gajewski S., Webb M. R., Galkin V., et al.,** Crystal structure of the phage T4 recombinase UvsX and its functional interaction with the T4 SF2 helicase UvsW, J. Mol. Biol. 405 (1) (2011) 65–76.

11. **Alekseev A., Morozova N., Vedyaykin A., et al.**, Single-molecule characterization of compressed RecA nucleoprotein filaments, Biochem. Biophys. Res. Commun. 614 (Apr 30) (2022) 29–33.

12. **Alekseev A., Serdakov M., Pobegalov G., et al.**, Single-molecule analysis reveals two distinct states of the compressed RecA filament on single-stranded DNA, FEBS Lett. 594 (21) (2020) 3464–3476.

13. **Del Val E., Nasser W., Abaibou H., Reverchon S.,** RecA and DNA recombination: A review of molecular mechanisms, Biochem. Soc. Trans. 47 (5) (2019) 1511–1531.

14. **Bianco P. R., Lu Y.,** Single-molecule insight into stalled replication fork rescue in *Escherichia coli*, Nucleic Acids Res. 49 (8) (2021) 4220–4238.

15. **Kaushik V., Tiwari M., Tiwari V.**, Interaction of RecA mediated SOS response with bacterial persistence, biofilm formation, and host response, Int. J. Biol. Macromol. 217 (Sep 30) (2022) 931–943.

16. **Mortier-Barrière I., De Saizieu A., Claverys J. P., Martin B.,** Competence-specific induction of RecA is required for full recombination proficiency during transformation in *Streptococcus pneumoniae*, Mol. Microbiol. 27 (1) (1998) 159–170.

17. **Le S., Serrano E., Kawamura R., et al.,** Bacillus subtilis RecA with DprA–SsbA antagonizes RecX function during natural transformation, Nucleic Acids Res. 45 (15) (2017) 8873–8885.

18. **Cory M. B., Li A., Hurley C. M., et al.,** The LexA–RecA* structure reveals a cryptic lock-and-key mechanism for SOS activation, Nat. Struct. Mol. Biol. 31 (10) (2024) 1522–1531.

19. **Cox J. M., Tsodikov O. V., Cox M. M.,** Organized unidirectional waves of ATP hydrolysis within a RecA filament, PLoS Biol. 3 (2) (2005) e52.

20. **Tennstedt P., Fresow R., Simon R., et al.**, RAD51 overexpression is a negative prognostic marker for colorectal adenocarcinoma, Int. J. Cancer. 132 (9) (2013) 2118–2126.

21. **Orhan E., Velazquez C., Tabet I., et al.**, Regulation of RAD51 at the transcriptional and functional levels: what prospects for cancer therapy? Cancers (Basel). 13 (12) (2021) 2930.

22. **Budke B., Lv W., Kozikowski A. P., Connell P. P.,** Recent developments using small molecules to target RAD51: How to best modulate RAD51 for anticancer therapy? ChemMedChem. 11 (22) (2016) 2468–2473.

23. **Tombline G., Fishel R.,** Biochemical characterization of the human Rad51 protein: I. ATP hydrolysis, J. Biol. Chem. 277 (17) (2002) 14417–14425.

24. **Wang L., Li Y., Wang P., et al.,** Enhanced recombinase polymerase amplification via UvsX engineering and reaction optimization for rapid detection of *Vibrio parahaemolyticus*, Lett. Appl. Microbiol. 78 (6) (2025) ovaf081.

25. **Ji T., Fang X., Gao Y., et al.,** Research progress on the application of RPA-CRISPR/Cas12a in the rapid visual detection of pathogenic microorganisms, Front. Cell. Infect. Microbiol. 15 (Jul 30) (2025) 1640938.

26. **Formosa T., Alberts B.,** Purification and characterization of the T4 bacteriophage uvsX protein, J. Biol. Chem. 261 (13) (1986) 6107–6118.

27. **Farb J. N., Morrical S. W.,** Role of allosteric switch residue histidine 195 in maintaining active-site asymmetry in presynaptic filaments of bacteriophage T4 UvsX recombinase, J. Mol. Biol. 385 (2) (2009) 393–404.

28. **Subramanyam S., Kinz-Thompson C. D., Gonzalez Jr R. L., Spies M.,** Observation and analysis of RAD51 nucleation dynamics at single-monomer resolution, Methods Enzymol. 600 (Jul 5) (2018) 201–232.

29. **Hegner M., Smith S. B., Bustamante C.,** Polymerization and mechanical properties of single RecA–DNA filaments, Proc. Natl. Acad. Sci. U.S.A. 96 (18) (1999) 10109–10114.

30. **Yu X., Egelman E. H.,** DNA conformation induced by the bacteriophage T4 UvsX protein appears identical to the conformation induced by the *Escherichia coli* RecA protein, J. Mol. Biol. 232 (1) (1993) 1–4.

31. **Xu J., Zhao L., Xu Y., et al.,** Cryo-EM structures of human RAD51 recombinase filaments during catalysis of DNA-strand exchange, Nat. Struct. Mol. Biol. 24 (1) (2017) 40–46.

32. **Alekseev A., Pobegalov G., Morozova N., et al.,** A new insight into RecA filament regulation by RecX from the analysis of conformation-specific interactions, eLife. 11 (Jun 22) (2022) e78409.

33. **Prasad T. K., Yeykal C. C., Greene E. C.,** Visualizing the assembly of human Rad51 filaments on double-stranded DNA, J. Mol. Biol. 363 (3) (2006) 713–728.

34. **Kojima K., Juma K. M., Akagi S., et al.,** Solvent engineering studies on recombinase polymerase amplification, J. Biosci. Bioeng. 131 (2) (2021) 219–224.

35. **Short J. M., Liu Y., Chen S., et al.,** High-resolution structure of the presynaptic RAD51 filament on single-stranded DNA by electron cryo-microscopy, Nucleic Acids Res. 44 (19) (2016) 9017–9030.

36. **Mazin A. V., Zaitseva E., Sung P., Kowalczykowski S. C.,** Tailed duplex DNA is the preferred substrate for Rad51 protein-mediated homologous pairing, EMBO J. 19 (5) (2000) 1148–1156.

37. **Kim S. H., Ragunathan K., Park J., et al.,** Cooperative conformational transitions keep RecA filament active during ATPase cycle, J. Am. Chem. Soc. 136 (42) (2014) 14796–14800.

38. **Brister J. R., Nossal N. G.,** Multiple origins of replication contribute to a discontinuous pattern of DNA synthesis across the T4 genome during infection, J. Mol. Biol. 368 (2) (2007) 336–348.

СПИСОК ЛИТЕРАТУРЫ

1. **Stewart M. D., Merino Vega D., Arend R. C., Baden J. F., Barbash O., Beaubier N., Collins G., French T., Ghahramani N., Hinson P.** Homologous recombination deficiency: concepts, definitions, and assays // The Oncologist. 2022. Vol. 27. No. 3. Pp. 167–174.

2. **Ito M., Shinohara A.** Chromosome architecture and homologous recombination in meiosis // Frontiers in Cell and Developmental Biology. 2023. Vol. 10. 6 January. P. 1097446.

3. **Yang H., Pavletich N. P.** Insights into homology search from cryo-EM structures of RecA-DNA recombination intermediates // Current Opinion in Genetics & Development. 2021. Vol. 71. December. Pp. 188–194.

4. **McIlwraith M. J., Van Dyck E., Masson J.-Y., Stasiak A. Z., Stasiak A., West S. C.** Reconstitution of the strand invasion step of double-strand break repair using human Rad51 Rad52 and RPA proteins // Journal of Molecular Biology. 2000. Vol. 304. No. 2. Pp. 151–164.

5. **Bonilla B., Hengel S. R., Grundy M. K., Bernstein K. A.** RAD51 gene family structure and function // Annual Review of Genetics. 2020. Vol. 54. November. Pp. 25–46.

6. **Pan Y., Xie N., Zhang X., Yang S., Lv S.** Computational insights into the dynamic structural features and binding characteristics of recombinase UvsX compared with RecA // Molecules. 2023. Vol. 28. No. 8. P. 3363.

7. **Yang S., VanLoock M. S., Yu X., Egelman E. H.** Comparison of bacteriophage T4 UvsX and human Rad51 filaments suggests that RecA-like polymers may have evolved independently // Journal of Molecular Biology. 2001. Vol. 312. No. 5. Pp. 999–1009.

8. **Bleuit J. S., Xu H., Ma Y., Wang T., Liu J., Morrical S. W.** Mediator proteins orchestrate enzyme–ssDNA assembly during T4 recombination-dependent DNA replication and repair // Proceedings of the National Academy of Sciences. 2001. Vol. 98. No. 15. Pp. 8298–8305.

9. **Chen Z., Yang H., Pavletich N. P.** Mechanism of homologous recombination from the RecA–ssDNA/dsDNA structures // Nature. 2008. Vol. 453. No. 7194. Pp. 489–494.

10. **Gajewski S., Webb M. R., Galkin V., Egelman E. H., Kreuzer K. N., White S. W.** Crystal structure of the phage T4 recombinase UvsX and its functional interaction with the T4 SF2 helicase UvsW // Journal of Molecular Biology. 2011. Vol. 405. No. 1. Pp. 65–76.

11. **Alekseev A., Morozova N., Vedyaykin A., Yakimov A., Khodorkovskii M., Pobegalov G.** Single-molecule characterization of compressed RecA nucleoprotein filaments // Biochemical and Biophysical Research Communications. 2022. Vol. 614. 30 April. Pp. 29–33.

12. **Alekseev A., Serdakov M., Pobegalov G., Yakimov A., Bakhlanova I., Baitin D., Khodorkovskii M.** Single-molecule analysis reveals two distinct states of the compressed RecA filament on single-stranded DNA // FEBS Letters. 2020. Vol. 594. No. 21. Pp. 3464–3476.

13. **Del Val E., Nasser W., Abaibou H., Reverchon S.** RecA and DNA recombination: a review of molecular mechanisms // Biochemical Society Transactions. 2019. Vol. 47. No. 5. Pp. 1511–1531.

14. **Bianco P. R., Lu Y.** Single-molecule insight into stalled replication fork rescue in *Escherichia coli* // Nucleic Acids Research. 2021. Vol. 49. No. 8. Pp. 4220–4238.

15. **Kaushik V., Tiwari M., Tiwari V.** Interaction of RecA mediated SOS response with bacterial persistence, biofilm formation, and host response // International Journal of Biological Macromolecules. 2022. Vol. 217. 30 September. Pp. 931–943.

16. **Mortier-Barrière I., De Saizieu A., Claverys J. P., Martin B.** Competence-specific induction of RecA is required for full recombination proficiency during transformation in *Streptococcus pneumoniae* // Molecular Microbiology. 1998. Vol. 27. No. 1. Pp. 159–170.

17. **Le S., Serrano E., Kawamura R., Carrasco B., Yan J., Alonso J. C.** Bacillus subtilis RecA with DprA–SsbA antagonizes RecX function during natural transformation // Nucleic Acids Research. 2017. Vol. 45. No. 15. Pp. 8873–8885.

18. **Cory M. B., Li A., Hurley C. M., Carman P. J., Pumroy R. A., Hostetler Z. M., Perez R. M., Venkatesh Y., Li X., Gupta K.** The LexA–RecA* structure reveals a cryptic lock-and-key mechanism for SOS activation // Nature Structural & Molecular Biology. 2024. Vol. 31. No. 10. Pp. 1522–1531.

19. **Cox J. M., Tsodikov O. V., Cox M. M.** Organized unidirectional waves of ATP hydrolysis within a RecA filament // PLoS Biology. 2005. Vol. 3. No. 2. P. e52.

20. **Tennstedt P., Fresow R., Simon R., Marx A., Terracciano L., Petersen C., Sauter G., Dikomey E., Borgmann K.** RAD51 overexpression is a negative prognostic marker for colorectal adenocarcinoma // International Journal of Cancer. 2013. Vol. 132. No. 9. Pp. 2118–2126.

21. **Orhan E., Velazquez C., Tabet I., Sardet C., Theillet C.** Regulation of RAD51 at the transcriptional and functional levels: What prospects for cancer therapy? // Cancers. 2021. Vol. 13. No. 12. P. 2930.

22. **Budke B., Lv W., Kozikowski A. P., Connell P. P.** Recent developments using small molecules to target RAD51: how to best modulate RAD51 for anticancer therapy? // ChemMedChem. 2016. Vol. 11. No. 22. Pp. 2468–2473.

23. **Tombline G., Fishel R.** Biochemical characterization of the human Rad51 protein: I. ATP hydrolysis // Journal of Biological Chemistry. 2002. Vol. 277. No. 17. Pp. 14417–14425.

24. **Wang L., Li Y., Wang P., Zhang Y., Liu Q.** Enhanced recombinase polymerase amplification via UvsX engineering and reaction optimization for rapid detection of *Vibrio parahaemolyticus* // Letters in Applied Microbiology. 2025. Vol. 78. No. 6. P. ovaf081.

25. **Ji T., Fang X., Gao Y., Yu K., Gao X.** Research progress on the application of RPA-CRISPR/Cas12a in the rapid visual detection of pathogenic microorganisms // Frontiers in Cellular and Infection Microbiology. 2025. Vol. 15. 30 July. P. 1640938.

26. **Formosa T., Alberts B.** Purification and characterization of the T4 bacteriophage uvsX protein // Journal of Biological Chemistry. 1986. Vol. 261. No. 13. Pp. 6107–6118.

27. **Farb J. N., Morrical S. W.** Role of allosteric switch residue histidine 195 in maintaining active-site asymmetry in presynaptic filaments of bacteriophage T4 UvsX recombinase // Journal of Molecular Biology. 2009. Vol. 385. No. 2. Pp. 393–404.

28. **Subramanyam S., Kinz-Thompson C. D., Gonzalez Jr R. L., Spies M.** Observation and analysis of RAD51 nucleation dynamics at single-monomer resolution // Methods in enzymology. 2018. Vol. 600. 5 July. Pp. 201–232.

29. **Hegner M., Smith S. B., Bustamante C.** Polymerization and mechanical properties of single RecA–DNA filaments // Proceedings of the National Academy of Sciences. 1999. Vol. 96. No. 18. Pp. 10109–10114.

30. **Yu X., Egelman E. H.** DNA conformation induced by the bacteriophage T4 UvsX protein appears identical to the conformation induced by the *Escherichia coli* RecA protein // Journal of Molecular Biology. 1993. Vol. 232. No. 1. Pp. 1–4.

31. **Xu J., Zhao L., Xu Y., Zhao W., Sung P., Wang H.-W.** Cryo-EM structures of human RAD51 recombinase filaments during catalysis of DNA-strand exchange // Nature Structural & Molecular Biology. 2017. Vol. 24. No. 1. Pp. 40–46.

32. **Alekseev A., Pobegalov G., Morozova N., Vedyaykin A., Cherevatenko G., Yakimov A., Baitin D., Khodorkovskii M.** A new insight into RecA filament regulation by RecX from the analysis of conformation-specific interactions // eLife. 2022. Vol. 11. 22 June. P. e78409.

33. **Prasad T. K., Yeykal C. C., Greene E. C.** Visualizing the assembly of human Rad51 filaments on double-stranded DNA // Journal of Molecular Biology. 2006. Vol. 363. No. 3. Pp. 713–728.

34. **Kojima K., Juma K. M., Akagi S., Hayashi K., Takita T., O'Sullivan C. K., Fujiwara S., Nakura Y., Yanagihara I., Yasukawa K.** Solvent engineering studies on recombinase polymerase amplification // Journal of Bioscience and Bioengineering. 2021. Vol. 131. No. 2. Pp. 219–224.

35. **Short J. M., Liu Y., Chen S., Soni N., Madhusudhan M. S., Shivji M. K., Venkitaraman A. R.** High-resolution structure of the presynaptic RAD51 filament on single-stranded DNA by electron cryo-microscopy // Nucleic Acids Research. 2016. Vol. 44. No. 19. Pp. 9017–9030.

36. **Mazin A. V., Zaitseva E., Sung P., Kowalczykowski S. C.** Tailed duplex DNA is the preferred substrate for Rad51 protein-mediated homologous pairing // The EMBO Journal. 2000. Vol. 19. No. 5. Pp. 1148–1156.

37. **Kim S. H., Ragunathan K., Park J., Joo C., Kim D., Ha T.** Cooperative conformational transitions keep RecA filament active during ATPase cycle // Journal of the American Chemical Society. 2014. Vol. 136. No. 42. Pp. 14796–14800.

38. **Brister J. R., Nossal N. G.** Multiple origins of replication contribute to a discontinuous pattern of DNA synthesis across the T4 genome during infection // Journal of Molecular Biology. 2007. Vol. 368. No. 2. Pp. 336–348.

THE AUTHORS

GONCHAROV Ivan D.
Peter the Great St. Petersburg Polytechnic University
29 Politechnicheskaya St., St. Petersburg, 195251, Russia
bing_fox.2001@inbox.ru

SADOVA Aleksandra I.
Peter the Great St. Petersburg Polytechnic University
29 Politechnicheskaya St., St. Petersburg, 195251, Russia
aleksa.sadova@yandex.ru

NUZHIN Ilia M.
Peter the Great St. Petersburg Polytechnic University
29 Politechnicheskaya St., St. Petersburg, 195251, Russia
ilia.nuzhin@yandex.ru

TENITSKAYA Polina A.
Peter the Great St. Petersburg Polytechnic University
29 Politechnicheskaya St., St. Petersburg, 195251, Russia
89818372011@mail.ru

KURDYUMOVA Inna V.
Peter the Great St. Petersburg Polytechnic University
29 Politechnicheskaya St., St. Petersburg, 195251, Russia
tyzik03@gmail.com

GORKOVSKAIA Aleksandra A.
Peter the Great St. Petersburg Polytechnic University
29 Politechnicheskaya St., St. Petersburg, 195251, Russia
alexgorkovskaya@gmail.com

KHODORKOVSKIY Mikhail A.
Peter the Great St. Petersburg Polytechnic University
29 Politechnicheskaya St., St. Petersburg, 195251, Russia
khodorkovskii@gmail.com
ORCID: 0000-0003-0562-0156

ALEKSEEV Aleksandr A.
Peter the Great St. Petersburg Polytechnic University
29 Politechnicheskaya St., St. Petersburg, 195251, Russia
alex35093@gmail.com
ORCID: 0000-0003-4371-265X

СВЕДЕНИЯ ОБ АВТОРАХ

ГОНЧАРОВ Иван Дмитриевич – *лаборант-исследователь лаборатории молекулярной микробиологии Санкт-Петербургского политехнического университета Петра Великого.*
195251, Россия, г. Санкт-Петербург, Политехническая ул., 29
bing_fox.2001@inbox.ru

САДОВА Александра Игоревна – *лаборант-исследователь лаборатории молекулярной биологии нуклеотид-связывающих белков Санкт-Петербургского политехнического университета Петра Великого.*
195251, Россия, г. Санкт-Петербург, Политехническая ул., 29
aleksa.sadova@yandex.ru

НУЖИН Илья Мулложонович – *студент Института биомедицинских систем и биотехнологий Санкт-Петербургского политехнического университета Петра Великого.*
195251, Россия, г. Санкт-Петербург, Политехническая ул., 29
ilia.nuzhin@yandex.ru

ТЕНИЦКАЯ Полина Алексеевна – *студентка Института биомедицинских систем и биотехнологий Санкт-Петербургского политехнического университета Петра Великого.*
195251, Россия, г. Санкт-Петербург, Политехническая ул., 29
89818372011@mail.ru

КУРДЮМОВА Инна Викторовна – *инженер Центра коллективного пользования «Аналитический центр нано- и биотехнологий» Санкт-Петербургского политехнического университета Петра Великого.*
195251, Россия, г. Санкт-Петербург, Политехническая ул., 29
tyzik03@gmail.com

ГОРЬКОВСКАЯ Александра Андреевна – *лаборант-исследователь лаборатории молекулярной микробиологии Санкт-Петербургского политехнического университета Петра Великого.*
195251, Россия, г. Санкт-Петербург, Политехническая ул., 29
alexgorkovskaya@gmail.com

ХОДОРКОВСКИЙ Михаил Алексеевич – *кандидат физико-математических. наук, директор Научно-исследовательского комплекса «Нанобиотехнологии» Санкт-Петербургского политехнического университета Петра Великого.*
195251, Россия, г. Санкт-Петербург, Политехническая ул., 29
khodorkovskii@gmail.com
ORCID: 0000-0003-0562-0156

АЛЕКСЕЕВ Александр Андреевич – *кандидат физико-математических. наук, инженер-исследователь лаборатории молекулярной биологии нуклеотид-связывающих белков Санкт-Петербургского политехнического университета Петра Великого.*
195251, Россия, г. Санкт-Петербург, Политехническая ул., 29
alex35093@gmail.com
ORCID: 0000-0003-4371-265X

Received 10.02.2026. Approved after reviewing 02.03.2026. Accepted 02.03.2026.
Статья поступила в редакцию 10.02.2026. Одобрена после рецензирования 02.03.2026. Принята 02.03.2026.

© Peter the Great St. Petersburg Polytechnic University, 2026

NUCLEAR PHYSICS

Original article
DOI: https://doi.org/10.18721/JPM.19213

AZIMUTHAL DEPENDENCES OF THE NUCLEAR MODIFICATION FACTORS OF π^0 MESONS IN CU+AU COLLISIONS AT AN ENERGY OF 200 GEV AND U+U COLLISIONS AT 193 GEV

E. V. Bannikov✉, *Ya. A. Berdnikov*, *D. M. Larionova*, *D. O. Kotov*, *K. N. Basirov*, *I. I. Borisov*

Peter the Great St. Petersburg Polytechnic University, St. Petersburg, Russia

✉ bannikov.ev.21@gmail.com

Abstract. The paper presents the results of calculating the nuclear modification factors of π^0 mesons as a function of their transverse momentum and azimuthal angle at different collision centralities of Cu+Au at an energy of 200 GeV and U+U at 193 GeV. As a result of the analysis of the obtained data, it was established that the azimuthal dependence of the nuclear modification factors of π^0 mesons in both collision systems demonstrated universality in the considered range of transverse momentum and could be explained by the dependence of parton energy losses on the length of their path in the quark-gluon plasma (QGP). It is advisable to use these azimuthal dependences of nuclear modification factors for clarification of the parameters in theoretical models describing the energy losses of partons in the QGP formed in collisions of deformed nuclei or in asymmetric collision systems.

Keywords: quark-gluon plasma, azimuthal anisotropy, nuclear modification factors, π^0 meson

Citation: Bannikov E. V., Berdnikov Ya. A., Larionova D. M., Kotov D. O., Basirov K. N., Borisov I. I., Azimuthal dependences of the nuclear modification factors of π^0 mesons in Cu+Au collisions at an energy of 200 GeV and U+U collisions at 193 GeV, St. Petersburg State Polytechnical University Journal. Physics and Mathematics. 19 (2) (2026) 160–170. DOI: https://doi.org/10.18721/JPM.19213

This is an open access article under the CC BY-NC 4.0 license (https://creativecommons.org/licenses/by-nc/4.0/)

© Bannikov E. V., Berdnikov Ya. A., Larionova D. M., Kotov D. O., Basirov K. N., Borisov I. I., 2026. Published by Peter the Great St. Petersburg Polytechnic University.

Научная статья
УДК 539.12
DOI: https://doi.org/10.18721/JPM.19213

АЗИМУТАЛЬНЫЕ ЗАВИСИМОСТИ ФАКТОРОВ ЯДЕРНОЙ МОДИФИКАЦИИ π^0-МЕЗОНОВ В СТОЛКНОВЕНИЯХ РЕЛЯТИВИСТСКИХ ЯДЕР МЕДИ И ЗОЛОТА ПРИ ЭНЕРГИИ 200 ГЭВ И ЯДЕР УРАНА ПРИ 193 ГЭВ

Е. В. Банников✉, *Я. А. Бердников*, *Д. М. Ларионова*, *Д. О. Котов*, *К. Н. Басиров*, *И. И. Борисов*

Санкт-Петербургский политехнический университет Петра Великого, Санкт-Петербург, Россия

✉ bannikov.ev.21@gmail.com

Аннотация. В работе представлены результаты расчета факторов ядерной модификации π^0-мезонов как функции от их поперечного импульса и азимутального угла в различных центральностях столкновений релятивистских ядер Cu+Au при энергии 200 ГэВ и U+U при 193 ГэВ. В результате анализа полученных данных было установлено, что характер азимутальной зависимости факторов ядерной модификации π^0-мезонов в обеих системах столкновений универсален в рассматриваемом диапазоне по поперечному импульсу и может быть объяснен зависимостью потерь энергии партонов от длины их пути в кварк-глюонной плазме (КГП). Азимутальные зависимости факторов ядерной модификации π^0-мезонов, рассчитанные в данной работе, целесообразно использовать для уточнения параметров теоретических моделей, описывающих потери энергии партонов в КГП, образующейся в столкновениях деформированных ядер или в асимметричных системах столкновений.

Ключевые слова: кварк-глюонная плазма, азимутальная анизотропия, фактор ядерной модификации, π^0-мезон

Ссылка для цитирования: Банников Е. В., Бердников Я. А., Ларионова Д. М., Котов Д. О., Басиров К. Н., Борисов И. И. Азимутальные зависимости факторов ядерной модификации π^0-мезонов в столкновениях релятивистских ядер меди и золота при энергии 200 ГэВ и ядер урана при 193 ГэВ // Научно-технические ведомости СПбГПУ. Физико-математические науки. 2026. Т. 2 № .19. С. 160–170. DOI: https://doi.org/10.18721/JPM.19213

Статья открытого доступа, распространяемая по лицензии CC BY-NC 4.0 (https://creativecommons.org/licenses/by-nc/4.0/)

Introduction

In the late 20th century, quantum chromodynamics predicted that matter could transition into a special state at extreme energy densities and/or temperatures, where its fundamental constituents, i.e., partons (quarks and gluons), become asymptotically free [1]. This state of matter was named the quark-gluon plasma (QGP). Subsequently, collider experiments showed that QGP can form in collisions of relativistic heavy ions [2].

Understanding the properties of the QGP is a pressing problem in high-energy physics; however, a major challenge in research is that the QGP lifetime is very short (~10 fm/c [3]), making direct experimental observation impossible. Experimental approaches to studying the formation and properties of the QGP in relativistic ion collisions are based on measuring the yields of produced particles and their angular characteristics.

The goal of this study was to measure the azimuthal dependences of hadron suppression at high transverse momenta ($p_T > 5$ GeV/c) [4].

© Банников Е. В., Бердников Я. А., Ларионова Д. М., Котов Д. О., Басиров К. Н., Борисов И. И., 2026. Издатель: Санкт-Петербургский политехнический университет Петра Великого.

Problem statement

One of the main facilities used for collisions of relativistic heavy ions is the Relativistic Heavy Ion Collider (RHIC). The PHENIX experiment [3] at RHIC discovered that the production of hadrons with high transverse momenta p_T in heavy-ion collisions (e.g., Au+Au) is suppressed compared to their production in proton–proton (p+p) collisions [5]. Hadron production at high p_T occurs predominantly through fragmentation of jets formed by high-energy partons [6]. As these high-energy partons traverse the dense QGP medium formed in heavy-ion collisions, they interact with it and lose energy, mainly via gluon bremsstrahlung [6]. The energy loss of the parent partons leads to a weakening of the hadronic jets, consequently reducing the transverse momentum of the hadrons in these jets (the jet quenching effect).

Thus, the observed suppression of hadron production at high p_T was interpreted as evidence for QGP formation in heavy-ion collisions [3].

The suppression of hadron production at high p_T is typically quantified using the nuclear modification factors R_{AB} (NMFs), defined as the ratio of hadron yields in nucleus–nucleus collisions to those in p+p collisions:

$$R_{AB}(p_T) = \frac{1}{\langle N_{coll} \rangle} \frac{d^2N_{AB}/dp_T dy}{d^2N_{pp}/dp_T dy},$$

where $\langle N_{coll} \rangle$ is the average number of binary inelastic nucleon–nucleon collisions; $d^2N_{AB}/dp_T dy$ is the p_T differential yield of the particles considered in (A+B) collisions; $d^2N_{pp}/dp_T dy$ is the p_T differential yield in p+p collisions; y is the rapidity.

The suppression of hadron production in nucleus–nucleus collisions due to the energy loss of high-energy partons causes the $R_{AB}(p_T)$ values to fall below unity at $p_T > 5$ GeV/c.

Previously measured $R_{AB}(p_T)$ of hadrons at $p_T > 5$ GeV/c in relativistic heavy-ion collisions were described by theoretical models that account for parton energy loss in the QGP medium [6–8]. One of the key parameters in these models is the transport coefficient $\hat{q}$, which characterizes the average squared transverse momentum exchanged between a high-energy parton and the QGP medium per unit path length.

The main difficulty with the theoretical models used to describe parton energy loss in the QGP is that different models yield different values of the transport coefficient $\hat{q}$ and different estimates of the path-length dependence of the energy loss [6]. Such differences make it impossible to unambiguously and accurately describe the measured $R_{AB}(p_T)$ dependences of hadrons and their azimuthal anisotropy (experimentally quantified by the elliptic flow v_2).

While existing models accurately describe the $R_{AB}(p_T)$ dependence of hadrons at $p_T >$ 5 GeV/c, they systematically underestimate v_2 [9]. A simultaneous description of $R_{AB}(p_T)$ and v_2 requires both accounting for the more complex initial collision geometry (which increases v_2 in model calculations) and adopting more sophisticated approaches, such as AdS/CFT [6]. However, these approaches require further separate investigation [9, 10]. Despite recent advances in modeling the interactions of hadronic jets with the QGP medium [11], this problem remains unresolved.

Thus, to gain a clearer understanding of parton energy loss processes, it is necessary to experimentally measure quantities that are more sensitive to the path length of partons in the QGP medium.

A more detailed analysis of the path-length dependence of parton energy loss in the QGP can be performed by varying the collision systems and measuring the $R_{AB}(p_T)$ function of hadrons at $p_T > 5$ GeV/c for different centrality classes. It is convenient to use π^0 mesons as probe hadrons, since they can be identified over a wide range of transverse momenta with relatively small measurement uncertainties.

This approach made it possible to measure the $R_{AB}(p_T)$ dependences for π^0 mesons up to about 20 GeV/c for different centrality bins in Au+Au [12], Cu+Au [13], and U+U [14] collisions. In particular, the measurements showed that the suppression pattern of π^0 mesons at $p_T > 5$ GeV/c does not depend on the initial collision geometry for similar values of N_{part} (the

number of participants characterizing the collision centrality and the volume of the QGP produced) [13, 14].

The overlap region of heavy nuclei generally has an ellipsoidal shape; therefore, the average path length traversed by a parent parton in the QGP depends on the azimuthal angle of its emission relative to the reaction plane $\Delta\varphi$ (the plane formed by the beam axis and the impact parameter vector). The degree of hadron suppression depends on the average path length of the parent partons in the QGP, so the suppression of hadron production is azimuthally anisotropic within a given centrality bin. This azimuthal anisotropy in momentum space is quantified by the elliptic flow.

The relationship between hadron suppression and the path length of parent partons in the QGP cannot be studied directly from the $R_{AB}(p_T)$ dependences, as the $R_{AB}(p_T)$ function is integrated over the azimuthal angle $\Delta\varphi$. However, the azimuthal functions $R_{AB}(p_T,\Delta\varphi)$, which have high sensitivity to the parton path length in the QGP, can be estimated by simultaneously using the measured NMFs and elliptic flows of hadrons as a function of p_T.

Such R_{AB} dependences on the two kinematic variables p_T and $\Delta\varphi$ have already been studied for π^0 mesons in different centrality bins of Au+Au collisions at $\sqrt{s_{NN}}$ = 200 GeV in [10, 12], where it was found that the degree of π^0 meson suppression for the same value of N_{part} (or in the same centrality bin) can differ by nearly a factor of two depending on the azimuthal angle relative to the reaction plane.

In this work, we consider two heavy-ion collision systems: copper–gold (Cu+Au) and uranium–uranium (U+U). Unlike collisions of symmetric gold nuclei, these collision systems have additional anisotropy of the nuclear overlap region relative to the reaction plane. Such anisotropy in Cu+Au collisions arises from the difference in the sizes of the copper and gold nuclei, leading to complete overlap of the copper nucleus in central collisions. Uranium nuclei are prolate-deformed; therefore, depending on their spatial orientation, the shape of the nuclear overlap region can differ even within the same centrality bin.

Thus, our paper is aimed at measuring the azimuthally dependent $R_{AB}(p_T,\Delta\varphi)$ values for π^0 mesons in Cu+Au collisions at $\sqrt{s_{NN}}$ = 200 GeV and in U+U collisions at $\sqrt{s_{NN}}$ = 193 GeV.

The results are expected to clarify the role of the initial collision geometry in the path-length dependence of parton energy loss in the QGP, and provide new bounds on the parameter values in theoretical models describing parton energy loss.

Methodology

The azimuthal anisotropy of the π^0 meson suppression can be calculated directly from the NMFs [10]:

$$R_{AB}\left(p_T,\Delta\varphi_i\right)=R_{AB}\left(p_T\right)\frac{\Delta N\left(p_T,\Delta\varphi_i\right)}{\frac{1}{k}\sum_{i=1}^{k}\Delta N\left(p_T,\Delta\varphi_i\right)},$$

where $\Delta N(p_T,\Delta\varphi_i)$ is the yield of π^0 mesons in the ith azimuthal bin $\Delta\varphi_i$ at transverse momentum p_T.

Summation in the denominator is performed over all ith angular bins (their number is k). For the calculations, we used the $R_{AB}(p_T)$ values for π^0 mesons in Cu+Au collisions at $\sqrt{s_{NN}}$ = 200 GeV and in U+U collisions at $\sqrt{s_{NN}}$ = 193 GeV from [13, 14]. The second factor in this expression characterizes the azimuthal dependence of the π^0 meson yields: it is the ratio of the yield in the $\Delta\varphi_i$ bin to the average yield over all bins at a given p_T. However, the measured $\Delta N(p_T,\Delta\varphi_i)$ values for π^0 mesons in different azimuthal bins in Cu+Au and U+U collisions have not been previously published, so we had to use an alternative approach to estimate the azimuthal anisotropy of particle production.

The inclusive (azimuthally integrated) $R_{AB}(p_T)$ dependences for π^0 mesons are measured experimentally as the ratio (normalized by $\langle N_{coll}\rangle$) of the pT differential yields of π^0 mesons in nuclear collisions to those in proton–proton collisions. To determine the azimuthal dependence of particle production, $R_{AB}(p_T,\Delta\varphi)$, the total invariant differential yield $E\cdot d^3N/d^3p$ can be expanded into a Fourier series in the azimuthal angle relative to the reaction plane [15]:

$$E\frac{d^3N}{d^3p}=\frac{1}{2\pi}\frac{d^2N}{p_T dp_T dy}\left(1+\sum_{n=1}^{\infty}2v_n\cos[n(\varphi-\Psi^{RP})]\right),$$

where φ is the particle azimuthal angle, y is the rapidity, v_n are the Fourier coefficients (anisotropic flow), Ψ^{RP} is the azimuthal angle of the reaction plane.

Thus, the azimuthal anisotropy of the transverse momentum distribution is characterized by the coefficients of anisotropic flow, where the elliptic flow v_2 (the second Fourier coefficient) dominates. The analytical representation of the expression for calculating $R_{AB}(p_T,\Delta\varphi)$ as a continuous function (for $k \to \infty$, $\Delta N(p_T,\Delta\varphi_i) \to dN/d\Delta\varphi$) then takes the following form:

$$R_{AB}(p_T,\Delta\varphi)=R_{AB}(p_T)\left[1+2v_2(p_T)\cos\left(2\Delta\varphi\right)\right],$$

where the azimuthal dependence of the π^0 meson yields is parameterized by the $v_2(p_T)$ values, and the angle $\Delta\varphi$ can take arbitrary values in the range $0 < \Delta\varphi < \pi/2$.

We took the $v_2(p_T)$ values from [16]. With these, all quantities necessary for calculating $R_{AB}(p_T,\Delta\varphi)$ are available.

We calculated the $R_{AB}(p_T,\Delta\varphi)$ values for π^0 mesons in four (or three) p_T bins in the range $5 < p_T < 10$ GeV/c and in four (or three) centrality bins for Cu+Au (or U+U) collisions. The choice of the p_T bins and centrality bins was guided by the previously measured $R_{AB}(p_T)$ and $v_2(p_T)$ values. We considered the azimuthal dependence of π^0 meson NMFs in six $\Delta\varphi$ bins in the range $0 < \Delta\varphi < \pi/2$.

Measurement results

Fig. 1 shows the calculated $R_{AB}(p_T,\Delta\varphi)$ values for π^0 mesons in four transverse momentum bins within $5 < p_T < 10$ GeV/c and in four centrality bins of Cu+Au collisions at $\sqrt{s_{NN}} = 200$ GeV. The calculated $R_{AB}(p_T,\Delta\varphi)$ values are shown in Fig. 1,*d* only for three centrality bins of Cu+Au collisions, because the $v_2(p_T)$ values for π^0 mesons in the range $8 < p_T < 10$ GeV/c for the 40–60% centrality bin are not available.

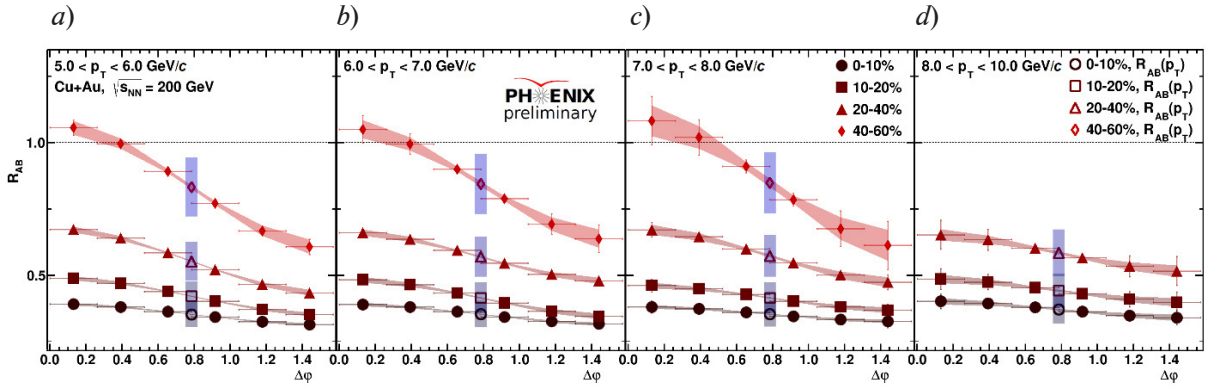


Fig. 1. $R_{AB}(p_T,\Delta\varphi)$ dependences for π^0 mesons calculated for four p_T bins (*a*–*d*) in the range $5 < p_T < 10$ GeV/c and for four centrality bins of Cu+Au collisions at $\sqrt{s_{NN}} = 200$ GeV
Centrality bins, %: 0–10, 10–20, 20–40 and 40–60. Inclusive $R_{AB}(p_T)$ values are shown by points at $\Delta\varphi = \pi/4$ (0.785 rad)

The solid symbols in Fig. 1 correspond to $R_{AB}(p_T,\Delta\varphi)$ values, the open symbols correspond to $R_{AB}(p_T)$ values. The uncertainties of the $R_{AB}(p_T,\Delta\varphi)$ values were obtained by propagating the uncertainties from the $v_2(p_T)$ values. The systematic uncertainties of the $R_{AB}(p_T,\Delta\varphi)$ values are shown in Fig. 1 as shaded bands whose width represents the magnitude of the systematic uncertainty. The systematic uncertainties from the inclusive $R_{AB}(p_T)$ values are shown in Fig. 1 as solid boxes $\Delta\varphi = \pi/4$ and apply to all $R_{AB}(p_T,\Delta\varphi)$ values of the corresponding series.

The azimuthal anisotropy of NMFs for π^0 mesons increases with increasing centrality, leading to a difference of about a factor of 1.7 between the $R_{AB}(p_T,\Delta\varphi)$ values in the reaction plane ($0 < \Delta\varphi < \pi/12$) and perpendicular to it ($5\pi/12 < \Delta\varphi < \pi/2$) in peripheral Cu+Au collisions (40–60%). The observed azimuthal anisotropy of the $R_{AB}(p_T,\Delta\varphi)$ values indicates that the degree of π^0 meson suppression depends on the emission angle. A high-energy parent parton emitted in the direction of the reaction plane traverses, on average, a shorter path in the QGP than a parton emitted perpendicular to it. The shorter path length in the QGP leads, on average, to weaker interactions of the parton with the strongly interacting medium and, consequently, to smaller energy losses. As a result, the hadronic jet formed by the high-energy parton is quenched to a lesser extent, and the transverse momentum of the π^0 mesons produced by its fragmentation is larger.

Thus, the observed azimuthal dependence of the π^0 meson suppression can be explained by the path-length dependence of the parent parton energy loss in the QGP before fragmentation.

Fig. 1 also shows that the inclusive and azimuthally dependent NMFs of π^0 mesons decrease from peripheral (40–60%) to central (0–10%) collisions. This observation indicates that the degree of π^0 meson suppression increases with the size of the QGP formed in Cu+Au collisions, as previously noted in [13].

The observed trends in the $R_{AB}(p_T,\Delta\varphi)$ dependence for π^0 mesons in Cu+Au collisions are universal across all four transverse momentum bins in the range $5 < p_T < 10$ GeV/c. This suggests that the mechanism of parton energy loss in the QGP is similar over the entire transverse momentum range considered.

Fig. 2 shows the calculated $R_{AA}(p_T,\Delta\varphi)$ values for π^0 mesons in three transverse momentum bins in the range $5 < p_T < 10$ GeV/c and in three centrality bins of U+U collisions at $\sqrt{s_{NN}} = 193$ GeV. Fig. 2,*c* shows the calculated $R_{AA}(p_T,\Delta\varphi)$ values only for two centrality bins of U+U collisions, because the $v_2(p_T)$ values for π^0 mesons in the range $8 < p_T < 10$ GeV/c for the 40–60% centrality bin are not available. The notations for the NMFs differ between the two collision systems: (A+B, R_{AB}) is used for collisions of different nuclei (Cu+Au), while (A + A, R_{AA}) is used for collisions of identical nuclei (U+U). The uncertainties of the $R_{AA}(p_T,\Delta\varphi)$ and $R_{AA}(p_T)$ values in Fig. 2 are shown similarly to Fig. 1.

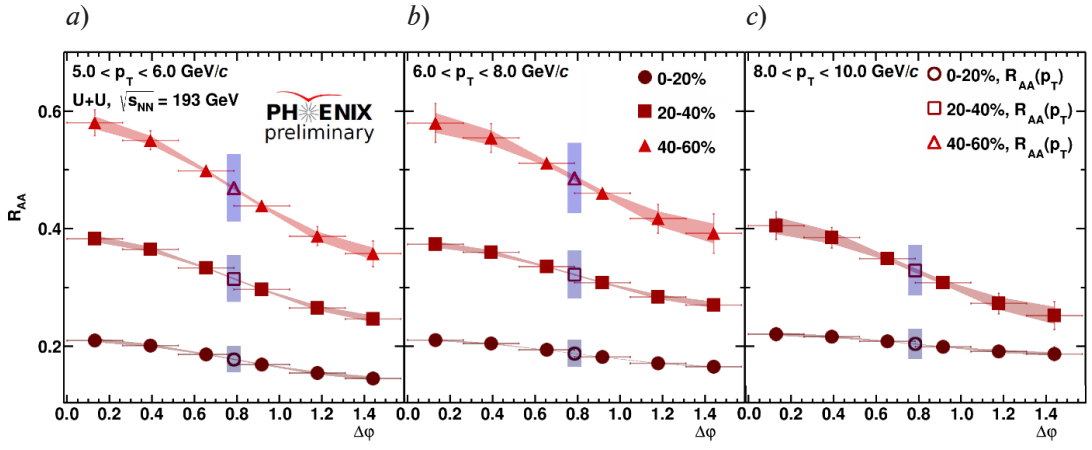


Fig. 2. $R_{AA}(p_T,\Delta\varphi)$ dependences for π^0 mesons, similar to those shown in Fig. 1, but for U+U collisions at $\sqrt{s_{NN}} = 193$ GeV, calculated for three p_T bins (*a*–*c*) in the same range and for three centrality bins: 0–20%, 20–40%, and 40–60% The inclusive $R_{AA}(p_T)$ values are shown by points at $\Delta\varphi = \pi/4$

The observations made for the $R_{AB}(p_T,\Delta\varphi)$ values for π^0 mesons in Cu+Au collisions also apply to the similar values in U+U collisions. It is worth noting that the ratio of the $R_{AA}(p_T,\Delta\varphi)$ values for π^0 mesons in the reaction plane and perpendicular to it reaches about 1.5 in the U+U system, which is smaller than in Cu+Au collisions. This difference is most likely due to non-flow effects (e.g., jet correlations [17, 18]). Such effects can bias the measured $v_2(p_T)$ values for π^0 mesons in peripheral Cu+Au collisions [16], leading to an overestimation of elliptic flow.

Conclusion

We calculated the azimuthally dependent nuclear modification factors of π^0 mesons for different transverse momentum bins within $5 < p_T < 10$ GeV/c and for different centrality bins in Cu+Au collisions at $\sqrt{s_{NN}} = 200$ GeV and U+U collisions at $\sqrt{s_{NN}} = 193$ GeV.

It was found that the azimuthally dependent nuclear modification factors of π^0 mesons in Cu+Au collisions are systematically larger than those in U+U collisions. This is explained by the larger volume of the QGP produced in U+U collisions. The trends observed in the $R_{AB}(p_T,\Delta\varphi)$ dependence of π^0 mesons in these collisions are universal across all transverse momentum ranges within $5 < p_T < 10$ GeV/c: the azimuthal anisotropy of the π^0 meson nuclear modification factors is larger in peripheral collisions than in central collisions, while the degree of hadron suppression is smaller. The observed behavior of the calculated $R_{AB}(p_T,\Delta\varphi)$ values for π^0 mesons in Cu+Au and U+U collisions is consistent with the path-length dependence of parton energy loss in the QGP.

The ratio of $R_{AB}(p_T,\Delta\varphi)$ values for π^0 mesons in the reaction plane and perpendicular to it reaches about 1.5 in the U+U system and 1.7 in Cu+Au collisions One possible reason for this difference could be non-flow effects, whose influence on the measured $v_2(p_T)$ values for π^0 mesons in peripheral Cu+Au collisions [16] leads to an overestimation of elliptic flow values.

The calculated $R_{AB}(p_T,\Delta\varphi)$ values for π^0 mesons can be used to refine the parameters of theoretical models describing parton energy loss in the quark-gluon plasma produced in collisions of deformed nuclei or in asymmetric collision systems.

REFERENCES

1. **Shuryak E.,** Quantum chromodynamics and the theory of superdense matter, Phys. Rept. 61 (2) (1980) 71–158.

2. **Matsui T., Satz H.,** J/ψ suppression by quark-gluon plasma formation, Phys. Lett. B. 178 (4) (1986) 416–422.

3. **Adcox K., Adler S., Afanasiev S., et al.** (PHENIX Collaboration), Formation of dense partonic matter in relativistic nucleus–nucleus collisions at RHIC: Experimental evaluation by the PHENIX Collaboration, Nucl. Phys. A. 757 (1–2) (2005) 184–283.

4. **Cao. S., Wang X.-N.,** Jet quenching and medium response in high-energy heavy-ion collisions: a review, Rept. Prog. Phys. 84 (2) (2021) 024301.

5. **Adcox K., Adler S., Ajitanand N., et al.** (PHENIX Collaboration), Suppression of hadrons with large transverse momentum in central Au+Au collisions at $\sqrt{s_{NN}}$ = 130 GeV, Phys. Rev. Lett. 88 (2) (2001) 022301.

6. **d'Enterria D.,** Jet quenching, Section 6.4. in book: Landolt – Börnstein – Group I: "Elementary Particles, Nuclei and Atoms", Vol. 23 (2010) 471–520.

7. **Cunqueiro L., Sickles A.,** Studying the QGP with jets at the LHC and RHIC, Prog. Part. Nucl. Phys. 124 (May) (2022) 103940.

8. **Harris J. W., Müller B.** "QGP signatures" revisited, Eur. Phys. J. C. 84 (3) (2024) 247.

9. **Adare A., Afanasiev S., Aidala C., et al.** (PHENIX Collaboration), Azimuthal anisotropy of π^0 production in Au+Au collisions at $\sqrt{s_{NN}}$ = 200 GeV: Path-length dependence of jet quenching and the role of initial geometry, Phys. Rev. Lett. 105 (2) (2010) 142301.

10. **Adare A., Afanasiev S., Aidala C., et al.** (PHENIX Collaboration), Neutral pion production with respect to centrality and reaction plane in Au+Au collisions at $\sqrt{s_{NN}}$ = 200 GeV, Phys. Rev. C. 87 (3) (2013) 034911.

11. **Acharya S., Adamová D., Adler A., et al.** (ALICE Collaboration), The ALICE experiment: A journey through QCD, Eur. Phys. J. C. 84 (14 Aug) (2024) 813.

12. **Afanasiev S., Aidala C., Ajitanand N., et al.** (PHENIX Collaboration), High-p_T π^0 production with respect to the reaction plane in Au+Au collisions at $\sqrt{s_{NN}}$ = 200 GeV, Phys. Rev. C. 80 (5) (2009) 054907.

13. **Aidala C., Ajitanand N., Akiba Y., et al.** (PHENIX Collaboration), Production of π^0 and η mesons in Cu+Au collisions at $\sqrt{s_{NN}}$ = 200 GeV, Phys. Rev. C. 98 (5) (2018) 054903.

14. **Acharya U., Aidala C., Ajitanand N., et al.** (PHENIX Collaboration), Production of π^0 and η mesons in U+U collisions at $\sqrt{s_{NN}}$ = 192 GeV, Phys. Rev. C. 102 (6) (2020) 064905.

15. **Voloshin S., Zhang Y.,** Flow study in relativistic nuclear collisions by Fourier expansion of azimuthal particle distributions, Z. Phys C. 70 (4) (1996) 665–671.

16. **Bannikov E. V., Berdnikov Ya. A., Larionova D. M., Kotov D. O.,** Comparison of π^0 meson elliptic flow in Cu+Au collisions at the energy of 200 GeV and U+U collisions at 193 GeV, St. Petersburg State Polytechnical University Journal. Physics and Mathematics. 19 (1) (2026) 144–157.

17. **Adare A., Afanasiev S., Aidala C., et al.** (PHENIX Collaboration), Azimuthal anisotropy of π^0 and η mesons in Au+Au collisions at $\sqrt{s_{NN}}$ = 200 GeV // Phys. Rev. C. 88 (6) (2013) 064910.

18. **Jia, J.,** Ways to constrain the away-side jet in Au+Au collisions in PHENIX, Nucl. Phys. A. 783 (1–4) (2007) 501–506.

СПИСОК ЛИТЕРАТУРЫ

1. **Shuryak E.** Quantum chromodynamics and the theory of superdense matter // Physics Reports. 1980. Vol. 61. No. 2. Pp. 71–158.

2. **Matsui T., Satz H.** J/ψ suppression by quark-gluon plasma formation // Physics Letters B. 1986. Vol.178. No. 4. Pp. 416 –422.

3. **Adcox K., Adler S., Afanasiev S., et al.** (PHENIX Collaboration). Formation of dense partonic matter in relativistic nucleus–nucleus collisions at RHIC: Experimental evaluation by the PHENIX Collaboration // Nuclear Physics A. 2005. Vol. 757. No. 1–2. Pp. 184–283.

4. **Cao. S., Wang X.-N.** Jet quenching and medium response in high-energy heavy-ion collisions: A review // Reports on Progress in Physics. 2021. Vol. 84. No. 2. P. 024301.

5. **Adcox K., Adler S., Ajitanand N., et al.** (PHENIX Collaboration). Suppression of hadrons with large transverse momentum in central Au+Au collisions at $\sqrt{s_{NN}}$ = 130 GeV // Physical Review Letters. 2001. Vol. 88. No. 2. P. 022301.

6. **d'Enterria D.** Jet quenching (Section 6.4) // Landolt – Börnstein – Group I: "Elementary Particles, Nuclei and Atoms". 2010. Vol. 23. Pp. 471–520.

7. **Cunqueiro L., Sickles A.** Studying the QGP with jets at the LHC and RHIC // Progress in Particle and Nuclear Physics. 2022. Vol. 124. May. P. 103940.

8. **Harris J. W., Müller B.** "QGP signatures" revisited // The European Physical Journal C. 2024. Vol. 84. No. 3. P. 247.

9. **Adare A., Afanasiev S., Aidala C., et al.** (PHENIX Collaboration). Azimuthal anisotropy of π^0 production in Au+Au collisions at $\sqrt{s_{NN}}$ = 200 GeV: Path-length dependence of jet quenching and the role of initial geometry // Physical Review Letters. 2010. Vol. 105. No. 2. P. 142301.

10. **Adare A., Afanasiev S., Aidala C., et al.** (PHENIX Collaboration). Neutral pion production with respect to centrality and reaction plane in Au+Au collisions at $\sqrt{s_{NN}}$ = 200 GeV // Physical Review C. 2013. Vol. 87. No. 3. P. 034911.

11. **Acharya S., Adamová D., Adler A., et al.** (ALICE Collaboration). The ALICE experiment: A journey through QCD // The European Physical Journal C. 2024. Vol. 84. 14 August. P. 813.

12. **Afanasiev S., Aidala C., Ajitanand N., et al.** (PHENIX Collaboration). High-p_T π^0 production with respect to the reaction plane in Au+Au collisions at $\sqrt{s_{NN}}$ = 200 GeV // Physical Review C. 2009. Vol. 80. No. 5. P. 054907.

13. **Aidala C., Ajitanand N., Akiba Y., et al.** (PHENIX Collaboration). Production of π^0 and η mesons in Cu+Au collisions at $\sqrt{s_{NN}}$ = 200 GeV // Physical Review C. 2018. Vol. 98. No. 5. P. 054903.

14. **Acharya U., Aidala C., Ajitanand N., et al.** (PHENIX Collaboration). Production of π^0 and η mesons in U+U collisions at $\sqrt{s_{NN}}$ = 192 GeV // Physical Review C. 2020. Vol. 102. No. 6. P. 064905.

15. **Voloshin S., Zhang Y.** Flow study in relativistic nuclear collisions by Fourier expansion of azimuthal particle distributions // Zeitschrift für Physik C. 1996. Vol. 70. No. 4. Pp. 665–671.

16. **Банников Е. В., Бердников Я. А., Ларионова Д. М., Котов Д. О.** Сравнение эллиптических потоков π^0-мезонов в столкновениях Cu+Au при энергии 200 ГэВ и U+U при 193 ГэВ // Научно-технические ведомости СПбГПУ. Физико-математические науки. 2026. Т. 19. № 1. С. 144–157.

17. **Adare A., Afanasiev S., Aidala C., et al.** (PHENIX Collaboration). Azimuthal anisotropy of π^0 and η mesons in Au+Au collisions at $\sqrt{s_{NN}}$ = 200 GeV // Physical Review C. 2013. Vol. 88. No. 6. P. 064910.

18. **Jia J.** Ways to constrain the away-side jet in Au+Au collisions in PHENIX // Nuclear Physics A. 2007. Vol. 783. No. 1–4. Pp. 501–506.

THE AUTHORS

BANNIKOV Egor V.
Peter the Great St. Petersburg Polytechnic University
29 Politechnicheskaya St., St. Petersburg, 195251, Russia
bannikov.ev.21@gmail.com
ORCID: 0000-0002-9820-062X

BERDNIKOV Yaroslav A.
Peter the Great St. Petersburg Polytechnic University
29 Politechnicheskaya St., St. Petersburg, 195251, Russia
berdnikov@spbstu.ru
ORCID: 0000-0003-0309-5917

LARIONOVA Daria M.
Peter the Great St. Petersburg Polytechnic University
29 Politechnicheskaya St., St. Petersburg, 195251, Russia
dashalario@gmail.com
ORCID: 0009-0007-7019-5586

KOTOV Dmirty O.
Peter the Great St. Petersburg Polytechnic University
29 Politechnicheskaya St., St. Petersburg, 195251, Russia
dmitriy.kotov@gmail.com
ORCID: 0000-0002-3395-0454

BASIROV Kirill N.
Peter the Great St. Petersburg Polytechnic University
29 Politechnicheskaya St., St. Petersburg, 195251, Russia
kirill.basirov@mail.ru

BORISOV Ivan I.
Peter the Great St. Petersburg Polytechnic University
29 Politechnicheskaya St., St. Petersburg, 195251, Russia
borisov.ii@edu.spbstu.ru

СВЕДЕНИЯ ОБ АВТОРАХ

БАННИКОВ Егор Викторович – *аспирант Высшей школы фундаментальных физических исследований Санкт-Петербургского политехнического университета Петра Великого.*
195251, Россия, **г**. Санкт-Петербург, Политехническая **ул., 29**
bannikov.ev.21@gmail.com
ORCID: 0000-0002-9820-062X

БЕРДНИКОВ Ярослав Александрович – *доктор физико-математических наук, профессор Высшей школы фундаментальных физических исследований Санкт-Петербургского политехнического университета Петра Великого.*
195251*, Россия, г. Санкт-Петербург, Политехническая ул., 29*
berdnikov@spbstu.ru
ORCID: 0000-0003-0309-5917

ЛАРИОНОВА Дарья Максимовна – *кандидат физико-математических наук, доцент Высшей школы фундаментальных физических исследований Санкт-Петербургского политехнического университета Петра Великого.*
195251, Россия, г. Санкт-Петербург, Политехническая ул., 29
dashalario@gmail.com
ORCID: 0009-0007-7019-5586

КОТОВ Дмитрий Олегович – *кандидат физико-математических наук, доцент Высшей школы фундаментальных физических исследований Санкт-Петербургского политехнического университета Петра Великого.*
195251, Россия, г. Санкт-Петербург, Политехническая ул., 29
dmitriy.kotov@gmail.com
ORCID: 0000-0002-3395-0454

БАСИРОВ Кирилл Наилевич – *инженер Высшей школы фундаментальных физических исследований Санкт-Петербургского политехнического университета Петра Великого.*
195251, Россия, г. Санкт-Петербург, Политехническая ул., 29
kirill.basirov@mail.ru

БОРИСОВ Иван Ильич – *студент Физико-механического института Санкт-Петербургского политехнического университета Петра Великого.*
195251, Россия, г. Санкт-Петербург, Политехническая ул., 29
borisov.ii@edu.spbstu.ru

Received 11.01.2026. Approved after reviewing 19.01.2026. Accepted 19.01.2026.
Статья поступила в редакцию 11.01.2026. Одобрена после рецензирования 19.01.2026. Принята 19.01.2026.

© Peter the Great St. Petersburg Polytechnic University, 2026

Original article
DOI: https://doi.org/10.18721/JPM.19214

DOUBLE LONGITUDINAL SPIN ASYMMETRY OF *J*/ψ MESONS PRODUCED IN PROTON-PROTON COLLISIONS WITH LONGITUDINAL POLARIZATION

D. V. Kruashvili✉, *Ya. A. Berdnikov*

Peter the Great St. Petersburg Polytechnic University, St. Petersburg, Russia

✉ kruashvili.dv@edu.spbstu.ru

Abstract. The paper puts forward an extension of the Pythia8 software package, which makes it possible to calculate collisions of longitudinally polarized protons with the production of J/ψ mesons. The transverse momentum spectra of J/ψ mesons and the double longitudinal spin asymmetry of them at an energy of 510 GeV have been obtained. The calculated results were compared with experimental data, and a satisfactory agreement between them was established. This success served as the basis for predicting the results of the SPD experiment at the NICA collider. The corresponding calculations of the transverse momentum spectrum and the double longitudinal spin asymmetry of the J/ψ meson at an energy of 27 GeV were presented. All conclusions were based on the collinear parton model.

Keywords: Pythia8, double longitudinal spin asymmetry, parton distribution function, parton cross section

Funding: The reported study was carried out within the framework of the State Assignment for Fundamental Research (Subject Code FSEG-2025-0009).

Citation: Kruashvili D. V., Berdnikov Ya. A., Double longitudinal spin asymmetry of J/ψ mesons produced in proton-proton collisions with longitudinal polarization, St. Petersburg State Polytechnical University Journal. Physics and Mathematics. 19 (2) (2026) 171–177. DOI: https://doi.org/10.18721/JPM.19214

This is an open access article under the CC BY-NC 4.0 license (https://creativecommons.org/licenses/by-nc/4.0/)

Научная статья
УДК 532.517
DOI: https://doi.org/10.18721/JPM.19214

ДВОЙНАЯ ПРОДОЛЬНАЯ СПИНОВАЯ АСИММЕТРИЯ (*J*/ψ)-МЕЗОНОВ, РОЖДЕННЫХ В ПРОДОЛЬНО-ПОЛЯРИЗОВАННЫХ ПРОТОН-ПРОТОННЫХ СТОЛКНОВЕНИЯХ

Д. В. Круашвили✉, *Я. А. Бердников*

Санкт-Петербургский политехнический университет Петра Великого,
Санкт-Петербург, Россия

✉ kruashvili.dv@edu.spbstu.ru

Аннотация. В работе предложено расширение программного пакета Pythia8, благодаря которому появилась возможность рассчитывать столкновения продольно-поляризованных протонов с рождением (J/ψ)-мезонов. Получены спектры по поперечному импульсу и двойная продольная спиновая асимметрия (J/ψ)-мезонов при энергии 510 ГэВ. Проведено сравнение расчетных результатов с экспериментальными данными и установлено их вполне удовлетворительное согласие. Этот успех послужил

© Kruashvili D. V., Berdnikov Ya. A., 2026. Published by Peter the Great St. Petersburg Polytechnic University.

основанием для предсказания результатов эксперимента SPD на коллайдере NICA. Представлены соответствующие вычисления спектра по поперечному импульсу и двойная продольная спиновая асимметрия (J/ψ)-мезона при энергии 27 ГэВ. Все выводы сделаны в рамках коллинеарной партонной модели.

Ключевые слова: Pythia8, двойная продольная спиновая асимметрия, функция распределения партонов, партонное сечение рассеяния

Финансирование: Работа выполнена в рамках Государственного задания на проведение фундаментальных исследований (код темы FSEG-2025-0009).

Ссылка для цитирования: Круашвили Д. В., Бердников Я. А. Двойная продольная спиновая асимметрия (J/ψ)-мезонов, рожденных в продольно-поляризованных протон-протонных столкновениях // Научно-технические ведомости СПбГПУ. Физико-математические науки. 2026. Т. 19. № 2. С. 171–177. DOI: https://doi.org/10.18721/JPM.19214

Статья открытого доступа, распространяемая по лицензии CC BY-NC 4.0 (https://creativecommons.org/licenses/by-nc/4.0/)

Introduction

Studies of J/ψ meson production in proton–proton (pp) collisions provide access to gluon distribution functions in the proton, which in turn makes it possible to estimate the gluon contribution to the proton spin [1].

The proton spin can be expressed using the Manohar–Jaffe sum rule [2]:

$$S_p = 1/2 = (1/2)\,\Delta\Sigma + \Delta G + L_q + L_g, \tag{1}$$

where $(1/2)\Delta\Sigma$ and ΔG are the contributions from quark and gluon helicities, respectively [3]; L_q and L_g are the contributions from the orbital angular momenta of quarks q and gluons g, respectively.

These contributions are given by [4]:

$$\Delta\Sigma = \sum_q \int \Delta f_q(x,Q^2)dx,\ \Delta G = \int \Delta g(x,Q^2)dx, \tag{2}$$

where

$$\Delta f_q(x,Q^2) = f_q^+(x,Q^2) - f_q^-(x,Q^2),\ \Delta g(x,Q^2) = g^+(x,Q^2) - g^-(x,Q^2) \tag{3}$$

(see [5]).

The quantities in (3) are defined as follows: $f_q^+(x,Q^2)$, $f_q^-(x,Q^2)$ are the quark distribution functions in protons with positive and negative helicities, with momentum fraction x at scale Q^2; $g^+(x,Q^2)$, $g^-(x,Q^2)$ are the gluon distribution functions in protons with positive and negative helicities, with momentum fraction x at scale Q^2.

In the literature, $\Delta f_q(x,Q^2)$ и $\Delta g(x,Q^2)$ are commonly referred to as the polarized quark and gluon distribution functions in the proton [5]. It should be noted, however, that according to [3], the $\Delta g(x,Q^2)$ functions are not as well studied as the $\Delta f_q(x,Q^2)$ functions.

This study was motivated by two factors: the limited knowledge of the polarized gluon distribution functions, and the fact that gluon-initiated processes are central to J/ψ meson production in proton–proton collisions [5].

Our goal was to investigate the conditions and features of J/ψ meson production in collisions of polarized and unpolarized protons.

© Круашвили Д. В., Бердников Я. А., 2026. Издатель: Санкт-Петербургский политехнический университет Петра Великого.

Computational procedure

The double longitudinal spin asymmetry (DLSA) [4] in collisions of longitudinally polarized protons is defined as:

$$A_{LL} = \frac{d\sigma^{(++)} - d\sigma^{(+-)}}{d\sigma^{(++)} + d\sigma^{(++)}} = \frac{d\Delta\sigma}{d\sigma}, \tag{4}$$

where $d\sigma^{(++)}$, $d\sigma^{(+-)}$ are the cross sections for collisions of protons with the same (++) and opposite (+−) helicities; $d\Delta\sigma^{(++)}$, $d\Delta\sigma^{(+-)}$ are the cross sections for J/ψ meson production in collisions of polarized and unpolarized protons (i.e., polarized and unpolarized cross sections, respectively) [4].

According to the factorization theorem [6], the unpolarized cross section

$$d\sigma(pp \to J/\psi + X)$$

for J/ψ meson production in semi-inclusive proton−proton collisions can be written as a convolution of the unpolarized parton distribution functions $f_a(x_a, Q^2)$ and $f_b(x_b, Q^2)$ [7, 8]:

$$d\sigma\left(pp \to J/\psi + X\right) = \sum_{a,b,d} \int dx_a f_a\left(x_a, Q^2\right) \int dx_b \cdot f_b\left(x_b, Q^2\right) \cdot d\sigma^{(ab\to(cc)d)} \hat{\sigma}\bar{c}. \tag{5}$$

The polarized cross section

$$d\Delta\sigma(pp \to J/\psi + X)$$

for $J//\psi$ meson production in semi-inclusive longitudinally polarized proton−proton collisions is written as a convolution of the longitudinally polarized parton distribution functions $\Delta f_a(x_a, Q^2)$ and $\Delta f_b(x_b, Q^2)$ [7−9]:

$$d\Delta\sigma\left(pp \to J/\psi + X\right) = \sum_{a,b,d} \int dx_a \Delta f_a\left(x_a, Q^2\right) \int dx_b \cdot \Delta f_b\left(x_b, Q^2\right) \cdot d\Delta\hat{\sigma}^{(ab\to(c\bar{c})d)}. \tag{6}$$

In expressions (5) and (6), a, b are the partons (quarks, gluons) of the colliding protons; the notation $(c\bar{c})d$ denotes the charm quark−antiquark pair $(c\bar{c})$ and the parton $d$produced in the process $ab \to (c\bar{c})d$; x_a, x_b are the momentum fractions carried by parton a from the first proton and by parton $b$from the second proton.

In the same expressions (5) and (6), $d\hat{\sigma}^{(ab\to(c\bar{c})d)}$, $d\Delta\hat{\sigma}^{(ab\to(c\bar{c})d)}$ are, respectively, the unpolarized and polarized parton scattering cross sections for $ab \to (c\bar{c})d$.

Within the color-octet model, the cross sections for J/ψ meson production take the following form [10]:

$$d\sigma\left(pp \to J/\psi + X\right) = \sum_{a,b,d} \int dx_a f_a\left(x_a, Q^2\right) \int dx_b \cdot f_b\left(x_b, Q^2\right) \sum_n \left\langle \mathcal{O}^{J/\psi}[n] \right\rangle \times \\ \times d\hat{\sigma}(ab \to c\bar{c}[n]d), \tag{7}$$

$$d\Delta\sigma\left(pp \to J/\psi + X\right) = \sum_{a,b,d} \int dx_a \Delta f_a\left(x_a, Q^2\right) \int dx_b \cdot \Delta f_b\left(x_b, Q^2\right) \sum_n \left\langle \mathcal{O}^{J/\psi}[n] \right\rangle \times \\ \times d\Delta\hat{\sigma}(ab \to c\bar{c}[n]d). \tag{8}$$

In expressions (7) and (8), the parton cross section is expressed as a sum over all possible $[n]$ states of the $c\bar{c}$ pair composed of the charm quark c and antiquark $\bar{c}$ [10]:

$$^3S_1^{(1)},\ ^3S_1^{(8)},\ ^3S_0^{(8)},\ ^3P_0^{(8)},\ ^3P_1^{(8)},\ ^3P_2^{(8)}. \tag{9}$$

The coefficients $\langle \mathcal{O}^{J/\psi}[n] \rangle$ are the probabilities for J/ψ meson production from a given state [10] (n is the index of the possible quark-antiquark state $c\bar{c}$ of the charm quark pair).

The following interaction processes of gluons g, quarks q, and antiquarks $\bar{q}$ that can produce J/ψ mesons were taken into account in this study:

$$gg \to (c\bar{c}) + g \to J/\psi + g,$$
$$qg \to (c\bar{c}) + q \to J/\psi + q,$$
$$q\bar{q} \to (c\bar{c}) + g \to J/\psi + g,$$

In the native version of the Pythia8 software package [11], unpolarized distribution functions are convolved with unpolarized parton cross sections to generate proton–proton collisions, which yields the unpolarized cross section (6). To obtain the polarized cross section (7), which is needed for calculating the DLSA, the unpolarized distribution functions and unpolarized parton cross sections should be replaced with polarized ones, which was done in this work. To generate J/ψ meson production, we modified the SigmaOnia.cc file in Pythia8. Polarized parton cross sections were used in this file instead of the original parton cross sections [10].

The distribution functions were replaced directly in the code using the command:

pythia.readString(«PDF: pSet = LHAPDF6:»+ name_pdf_set).

The original unpolarized distribution functions were replaced with the polarized ones [12].

This modification of Pythia8 allowed us to compute the polarized cross section $d\Delta\sigma$ for the J/ψ meson. This, in turn, made it possible to calculate the DLSA.

Computational results

To validate the algorithm proposed in this work and the modification of the program for calculating the DLSA of J/ψ mesons produced in longitudinally polarized proton–proton collisions, we obtained the following computational results at 510 GeV:

transverse momentum spectra of (J/ψ)- mesons produced in unpolarized proton–proton collisions (Fig. 1);

DLSA for the J/ψ meson (Fig. 2).

The choice of this energy was motivated by the results of the STAR and PHENIX experiments at the Brookhaven National Laboratory (USA) [3, 13]. The spectra shown in Fig. 1 are multiplied by the branching ratio (BR) for the J/ψ meson decay into muon and anti-muon. The BR is the relative fraction of a specific decay channel with respect to the total number of decays of the given particle: it shows how often a meson decays via this particular channel, and is defined as the ratio of the partial decay width Γ_i to the total decay width Γ_{tot}: Γ_i/Γ_{tot}.

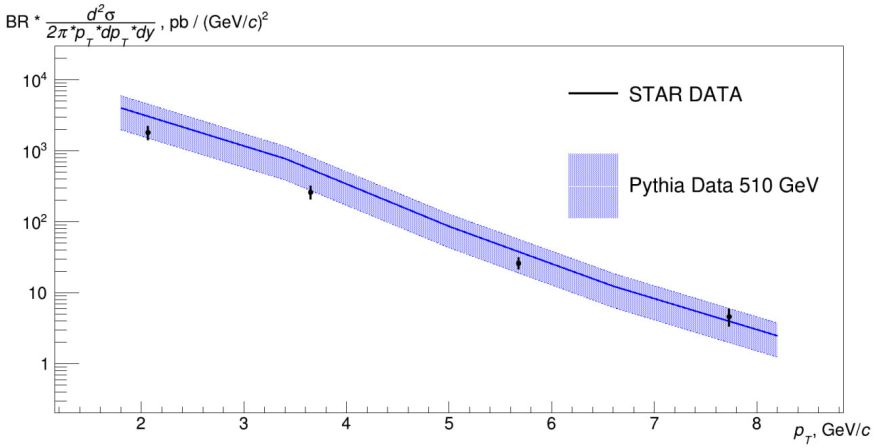


Fig. 1. Invariant p_T spectrum of J/ψ mesons produced in unpolarized proton–proton collisions at 510 GeV (the data are multiplied by the branching ratio BR for the $J/\psi \to \mu^+\mu^-$ decay)
Our simulation results are shown by the blue solid curve (the shaded band around it reflects the range of uncertainties due to PDF errors). The experimental data from the STAR Collaboration [13] are shown by points for comparison

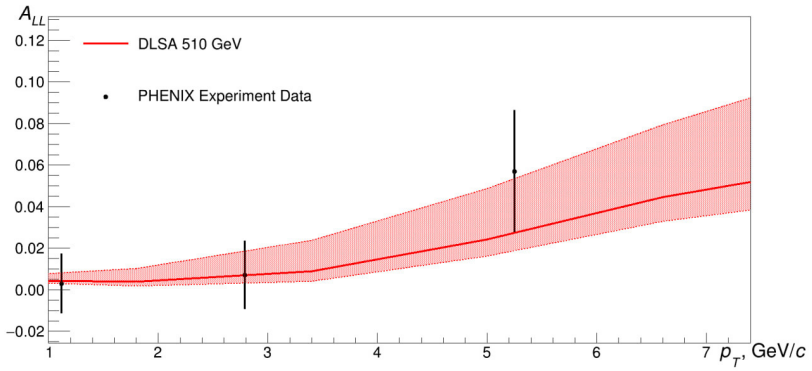


Fig. 2. Double longitudinal spin asymmetry of J/ψ mesons produced in longitudinally polarized proton–proton collisions at 510 GeV as a function of transverse momentum
Our simulation results are shown by the red solid curve (the shaded band around it reflects the range of uncertainties due to PDF errors [12]). The experimental data from the PHENIX Collaboration [3] are shown by points (the error bars represent the uncertainties) for comparison

Analyzing the data in Figs. 1 and 2, we reached the following conclusions:

the simulation data obtained with the modified Pythia8 program are in good agreement (within uncertainties) with the experimental p_T spectrum of J/ψ mesons produced in unpolarized proton–proton collisions at 510 GeV (Fig. 1);

our calculations with Pythia8 are also in good agreement (within uncertainties) with the experimental DLSA dependence of J/ψ mesons produced in longitudinally polarized proton–proton collisions at 510 GeV as a function of transverse momentum.

The satisfactory agreement between our calculations and the experimental data (see Figs. 1 and 2) makes it possible to predict the behavior of the DLSA dependences for J/ψ mesons in interactions of polarized protons. The results of such calculations were obtained in this work (Fig. 3) at 27 GeV, which is the energy characteristic of the planned SPD experiment at the NICA collider.

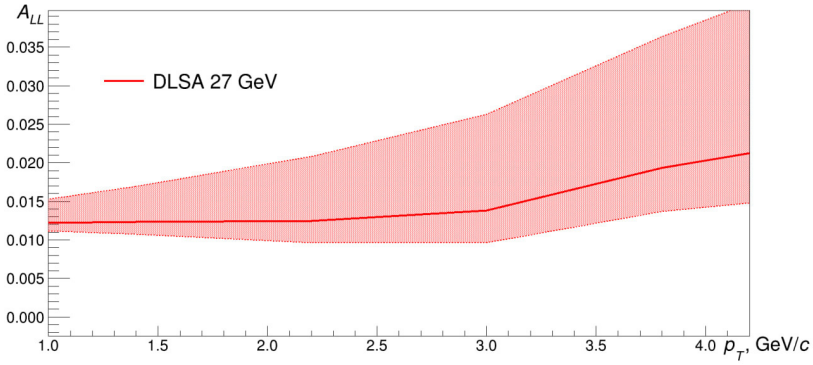


Fig. 3. Predicted DLSA dependence of J/ψ mesons produced in longitudinally polarized proton–proton collisions as a function of p_T. The calculated data are similar to those shown in Fig. 2, but for 27 GeV (instead of 510 GeV in Fig. 2)

Conclusion

In this work, we investigated the feasibility of calculating the double longitudinal spin asymmetry (DLSA) using the Pythia8 software package by modifying parts of the Pythia8 source code. This modification allows calculating the DLSA for J/ψ mesons in proton–proton collisions at various energies. We compared our calculated results with experimental data at 510 GeV and found them to be in satisfactory agreement. This agreement served as the basis for making predictions for the planned NICA experiment (see Fig. 3).

REFERENCES

1. **Ji X., Xiong X., Yuan F.,** Proton spin structure from measurable parton distributions, Phys. Rev. Lett. 109 (15) (2012) 152005.

2. **Jaffe R. L., Manohar A.,** The g_1 problem: Deep inelastic electron scattering and the spin of the proton, Nucl. Phys. B. 337 (3) (1990) 509–546.

3. **Adare A., Aidata C., Ajitanand N. N., et al.,** Measurements of double-helicity asymmetries in inclusive J/ψ production in longitudinally polarized $p + p$ collisions at $s = 510$ GeV, Phys. Rev. D. 94 (11) (2016) 112008.

4. **Saleev V. A., Shipilova A. V.,** Double longitudinal-spin asymmetries in direct photon production at NICA, Phys. Part. Nuclei. Lett. 20 (3) (2023) 400–403.

5. **Stratmann M.** Polarized parton densities and processes, New Trends in HERA Physics 1999: Proc. Ringberg Workshop Held at Tegernsee, Germany, 30 May–4 June 1999, Springer Berlin Heidelberg (2001) 83–97.

6. **Collins J. C., Soper D. E., Sterman G.** Factorization of hard processes in QCD, Adv. Ser. Dir. High Energy Phys. 5 (1988) 1–91.

7. **Sivers D. W.,** Single-spin production asymmetries from the hard scattering of pointlike constituents, Phys. Rev. D. 41 (1) (1990) 83–90.

8. **Collins J. C.,** Fragmentation of transversely polarized quarks probed in transverse momentum distributions, Nucl. Phys. B. 396 (1) (1993) 161–182.

9. **Bomhof C. J., Mulders P. J.,** Gluonic pole cross sections and single spin asymmetries in hadron-hadron scattering, J. High Energy Phys. 2007 (2) (2007) 029.

10. **Klasen M., Kniehl B. A., Mihaila L. N., Steinhauser M.,** Charmonium production in polarized high-energy collisions, Phys. Rev. D. 68 (3) (2003) 034017.

11. **Ciesielski R., Goulianos K.,** MBR Monte Carlo simulation in PYTHIA8, arXiv preprint arXiv:1205.1446 (2012).

12. **Gehrmann T., Stirling W. J.,** Spin-dependent parton distributions from polar-ized structure function data, Z. Phys. C. 65 (3) (1995) 461–470.

13. **Adam J., Adamczyk L., Adams J. R., et al.,** Measurements of the transverse-momentum-dependent cross sections of J/ψ production at mid-rapidity in proton + proton collisions at $s = 510$ and 500 GeV with the STAR detector, Phys. Rev. D. 100 (5) (2019) 052009.

СПИСОК ЛИТЕРАТУРЫ

1. **Ji X., Xiong X., Yuan F.** Proton spin structure from measurable parton distributions // Physical Review Letters. 2012. Vol. 109. No. 15. P. 152005.

2. **Jaffe R. L., Manohar A.** The g_1 problem: Deep inelastic electron scattering and the spin of the proton // Nuclear Physics. B. 1990. Vol. 337. No. 3. 509–546.

3. **Adare A., Aidata C., Ajitanand N. N., et al**. Measurements of double-helicity asymmetries in inclusive J/ψ production in longitudinally polarized $p + p$ collisions at $s = 510$ GeV // Physical Review D. 2016. Vol. 94. No. 11. P. 112008.

4. **Салеев В. А., Шипилова А. В.** Двойные продольные спиновые асимметрии в прямом рождении фотонов на коллайдере NICA // Письма в журнал «Физика элементарных частиц и атомного ядра». 2023. Т. 20. № 3(248). С. 417–421.

5. **Stratmann M.** Polarized parton densities and processes // New Trends in HERA Physics 1999: Proceedings of the Ringberg Workshop Held at Tegernsee, Germany, 30 May – 4 June 1999, Berlin, Heidelberg: Springer Berlin Heidelberg, 2001. С. 83–97.

6. **Collins J. C., Soper D. E., Sterman G.** Factorization of hard processes in QCD // Advanced Series on Directions in High Energy Physics. 1988. Vol. 5. Pp. 1–91.

7. **Sivers D. W.** Single spin production asymmetries from the hard scattering of pointlike constituents // Physical Review D. 1990. Vol. 41. No. 1. Pp. 83–90.

8. **Collins J. C.** Fragmentation of transversely polarized quarks probed in transverse momentum distributions // Nuclear Physics B. 1993. Vol. 396. No. 1. Pp. 161–182.

9. **Bomhof C. J., Mulders P. J.** Gluonic pole cross sections and single spin asymmetries in hadron-hadron scattering // Journal of High Energy Physics. 2007. Vol. 2007. No. 2. P. 029.

10. **Klasen M., Kniehl B. A., Mihaila L. N., Steinhauser M.** Charmonium production in polarized high-energy collisions // Physical Review D. 2003. Vol. 68. No. 3. P. 034017.
11. **Ciesielski R., Goulianos K.** MBR Monte Carlo simulation in PYTHIA8 // arXiv preprint arXiv:1205.1446. 2012.
12. **Gehrmann T., Stirling W. J.** Spin-dependent parton distributions from polarized structure function data // Zeitschrift für Physik C.: Particles and Fields. 1995. Vol. 65. No. 3. Pp. 461–470.
13. **Adam J., Adamczyk L., Adams J. R., et al.** Measurements of the transverse-momentum-dependent cross sections of J/ψ production at mid-rapidity in proton+ proton collisions at $s = 510$ and 500 GeV with the STAR detector // Physical Review D. 2019. Vol. 100. No. 5. P. 052009.

THE AUTHORS

KRUASHVILI Dmitry V.
Peter the Great St. Petersburg Polytechnic University
29 Politechnicheskaya St., St. Petersburg, 195251, Russia
kruashvili.dv@edu.spbstu.ru

BERDNIKOV Yaroslav A.
Peter the Great St. Petersburg Polytechnic University
29 Politechnicheskaya St., St. Petersburg, 195251, Russia
berdnikov@spbstu.ru
ORCID: 0000-0003-0309-5917

СВЕДЕНИЯ ОБ АВТОРАХ

КРУАШВИЛИ Дмитрий Васильевич – *инженер Высшей школы фундаментальных физических исследований Санкт-Петербургского политехнического университета Петра Великого.*
195251, Россия, г. Санкт-Петербург, Политехническая ул., 29
kruashvili.dv@edu.spbstu.ru

БЕРДНИКОВ Ярослав Александрович – *доктор физико-математических наук, профессор Высшей школы фундаментальных физических исследований Санкт-Петербургского политехнического университета Петра Великого.*
195251, Россия, г. Санкт-Петербург, Политехническая ул., 29
berdnikov@spbstu.ru
ORCID: 0000-0003-0309-5917

Received 16.02.2026. Approved after reviewing 03.03.2026. Accepted 03.03.2026.
Статья поступила в редакцию 16.02.2026. Одобрена после рецензирования 03.03.2026. Принята 03.03.2026.

© Peter the Great St. Petersburg Polytechnic University, 2026

MECHANICS

Original article
DOI: https://doi.org/10.18721/JPM.19215

THE DAMPING OF PENDULAR OSCILLATIONS USING A PARAMETRIC CONTROLLER

N. A. Smirnova✉

Peter the Great St. Petersburg Polytechnic University, St. Petersburg, Russia

✉ smirnova_na@spbstu.ru

Abstract. In the paper, the efficiency of a parametric damping system for the oscillations of a linear, initially, lightly damped pendulum has been studied. A closed-loop stabilization system included the feedback based on the deviation of the simple pendulum's position from the prearranged one. Our system was equipped with a controller whose structure followed from the Mathieu equation, and the variable coefficients were selected taking into account the proposed methodology. The parametric controller (PC) was shown to be able to shorten the settling time via increasing the damping. Because of this, it makes sense to add the PC to a system with a traditional offset-based P-controller to improve dynamic performance and to increase accuracy in the steady state. Moreover, the PC successfully suppressed harmonic external disturbances. The PC based on the offset of one link was constructed for a planar two-link pendulum. The controller damped lower frequency oscillations, but this turned out to be enough to significantly improve the stabilization response.

Keywords: linear lightly damped pendulum, first parametric resonance, feedback system, parametric controller

Citation: Smirnova N. A., The damping of pendulum oscillations using a parametric controller, St. Petersburg State Polytechnical University Journal. Physics and Mathematics. 19 (2) (2026) 178–188. DOI: https://doi.org/10.18721/JPM.19215

This is an open access article under the CC BY-NC 4.0 license (https://creativecommons.org/licenses/by-nc/4.0/)

Научная статья
УДК 531.53
DOI: https://doi.org/10.18721/JPM.19215

ПОДАВЛЕНИЕ КОЛЕБАНИЙ МАЯТНИКА С ПОМОЩЬЮ ПАРАМЕТРИЧЕСКОГО РЕГУЛЯТОРА

Н. А. Смирнова✉

Санкт-Петербургский политехнический университет Петра Великого,
Санкт-Петербург, Россия

✉ smirnova_na@spbstu.ru

Аннотация. В работе исследована эффективность системы параметрического демпфирования колебаний линейного, изначально слабодемпфированного маятника. Для этого построена система стабилизации с обратной связью по отклонению положения однозвенного маятника от заданного. В замкнутой системе использован регулятор, структура которого следует из уравнения Матье, а варьируемые коэффициенты подобраны с учетом предложенной методики. Установлено, что параметрический регулятор (ПР) способен сократить время установления благодаря увеличению демпфирования. Поэтому ПР целесообразно добавлять в систему с традиционным пропорциональным регулятором

© Smirnova N. A., 2026. Published by Peter the Great St. Petersburg Polytechnic University.

по отклонению для улучшения динамических показателей и повышения точности в установившемся режиме. Показано, что ПР успешно подавляет гармонические внешние возмущения. Для плоского двухзвенного маятника построен ПР по отклонению одного звена. Регулятор демпфирует колебания с низшей частотой, но этого оказывается достаточно для существенного повышения быстродействия при стабилизации.

Ключевые слова: линейный слабодемпфированный маятник, первый параметрический резонанс, замкнутая система, параметрический регулятор, метод стационаризации

Ссылка для цитирования: Смирнова Н. А. Подавление колебаний маятника с помощью параметрического регулятора // Научно-технические ведомости СПбГПУ. Физико-математические науки. 2026. Т. 2 № .19. С. 178–188. DOI: https://doi.org/10.18721/JPM.19215

Статья открытого доступа, распространяемая по лицензии CC BY-NC 4.0 (https://creativecommons.org/licenses/by-nc/4.0/)

Introduction

Parametric excitation can destabilize a system if parametric resonance occurs [1], or it can stabilize an unstable system [2]. Studies of oscillatory processes in periodically nonstationary dynamical systems focus primarily on constructing and refining the resonance regions in the plane of the parameters of the periodic coefficient [3, 4] or, when damping is included, in three-dimensional space [5]. Domains of vibrational stabilization of unstable systems lie outside the parametric resonance regions [6–8]. The boundaries of the parametric excitation zones are generally found by seeking approximate periodic solutions that separate the regions of stable and unstable motion. The most common asymptotic methods include the method of multiple scales [9], the averaging (van der Pol) method [10], the harmonic balance method, and others [11–13]. The method of stationarization of a periodic parameter [14], which we use in this work, is an extension of harmonic linearization. To apply it, the filter hypothesis for the linear part of the system must be satisfied, but it is not necessary to isolate a small parameter or assume slow variation of the oscillation envelope.

Parametric excitation can serve not only to stabilize oscillations of unstable objects but also to increase damping, thereby accelerating the stabilization of stable objects. Parametric anti-resonance is observed in systems with multiple degrees of freedom [15]. Its mechanism relies on coupling slow modal motions through parametric excitation. In accordance with Floquet theory, a monodromy matrix is constructed for the fundamental matrix of slow motion. Then the characteristic numbers (multipliers) are calculated for a fixed frequency and amplitude of the parameter. It was established that parametric excitation at a certain frequency (a combination of the object's natural frequencies) shifts the characteristic multipliers of the monodromy matrix toward the center of the unit circle [16]. The damping effect is significant for oscillations at the lowest elastic frequency. The damping system is implemented as open-loop control because the frequency of parametric excitation is calculated from the object model.

Another approach to increasing damping is implemented in a closed-loop system, where the damping properties depend on the balance of amplitudes and phases of the signals circulating in the loop. For linear closed-loop systems, these properties are known as stability margins and are determined by the Nyquist criterion at the crossover frequency. Increased damping in a closed-loop system can be achieved by creating excitation conditions that are similar to those of the first parametric resonance in terms of the frequency and amplitude of the parameter oscillations, but differ in the value of the time (phase) shift between the oscillations of the parameter and those of the output variable. When parametric resonance is excited, a specific shift is established. The stability margins of the closed-loop system can be adjusted by controlling this shift. Thus, parametric damping can be achieved instead of parametric resonance. The time shift between the periodic variation of the parameter and the oscillations of the output coordinate was used in [17, 18] to damp the output oscillations. It was found in [19] for vibrational stabilization of a flexible long rod under various boundary conditions that the basin of attraction of the vertical position depends significantly on the initial phase of the base oscillations.

© Смирнова Н. А., 2026. Издатель: Санкт-Петербургский политехнический университет Петра Великого.

In this work, we investigate the efficiency of parametric damping in pendulum stabilization problems, implemented via a feedback control system. We propose a procedure for adjusting the variable coefficients of a parametric controller. The results of numerical simulation confirm the robustness of the stabilization algorithm.

Model of parametric controller in closed-loop stabilization system

Consider the problem of controlled stabilization of the stable equilibrium position of a pendulum. The objective of control is to improve the speed of the stabilization response. We take a linear model of a single-link pendulum as the plant. A fundamental feature of the plant is its light damping, which prevents the closed-loop system with a proportional controller from achieving acceptable performance.

The Mathieu equation describing the oscillations of a linear pendulum caused by a periodic variation of a parameter has the form

$$\ddot{\alpha}(t) + 2\nu\dot{\alpha}(t) + [1 + \mu\sin(kt - \varphi)]\alpha(t) = 0, \tag{1}$$

where t is the dimensionless time, $t = \omega_0$ (ω_0 is the natural frequency of the pendulum, is the dimensional time); α is the deviation of the pendulum from the equilibrium position, $\alpha^d = 0$; k is the ratio of the parameter oscillation frequency to ω_0; μ is the dimensionless amplitude of the parameter oscillations ($\mu < 1$); φ is the phase shift between the parameter oscillations and the pendulum motion; ν is the relative damping.

We rewrite Eq. (1) in the form

$$\ddot{\alpha} + 2\nu\dot{\alpha} + \alpha = -[\mu\sin(kt - \varphi)]\alpha = u \tag{2}$$

and regard the right-hand side of Eq. (2) as the control input u. Then the expression in square brackets is the parametric control law, and Eq. (2) describes the model of a closed-loop system.

Consequently, an unstable oscillatory process with the dimensionless frequency $k/2$, called the first parametric resonance, may occur in the closed-loop system. The goal of the study is to determine values of the variable controller coefficients that can suppress the output oscillations $\alpha(t)$. The quality of oscillation suppression in the closed-loop system is assessed by the settling time.

Let us determine the boundaries of the first parametric resonance in the closed-loop system. Suppose that in Eq. (2), there exist sustained oscillations of the variable

$$\alpha(t) = A\sin(k/2)t,$$

where A is the amplitude, $k/2$ is the dimensionless frequency.

Then the control law takes the form

$$u = -\mu A\cdot\sin[(k/2)t]\cdot\sin(kt - \varphi) = -0.5\mu A\{\cos[(k/2)t - \varphi] - \cos[(3k/2)t - \varphi]\}. \tag{3}$$

If $k/2 \approx 1$, i.e., close to the natural frequency of the oscillator, the second term on the right-hand side of Eq. (3) can be neglected, so after trigonometric transformations we obtain the approximate control law

$$u = -0.5\mu\{\sin\varphi + [(2/k)\cos\varphi]d\}\cdot A\sin(k/2)t \tag{3a}$$

where d is the differentiation operator with respect to dimensionless time.

Control law (3a) transforms the harmonic negative-feedback signal into a harmonic control signal of the same frequency $k/2$.

Since the equality

$$\{\sin\varphi + [(2/k)\cos\varphi]d\}|_{d=ik/2} = \exp\{i[(\pi/2) - \varphi)]\},$$

holds true, the model of the parametric controller for determining the resonance boundary can be written as a complex transfer coefficient [14]:

$$W(i\varphi) = (\mu/2)\cdot\exp\{i[(\pi/2) - \varphi]\}. \tag{4}$$

Consider a system closed by unity-gain negative feedback; its forward path consists of the parametric controller series-connected to the oscillator wtih a transfer function

$$H(p) = \frac{1}{p^2 + 2\nu p + 1}.$$

According to the Nyquist criterion, a periodic regime with the frequency $k/2$ is established in the closed-loop system assuming the equal magnitudes

$$|W(i\varphi)| = \left| H^{-1}(i\frac{\omega}{\omega_0}) \right|_{\frac{\omega}{\omega_0}=\frac{k}{2}},$$

therefore,

$$\frac{\mu}{2} = \sqrt{\left(1 - \frac{k^2}{4}\right)^2 + \nu^2 k^2}, \tag{5}$$

and the phases are also equal:

$$\pi/2 - \varphi - \text{arctg}[\nu k/(1 - k^2/4)] = -\pi. \tag{6}$$

For the case $k = 2$, Eqs. (5) and (6) give the values of the amplitude $\mu = 4\nu$ and phase shift $\varphi = \pi$ at which the closed-loop system is on the stability boundary. The procedure for adjusting the controller coefficients is as follows.

Step 1. Fix the parameter oscillation frequency at $k = 2$.

Step 2. Choose the parameter oscillation amplitude from the range $4\nu < \mu < 1$ within the parametric resonance region.

Step 3. Select the phase shift φ so as to provide a sufficient phase margin in the closed-loop system.

The question of whether the stabilization process can be accelerated compared to the uncontrolled process was answered by numerical experiment. The main goal in the numerical implementation of the parametric controller was to generate a signal with a prescribed oscillation period from accurate measurements of the damped output oscillations $\alpha(t)$. To this end, the output $\alpha(t)$ was processed in the Simulink environment by passing it successively through a quadratic function, a differentiator, and a pure delay block with the transfer function

$$H_{dl}(p) = \exp(-\tau p)$$

and then fed to a bistable relay [17]. The relay output produced a rectangular signal with a period half that of the oscillation 'period' of the output $\alpha(t)$ and phase-shifted by $\varphi = (\pi/2) - k\tau$.

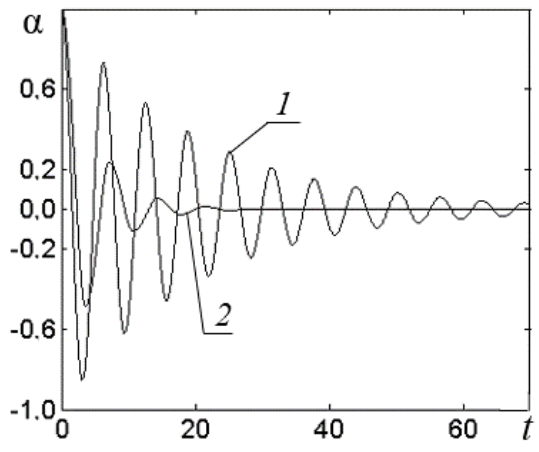


Fig. 1. Waveforms of free oscillations of the pendulum at relative damping $\nu = 0.05$ (curve *1*) and of the closed-loop system output $\alpha(t)$ at parametric controller coefficients $\mu = 0.5$ and $\tau = 0$ (curve *2*)

Fig. 1 shows the output waveform of the closed-loop system stabilizing the pendulum at the equilibrium position $\alpha^d = 0$ and the free oscillation waveform of the pendulum at $\alpha(0) = 1$. The settling time in the closed-loop system was reduced by a factor of four.

The stabilization efficiency is preserved when the amplitude μ and delay τ are varied over a wide range. It is recommended to choose μ closer to the upper bound for $\tau=0$. Thus, a distinctive feature of the parametric controller is its robustness.

Let us examine the performance of the parametric controller in the problem of suppressing an external harmonic disturbance. We add a harmonic disturbance torque to the right-hand side of Eq. (2). Replacing the periodic parameter by the complex coefficient (4) yields the approximate closed-loop equation:

$$\ddot{\alpha} + 2\nu\dot{\alpha} + \alpha + \frac{\mu}{2}\exp[i(\frac{\pi}{2} - \varphi)]\alpha = B\exp[i(\lambda t - \theta)], \tag{7}$$

where λ is the ratio of the disturbing torque frequency to the oscillator's natural frequency ω_0, B is the amplitude, θ is the disturbance phase.

The quality of suppression of forced oscillations is estimated from the frequency response of the closed-loop system. We seek the steady-state solution of Eq. (7) in the form

$$\alpha_\infty = A\exp\,[i\,(\lambda t - \psi)], \tag{8}$$

where A is the amplitude of the forced oscillations of the closed-loop output and ψ is the phase shift.

Note that the description of the parametric controller by the complex coefficient $W(i\varphi)$ becomes inadequate for $\lambda<1$, since the second term on the right-hand side of Eq. (3) cannot be neglected in the low-frequency range. Substituting solution (8) into Eq. (7), we obtain:

$$(B/A)\,\exp\,[i\,(\psi - \theta)] = H^{-1}(i\lambda) + W(i\varphi), \tag{9}$$

where $H^{-1}(i\lambda) = -\lambda^2 + 2\nu i\lambda + 1$.

The phase balance obtained from the graphical solution of Eq. (9) shows that a forced oscillation regime is fundamentally possible. The magnitude balance in Eq. (9) yields the frequency response of the closed-loop system:

$$\frac{A}{B} = \frac{1}{\sqrt{(1-\lambda^2 + \frac{\mu}{2}\sin\varphi)^2 + (2\nu\lambda + \frac{\mu}{2}\cos\varphi)^2}}. \tag{10}$$

If we set $\varphi=0$ in Eq. (10), which together with $4\nu<\mu<1$ provides the shortest settling time in the closed-loop system, the frequency response is reduced to

$$\frac{A}{B} = \frac{1}{\sqrt{(1-\lambda^2)^2 + (2\nu\lambda + \frac{\mu}{2})^2}}. \tag{11}$$

The closed-loop response at the natural frequency $\lambda = 1$ is

$$\left.\frac{A}{B}\right|_{\lambda=1} = \frac{1}{2\nu + \frac{\mu}{2}}$$

and decreases with increasing μ.

The dots in Fig. 2 mark the amplitudes of forced oscillations obtained from numerical experiments at $B = 1$. The frequency response (solid line) calculated from Eq. (11) is also shown for comparison.

The largest discrepancy is observed in the low-frequency range and is apparently due to the inadequate description of the parametric controller by the complex coefficient. Importantly, the closed-loop response at $\lambda=1$ is far below the resonance value of the linear oscillator, $A_{osc} = 1/2\nu$.

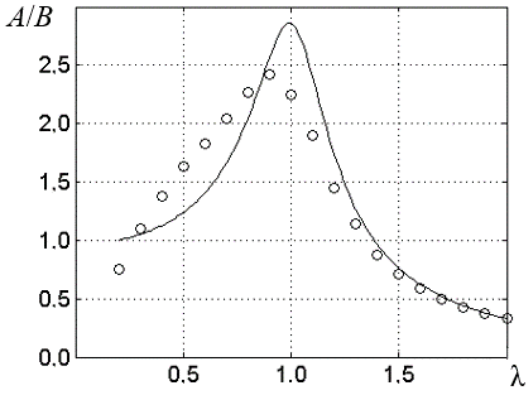


Fig. 2. Frequency responses of the closed-loop system obtained from Eq. (11) (solid line) and numerically (symbols). Amplitudes A of forced oscillations are calculated at $B = 1$, $\nu = 0.05$, $\mu = 0.5$, $\tau = 0$

Parametric controller as an addition to a conventional proportional controller

Consider the problem of controlled stabilization of an arbitrary position $\alpha^d \neq 0$ that does not coincide with the stable equilibrium position of the pendulum. Let us supplement the pendulum model with an actuator model, assumed to be a first-order lag element. The model of a closed-loop system with a proportional controller (P-controller) takes the form

$$(Td + 1)(d^2 + 2\nu d + 1)\alpha(t) = K_p[\alpha^d - \alpha(t)],$$

where d is the differentiation operator with respect to dimensionless time; $T = \omega_0$ is the dimensionless time constant of the lag element; K_p is the gain of the P-controller.

The efficiency of the P-controller in this problem is limited by the need to compromise between the requirements for the transient and steady-state (α_∞) regimes. To reduce the steady-state error

$$e_\infty = \alpha^d - \alpha_\infty = \alpha^d/(1 + K_p),$$

The gain K_p should be increased. To ensure the stability of a closed-loop system, the value of the coefficient K_p must satisfy the inequality

$$1 + K_p < (2\nu/T)\,(1 + 2\nu/T). \qquad (12)$$

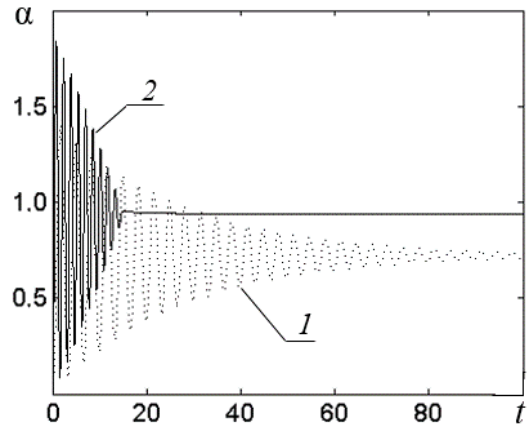


Fig. 3. Transient responses in the closed-loop system with the P-controller (gain K_p =2.6, curve *1*) and with the P-controller (gain K_p = 15) plus the parametric controller at μ=0.5 and τ=0 (curve *2*)

Fig. 3 shows the transient response ($\alpha^d = 1$) in the closed-loop system with the P-controller whose gain $K_p = 2.6$ provides a standard 60° phase margin in the closed-loop system for the chosen plant parameters $\nu = 0.05$, $T = 0.01$.

Let us include a parametric controller in the block diagram of the closed-loop system so that the controller's output is added to the P-controller output. The addition of the parametric controller makes it possible to achieve faster transient settling in the closed-loop system for the same K_p. Furthermore, it significantly extends (compared to condition (12)) the range of K_p values for which the closed-loop system is stable. This, in turn, allows reducing the steady-state error in the closed-loop system. Fig. 3 shows the transient response in the closed-loop system that includes the P-controller with K_p = 15 and the parametric controller. As a result, the steady-state error was reduced by a factor of 4.5 and the settling time by a factor of 5.6.

Stabilization of a planar two-link pendulum

Consider the problem of controlled stabilization of the stable equilibrium position of a planar two-link pendulum. We use a linear model of the two-link pendulum, assuming for simplicity that the end masses and the lengths of both links are equal. We write the model in dimensionless form (as was done in [20, 21]), introducing the natural frequency of a single-link pendulum ω_0 and a dimensionless time $t = \omega_0$:

$$M\begin{bmatrix}\ddot{\alpha}_1\\ \ddot{\alpha}_2\end{bmatrix}+2B\begin{bmatrix}\dot{\alpha}_1\\ \dot{\alpha}_2\end{bmatrix}+C\begin{bmatrix}\alpha_1\\ \alpha_2\end{bmatrix}=\begin{bmatrix}u\\ 0\end{bmatrix}, \tag{13}$$

where α_1 is the deviation of the first link from the vertical, $\alpha^d = 0$; α_2 is the deviation of the second link from the extension line of the first link; ν is the relative damping, assumed equal in both joints; M, B, C are the matrices of inertial, dissipative and quasi-elastic coefficients, respectively; u is the control input at the suspension point.

The square matrices take the form

$$M=\begin{bmatrix}5 & 2\\ 2 & 1\end{bmatrix},\ B=\begin{bmatrix}\nu & 0\\ 0 & \nu\end{bmatrix},\ C=\begin{bmatrix}3 & 1\\ 1 & 1\end{bmatrix}.$$

Since

$$B = \nu(2C - M),$$

the characteristic polynomial of model (13) has the form

$$x(p) = \det[M(p^2 - 2\nu p) + C(1 + 4\nu p)],$$

and, therefore,

$$x(p) = [p^2 - 2\nu p + (\omega_1)^2(1 + 4\nu p)]\cdot[p^2 - 2\nu p + (\omega_2)^2(1 + 4\nu p)], \tag{14}$$

where ω_1, ω_2 are the dimensionless natural frequencies of the double pendulum;

$$\omega_1 = \sqrt{2-\sqrt{2}} \approx 0.77,\ \omega_2 = \sqrt{2+\sqrt{2}} \approx 1.85.$$

Taking the variable $\alpha_1(t)$ as the output, we write the model of the plant

$$\alpha_1(p) = H_2(p)u(p),$$

where $H_2(p)=\dfrac{p^2+2\nu p+1}{x(p)}$ is the transfer function.

The processes in the closed-loop system with the parametric controller

$$u = -[\mu \sin(kt - \varphi)]\alpha_1 \tag{15}$$

satisfy the equation

$$H_2^{-1}(d)\cdot\alpha_1 + [\mu\cdot\sin(kt - \varphi)]\cdot\alpha_1 = 0. \tag{16}$$

The range of admissible values of the dimensionless amplitude μ is calculated in the same way as for the Mathieu equation:

$$\mu < H_2^{-1}(0) = \omega_1^2\omega_2^2 = 2.$$

To determine the boundary of the first parametric resonance, we use the complex transfer coefficient (4) as an approximate model of the parametric controller. Varying μ, we calculate the frequencies that are roots of the equation

$$\left|W^{-1}(i\varphi)\right| = \frac{2}{\mu} = \left|H_2(i\frac{\omega}{\omega_0})\right|\Big|_{\frac{\omega}{\omega_0}=\frac{k}{2}}. \tag{17}$$

Eq. (17) may have four roots; therefore, the excitation region of the first parametric resonance for the two-link pendulum consists of two sub-regions near the doubled natural frequencies. Parametric resonance in the closed-loop system (16) occurs if the frequency of the parameter k is close to twice the first natural frequency ω_1 or twice the second natural frequency ω_2. It is convenient to determine the resonance boundaries using Bode diagrams:

$$L_2 = 20 \log|H_2(i\omega/\omega_0)|.$$

Fig. 4,*a* shows the Bode diagram L_2 at $\nu = 0.05$, which can have only two intersection points with the line

$$L_1 = 20 \log(2/\mu) \text{ at } \mu < 2.$$

Therefore, the excitation region of the first parametric resonance in the closed-loop system under consideration is located near the doubled first natural frequency. Fig. 4,*b* shows the boundary of the first parametric resonance.

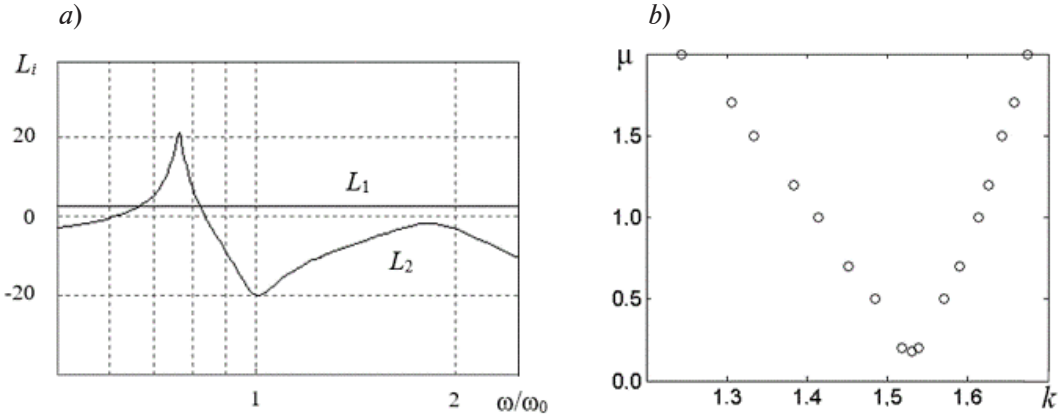


Fig. 4. Graphical representation of the solution of Eq. (17) for coefficients $\nu = 0.05$, $\mu = 1.5$ (*a*); dependence $\mu(k)$, which is the boundary of the first parametric resonance (*b*)

The parametric controller (15) is implemented approximately (as described above): for this reason, the measured angle $\alpha_1(t)$ is squared as a first step to generate a periodic signal. However, the free oscillations of the two-link pendulum for arbitrary initial conditions are a two-frequency process, since the roots of the characteristic polynomial (14) take the form

$$p_{12} = -(3-2\sqrt{2})\nu \pm i\sqrt{2-\sqrt{2}-(17-12\sqrt{2})\nu^2};$$

$$p_{34} = -(3+2\sqrt{2})\nu \pm i\sqrt{2+\sqrt{2}-(17+12\sqrt{2})\nu^2}.$$

Therefore, the variable $\alpha_1(t)$ is a superposition of exponentially decaying oscillations with frequencies depending on ν. For $\nu = 0.05$, the logarithmic decrement of damped oscillations with the second frequency is 14.2 times larger than that with the first frequency. Therefore, the main objective of parametric control is to damp the lower-frequency oscillations. It is expected that only the lower-frequency component remains in the measurements of $\alpha_1(t)$ in the closed-loop system (16) after a certain time. The parametric controller can efficiently damp the oscillations $\alpha_1(t)$ provided that the amplitude μ is sufficient and the phase shift φ ensures the stability of the closed-loop system.

Since no active control input is provided at the joint between the two links, the variable $\alpha_2(t)$ varies in accordance with the equation

$$\ddot{\alpha}_2 + 2\nu\dot{\alpha}_2 + \alpha_2 = -2\ddot{\alpha}_1 - \alpha_1.$$

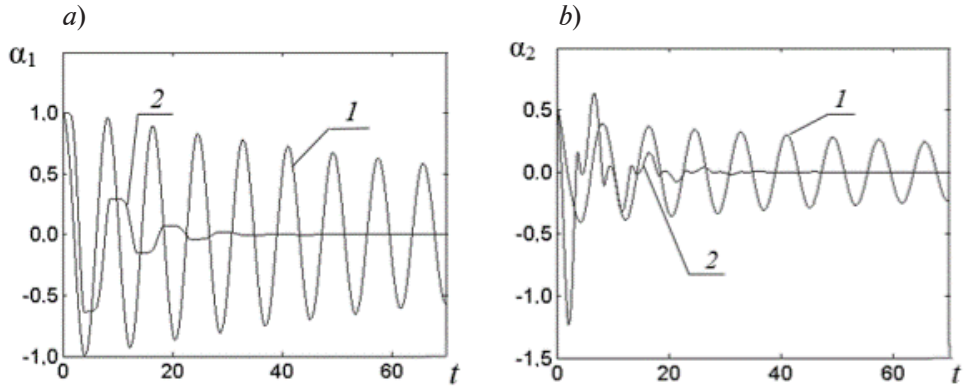


Fig. 5. Waveforms of variables α_1 (*a*) and α_2 (*b*):
free oscillations at $\nu = 0.05$ (curves *1*) and responses in the closed-loop system
with the parametric controller at $\mu = 1.5$, $\tau = 0$ (curves *2*)

The results of numerical simulation of the closed-loop system, which differs from Eq. (16) by the approximate implementation of the parametric controller, are shown in Fig. 5. To demonstrate the efficiency of the parametric controller, the free oscillation waveforms of the lightly damped two-link pendulum are also shown for comparison.

The settling time in the closed-loop system was significantly reduced compared to that of the free oscillations.

Conclusion

We examined the performance of a parametric controller incorporated into a closed-loop system designed to accelerate stabilization. A procedure for adjusting the controller's variable coefficients was proposed. Numerical simulation shows that exact tuning is not required to achieve parametric damping; it is sufficient to choose the amplitude and delay from the calculated range, while the frequency automatically doubles. We solved various stabilization problems for a lightly damped oscillator, where parametric control proved efficient.

REFERENCES

1. **Bolotin V. V.,** On the transverse vibrations of rods excited by periodic longitudinal forces, In collected works: "Transverse vibrations and critical velocities", No. 1., USSR Acad. Sci. Publ., Moscow (1951) 46 −77 (in Russian).

2. **Kapitsa P. L.,** Pendulum with vibrating suspension, Physics-Uspekhi. 44 (1) (1951) 7−20 (in Russian).

3. **Butikov E. I.,** Rasshirennyy i utochnennyy kriteriy ustoychivosti mayatnika Kapitsy [Extended and stable criteria of Kapitsa's pendulum], Computer Tools in Education journal. (2) (2011) 16−26 (in Russian).

4. **Belomytseva E. G., Kurin A. F., Tulenko E. B.,** The Cauchy problem for the Mathieu equation with damping at parametric resonance, Bulletin of Voronezh State University. Series: Physics. Mathematics. (3) (2018) 105−125 (in Russian).

5. **Mailybayev A. A., Seyranian A. P.,** Parametric resonance in systems with small dissipation, J. Appl. Math. Mech. 65 (5) (2001) 755−767.

6. **Seyranyan A. P., Maylybayev A. A.,** Vibrational stabilization of statically unstable systems, Doklady Physics. 54 (6) (2009) 294−300.

7. **Arkhipova I. M.,** On stabilization of a triple inverted pendulum via vibration of a support point with an arbitrary frequency, Vestnik of the St. Peterburg University.Mathematics.52 (2) (2019) 194−198.

8. **Belyayev A. K., Tovstik T. P., Morozov N. F., Tovstik P. E.,** The stability of a flexible vertical rod on a vibrating support, Vestnik of the St. Petersburg University. Mathematics. 51 (3) (2018) 296−304.

9. **Nayfeh A. H.,** Introduction to perturbation techniques, John Wiley & Sons, New York, 1981.

10. **Trubetskov D. I.,** Oscillations and waves: In linear and nonlinear systems (Book series "Mathematics and its applications"), Springer Netherlands, Dordrecht, 2011.

11. **Blekhman I. I.,** Vibrational mechanics. Nonlinear dynamic effects, general approach, applications, World Scientific Publishing Co. Pte Ltd., Singapore, 2000.

12**. Kuznetsov A. P., Kuznetsov S. P., Ryskin N. M.,** Nelineynyye kolebaniya [Nonlinear oscillations], Fizmatlit Publishing, Moscow, 2002 (in Russian).

13. **Budanov V. M.,** Reduction of the Mathieu equation to a nonlinear equation of the first order, Moscow University Mechanics Bulletin. 71 (4) (2016) 98–101.

14. **Chechurin L. S.,** Harmonic stationarization method and evaluation of robustness of periodic time-variant control systems, In collection of scientific papers "Large-scale Systems Control", Iss. 22, Institute of Control Sciences RAS, Moscow (2008) 70–85 (in Russian).

15. **Tondl A., P□st L.,** To the parametric anti-resonance application, Eng. Mech. 17 (2) (2010) 135–144.

16. **Dohnal F.,** Damping by parametric stiffness excitation: Resonance and anti-resonance, J. Vib. Control. 2008. Vol. 14 (5) (2008) 669–688.

17. **Chechurin L., Chechurin S.,** Physical fundamentals of oscillations: Frequency analysis of periodic motion stability, Springer International Publishing, Cham, Switzerland, 2018.

18. **Chechurin L., Mandrik A., Vostrov K., Chechurin S.,** Parametric and coordinate control of oscillating systems: Physics-based oscillation feedback design, IEEE Access. 9 (03 Aug) (2021) 113500–113507.

19. **Kulizhnikov D. B., Tovstik P. E., Tovstik T. P.,** The basin of attraction in the generalized Kapitsa problem, Vestnik of the St. Petersburg University. Mathematics. 52 (3) (2019) 309–316.

20. **Smirnov A. S., Smolnikov B. A.,** Optimization of oscillation damping modes of a spatial double pendulum: 1. Formulation of the problem, Vestnik of the St. Petersburg University. Mathematics. 55 (2) (2022) 243–248.

21. **Smirnov A. S., Smolnikov B. A.,** Optimization of oscillation damping modes of a spatial double pendulum: 2. Solution of the problem and analysis of the results, Vestnik of the St. Petersburg University. Mathematics. 56 (1) (2023) 93–106.

СПИСОК ЛИТЕРАТУРЫ

1. **Болотин В. В.** О поперечных колебаниях стержней, вызываемых периодическими продольными силами // Сб. статей «Поперечные колебания и критические скорости». Вып. 1. Изд. АН СССР, 1951. С. 46–77.

2. **Капица П. Л.** Маятник с вибрирующим подвесом // Успехи физических наук. 1951. Т. 44. № 1. С. 7–20.

3. **Бутиков Е. И.** Расширенный и уточненный критерий устойчивости маятника Капицы // Компьютерные инструменты в образовании. 2011. № 2. С. 16–26.

4. **Беломытцева Е. Г., Курин А. Ф., Туленко Е. Б.** Задача Коши для уравнения Матье с затуханием при параметрическом резонансе // Вестник Воронежского государственного университета. Серия: Физика. Математика. 2018. № 3. С. 105–125.

5. **Майлыбаев А. А., Сейранян А. П.** Параметрический резонанс в системах с малой диссипацией // Прикладная математика и механика. 2001. Т. 65. № 5. С. 779–792.

6. **Сейранян А. П., Майлыбаев А. А.** Вибрационная стабилизация статически неустойчивых систем // Доклады Академии наук. 2009. Т. 426. № 4. С. 480–486.

7. **Архипова И. М.** О стабилизации тройного перевернутого маятника с помощью вибрации точки опоры произвольной частоты // Вестник Санкт-Петербургского университета. Математика. Механика. Астрономия. 2019. Т. 6. № 2. С. 281–287.

8. **Беляев А. К., Морозов Н. Ф., Товстик П. Е., Товстик Т. П.** Устойчивость гибкого вертикального стержня на вибрирующем основании // Вестник Санкт-Петербургского университета. Математика. Механика. Астрономия. 2018. Т. 5. № 3. С. 477–488

9. **Найфэ А. Х.** Введение в методы возмущений. М.: Мир, 1984. 535 с.

10. **Трубецков Д. И., Рожнёв А. Г.** Линейные колебания и волны. М.: Физматлит, 2001. 415 с.

11. **Блехман И. И.** Вибрационная механика. М.: Наука, 1994. 400 с.

12. **Кузнецов А. П., Кузнецов С. П., Рыскин Н. М.** Нелинейные колебания. (Серия «Современная теория колебаний и волн»). М.: Физматлит, 2002. 292 с.

13. **Буданов В. М.** Редукция уравнения Матье к нелинейному уравнению первого порядка // Вестник Московского университета. Серия 1. Математика. Механика. 2016. № 4. С. 66–69.

14. **Чечурин Л. С.** Метод гармонической стационаризации и оценка робастности периодически нестационарных систем управления // Сб. трудов «Управление большими системами». Вып. 22. М.: ИПУ РАН, 2008. С. 70–85.

15. **Tondl A., Půst L.** To the parametric anti-resonance application // Engineering Mechanics. 2010. Vol. 17. No. 2. Pp. 135–144.

16. **Dohnal F.** Damping by parametric stiffness excitation: Resonance and anti-resonance // Journal of Vibration and Control. 2008. Vol. 14. No. 5. Pp. 669–688.

17. **Чечурин С. Л., Чечурин Л. С.** Физические основы теории колебаний. СПб.: Изд-во СПбГПУ, 2005. 256 с.

18. **Chechurin L., Mandrik A., Vostrov K., Chechurin S.** Parametric and coordinate control of oscillating systems: Physics-based oscillation feedback design // IEEE Access. 2021. Vol. 9. 03 August. Pp. 113500–113507.

19. **Кулижников Д. Б., Товстик П. Е., Товстик Т. П.** Области притяжения в обобщенной задаче Капицы // Вестник Санкт-Петербургского университета. Математика. Механика. Астрономия. 2019. Т. 6. № 3. С. 482–492.

20. **Смирнов А. С., Смольников Б. А.** Оптимизация режимов гашения колебаний пространственного двойного маятника. I. Постановка задачи // Вестник Санкт-Петербургского университета. Математика. Механика. Астрономия. 2022. Т. 9. № 2. С. 357–365.

21. **Смирнов А. С., Смольников Б. А.** Оптимизация режимов гашения колебаний пространственного двойного маятника. II. Решение задачи и анализ результатов // Вестник Санкт-Петербургского университета. Математика. Механика. Астрономия. 2023. Т. 10. № 1. С. 121–138.

THE AUTHOR

SMIRNOVA Nina A.
Peter the Great St. Petersburg Polytechnic University
29 Politechnicheskaya St., St. Petersburg, 195251, Russia
smirnova_na@spbstu.ru
ORCID: 0000-0001-8831-743x

СВЕДЕНИЯ ОБ АВТОРЕ

СМИРНОВА Нина Анатольевна – *кандидат технических наук, доцент Высшей школы механики и процессов управления Санкт-Петербургского политехнического университета Петра Великого.*
195251, Россия, г. Санкт-Петербург, Политехническая ул., 29
smirnova_na@spbstu.ru
ORCID: 0000-0001-8831-743x

Received 16.01.2026. Approved after reviewing 09.02.2026. Accepted 09.02.2026.
Статья поступила в редакцию 16.01.2026. Одобрена после рецензирования 09.02.2026. Принята 09.02.2026.

© Peter the Great St. Petersburg Polytechnic University, 2026

Научное издание

НАУЧНО-ТЕХНИЧЕСКИЕ ВЕДОМОСТИ САНКТ-ПЕТЕРБУРГСКОГО ГОСУДАРСТВЕННОГО ПОЛИТЕХНИЧЕСКОГО УНИВЕРСИТЕТА. ФИЗИКО-МАТЕМАТИЧЕСКИЕ НАУКИ

«ST. PETERSBURG STATE POLYTECHNICAL UNIVERSITY JOURNAL. PHYSICS AND MATHEMATICS»

ТОМ 19, № 2, 2026

Учредитель и издатель – Федеральное государственное автономное образовательное учреждение высшего образования «Санкт-Петербургский политехнический университет Петра Великого»

Журнал зарегистрирован Федеральной службой по надзору в сфере информационных технологий и массовых коммуникаций (Роскомнадзор).
Свидетельство о регистрации ПИ № ФС77-52144 от 11.12.2012 г.

Редакция

д-р физ.-мат. наук, профессор *В. К. Иванов* – председатель ред. коллегии
д-р физ.-мат. наук, профессор *А. Э. Фотиади* – зам. председателя ред. коллегии
д-р физ.-мат. наук, профессор *В. В. Дубов*
д-р физ.-мат. наук, профессор *П. А. Карасёв*
канд. физ.-мат. наук, доцент *В. М. Капралова*
канд. физ.-мат. наук *О. А. Яцуржинская* – научный редактор, корректор
А. С. Колгатина – переводчик
Н. А. Бушманова – ответственный секретарь

Телефон редакции 8 (812) 552-62-16

Сайт https://physmath.spbstu.ru/

E-mail: physics@spbstu.ru

Компьютерная верстка *Н. А. Бушмановой*

Подписано в печать 30.06.2026 г. Дата выхода в свет 30.07.2026 г.
Формат 60x84/8. Печать цифровая.
Усл. печ. л. Тираж 1000. Заказ .
Цена: Бесплатно.

Отпечатано с готового оригинал-макета, предоставленного ИЦ "ИКИ",
в Издательско-полиграфическом центре
Санкт-Петербургского политехнического университета.
195251, Санкт-Петербург, Политехническая ул., 29.
Тел.: (812) 552-77-17; 550-40-14.

УСЛОВИЯ ПУБЛИКАЦИИ СТАТЕЙ

в журнале «Научно-технические ведомости
Санкт-Петербургского государственного политехнического университета.
Физико-математические науки»

1.ОБЩИЕ ПОЛОЖЕНИЯ

Журнал «Научно-технические ведомости Санкт-Петербургского государственного политехнического университета. Физико-математические науки» является периодическим печатным научным рецензируемым изданием. Зарегистрирован в Федеральной службе по надзору в сфере информационных технологий и массовых коммуникаций (Свидетельство ПИ №ФС77-52144 от 11 декабря 2012 г.) и распространяется по подписке агентства «Роспечать» (индекс издания 71823).

С 2008 года журнал издавался в составе сериального издания "Научно-технические ведомости СПбГПУ". **Сохраняя преемственность и продолжая научные и публикационные традиции сериального издания «Научно-технические ведомости СПбГПУ», журнал издавали под сдвоенными международными стандартными сериальными номерами ISSN 1994-2354 (сериальный) 2304-9782.** В 2012 году он зарегистрирован как самостоятельное периодическое издание **ISSN 2304-9782** (Свидетельство о регистрации ПИ № ФС77-52144 от 11 декабря 2012 г.). С 2012 г. начат выпуск журнала в двуязычном оформлении.

Издание входит в Перечень ведущих научных рецензируемых журналов и изданий (перечень ВАК) и принимает для печати материалы научных исследований, а также статьи для опубликования основных результатов диссертаций на соискание ученой степени доктора наук и кандидата наук по следующим основным научным направлениям: **Физика, Математика, Механика**, включая следующие шифры научных специальностей: 1.1.8., 1.1.9., 1.3.2., 1.3.3., 1.3.4., 1.3.5., 1.3.6., 1.3.7., 1.3.8., 1.3.11., 1.3.19.

Журнал представлен в Реферативном журнале ВИНИТИ РАН и включен в фонд научно-технической литературы (НТЛ) ВИНИТИ РАН, а также в международной системе по периодическим изданиям «Ulrich's Periodicals Directory». Индексирован в базах данных «Российский индекс научного цитирования» (РИНЦ), Web of Science (Emerging Sources Citation Index).

Периодичность выхода журнала – 4 номера в год.

Редакция журнала соблюдает права интеллектуальной собственности и со всеми авторами научных статей заключает издательский лицензионный договор.

2. ТРЕБОВАНИЯ К ПРЕДСТАВЛЯЕМЫМ МАТЕРИАЛАМ

2.1. Оформление материалов

1. Рекомендуемый объем статей – 12-20 страниц формата А-4 с учетом графических вложений. Количество графических вложений (диаграмм, графиков, рисунков, фотографий и т.п.) не должно превышать шести.

2. Число авторов статьи, как правило, не должно превышать пяти человек.

3. Авторы должны придерживаться следующей обобщенной структуры статьи: вводная часть (актуальность, существующие проблемы – объем 0,5 – 1 стр.); основная часть (постановка и описание задачи, методика исследования, изложение и обсуждение основных результатов); заключительная часть (предложения, выводы – объем 0,5 – 1 стр.); список литературы (оформление по ГОСТ 7.0.5-2008).

В списки литературы **рекомендуется** включать ссылки на научные статьи, монографии, сборники статей, сборники конференций, электронные ресурсы с указанием даты обращения, патенты.

Как правило, **нежелательны** ссылки на диссертации и авторефераты диссертаций (такие ссылки допускаются, если результаты исследований еще не опубликованы, или не представлены достаточно подробно).

В списки литературы **не рекомендуется** включать ссылки на учебники, учебно-методические пособия, конспекты лекций, ГОСТы и др. нормативные документы, на законы и постановления, а также на архивные документы (если все же необходимо указать такие источники, то они оформляются в виде сносок).

Рекомендуемый объем списка литературы для обзорных статей – не менее 50 источников, для остальных статей – не менее 10.

Доля источников давностью менее 5 лет должна составлять не менее половины. Допустимый процент самоцитирования – не выше 10 – 20. Объем ссылок на зарубежные источники должен быть не менее 20%.

4. УДК (UDC) оформляется и формируется в соответствии с ГОСТ 7.90-2007.

5. Набор **текста** осуществляется в редакторе **MS Word.**

6. **Формулы** набираются в редакторе MathType (не во встроенном редакторе Word) (мелкие формулы, символы и обозначения набираются без использования редактора формул). **Таблицы** набираются в том же формате, что и основной текст. В тексте буква «ё» заменяется на букву «е» и оставляется только в фамилиях.

7. **Рисунки** (в формате .tiff, .bmp, .jpeg) и **таблицы** оформляются в виде отдельных файлов. Шрифт – **Times New Roman**, размер шрифта основного текста – 14, интервал – 1,5. Таблицы большого размера могут быть набраны кеглем 12. Параметры страницы: поля слева – 3 см, сверху и снизу – 2 см, справа – 1,5 см. Текст размещается без знаков переноса. Абзацный отступ – 1 см.

2.2. Представление материалов

1. Представление всех материалов осуществляется в электронном виде через электронную редакцию (http://journals.spbstu.ru). После регистрации в системе электронной редакции автоматически формируется персональный профиль автора, позволяющий взаимодействовать как с редакцией, так и с рецензентом.

2. Вместе с материалами статьи должно быть представлено экспертное заключение о возможности опубликования материалов в открытой печати.

3. Файл статьи, подаваемый через электронную редакцию, должен содержать только сам текст без названия, списка литературы, аннотации и ключевых слов, фамилий и сведений об авторах. Все эти поля заполняются отдельно через электронную редакцию.

2.3. Рассмотрение материалов

Предоставленные материалы (п. 2.2) первоначально рассматриваются редакционной коллегией и передаются для рецензирования. После одобрения материалов, согласования различных вопросов с автором (при необходимости) редакционная коллегия сообщает автору решение об опубликовании статьи. В случае отказа в публикации статьи редакция направляет автору мотивированный отказ.

При отклонении материалов из-за нарушения сроков подачи, требований по оформлению или как не отвечающих тематике журнала материалы не публикуются и не возвращаются.

Редакционная коллегия не вступает в дискуссию с авторами отклоненных материалов.

При поступлении в редакцию значительного количества статей их прием в очередной номер может закончится **ДОСРОЧНО**.

E-mail: physics@spbstu.ru,
Тел. редакции 8 (812) 552-62-16.
Сайт журнала: https://physmath.spbstu.ru/